SED & Variability Studies of AGN

HUTTON, SARAH JANE

SED & Variability Studies of AGN

Sarah Hutton

A Thesis presented for the degree of
Doctor of Philosophy

Extragalactic Astronomy and Cosmology
Department of Physics
Durham University
United Kingdom

2012

To Rob,

for making the stars seem not that far away.

The amazing thing is that every atom in your body came from a star that exploded. And, the atoms in your left hand probably came from a different star than in your right hand. It is really the most poetic thing I know about physics: You are all stardust...

The stars died so that you could be here today.

Lawrence Krauss

SED & Variability Studies of AGN

Sarah Hutton

Abstract

This thesis contains the results of studies into the causes of variability seen in the optical and X-ray emission from matter accreting onto supermassive black holes (SMBHs) in active galactic nuclei (AGN).

The first chapter provides a brief overview of the history of optical and X-ray astronomy along with a summary of the principle properties of AGN. The second chapter investigates the dust-to-gas relationship for a sample of 1,201 X-ray detected quasars. We carry out an in-depth optical and X-ray spectral analysis and produce composite spectra for gas absorbed and dust reddened quasars. We find that the objects with the largest gas column densities are not the objects with the largest amounts of dust reddening. This study also highlights problems in constraining absorption levels in objects with low-quality X-ray spectra.

We then present optical-to-X-ray spectral energy distributions (SEDs) for 170 Type 1 AGN. We use a new broadband SED model, which combines the standard disc emission with low- and high- temperature Comptonisation components through the introduction of a coronal radius. We find that objects that have an Eddington ratio greater than unity have larger disc luminosities, lower black hole mass, higher mass accretion rate and smaller coronal radii, than the rest of the sample.

We conduct a detailed optical and X-ray variability study on a subset of 41 of these objects in the fourth chapter. We combined optical light curves from the Catalina Sky Survey (CSS) with long duration X-ray observations from the *XMM-Newton* satellite. We found that the objects with the lowest black hole masses were the least variable. However, we did not find the expected relationship between luminosity and variability, probably due to the wavelength range observed by CSS and selection biases in our sample.

The final two chapters report results from pilot studies based on data from the Pan-STARRS telescope. In the fifth chapter we present an in-depth study of a highly variable object discovered as part of the Pan-STARRS supernovae search, and in the sixth chapter we investigate a subset of the light curves produced in the Medium Deep Survey (MDS) by analysing the light curves of 39 quasars including 12 broad absorption line quasars (BALQSOs). Finally, we also examine the potential for future studies, by cross-matching a large sample of spectroscopically identified Seyfert 2 AGN to the large area 3π catalogue.

Contents

List of Figures

Declaration

The work described in this thesis was undertaken between October 2008 and August 2012 while the author was a research student under the supervision of Professor Martin Ward in the Department of Physics at Durham University. This work has not been submitted for any other degree at Durham University or any other University.

Various figures in the thesis are reproduced from the work of other authors for illustration or discussion. Such figures are always credited in the text.

The work described in Chapters 2, 3, 4, 5 and 6 was performed in collaboration with others. All text was written by myself.

The initial X-ray analysis of the quasar sample in Chapter 2 was completed by Dr. S. Mateos and Dr. A. Scott, after I created the sample. All further X-ray analysis and the optical analysis was performed by myself.

Dr. J. Gelbord provided me with the samples obtained from cross-matching the SDSS and *XMM-Newton* catalogues used in Chapters 3 and 4. Dr. J. Mullaney wrote the original emission line fitting routines used in Chapter 3, that I then developed for use in Chapters 3 and 5.

The broadband SED model used in Chapter 3 was developed by Prof. Chris Done but all of the fits and analysis were performed by myself.

The object discussed in Chapter 5 was found by the Belfast PS1 Transient Team and the optical spectroscopic and photometric data was obtained by their ongoing campaigns. All analysis of this data was performed by myself.

The parent sample used in Chapter 6 is part of an ongoing spectroscopic campaign on quasar targets in the Pan-STARRS MDS fields lead by Prof. P. Green. All of the spectroscopic analysis and all Pan-STARRS data reduction and analysis was performed by myself.

Acknowledgements

I would like to begin by thanking my supervisor Prof. Martin Ward. Without his constant guidance and support over the last 4 years, this thesis wouldn't exist. I would also like to thank Prof. Dave Alexander for introducing me to the world of research during my fourth year project, and continuing that support during my PhD. Special thanks must also go to Prof. Chris Done, whose insightful comments and observations over the last 4 years have helped shaped my research. 'Whiteboard torture' might not be the easiest thing to persevere through at 9 am, but it definitely helped me make some headway into understanding accretion physics!

The astronomy department at Durham University is a unique gathering of people, all of whom have proven to be extremely helpful and approachable during my time here and I will miss being part of such an environment.

I would like to thank my partners in crime, Alice Mills and Rachael Livermore for providing me with much needed light relief as we dash across the North East trying to teach anybody who will listen about the wonders of Space and 'Science!'

On that note I would also like to thank Wayne Dobby and his amazing team of technicians who have always gone above in beyond in helping us sort out equipment and have never said a word of reproach for the state in which we return the planetarium.

I would like to thank all of the Ph.D. students and post-docs, both past and present, without whom my time in Durham would have been a lot less enjoyable. In no particular order I would like to mention Mike Hogan, Nicholas Tejos, Daniel Farrow, James Mullaney, John Stott, Julie Wardlow, Ryan Hickox, Jeanette Gladstone and Andy Goulding. I must also thank Lynn for keeping me supplied with tea and, most importantly, letting me know when free food is available in the Bransden Room.

Finally, I am eternally grateful to my family for their unwavering support through the years, and I can never repay them for taking an 11 year old girl with stars in her eyes to see the Saturn V moon rocket at the Kennedy Space Centre during a tropical storm. That visit is responsible for so much of who I am today. Thank you!

Chapter 1 | *Introduction*

1.1 The night sky

For millennia people from cultures all over the world have tried to understand what they saw above them in the night sky. Many people have been inspired to make great advances in science, technology and theology in their quest to understand the heavens. Most ancient civilisations have structures that were built to coincide with and record astronomical events. Here in the UK, our most famous example is Stonehenge near Salisbury. This stone circle was designed by druids to highlight the positions of both the Sun and the Moon at the summer and winter solstices and thus mark the longest and shortest days of the year.

Recording the solstices was a common occurrence in pre-historic cultures. At County Meath in Ireland, passage tombs were built to light up with the light of the Sun at the winter solstice. The Mayans also chose to mark the winter solstice, which they termed the annual 'death' of the Sun, with the creation of Chichén Itzá in Yucatan. Other cultures focused on the summer solstice, with the Anasazi tribe in New Mexico building the Great Kiva (an underground chamber) in Chaco Canyon to mark the sunrise at midsummer (Ruggles & Hoskin, 1996).

The cycle of the Sun and Moon had an enormous impact on the lives of these civilisations and it is understandable that structures and belief systems were built around them. Other cultures went further than just recording these events, taking precise measurements in order to closely monitor and sometimes predict events on Earth that coincided with those taking place in the sky. In Ancient Egypt, life revolved around the annual flooding of the river Nile. Only after the waters had mysteriously risen and subsided could the crops be planted and subsequently harvested. Accurately predicting the flood was key to a productive harvest and peaceful rulership. The brightest star in the sky is Sirius (or Sothis, as it was then known). For part of the year Sirius is made invisible by the glare of the Sun, but will re-appear briefly in the eastern sky just before dawn. Fortuitously, this appearance coincided with the flooding and gave the Egyptians the ability not only to predict the event, but also to

regulate their calendar to 365.25 days (North, 1994).

In Mesopotamia, the Babylonians were actively studying the sky from as early as 3000 BC, and their thorough records are recognised as containing the earliest known astronomical observations. They are credited with identifying constellations, developing a calendar tied to certain annual astronomical events and using this calendar to predict such events with incredible accuracy, particularly the motions of Venus.

As time progressed, so did the observations of the night sky and the knowledge that could be gleaned from them. The Greeks became the frontrunners in developing new theories to describe what was seen. Anaximander was the first to describe an eclipse without the need for mythology or supernatural beings. The philosopher Parmenides stated that the Earth was spherical and the Moon received its light from the Sun, while Empedocles of Acragas inferred that the Moon moving in front of the Sun caused solar eclipses. It was even proposed by Aristarchus that the Sun, not the Earth, was at the centre of the Universe and that we orbited around it. This theory fell out of fashion very quickly, superseded when Ptolomy expanded Aristotle's geocentric model to include complicated deferents and epicycles to explain the retrograde motion of the planets, keeping Earth at the centre of the Universe (Toomer, 1996).

It was also in Greece that the first star catalogues were made. Hipparchus developed a system for classifying stars on a six-degree scale ranging from one for the brightest to six for the faintest, with the magnitudes being determined by eye. Remarkably this system has persisted to this day, though it has been redefined and extended to account for our ever-increasing observing power.

During the Dark Ages in Western Europe, the Middle East became the hotbed of scientific advancement. The Greek texts were brought in, translated and improved upon. Stellar catalogues were developed, eclipses accurately predicted, the position of the ecliptic determined and the length of the year improved.

During this time, the cosmological viewpoint of Aristotle and Ptolomy's geocentric model still held, and it was only when the Arabic and Greek texts returned to Europe that this began to change. The Renaissance saw a transformation in astronomy more profound and fundamental than any time in the previous 3000 years. Devastatingly critical remarks on contemporary astronomy made by Johannes Müller, known as Regiomontanus, brought to light the errors of Ptolomy's work and their application by contemporary astronomers. Correcting

these errors required the observations of Tycho, Kepler's theories and Galileo's telescope as well as the development of Copernicus's heliocentric theory with the Sun at the centre of the Universe. When pointing out the errors he found, Regiomontanus could not have known that he would initiate a total reform of astronomy during the sixteenth and seventeenth centuries (Swerdlow, 1996).

Tycho Brahe was the last astronomer to work without the aid of the telescope, and it was thanks to his meticulous observations that Kepler was able to derive and publish his three laws on planetary motion (Kepler, 1609; Kepler et al., 1619).

While Kepler was deriving how planets moved in their celestial dance, Galileo Galilei was using the first astronomical telescope to study the sky. He found evidence of seas (craters) on the Moon as shown in Figure 1.1 and blemishes on the Sun that today we understand to be sunspots. After multiple observations of these blemishes, Galileo concluded that the Sun was actually rotating on its axis. At this time the moons of Jupiter were being discovered; Galileo was able to observe four of them and for the first time provided evidence that not everything visible in the sky orbited the Earth.

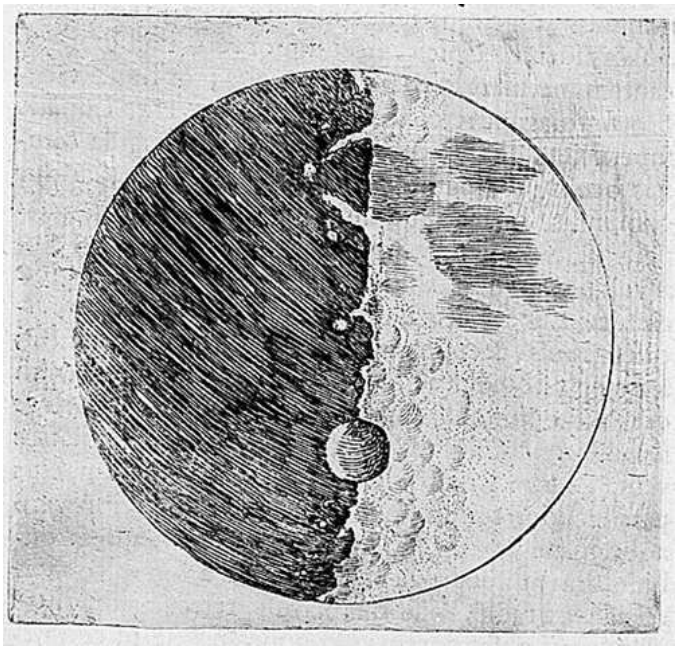

Figure 1.1: Drawing of the Moon, which he first observed on November 30th 1609, as seen through Galileo's telescope. (This image was taken from http://www.hps.cam.ac.uk/starry/galileo.html)

The next major leap forward in astronomical theory came with a physicist born the

same year that Galileo died. Isaac Newton and his book *Principia* (1687) with its theories of gravity (amongst many others) presented a force that could not only govern actions on Earth, but could also be expanded to encompass everything in the Universe. It was the expansion of this theory and its implications that lead to the discovery of the outer planets of Uranus, Neptune and Pluto.

Since then, astronomers have been driven to create more detailed observations of the sky, and with the desire to create better observations came the need for a re-evaluation of the classification system used for stars. In 1953, Johnson & Morgan developed a revision of the magnitude scale that is still used today. This system is designed such that the star Vega, in the constellation Lyrae, is defined to have a magnitude of zero. This provides a zero-point that the brightness of every star can be compared to, and therefore each star can have its brightness derived on this logarithmic scale. But while it is helpful to know how bright these objects appear to be to us this does not tell us how intrinsically bright the objects are. In order to solve this problem astronomers created the absolute magnitude scale, which is the magnitude we would observe the star to be if it was situated at a distance of 10 parsecs.

The invention of photography revolutionised the ease with which astronomers could record the sky. Photographic plates of images could also be studied to quantify the magnitude of the stars they captured. Most photographic plates are most sensitive to blue, but when we observe the sky we find that stars emit a multitude of colours. In order to standardise these measurements it was decided that the luminosity of stars would be measured at three distinct wavelengths: one in the ultraviolet (U) at $\sim$ 3600 Å, one in the blue (B) at $\sim$ 4300 Å and one in the visible (V) at $\sim$ 5500 Å. The differences in these three values form two colours *(U - B)* and *(B - V)* that are used to define the colour of a star.

Another method that allows us to characterise the properties of stars is via their optical spectrum. While the credit for obtaining the first stellar spectrum of the Sun goes to Joseph Fraunhofer, who discovered the absorption lines in the spectrum (now called Fraunhofer lines), it was only through the work of such notable scientists as the chemist Bunsen and the physicist Kirchhoff that the Fraunhofer lines were linked to those observed when different elements are burned on Earth, particularly sodium. This led to the conclusion that not only was sodium present in the Sun, but so were many other elements readily identifiable by the appropriate Fraunhofer lines.

With the appropriate elements found, astronomers could use this knowledge to begin to

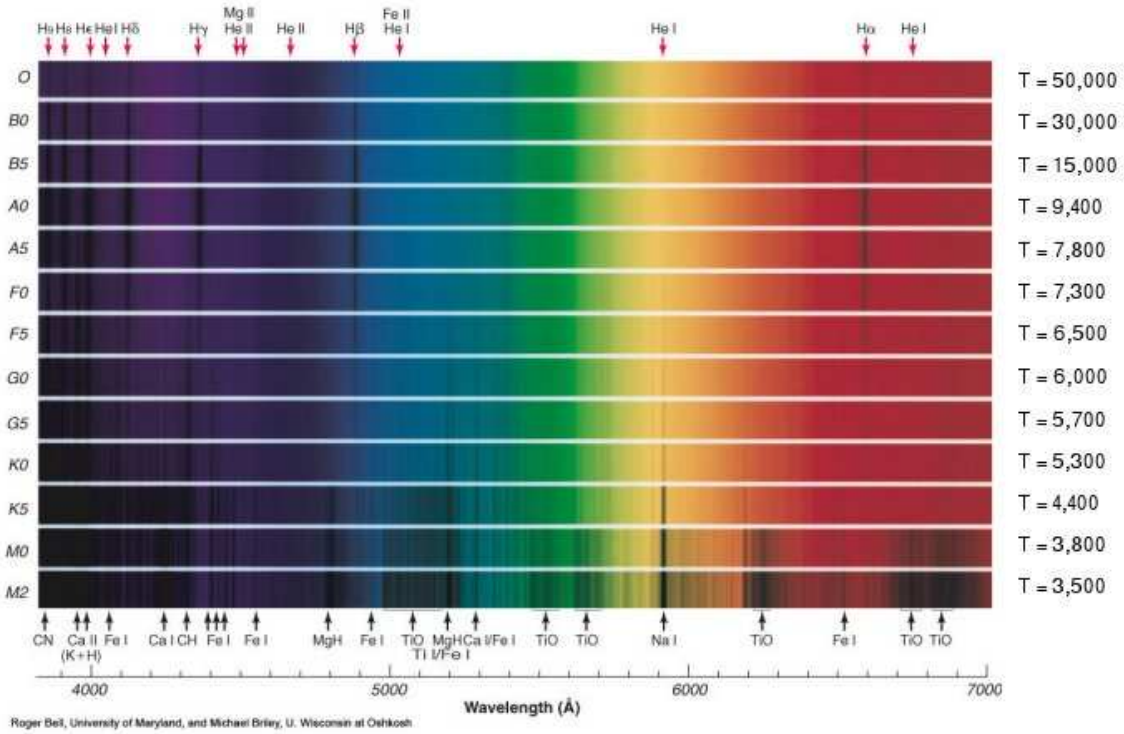

Figure 1.2: Spectra for a range of stellar types, demonstrating a range of lines and line strengths. The approximate temperatures of the star type are shown down the right of the image. (This image was taken from http://www.ifa.hawaii.edu/∼barnes/ast110_06/tlos.html)

classify stars. They began by ranking stars according to the strength of their hydrogen lines, beginning with A for those with the strongest lines, working alphabetically down through B, F, G, K, M, N, O and R to S to denote those with the weakest lines. However, it was discovered that this was not the full story as, while the hydrogen line luminosity decreased through this scale, other lines varied randomly, as did the colours. Morgan, Kellman & Hoffleit in 1943 finally established the sequence that is still in current use: O, B, A, F, G, K, M, N & S. The only addition, in modern times has been the introduction of subclasses, B0, B1, B2, ... B9, followed by A0. Figure 1.2 shows examples of stellar spectra classified by this system.

While thousands of years had been spent developing our knowledge of the cosmos through studies of the stars, our understanding was hampered by the fact that we could only use our eyes and optical light to aid us in our quest for comprehension of the Universe. Then during

the 1940s our view of the Universe was changed forever as new wavelengths became observable by astronomers. New branches of astronomy emerged and new discoveries abounded with the rise of radio astronomy. Millimetre, infrared (IR), ultraviolet (UV), X-rays and γ-rays all rapidly followed. These new disciplines allowed for the development of new areas of astrophysics, several of which are mentioned in the following sections.

1.2 The X-ray view of the night sky

The discovery of X-rays is credited to the resolute nature of Professor Wilhelm Röntgen. In 1885 Röntgen was carrying out a series of experiments into the external effects of various types of vacuum tube equipment when an electrical discharge was passed through them, when he noticed that the cathode rays he was producing were having unexpected results. On the 8th November 1895 he conducted an experiment to explore this phenomenon; the results he acquired made him suspect a new type of ray was responsible. As he was unsure of the nature of this new ray he had found, and as he had carried out the experiment on a Friday, he spent the weekend checking his results before announcing what he had discovered. Once set on a task Röntgen was hard to distract and moved in to the laboratory to work on his new project. Within two weeks he had built a device able to picture these new X-rays, so named as X is the mathematical notation for something unknown. The first picture of a human taken in X-rays is an image of Röntgen's wife's hand shown in Figure 1.3, where the rings she was wearing can clearly be seen, even if the picture is not as clear as modern X-ray images.

Just 50 days after first recording X-rays he published a paper (Stanton, 1896), and while he refused to comment on the nature of this new type of light, he did describe it as 'a new type of motion' (Dam, 1896). The discovery of Röntgen rays, or X-rays as they persisted to be called despite Röntgen's objections, earned him the first ever Nobel Prize for Physics just 6 years later in 1901.[1]

While the discovery allowed research into the world of X-rays, it was only when its wave nature was discovered (Laüe, 1913; Bragg, 1913) that X-rays began to be used in the areas with which we now associate them. Their highly penetrating nature made their use in medicine an obvious application, as they are not only used in radiography but were also

[1] http://nobelprize.org/nobel prizes/physics/

Figure 1.3: Hand mit Ringen (Hand with Rings). This a copy of a print of one of the first X-ray images taken. It is the left hand of Röntgen's wife Anna Bertha Ludwig. This print was presented to Professor Ludwig Zehnder of the Physik Istitut, University of Freiburg, on 1 January 1896. (This image was taken from http://science.hq.nasa.gov/kids/imagers/ems/xrays.html)

used by Rosalind Franklin to analyse the structure of DNA.

With X-rays contributing to our understanding of so many different areas of science, it was only to be expected that astronomers would want to use them to study the sky, but this is where astronomers ran into a problem that did not affect other branches of science: the atmosphere. One of the major advantages of the atmosphere that surrounds our planet is that it absorbs potentially harmful radiation before it can reach the ground; this includes X-rays. As Figure 1.4 shows, an X-ray detector would have to be placed at least 100 km above the ground to detect X-rays from space, a height only achieved by rockets and satellites. In 1948 the US Naval Research Laboratory launched a rocket equipped with beryllium filters, which allowed astronomers to get their first view of the Sun in X-rays and heralded the beginning of X-ray astronomy; this was quantified a year later when counter detectors replaced the photographic plates.

Unlike the discovery of X-rays themselves, X-ray astronomy did not immediately change

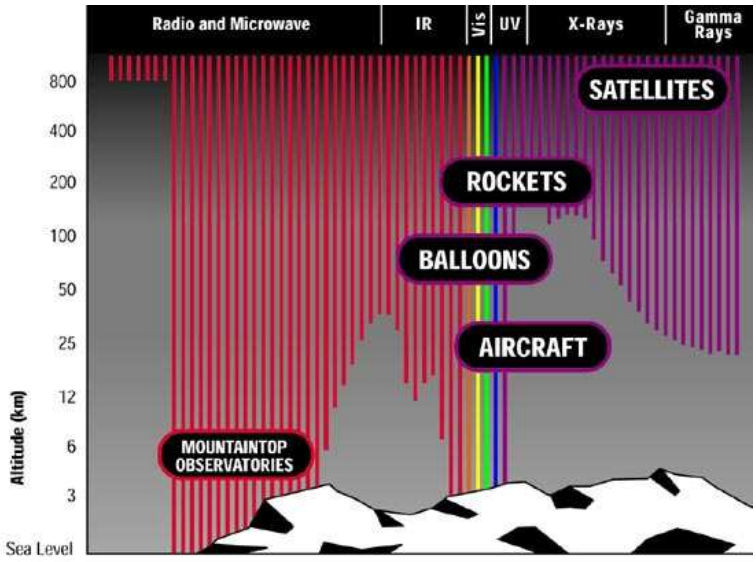

Figure 1.4: Diagram showing the absorption of light by the Earth's atmosphere. It can be seen that infrared, ultraviolet and high energy radiation (X-rays and γ rays) are absorbed well above the ground; spacecraft are needed to see these wavelengths. (This image was taken from http://snap.lbl.gov/science/space.php)

the way we saw the Universe. Early studies focused on the Sun which, despite being an incredibly bright X-ray source in our local sky, is only so due to its proximity. This left many astronomers disheartened, and even though extra-stellar detections were made they were largely ignored as they were part of a series of experiments on the interactions of X-rays with the ionosphere (interested readers should look at Kupperian & Friedman, 1958; Friedman, 1959; Friedman, 1960). However, some persevered and by 1969 enough discoveries had been made to host an IAU symposium on 'Non-Solar X- and Gamma-ray Astronomy' in Rome. This meeting highlighted the major discoveries in X-ray astronomy during the 1960s and showcased the discovery of the pulsar at the centre of the Crab nebula[2] (Bowyer et al., 1964; and references therein).

After the initial X-ray sources were discovered, sounding rockets with X-ray detectors on them were used to pinpoint sources with greater accuracy; once point-sources were discovered optical telescopes could then be used to find the optical counterpart to these objects. One

[2]Pulsars are rapidly rotating neutron stars that are highly magnetised and emit a beam of high energy photons along their axis. When this axis is inclined to the rotational axis, we can observe the beam as flashes as it passes through our line of sight.

such discovery highlighted a binary object; this led to the first theories suggesting that the X-ray source was fuelled by a matter transfer from the star to a more massive but compact companion, such as a white dwarf, neutron star or black hole, and proved to be the starting point for the field of accretion physics discussed in later sections.

While the era of sounding rockets was a successful one for X-ray astronomy, in order to advance the field further an orbital X-ray programme was required. The first orbiting satellite launched was the *UHURU* satellite; launched in 1970, its mission was to provide the first all-sky survey in the 2 - 20 keV energy range. Within 2 years it had identified more than 150 discreet X-ray sources; by the time the final catalogue was produced in 1978 it had identified 339 objects. It found that for the most part, the brightest sources were associated with binary systems and supernovae remnants.

The UK's first major foray into this field was with the *Copernicus* satellite, which was launched in 1972 in collaboration with the National Aeronautics and Space Administration's (NASA's) *Orbiting Astronomical Observatories* (OAO) programme. The UK's contribution to the on-board instruments was the X-ray astronomy experiment, developed by University College London/Mullard Space Science Laboratory. Princeton University provided the UV telescope. These two instruments worked together, allowing project scientists to identify X-ray sources by their UV characteristics. This led to the discovery of several long-period pulsars and rapid, intense variability from a radio source designated as Cen A.

The mid-to-late 1970s saw a number of X-ray satellites launched covering the energy range 0.1 - 55 keV and monitoring the whole sky. As part of these campaigns long-period pulsars were found with periodicities of minutes along with several X-ray transients.[3] Work was also done during this time to measure the X-ray background. The crowning glory of X-ray astronomy during the 1970s were the *High Energy Astronomy Observatory (HEAO)* and *HEAO-2* (better known as the *Einstein* observatory satellites). Between these two missions the first comprehensive measurement of the X-ray background was taken and timing studies on millisecond timescales were performed.

The next major mission launched was *Röntgensatellit* (or ROSAT; Trümper, 1982) in 1990. This was a mission funded by Germany, the UK and the USA and it carried three instruments designed to operate in the soft X-rays (0.1 - 2.4 keV) and the extreme ultraviolet

[3]Transients are sources that either brighten considerably or appear to emit for short periods before dimming or disappearing completely.

(EUV, 0.06 - 0.2 keV). The first six months were dedicated to an all-sky survey, which monitored $\sim$ 98% of the sky in the 0.25, 0.75 and 1.5 keV bands (Snowden et al, 1995). This part of the mission resulted in cataloguing more than 150,000 objects, the data from which are still heavily used today. The *Advance Satellite for Cosmology and Astrophysics (ASCA*; Tanka, Inoue & Holt, 1994) was the first X-ray observatory to use CCD detectors and was capable of allowing emission and absorption features in X-ray spectra to be resolved. The Rossi X-ray Timing Explorer *(RXTE)* was launched in the December of 1995 from the Kennedy Space Flight Centre to observe the 2 - 250 keV energy range. The satellite is still in use today, stationed in a low-Earth, 90 minute circular orbit. The launch of this satellite has provided an excellent opportunity for the study of timing variability, tagging events with an unprecedented timing resolution of microseconds. It has played a vital role in the analysis and understanding of Galactic sources and has paved the way for the current studies into the fractional variability of X-ray spectra discussed in Chapter 4.

The two major X-ray observatories that form the current generation were launched within five months of each other in 1999. These satellites help provide astronomers with unprecedented spectral and spatial resolution. First to launch was NASA's *Chandra* satellite (formerly the *Advanced X-ray Astrophysics Facility, AXAF*; Holt, 1993; Weisskopf, 1999), launched by the Space Shuttle. *Chandra* has remarkable sub-arcsecond imaging capabilities. Next came the European Space Agency's *X-ray Multi-mirror Mission*, known as *XMM-Newton* (Mason et al., 1995). *XMM-Newton* has a large collecting area and fantastic spectral resolution. Originally only intended to last for 10 years, both of these missions have had their life-spans extended indefinitely as they continue to provide high resolution X-ray spectra of a wide range of astrophysical objects and markedly advance our knowledge of both discrete and diffuse sources across a wide range of size scales.

1.3 The Milky Way and the birth of extragalactic astronomy

The Universe is a vast sea of galaxies, each made up of billions of stars. They appear in a multitude of shapes and sizes, from many of the regular spirals and ellipticals that we see around us today, to the first irregular, heavily star-forming galaxies that we see out towards the Big Bang. The process behind how galaxies formed and evolved to the structures that

we see today is one of the most important questions in astronomy.

It was relatively late in the history of astronomy that we first began to see things outside of our own Galaxy, the Milky Way. Galileo was the first to record that that the Milky Cloud seen stretching across great swaths of the sky was actually composed of millions and millions of stars. Over time this idea evolved until astronomers came to think that these stars all existed in a plane, with the Sun at the centre. As we live within the plane of the Galaxy, the actual position of the Sun relative to the Galaxy is extremely difficult to determine. It took Harlow Shapley and a novel approach to shed new light on this problem.

Previous attempts to determine the shape of the Milky Way had been limited to star counting, which had failed due to the effects of interstellar dust. In 1918 Shapley instead used globular clusters; compact, spherical clusters of thousands of stars. He determined that the clusters must be isotropically distributed about the centre of the Galaxy. In one fell swoop he was able to displace the Sun from the centre of the Galaxy and find the centre of the Galaxy to be approximately 17 kpc from the Solar System.

While this was going on other people had been busy cataloguing strange nebulae seen in the sky. The most famous example of this is the Messier catalogue by Charles Messier. The catalogue contains 103 miscellaneous objects, which were divided into star clusters, globular clusters, gaseous nebulae and spiral nebulae. The Earl of Rosse named the last category after their shape; an example of one, M51, is shown in Figure 1.5. These spiral nebulae provoked debate amongst astronomers between those who believed that they were giant groups of stars within our own galaxy and those who believed that they were 'island universes' of stars, just like the Milky Way, but much further away.

The debate was resolved with Edwin Hubble's observations from the 100-inch reflecting telescope on Mount Wilson (Hubble, 1922). He discovered that there were thousands of these 'island universes' and that they were galaxies like the Milky Way, each containing millions and millions of stars. Hubble calculated the distance to our closest neighbouring galaxy, Andromeda, using Cepheid variables. He determined a distance of 250 kpc which, while falling far short of the true value, did lie at too great a distance to be part of the Milky Way. While measuring the distances to galaxies he also determined their velocities. He found that all galaxies were moving away from us and the further away a galaxy was, the faster it was moving away. The Universe, he discovered, is expanding and so extragalactic astronomy was born.

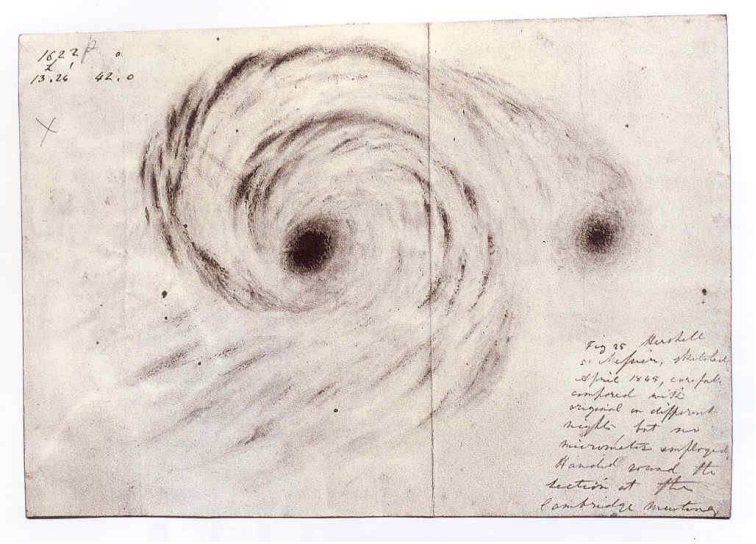

Figure 1.5: William Parsons, the third Earl of Rosse, used what was then the world's largest telescope to discover that some nebulae are spiral in shape. April 1845, Rosse discovered the spiral structure of Messier 51 (M51), the "Whirlpool Galaxy." (This image was taken from http://www.wsanford.com/∼wsanford/e xo/rosse/)

1.4 Active Galactic Nuclei

The study of active galaxies is a fast developing area of current astronomical research. In order to probe the environment of these objects, new techniques on the most sophisticated telescopes in the world have to be developed and harnessed. Astronomers need to observe over the entire electromagnetic spectrum, from radio to γ-rays, in order to understand what is happening in these objects, and thus need both ground- and spaced-based telescopes.

In order to understand what an active galactic nucleus (AGN) is, it is first necessary to set the scene. We live in the Milky Way, a fairly regular barred spiral galaxy with a very quiet black hole at its centre. The Galaxy's radiative luminosity is made up of the combined output of its stars. Now imagine a galaxy that at its centre harbours a power source so potent that it emits more than a thousand times the energy emitted from the Milky Way. Furthermore all this radiation comes from a volume roughly equivalent to the Solar System. These objects are called quasars and they are the most powerful members of the AGN family. In a quasar the central source is so luminous that it easily outshines the light from the surrounding stars of the host galaxy, leaving us no longer observing the

galaxy of stars, but rather just the small, exceptionally bright central source.

It is now accepted that all massive galaxies host at their centre a supermassive black hole (SMBH; Kormendy & Richstone, 1995; Magorrian et al., 1998, and discussed in the next section). These SMBHs have grown through mass accretion events, interspersed with quiescent periods when there is very little or no mass falling onto the black hole. When the SMBH is actively accreting matter, the matter is drawn gravitationally down towards the SMBH and conservation of angular momentum causes a flattened rotating disc to form: an accretion disc. The luminous output from this central region comes from when the gravitational potential of the in-falling matter is converted to radiative energy. When the SMBH is in this state it is called an active galactic nucleus.

1.4.1 Seyfert Galaxies

The first AGN was discovered by Edward Fath in 1908 while analysing the spectrum from the nucleus of the 'spiral nebula' NGC 1064. As this was before Hubble's pioneering work objects external to the Milky Way were unknown, but Fath (1908) documented the first case of a galaxy showing strong *emission lines* as well as the absorption lines and continuum that were typically observed in these 'nebulae'. By 1943, 12 of these 'emission line nebulae' had been discovered and were published by Carl Seyfert in Seyfert (1943). An in-depth look at the spectral properties of the brightest six objects in this sample lead Seyfert to conclude that the emission line luminosity roughly correlated with increasing absolute magnitude, and that most of the luminosity for the objects was produced from the central nucleus. Finally, Seyfert also noted that all of these galaxies had emission line profiles that were significantly broader than any other previously measured lines from 'normal' nebulae. As a tribute to this seminal work this class of AGN became known as Seyfert galaxies.

Seyfert galaxies are spiral galaxies where the emission from the central nucleus is comparable to the total, or bolometric, luminosity from the host galaxy. Depending on what optical selection criteria are used it is found that between 5 and 10 percent of all galaxies in the local Universe can be classed as Seyfert galaxies (see Maiolino & Rieke 1995; Ho et al. 1997). The Seyfert galaxies were divided into two subgroups by Khachikian & Weedman (1974) based on the Balmer ('permitted') emission line width. One group, Type-1 Seyfert galaxies (Sy1s), are those with Doppler-broadened Balmer lines measured at full-width half-maximum (FWHM) to be greater than $\sim$ 1000 km s^{-1}, while the second group, Type-2

Seyfert galaxies (Sy2s), only appear to have the narrow component of the Balmer emission line present. This classification scheme for Seyfert galaxies provided the basis for the 'unified model' for AGN.

1.4.2 The unified model

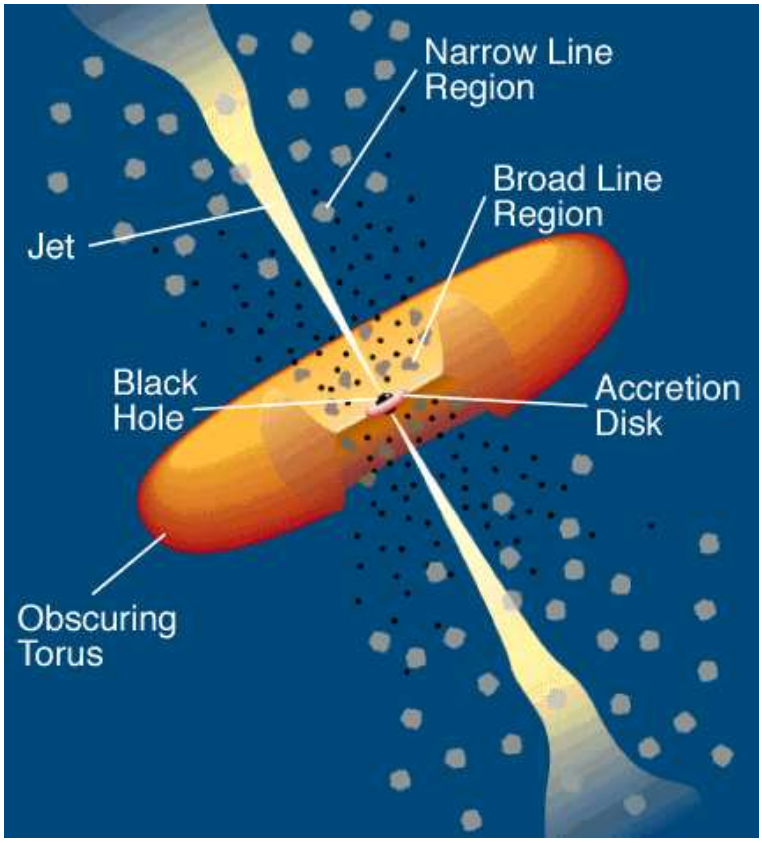

Figure 1.6: A schematic of the central engine of an AGN in the unified model. This clearly indicates how the torus can play a huge role in determining the spectrum of emission seen depending on the viewing angle. When the object is viewed so that the torus is not obscuring the view of the central region all of the primary optical, UV and X-ray radiation of an accreting black hole can be seen. If the torus obscures the view then secondary, reprocessed infrared emission is seen. This figure is adapted from Urry & Padovani (1995).

Further spectropolarimetry observations of a sample of Sy2s indicated the presence of weak, broad, permitted emission lines which are understood to be scattered by free electrons in the corona of the AGN (Antonucci & Miller 1985; Miller & Goodrich 1990). From these observations Antonucci (1993) presented a 'unified model' of AGN which was further explored

in the review by Urry & Padovani (1995). In this model the different Seyfert classifications can be understood as a single object viewed from different angles, which is shown in Figure 1.6. Due to the presence of a torus of gas and dust around the central engine the central region can be obscured if the direct line-of-sight to it passes through this torus. The region where the broad permitted lines are produced, the broad line region (BLR), is thought to be close to the central engine and thus can be easily obscured by the torus. If an object is classed as a Seyfert 1 then the observer has a direct line-of-sight to an unobscured BLR. With a Seyfert 2 the observer is looking through the torus, so the central region and the surrounding BLR is hidden by the optically thick material, leaving only the larger narrow line region (NLR) visible.

When there is a direct line-of-sight to the BLR, classification of AGN based on their broadened emission lines is straightforward. However, in cases such as Seyfert 2s, when only narrow emission lines are produced, the classification process can be problematic. In order to solve this issue an emission line flux ratio classification scheme was created by Baldwin et al. (1981; BPT diagnostics). This scheme uses the emission from the permitted lines of Hα and Hβ and the forbidden lines [O III] λ5007 Å and [N II] λ6583 Å. It works on the hypothesis that AGN should have a greater [O III] λ5007 Å/Hβ ratio than galaxies that just produce stellar emission. This is because the creation of [O III] λ5007 Å by photoionisation requires $\sim$ 35 eV and is found in AGN or the most massive stars, meaning that it is not commonly found in typical star-forming galaxies. A similar argument states that AGN also have a higher [N II] λ6583 Å/Hα ratio than normal galaxies. These two facts can be combined so that on a plot of [N II] λ6583 Å/Hα against [O III] λ5007 Å/Hβ AGN occupy a unique region; Seyfert 2s can generally be classified as having [O III] λ5007 Å/Hβ $\gtrsim$ 3 and [N II] λ6583 Å/Hα $\gtrsim$ 0.5. Figure 1.7 is a reproduction of Figure 1 from Kauffmann et al. (2003). It shows an example of a BPT diagram for a sample of 55,757 objects from the Sloan Digital Sky Survey (SDSS). The dotted curve shows the demarcation between starburst galaxies and AGN defined by Kewley et al (2001). The dashed curve shows the revised relationship of Kauffmann et al. (2003).

Heckman (1980) introduced another class of low-luminosity narrow line Seyfert galaxies called low ionisation nuclear emission regions (LINERs). LINERs are extremely common in the Universe and tend to be hosted by large spiral (with a Hubble classification S0) or elliptical galaxies. The power source for LINERs is currently unknown as several have been

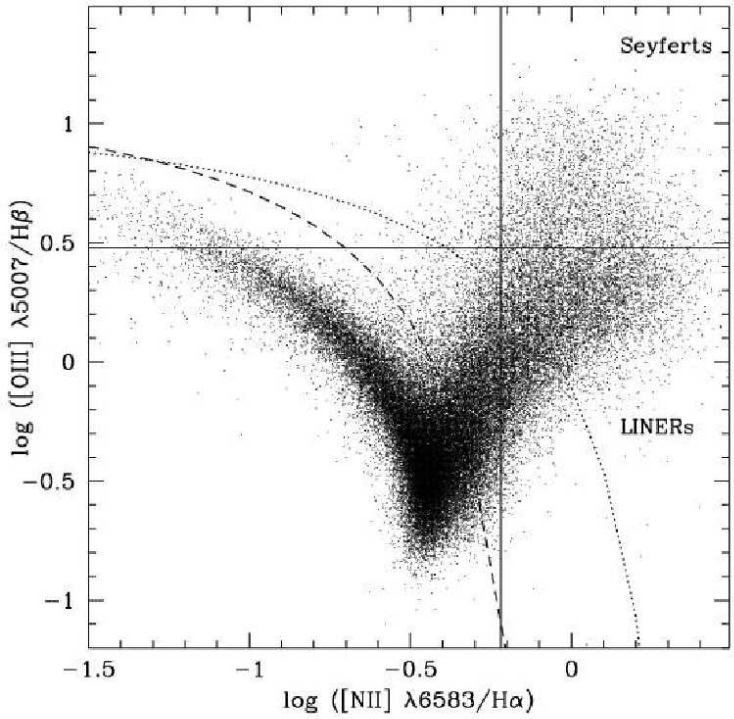

Figure 1.7: A reproduction of Figure 1 from Kauffmann et al. (2003). It is an example of a BPT diagram for a sample of 55,757 objects from the Sloan Digital Sky Survey (SDSS). The dotted curve shows the demarcation between starburst galaxies and AGN defined by Kewley et al (2001), with the dashed curve showing the revised relationship of Kauffmann et al. (2003)

shown to be powered by post-AGB stars rather than a central SMBH (Sarzi et al. 2010).

1.4.3 Quasars

After the Second World War, radio astronomy - started by Karl Janksy - became important and through a collaboration of radio telescopes based in Australia and England, combined with data from optical telescopes for the same objects, radio galaxies were discovered. They were found to have a similar spectrum and appearance to Seyfert galaxies, with both groups displaying a star-like central nucleus in the optical, and in most cases with a host galaxy visible surrounding the nucleus.

As more and more of these radio sources were discovered it became increasingly important to identify them. In the 1960s Thomas Matthews and Allan Sandage found an optical stellar-like counterpart to the radio source 3C 48 that had a unique spectrum. In 1963 another object, 3C 273, was found to even have a jet visible in the optical (Greenstein & Schmidt, 1964). Nobody could understand what these objects were and so they were called quasi-stellar objects or *quasars; QSOs*. That same year Maarten Schmidt perceived that the previously unknown emission lines in the spectrum of 3C 273 were actually just the Balmer lines for hydrogen redshifted to unfamiliar wavelengths (Schmidt & Matthews, 1964). In one leap of understanding, quasars went from being completely unknown to the most distant and luminous objects known in the Universe.

1.4.3.1 Broad Absorption Line quasars

Broad absorption line quasars (BALs) are AGN that are characterised by the presence of strong, blueshifted absorption troughs in their UV spectra. They account for 10 - 15% of optically selected quasars (Reichard et al., 2003; Hewett & Foltz, 2003). However, recent studies have shown that the true fraction could be higher, as the method of optical colour selection for quasars is biased against BALs (see Dai et al., 2008 and Allen et al,. 2011). The broad absorption troughs are credited to material outflowing from the nucleus with a velocity of between 5,000 to 50,000 km s^{-1}(Green et al., 2001). In general BALs have a higher optical-UV polarization than non-BALs.

The dichotomy that exists between BALs and non-BALs is currently a vibrant area of research. One theory is that the difference arises as a consequence of orientation. The similarities between the optical and UV emission lines as well as the underlying continuum in both BALs and non-BALs (Reichard et al., 2003) allows for the development of a scenario where there is wind present in all AGN, but the covering fraction of it directly relates to the observed fraction of BALs (Goodrich & Miller, 1995; Hines & Wills, 1995). However, recent studies by DiPompeo et al. (2010) in spectropolarimetry of a radio-loud sample does not support an orientation based argument to explain BALs, while Allen et al. (2011) found a redshift dependence in the fraction of BALs that have absorption troughs related to C IV. Both of these studies highlight that BALs cannot be solely due to an orientation effect. An alternative argument is that all quasars host a massive nuclear wind for a fraction of their lives, where the fraction of BALs that we see is a direct indication of the duration of

this phase. This means that BALs are actually tracing an evolutionary stage that lasts for 10 - 15% of a quasar's life (Hazard et al., 1984; Giustini et al., 2008) However, this theory requires a large amount of gas and dust to be present around the central source which should be observed as enhanced emission in the far-infrared and the submillimetre regions (Giustini et al., 2008). Currently though, there is very little evidence to support this (Willott et al., 2003; Priddey et al., 2007).

While we understand that radiative acceleration could be the main mechanism behind BALs, there is no clear picture for the physics behind the winds/outflows seen, with radiative acceleration, magnetohydrodynamic- (MHD)driven winds and thermally-driven winds seen as the main contenders (see Proga, 2007 for a review). However, in recent years the interest in BALQSO outflows has risen sharply due to the realisation that such high-velocity outflows can carry a substantial amount of energy and momentum into the interstellar medium (ISM) and therefore may be important in driving AGN feedback, where emission from the AGN influences the host galaxy, as well as providing a physical model for quenching star formation. Currently, it has been shown that that AGN feedback can affect star formation rates both theoretically (Hopkins & Elvis, 2010) and observationally (Cano-Diaz et al., 2012).

1.4.4 Narrow line Seyfert 1 galaxies

Narrow line Seyfert 1 galaxies (NLSy1s) are a subset of AGN. They have the appearance of a Seyfert 1 continuum, with the absence of the obvious broad emission lines typically associated with Seyfert 1, but do not have the continuum or the emission line ratios associated with Seyfert 2s. NLSy1s are defined by the width of the broad component of their optical Balmer hydrogen emission lines, in combination with the relative weakness of the emission from [O III] λ5007 Å. This is typically defined as $\mathrm{FWHM}_{\mathrm{H}\beta} < 2000$ km s^{-1} and [O III] λ5007 Å/H$\beta < 3$ (Osterbrock & Pogge, 1985; Goodrich, 1989).[1] Furthermore, NLSy1s show an anticorrelation in the strength of the Fe II emission with both the [O III] emission and the Balmer line width.

With the weakest Balmer lines and strongest Fe II emission of any type of AGN, NLSy1s

[1]While a strict cut-off using a FWHM is a very simplified method for classification, it is still the most commonly adopted practice. In reality, the best approach would be to include the source luminosity (Veron-Cetty et al., 2001); however there is evidence that AGN properties do significantly change at $\mathrm{FWHM}_{\mathrm{H}\beta} \approx$ 4000 km s^{-1} (Sulentic et al., 2008 and references therein).

occupy a unique region at one extreme of AGN correlation space. As these correlations are expected to provide the strongest constraints on the physical conditions in the centres of AGN, the study of NLSy1s is particularly interesting.

Observations of NLSy1s indicate that they have smaller black hole masses than typical Seyfert 1s, and it is thought that they may provide a significant link with the currently poorly understood and elusive intermediate mass black holes. There are several different lines of evidence that indicate that a smaller than expected black hole resides at the centre of a NLSy1.

There are several ways to determine the mass of SMBHs (M_{BH}), which are discussed in greater detail in the next section. The main method used is the BLR size - luminosity relation calibrated from reverberation mapped samples (Peterson et al., 2004; Kaspi et al., 2005). As very few NLSy1s have been reverberation-mapped (Peterson & Wandel, 2000) there is often an assumption that the relation applying to Sy1s also holds for NLSy1s. Using the BLR size-luminosity relationship for NLSy1s tends to find that NLSy1s systematically have smaller M_{BH} than their Sy1 counterparts (Boroson, 2002; Grupe & Mathur, 2004, Mathur & Grupe, 2005a,b; Komossa & Xu 2007). Since their discovery there has been some discussion that maybe NLSy1s are seen at preferred viewing angles, close to pole-on, that could contribute to and even dominate their extreme properties (Osterbrock & Pogge, 1985; Collin & Kawaguchi, 2004). While several arguments counter this (Boroson & Green 1992; Smith et al. 2002, 2004), there is growing evidence that orientation may well play a secondary part in explaining AGN emission line correlations, in particular NLSy1 properties (Sulentic et al., 2000; Boroson, 2002; Bian & Zhao, 2004b; Collin et al., 2006).

In light of this, attempts have been made to correct for these possible inclination effects, and while these studies do find a higher M_{BH} it remains offset from the main broad line AGN population (Collin et al., 2006; Watson, 2007). Independently, X-ray observations have provided evidence of small M_{BH} in these objects from variability studies (Hayashida, 2000; Zhou et al., 2007).

1.4.4.1 The NLSy1-BAL link

There have been many similarities found between BALs and NLSy1s, mostly arising from analysis of their optical line properties (Brandt & Gallagher, 2000; Boroson, 2002; Grupe et al., 2007b and references therein). Boroson (2002) finds that while both populations have a

similar, very high L/L_{Edd} ratio, NLSy1s have a much lower mass accretion rate ($\dot{M}$) and M_{BH}, which is taken from a variation on the BLR size-luminosity relation. It is suggested that a change in $\dot{M}$ could account for the differences in the populations. An interesting study into the similarities of these two populations can be seen in the NLSy1 galaxy WPVS007, which exhibited a dramatic drop in X-ray flux (Grupe et al., 1995, 2007a) that was apparently accompanied by the beginnings of BAL activity in the UV (Leighly et al., 2006).

1.5 Black holes

The concept of an object so massive that nothing, not even light, can escape it is not a modern theory. Over 200 years ago both Laplace and Mitchell suggested scenarios where this could be possible. John Mitchell was an English geologist who, using purely classical arguments, wrote to the Royal Society venturing a novel theory that:

> if the semi-diameter of a sphere of the same density as the Sun were to exceed that of the Sun in the proportion of 500 to 1, a body falling from an infinite height towards it would have acquired at its surface greater velocity than that of light and consequently supposing light to be attracted by the same force in proportion to its *vis intertiae* (inertial mass), with other bodies, all light emitted from such a body would be made to return towards it by its own proper gravity (Mitchell, 1783).

However he did think that such a scenario was extremely unlikely and the concept was ignored as a theoretical oddity, mainly because at the time gravity was not thought to influence light.

It was at the dawn of the 20th Century with the development and publication of Albert Einstein's theories on gravity and general relativity that major headway was made in this subject. Once Einstein had published his theories in 1916, Karl Schwarzschild used them to work out his solution for the gravitational field for a point mass, which showed that these compact objects could, at least, *theoretically* exist. This equation predicts a 'true singularity', a point at which an object with mass becomes infinitely dense if observed through space-time. The singularity is hidden from our view, however, by an 'event horizon'. This event horizon forms a sphere around it, the surface of which has an escape velocity equal to the

speed of light and is found at the Schwarzschild radius, R_s:

$$R_S = \frac{2G\mathsf{M}_{BH}}{c^2} \approx 3\mathsf{x}10^3 \frac{\mathsf{M}_{BH}}{M_\odot} \tag{1.1}$$

where G is the gravitational constant, M_{BH} is the mass of the black hole and c is the speed of light. The last stable path (innermost stable circular orbit; ISCO) is found further out at $3R_S$ and is the closest distance to the singularity at which the material can orbit a non-spinning compact object (Schwarzschild, 1916). This led on to the 1920s, when Chandrasekhar argued that special relativity demonstrated that a non-radiating body would, above a certain mass, collapse into a black hole.

It was in 1963 that the generalised solutions for an uncharged, spinning mass were found by Kerr (1963), with the actual term 'black hole' being coined by John Wheeler during the 1960s. An interesting result of these theoretical studies is the uniqueness theorem, colloquially known as the 'no-hair' theorem. This theorem states that just three parameters can both uniquely and completely define a black hole: its mass, M_{BH}, angular momentum, J, and charge, Q. From this, we draw the implication that any information that is considered to be intrinsic to matter that falls into a black hole is lost, metamorphosing into these three parameters. Using the most physically realistic scenarios we can assume $Q = 0$, as matter that will make up the black hole can be considered neutral overall and any net charge will be dissipated and neutralised by the environment. In the 'no-hair' theorem, angular momentum is expressed as $a = J/\mathsf{M}_{BH}$, so any black holes that have the same values of a and M_{BH} are indistinguishable from each other. This has lead to two of the central themes of black hole research; determining their spin and mass.

There is no theoretical limit to the mass of a black hole, but a is constrained to lie between 0 and 0.998 $G\mathsf{M}_{BH}/c$, from Thorne (1974) which is based on the considerations of the torque exerted by radiation from the accretion which falls upon the black hole.

As this thesis is focused on the observational properties of black holes, it is useful to highlight some of the key results from the theoretical studies in this field. Distance scales associated with black holes are often given in units of R_S or gravitational radii, R_g, where:

$$R_g = \frac{G\mathsf{M}_{BH}}{c^2} = \frac{1}{2}R_S \tag{1.2}$$

If a black hole is spinning, the 'event horizon' for that object will reduce to just over 1 R_g for maximally spinning Kerr black holes. The ISCO for maximally spinning Kerr black holes

is also smaller, reducing to $\approx 1.24\,R_g$. When considering the properties of radiation from accreting matter, the characteristic timescale associated with black holes, the 'light-crossing time' t_{lc} is important, where:

$$t_{lc} = \frac{R_g}{c} \tag{1.3}$$

These relationships and results allow us to consider the evidence of black holes that we have obtained, from the small stellar-mass black holes in our Galaxy, to the supermassive black holes in AGN. They allow us to link these different sizes together and expand what is known and understood for stellar-mass black holes to develop models for the much harder to observe SMBHs, which are the focus of this thesis.

1.5.1 Observing Black Holes

Black holes occupy the highest possible position on the density scale and have a gravity so extreme that from within the event horizon not even light can escape. So, as stated on a popular 1980s TV show in response to why the black hole that the ship is hurtling towards was not spotted by the ship's computer: "the thing about a black hole - its main distinguishing feature - is it's black. And the thing about space, your basic space colour, is black. So how are you supposed to see them?" (Holly, *Red Dwarf*, Series 3, Episode 2). The most obvious answer to this question is that we cannot. However, while it is true that we cannot observe these sources directly, we can observe them via their impact on their surroundings.

1.5.1.1 Stellar Mass Black Holes

The most convincing evidence for the existence of black holes within our Galaxy is the compact object in the X-ray binary source Cygnus X-1. There are several physical limitations that restrict the maximum mass an object can have. For a white dwarf star that is held up by electron degeneracy pressure, the maximum mass it can have is 1.4 $M_\odot$. A neutron star's mass has an upper mass limit of $\sim$ 2.2 $M_\odot$ from the limiting equation of state for neutral matter (found at the point where the speed of sound is equal to the speed of light; Kalogera & Baym, 1996). In Cygnus X-1, the compact object was found to be greater than either of these two limits (Webster & Murdin, 1972), making it a strong Galactic black hole candidate. Recent work on the compact object in this source has derived its mass to be $\sim$

15 $M_\odot$ (Orosz et al., 2011 and references therein), providing convincing evidence that this is indeed a black hole. Since the early forays into this field several other Galactic black hole candidates (GBHCs) have been discovered, such as GX 339-4 (Hynes et al., 2003), GRO J1655-40 (Zhang et al., 1994) and XTE J1550-564 (Chaty et al., 2011). The masses of these black holes are thought to lie in the region of $\sim$ 6 - 15 $M_\odot$.

The formation of stellar mass black holes is thought to be caused by the collapse of very massive stars. There are several possible scenarios in which this can occur. One is that at the end of the life of a massive star it will run out of the fuel that it requires for fusion and will collapse under its own gravity and form a black hole. Another possible avenue is that if there are two massive stars in a binary system one may collapse to form a neutron star. This star can subsequently strip matter from its massive companion until it acquires enough mass to push it over the limit for neutron degeneracy and forms a black hole. The formation of a black hole is usually associated with an extremely violent ejection of matter in a supernova explosion and may be accompanied by a γ-ray burst.

1.5.1.2 Supermassive Black Holes

Shortly after the discovery of quasars, it was proposed that their titanic energy outputs could be described by supermassive black holes (SMBHs; Salpeter ,1964; Lynden-Bell, 1969). The huge power output and distance to these objects posed enormous problems for the mechanics behind energy generation known at the time; even nuclear fusion failed to explain the output seen. Early arguments tried to dismiss the necessity for black holes by refuting the cosmological explanation of the redshift of the objects and classing them as residing within the Milky Way. However, once accretion physics developed by Shakura & Syunyaev (1973) and Shields (1978) produced spectra similar to those seen from quasars it became clear that accretion is the most viable candidate for the observed energy outputs, and that the cosmological distances to these objects were indeed accurate.

Confirmation of the hypothesis for SMBHs came with observations of the motions of stars in the centre of the Milky Way and observations of the nearby galaxy, M87, with the *Hubble Space Telescope* (HST). The HST images of M87 indicated the presence of a disc of gas at the centre of the galaxy, which further study revealed to be Keplerian in motion, and containing within it a mass of $\sim 2.4 \times 10^9$ $M_\odot$ in a region just 32 parsecs in diameter (Harms et al., 1994). This strongly suggests a black hole and more recent measurements suggest

an even higher enclosed mass of $\sim 6.4 \times 10^9$ $M_\odot$ (Gebhardt & Thomas, 2009). In our own Galaxy a more unambiguous signature of a SMBH can be found by looking at the motions of stars around the central point of the Milky Way. The motions of these stars, observed in the near-infrared, can be used to constrain the mass in the centre of the Galaxy to 4.31 x 10^6 $M_\odot$ (this method is described in greater detail in the next section; Gillessen et al., 2009). Despite previous suggestions that a cluster of smaller objects such as neutron stars could account for the central mass (Maoz, 1998), it is now accepted that a SMBH; a single, very compact object, is the best fit to the observed data.

The question of how supermassive black holes form is very difficult to address as they reside at great distances from us and their emission is difficult to disentangle from the emission of the host galaxy. However, the answer to this question is of fundamental importance and has been the focus of many studies. It is quite clear that a process is needed where large enough masses can collapse under their own gravity to form black holes. The most natural site for this to occur is at the centre of dark matter halos, which provide the initial seeds for galaxy formation. Numerous possible routes for the formation of supermassive black holes have been proposed over time since the earliest suggestions by Begelman & Rees (1978). The actual coalescing of mass may occur via the collapse of a large gas cloud (Loeb & Rasio, 1994) or through the collapse of the earliest stars (Volonteri & Rees, 2005). Despite the unresolved issues of the birth of supermassive black holes, studies into their observed properties can aid us in understanding their evolution and therefore, hopefully, improve our understanding of their formation. Furthermore, the counts of AGN along with assumptions about efficiency and accretion rate can be used to predict the density of supermassive black holes in the local Universe (Soltan, 1982). These studies have convincingly proved that even a moderate accretion rate can allow for the accretion of mass that we see in the supermassive black holes around us, and in turn provides a driving force behind the need to understand the accretion processes at work in these systems in greater detail.

1.5.2 Measuring supermassive black hole masses

The mass of a black hole is one of its fundamental properties and therefore methods for accurately establishing it are constantly being developed. One of the main problems is that black hole masses cover approximately nine orders of magnitude, from the small stellar mass black holes around us in the Milky Way to the largest supermassive black holes lurking at

the heart of massive elliptical galaxies. The magnitudes and distances involved mean that no single method can be developed. For nearby objects we can directly observe the impact of the black hole on its environment (such as in the case of nearby stellar black holes and the SMBHs of our Galaxy and M87), but the further away an object is, the more indirect the methods become. Much research is devoted to linking the less accurate methods to the more accurate ones; an ongoing process that is constantly improving as new techniques and instruments are developed. Below are summaries of five of the most commonly used methods:

- **Dynamical mass measurements**

  Dynamical mass measurements were the first accurate measurements of black hole mass and were used to discover the correlation between the SMBH and the host galaxy. The pioneering work in this field was based on the observed dynamics of the stars, carried out by Young et al. (1978) and Sargent et al. (1978). Measuring both the rotational velocity and dispersion of the stars as a function of radius allows us to analyse the underlying potential and draw an estimate for the black hole mass. The major drawback with this method is the difficulty of accurately measuring the stellar properties. A different approach to this method uses the gas that is present rather than the stellar dynamics (e.g. Harms et al., 1994). This measurement relies on the assumption that the gas is in circular orbits, but as gas can be easily perturbed, this may not be the case.

  Dynamical methods are far more accurate if the information can come from the inner radii of the galaxy close to the black hole, and lose their precision for the more distant galaxies where we are limited to only large scale observations. Theoretically, dynamical measurements can be made for every SMBH, but as we move out to more distant galaxies the apparent size of the black hole's sphere of influence - the region where the potential of the black hole dominates - reduces in size until it cannot be resolved by our current generation of instruments. Recent advances in this field have been aided by combining adaptive optics with integral field spectroscopy, pushing the current resolution constraints to their limits and allowing us to probe ever deeper into the centre of galaxies (e.g. the SAURON project; Bacon el al., 2001).

  Obviously this method works best on the closest galactic centre to us, Sgr A*, in the centre of the Milky Way. The measured stellar orbits in the vicinity of the central

potential region provide the best evidence for a SMBH. Due to its close proximity we can resolve the individual stars caught in the potential, and therefore measure the black hole mass (Genzel et al., 1996; Schödel et al., 2002; Ghez et al., 2008; Gillessen et al., 2009). Figure 1.8 shows three stills from the Max Planck Institute's Galactic Research team's movie of the orbits of stars in the Galactic Centre. The latest value for the black hole mass of Sgr A* is 4.31 x 10^6 M$\odot$ (Gillessen et al., 2009).

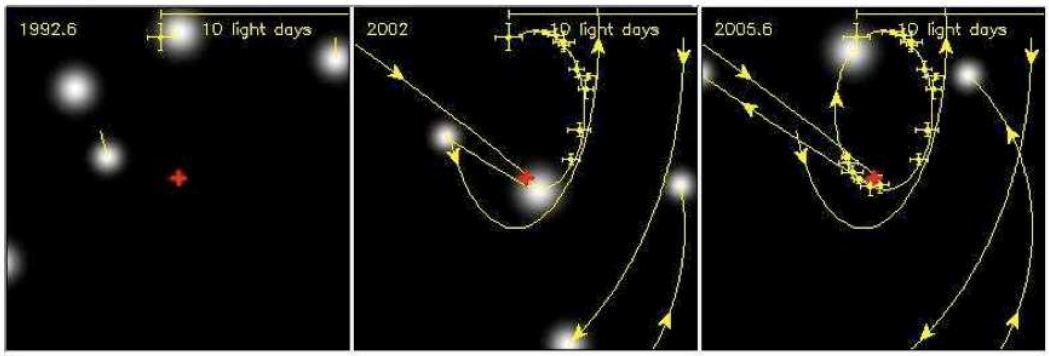

Figure 1.8: These three images are taken from the Max Planck Institute's Galactic Centre Research pages. They show how the potential of the mass at the centre of the image under the red cross results in the orbits of the stars seen. The stellar dynamics illustrated here can be used as an indirect method of determining the mass of the central object, which works out to be high enough that it can only be described as a SMBH. (This image was taken from http://www.mpe.mpg.de/ir/GC/index.php)

- **Reverberation mapping**

  As the continuum of AGN is known to vary on extremely short timescales, it was inferred that the emitting source must occupy a very small volume. The broad emission lines observed in certain types of these objects are thought to be ionised by the continuum emission and broadened by Doppler shifts that arise due to cloud bulk motions. Variability in these emission lines is linked to the variability of the ionising source. By measuring the delay in the appearance of the line variations over the continuum variations it is possible to acquire the light crossing time, and therefore the distance, from the central source to the broad line region cloud. If we assume that the gas in the broad line region is primarily accelerated by the gravitational force of the black hole, then we can apply the virial theorem:

$$T = \frac{V}{2} \tag{1.4}$$

where T is the kinetic energy and V is the gravitational energy. The black hole mass, M_{BH} is then given by:

$$\mathsf{M}_{BH} = \frac{v^2 R_{\mathsf{BLR}}}{G} \tag{1.5}$$

The reverberation mapping technique allows us to use the spectral delay to work out the size of R_{BLR} and give the black hole mass as:

$$\mathsf{M}_{BH} = \frac{f c \tau v^2}{G} \tag{1.6}$$

where τ is the measured time delay, c the speed of light, v the cloud velocity, G the gravitational constant and f a constant factor that allows for variations due to specific kinematics, geometry and emission line processes in the BLR. This theory was first developed by Blandford & McKee (1982), and the first sample of reverberation mapped black holes was given by Kaspi et al. (2000), which lead to the development of the BLR size-luminosity relationship described below.

- **Virial type relations - BLR size-luminosity relationship**

  Reverberation mapping requires a long timescale baseline in order to constrain the spectral delay and as a result, to date, relatively few black hole masses have been measured through this method. A far simpler but less precise method can be inferred from the radius-luminosity relation of the type $R_{BLR} \propto L^{\alpha}$, where L is the continuum luminosity at a given wavelength, typically $\lambda = 5100$ Å (Kaspi et al., 2000; 2005). The black hole mass is then calculated from this luminosity and the properties of the broad component of a broad line. The broad line used in this method is dependent on the redshift of the object, with the most work having been done on constraining the profiles of Hβ to match the black hole mass for reverberation mapped objects, which are all at a low redshift. As this training method is mainly limited to the low redshift at which the reverberation mapping technique works, moving to higher redshifts and the broad lines of Mg II and C IV leads to less precise relationships. The black hole mass can be calculated from the continuum luminosity at $\lambda = 5100$ Å and the Hβ broad component profiles by the equation:

$$\mathsf{M}_{BH} = 4.817 \left[\frac{\lambda L_{\lambda}(5100\mathring{A})}{10^{44}\text{ergs s}^{-1}}\right]^{0.7} \text{FMHM}^2 \tag{1.7}$$

  where FWHM refers to the full width at half maximum measurement of the broad component of the Hβ emission line.

- **Host galaxy correlations**

  Recently, correlations have been found between the properties of local host galaxies and the SMBH at their centre, which allow us to extend the measurements of black hole mass to galaxies where direct observations of the galactic centres fail. The $M_{BH} - \sigma$ relation (Ferrarese & Merritt 2000; Gebhardt et al., 2000) found the correlation between stellar velocity dispersion and black hole mass, where $M_{BH} \propto \sigma^4$. Recently, Gültekin et al. (2009) summarised the $M_{BH} - \sigma$ relation by considering all the well known black hole masses and plotting them against their velocity dispersions. They found that there is a tighter relation for elliptical galaxies than for spirals.

  There is also a correlation between black hole mass and bulge luminosity or bulge mass, the $M_{BH} - L_{bulge}$ relation (Magorrian et al., 1998; McLure & Dunlop, 2002; Marconi & Hunt, 2003; Häring & Rix, 2004). This relation reflects the dependence of the black hole on the hot spheroidal stellar component. This correlation varies depending on the wavelength band used for observing, as some wavelengths are better for tracing stellar mass and are clearer of extinction than others. Current research is looking at the redshift evolution of this relation to see if the relation established in the local Universe can be used to probe black hole mass at high redshifts.

- **Megamasers**

  Masers are a form of stimulated emission in the microwave range, which are very similar to their optical counterpart, lasers. This emission occurs when an incoming photon stimulates a molecule in a metastable excited state in such a way that it moves to a lower energy level. As the product of this event, a photon of the same energy as the incoming photon is emitted and its flux is amplified. Megamasers are a far greater luminous version of this event and have been detected in galactic centres. The process occurs in molecular clouds in the presence of an energy source; in the case of megamasers, this is emission from the AGN. To produce a megamaser, long path lengths are needed in order to produce enough amplification. This requires the molecular discs to be nearly edge-on.

  The type of megamaser detected in AGN is an amplified H_2O molecule transition occurring at a microwave frequency of 22 GHz; this has been observed for a few AGN (see Tarchi, 2012 for a review). By mapping the emission line velocity profiles as

a function of radius it is possible to measure the orbit parameters of the molecular clouds and in turn calculate the black hole mass (Nakai et al., 1993; Miyoshi et al., 1995). Due to the high resolution of data required for this technique the radii of the clouds observed are of the order ~ 0.1 parsec and the rotational curves seen are typically Keplerian. This means that this method allows for the direct detection of a thin Keplerian molecular disc, as is expected by the accretion onto a SMBH paradigm. However, due to the specific conditions required, only fourteen black holes have masses obtained from megamasers (Kuo et al., 2011).

1.6 Physical properties of AGN

As we have already discussed, AGN can be broken down into different subclasses based on luminosity and emission line width. Regardless of the obviously different observed properties of each category it is now almost universally agreed that all AGN are powered by the same physical process: the accretion of matter onto a SMBH (e.g. Salpeter, 1964; Lynden-Bell, 1969). In this section we cover basic AGN accretion physics, radiation processes and the relationship between gas and dust in AGN.

1.6.1 The central engine

It is now understood through comparisons between the mass density of SMBH in the local Universe and the total energy produced by AGN over cosmic time that SMBH grow through mass accretion events (Soltan, 1982; Rees, 1984, Marconi et al., 2004). During this process of mass accretion it is predicted that matter will lose angular momentum and spiral towards a black hole in the form of a Shakura-Sunyaev disc (Shakura & Sunyaev, 1973). The luminosity from the accretion process can be shown as:

$$L_{\mathsf{acc}} = \epsilon \dot{\mathsf{M}} c^2 \tag{1.8}$$

where $\dot{\mathsf{M}} = dM/dt$ is the mass accretion rate and ϵ is the efficiency parameter. The accretion efficiency is both strongly dependent on the compactness of the object onto which the matter is being accreted and directly related to the innermost stable orbit (r_{in}) of the black hole, where $\epsilon \sim 1/2r_{in}$. The accretion efficiency parameter has typical values of 0.06 - 0.31 depending on the spin of the black hole (see Done, 2010 for a recent review).

In a system that is steady and spherically symmetric, the luminosity from the accretion of fully ionised hydrogen protons onto a black hole will exert a radiation pressure on the electrons in the surrounding material due to the effects of Compton scattering:

$$F_{\mathsf{rad}} = L\frac{\sigma_T}{4\pi r^2 c} \tag{1.9}$$

While simultaneously, gravity exerts an inward force on the protons:

$$F_{\mathsf{Grav}} = \frac{GM_{\mathsf{BH}}(m_p + m_e)}{r^2} \approx \frac{GM_{\mathsf{BH}}m_p}{r^2} \tag{1.10}$$

The effect of gravity on the electrons in the equation above can be negated as their mass (m_e) is inconsequential when compared to that of the proton (m_p). The maximum achievable luminosity is the luminosity at the point where the two opposing forces balance, given as:

$$L_{\mathsf{Edd}} = \frac{4\pi GM_{\mathsf{BH}}m_p c}{\sigma_T} \approx 1.3 \,\mathsf{x}\, 10^{38}\left(\frac{M_{\mathsf{BH}}}{\mathsf{M}_\odot}\right)\ \mathsf{erg\,s^{-1}} \tag{1.11}$$

This is known as the Eddington luminosity. The model that forms the basis for this equation is, naturally, a gross over-simplification of the actual system of a black hole undergoing accretion. For example, the matter around the black hole is expected to form an accretion disc before falling in. Due to the specific geometry associated with this disc, the Eddington limit is likely to shift to higher luminosities for a black hole with a radiatively efficient thin disc. However, as the assumption of a spherically symmetric geometry is a good first-order approximation it is used throughout current literature (McLure & Dunlop, 2004; Marconi et al., 2004; Kollmeier et al., 2006).

The ratio of the observed accretion luminosity and the Eddington luminosity (called the Eddington ratio, λ_{Edd}) is used as a standard measure to compare SMBH accretion over a wide mass parameter space:

$$\lambda_{Edd} = \frac{L_{acc}}{L_{\mathsf{Edd}}} \tag{1.12}$$

For the typical range of SMBH for AGN ($\mathrm{M_{BH}} \approx 10^6 - 10^8\ \mathrm{M_\odot}$), Eddington ratios are estimated to be in the range of $\lambda \sim 0.001$ - 0.1. However, a small but increasingly significant fraction of sources have been observed with apparent 'super-Eddington' ratios (i.e., $\lambda_{Edd} > 1$), which suggests that these AGN are either undergoing significant mass accretion events and are outputting energy at such a rate that they are expelling the surrounding material, or that the objects in question have unusual geometries (e.g., beamed emission or slim discs). The physics behind super-Eddington accretion is explained below.

1.6.2 Super-Eddington Objects

Although the theoretical limit for spherically symmetric accretion is the Eddington limit, based on an assumed local equilibrium between radiation pressure and gravity, other systems do not obey this limit. Supernovae and gamma ray bursts (GRBs) can violate this limit by several orders of magnitude. In steady-state systems the limit can also be infringed in certain directions with the aid of relativistic or geometric beaming, with accretion funnels being the main example of this (Begelman, 2003).

Additionally, there are also theories where a disc may also be exempt from this limit. Indeed, a number of black hole X-ray binary sources are seen to exhibit luminosities in excess of this, including V404 Cyg and V4641 Sgr near the peak of their outbursts, as well as GRS 1915+105 and the HMXB SS433 (seen to accrete at super-Eddington rates: Begelman et al., 2006; Poutanen et al., 2007).

Disc instability models predict that the maximum luminosity is proportional to the size of the disc, so systems with a long orbital period and a large enough disc could potentially reach $L_{acc}/L_{\mathsf{Edd}} > 1$. If achieved, then high mass accretion rate outflows can be launched from closer to the black hole (the effective gravity goes as $1 - L_{acc}/L_{\mathsf{Edd}}$) and mass loss may become important for the structure of the disc, though not to the point where it would prevent the source from accreting above Eddington. Good examples of this in action are V404 Cyg and V4641 Sgr, which were observed in outburst at $L_{acc}/L_{\mathsf{Edd}} > 2 - 3$, where ejected material is seen to completely obscure the source (Tanaka & Lewin, 1995; Życki et al., 1999; Revnivtsev et al., 2002). Conversely, there have been examples of objects displaying quasi-steady super-Eddington accretion, as seen in the case of GRS 1915+105.

If the dynamic effects of the magnetic fields surrounding a globally accreting system are taken into account then super-Eddington accretion is also plausible in these situations. In an AGN the inner, luminous part of the accretion disc can theoretically break up into dense filaments with tenuous regions. Radiative flux will, on the whole, avoid these dense regions and instead flow through the small spaces in between. The effect of this is that the tenuous regions experience a net upward force while the filaments are pulled down by gravity.

Other theories develop this idea further and suggest the emergence of photon bubble instability. In these situations, material does not create long-lived filaments, but rather will cycle between high and low density phases dynamically (Arons, 1992; Gammie, 1998). The resultant photon bubble effect could allow accretion discs to radiate above the Eddington

limit. The theoretical maximum increases with M_{BH}, so that for AGN it predicts luminosities as high as 100 L_{Edd} (Begelman, 2002). It has been suggested that the possibility of true super-Eddington luminosities would be useful to explain ultra-soft AGN, such as RE J1034+396 (Middleton et al., 2009), and the rapid growth of black holes by accretion during the quasar era.

1.6.3 Radiation processes

There are a number of fundamental processes that are required to explain the radiation observed from AGN and black holes in general, some of which are outlined below. Further information on any of these processes can be found in many undergraduate textbooks (e.g. Serway 1996; Tipler 1999).

1.6.3.1 Blackbody Radiation

Thermal radiation is the radiation emitted by any object at any temperature above absolute zero. The characteristics of this emission are dependent on the physical properties of the object and the temperature. Radio and microwaves are emitted by astronomical objects at low temperatures (one of the best examples of this is the cosmic microwave background; CMB); as the temperature increases, the wavelength of the emitted radiation decreases through the infrared, optical, ultraviolet and through to the X-ray regime of the electromagnetic spectrum.

Usually on Earth the colour an object appears (for example, a blue ball or a yellow bag) is due to properties specific to the material of the object that determines which bands of the spectrum will be absorbed and/or emitted from the object, rather than being dependent on its temperature. However, there is one type of object that allows us to just focus on the thermal aspects of radiation, this object is known as a blackbody. A blackbody absorbs all radiation incident on it and re-emits it across the electromagnetic spectrum. The spectra of these sources varies with temperature. As the temperature of a blackbody increases, the amount of energy it releases also increases, which shifts the peak of the radiation to shorter and shorter wavelengths. This displacement in the peak of the emission obeys Wien's displacement law, which states:

$$\lambda_{max} T = 0.2898 \times 10^{-2} \text{ m K} \tag{1.13}$$

1.6.3.2 Comptonisation

Compton scattering, or the Compton effect, explains how energy is exchanged between photons and electrons. It is named after Arthur Compton, who first observed this effect in 1923 and was subsequently awarded the Nobel Prize for Physics in 1927.

It describes the collision of a particle of light (a photon) with an electron, a process that results in the photon losing energy to the electron as the latter recoils from the collision. This process is shown in Figure 1.9. This shows the electron gaining energy as it moves off in one direction as the photon moves off in another, in the rest frame of the electron.

However, this process is different if the electrons are relativistic. In this case the electrons have more energy than the surrounding photons. When they collide the photons gain energy and are said to have been 'upscattered' by the electron. This process is called 'inverse Compton scattering' and is also shown in Figure 1.8, again in the rest frame of the electron.

The more collisions that occur the more energy is given to the photons, which in turn increases the hard (high-energy) component of the X-ray spectrum. The limit to this 'up-scattering' is reached when the photons and electrons reach a state of energetic equilibrium. As both the rate of reaching, and opportunity to, reach this limit are related to the density of the material, at lower densities the equilibrium point may not be achieved.

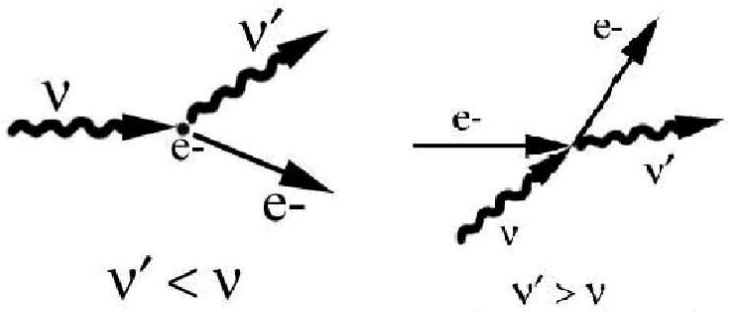

Figure 1.9: The processes and particles involved on a) Compton and b) Inverse Compton scattering. (This image is taken from http://venables.asu.edu/quant/proj/compton.htmp)

1.6.3.3 Discrete line emission

Spectral lines are the product of an interaction between atoms or atomic nuclei and an individual photon. The energy from this photon can allow a change in the energy state of the system. The results of this can allow an orbiting electron to transit between energy

states, or, if enough energy is provided (for example from a relatively high energy UV/X-ray photon), it can escape completely leaving behind a positively charged atom/particle. The latter case is known as the photoelectric effect and is discussed in greater detail in the next section. In the former case the photon is absorbed and the state of the system is considered to be excited. As the system relaxes the absorbed energy is re-emitted as either a single photon of the same frequency as the original, or in a cascade of photons, where the total sum of the energies will equal that which was absorbed, assuming that the system returns to its original state. An example of this is shown in Figure 1.10.

The direction of the new photon or photons will be unrelated to that of the original photon and will carry the characteristic energy difference of the states between which the electron transited as it was emitted. The transition will be observed as a discrete line feature in the spectrum. It can take the form of either an emission or an absorption line, depending on the type of material being observed and its position relative to the photon source. As the characteristic energy differences between the electron levels are unique to each type of atom, observations of these line features can unlock information relating to the constituents and abundances of these elements within the material that is being observed. It can also provide information about the density and temperature of the material.

Emission and absorption features are observed in a whole host of astronomical objects, including some discussed previously (for example the observed spectra of stars used for typing and the hydrogen emission seen in quasar 2C 372). They can also be observed across a broad range of wavelengths, including in X-rays (e.g. Fe-Kα emission from AGN; see Pounds et al. 1989).

1.6.3.4 Photoelectric effect

This effect was briefly mentioned in the previous section. It occurs when a high energy photon interacts with matter, when the photon has enough energy that it can be used to remove a bound electron from an atom. This produces two results: Firstly it ionises the atom, and secondly it removes the photon from the spectrum of the high energy source. The mechanics of this is shown in Figure 1.11. In this example an X-ray photon, carrying an energy E = hν (where h is Planck's constant and ν is the frequency of the photon), is completely absorbed during the collision. Some of the photon's energy is used to overcome the binding energy of an electron, where the binding energy $E_B \lesssim h\nu$, and the remaining

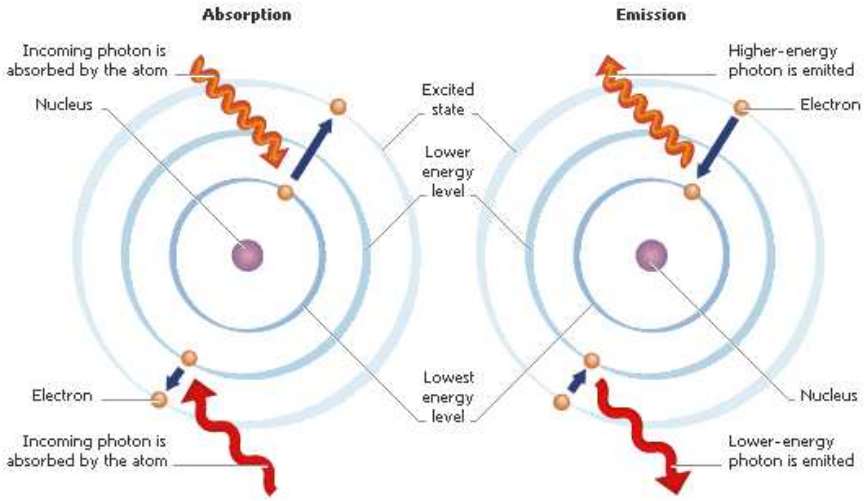

Figure 1.10: The physics of discrete line absorption and emission. (This image is taken from http://chandra.harvard.edu/xray_astro/discreteline.html)

energy goes into providing some velocity to the electron. If a photon carries less energy than the binding energy of the electron it can be instead absorbed and re-emitted as part of the process described in the previous section. This is an effect that is often observed in astrophysical sources, and is especially prevalent at lower energy X-rays. As the result of this effect is to cause a deficit at the low X-ray energies it is commonly known as X-ray absorption.

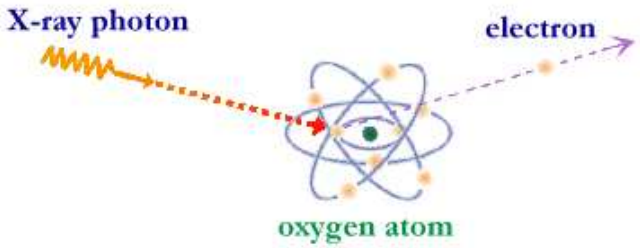

Figure 1.11: The photo-electric absorption effect. (This image is taken from http://chandra.harvard.edu/xray_astro/absorption.html)

1.6.4 Dust in AGN

The main modifier in the optical-UV part of the spectrum is dust, and the resultant reduction in flux in called 'dust extinction' in the literature. The main focus of earlier studies was interstellar dust in the Milky Way, where the optical-UV spectrum of stars of a known spectral type were used to estimate the modification due to dust (e.g. Bless & Savage, 1972). Studies found that the dust could best be characterised by a graphite-silicate grain model with a broad distribution in grain sizes and then extended these findings to the Large and Small Magellanic Clouds (Mathis et al., 1977; Pei, 1992).

The extinction, A_λ, expresses the observed increase in magnitude (a factor decrease in flux) at a wavelength λ due to dust extinction. The 'extinction curve' is the observationally determined variation in A_λ with wavelength, and is commonly normalised by the extinction in the optical B-band:

$$\xi(\lambda) = A_\lambda / A_B \tag{1.14}$$

In this form it is called the 'empirical' extinction curve. Usually the extinction curve is expressed as a colour excess $E(\lambda - V) = A_\lambda - A_V$. This gives the difference between the intrinsic $M_\lambda - M_V$ colour and the observed colour.

The terminology of 'reddening' to describe extinction is common to all branches of astronomy: all of the early studies show that dust will reduce flux at the blue-end of the optical-UV spectrum (the shorter wavelengths) compared to the flux at the red-end of the spectrum. If a spectrum has a greater ratio of red-to-blue flux it is said to be 'reddened' and the colour excess is used to represent this. This extinction curve is normalised by the $B-V$ colour excess $E(B-V)$, and is defined as:

$$\frac{E(\lambda - V)}{E(B-V)} = \xi(\lambda)(1 + R_V) - R_V \tag{1.15}$$

where $R_V = A_V / E(B-V)$, and is known as the 'total-to-selective' extinction. This parameter is a property of the dust that is responsible for extinction and, for Galactic dust, typically takes the value $R_V \approx 3.0$. $E(B-V)$ is a measure of the amount of dust present around the source.

The effect that Galactic dust can have on extragalactic observations is well known. There are publicly available maps of the Galactic dust distribution (e.g. Schlegel et al., 1998) and a well constrained Galactic extinction curve has been produced (Cardelli et al., 1989). This

means that it is easy to correct optical and UV observations of AGN to account for Galactic dust. Correcting for the dust intrinsic to the system being observed is far more difficult.

Early progress into this was made by Ward et al. (1987), where they found that in a sample of 26 AGN, their broadband optical-UV spectral energy distribution (SED; described in Section 1.7) shape could all be described by one shape, with variations in the intrinsic dust of each object accounting for any discrepancies seen. A study of the Seyfert galaxy NC 3227 by Crenshaw et al. (2001), produced a detailed extinction curve by comparing its spectrum to the unreddened spectrum of NCG 4151. The reddening curve produced in this study is similar to that derived for the SMC as they both lack a feature at 2175 Å that features prominently in the Galactic extinction curve, and both curves rise steeply towards the blue, shorter wavelengths.

Another study by Gaskell et al. (2004) compared a large sample of radio-loud and radio-quiet quasars and found that the extinction curve was much flatter in the UV, but still did not have a feature at 2175 Å. The conclusion of this study is that the dust grains in AGN are typically larger than those found in the Milky Way. This supported earlier findings by Maiolino et al. (2001), who also proposed that the dust grains found in AGN are larger than those found in our Galaxy, based on the low dust-to-gas ratios found in AGN when compared to those of our Galaxy. The origins of the extinction properties in AGN are uncertain, and a clear paradigm for the extinction curve is yet to emerge, as is the link between the gas and dust seen in AGN.

The work in Chapter 2 was done with the aim of quantifying the relationship between dust and gas in AGN, and in Chapters 3 and 4 we attempt to account for the effects of dust reddening in the SED fitting process.

1.6.4.1 The 'dust-to-gas' ratio in AGN

Gas and dust are known to exist in large quantities inside galaxies. As a result, many studies have focused on understanding the relationship between the two. In particular, Bohlin et al. (1978) measured the dust-to-gas ratios of the inter-stellar medium towards 100 stars in the Milky Way and found a correlation of $E(B-V)/N_H = 1.7 \times 10^{-22}$ mag cm^2 atoms^{-1} with a typical scatter of $\sim 30\%$. The study of this relationship in AGN has proven to be much more difficult. Multiple studies have been carried out to investigate the dust-to-gas ratio, with initially unexpected results.

Various studies have shown that X-ray and optical nuclear absorption do not match in AGN. In particular, the measured optical dust extinction is systematically lower than that inferred from the column density, N_H, measured in the X-rays, when assuming a Galactic dust-to-gas ratio (Maiolino et al., 2001a). The most important consequence of this observed effect is the mismatch between optical and X-ray classification, and in particular the existence of Type 1, broad line AGN with significant X-ray absorption (Wilkes et al., 2002; Hall et al., 2006; Szokoly et al., 2004; Silverman et al., 2005). An excellent example of extreme cases of this kind of mismatch are BALQSOs, whose X-ray spectrum is heavily absorbed, but whose optical spectrum shows little or no dust extinction (Gallagher et al., 2006; Braito et al., 2004; Maiolino et al., 2001b).

The origin of the difference between the optical extinction and X-ray absorption seen currently has two physically-possible favoured arguments. First, if the unified model holds then the BLR should be dust-free, as it is inside the dust sublimation radius. This means that if a large fraction of the X-ray absorbing column density is located within the BLR, as studies have shown it to be, then this naturally yields a reduced A_V /N_H. Second, the circumnuclear dusty medium of AGN is very dense (n $\sim 10^5$ cm^{-3}) and in such dense environments dust grains tend to be larger, therefore being less effective in absorbing the optical and UV radiation (Maiolino et al., 2001a). This would result in the appearance of fewer dust grains, as there is less apparent optical extinction, but in reality this absorption would be more likely seen in the IR regions.

Similar results have been obtained from the comparison between infrared and X-ray absorption. By using Spitzer mid-IR spectra Shirahata et al. (2007) found that the depth of the dust silicate feature at ~ 9.7 μm correlates with the X-ray absorption, though with a large scatter. However, in most cases the silicate feature is much shallower than expected from the N_H inferred from the X-rays, when assuming a Galactic gas-to-dust ratio. Also, the intensity and shape of the mid-IR continuum give few indications of being affected by the presence of X-ray absorption along the line-of-sight. More specifically, Silva et al. (2004) found that the shape and intensity of the nuclear mid-IR continuum of AGN is essentially unchanged and independent of the column density N_H measured in the X-rays. Only for extremely X-ray absorbed objects does the mid-IR SED appear reddened at wavelengths shorter than $\sim 10\,\mu$m, but the inferred extinction is still more than 1 order of magnitude lower than expected from the N_H inferred from the X-rays. Similar results were obtained by

Lutz et al. (2004) and Krabbe et al. (2001).

The motivations for the reduced IR absorption relative to the X-ray absorption are partly the same as for the case of the optical absorption. However, an important additional factor contributing IR/X-ray absorption mismatch is that the mid-IR emission is extended, at least on the parsec-scale: i.e. on a scale comparable to, or larger than, the dense X-ray absorbing medium.

1.7 The spectral energy distribution of AGN

As AGN were discovered to emit across the EM spectrum astronomers began to make broad-band templates to fit these spectra of emission and try to understand the roles played by the different processes occurring in the central engine, in producing the total emission.

The broadband emission is usually displayed as νF_ν against ν, where ν is the frequency of the emission and F_ν is the flux density at that point. Using this type of plot rather than just a simple F_ν vs. ν plot provides a more realistic representation to aid the identification of the parts of the spectrum that dominate the power output. This is important when we consider that we are looking across very large ranges in frequency. These plots are referred to as spectral energy distributions or SEDs.

If we take an observed SED to be the sum of blackbodies at different temperatures, then we can develop a relationship linking temperature and area. This leads us to the assessment that the X-ray emission must come from a region several R_S across (this translates to light hours for a 10^8 $M_\odot$ black hole) while a region thousands of R_S across (hundreds of light-days) can contribute to emission from the IR region.

A time-averaged SED over the optical to X-ray region is extremely similar for all AGN, regardless of radio-type or luminosity, with most of the apparent differences arising from differences in the reddening (Ward et al., 1987; Gaskell & Klimek, 2003). The seminal paper of Elvis et al. (1994) built on this foundation, constructing broadband AGN SEDs from observations of 47 quasars from a variety of missions. Their study mainly focused on the X-ray and UV properties, aiming to shed light on the processes occurring in the heart of the AGN. Their averaged SEDs for the radio-loud and radio-quiet quasars from their sample are reproduced in Figure 1.12. The most interesting point to note about these SEDs is the large difference in radio fluxes between radio-loud and radio-quiet quasars.

Further work on SEDs, while producing radio-to-far-X-ray SEDs, mainly focused on the radio and IR energy generation mechanisms. Polletta et al. (2000) reinforce the scenario that thermal reprocessing is responsible for the emission produced in the mid-IR region of the SED, and Kuraszkiewicz et al. (2003) conclude that the nature of the dust in the AGN supports a 'clumpy' rather than 'smooth' torus model.

An extensive study by Richards et al. (2006) presents SEDs of 259 quasars and, while highlighting the diversity seen in the previous, smaller studies, also illustrates the similarity in the shape of several key features across the SEDs, particularly in the optical/UV region. This reaffirms the conclusions of Fan (2006), shown in Figure 1.13, but over a far larger energy range.

Despite this topic being a major focus of work over past decades the Elvis et al. (1994) templates shown in Figure 1.12 are still regarded as the definitive work to understand the broadband emission from AGN. The origin of the propagation of the shapes seen in SEDs, particularly in the optical to X-ray region, are not well understood. This is especially true as any explanation of the shape of the SED must be consistent with the variability properties discussed below.

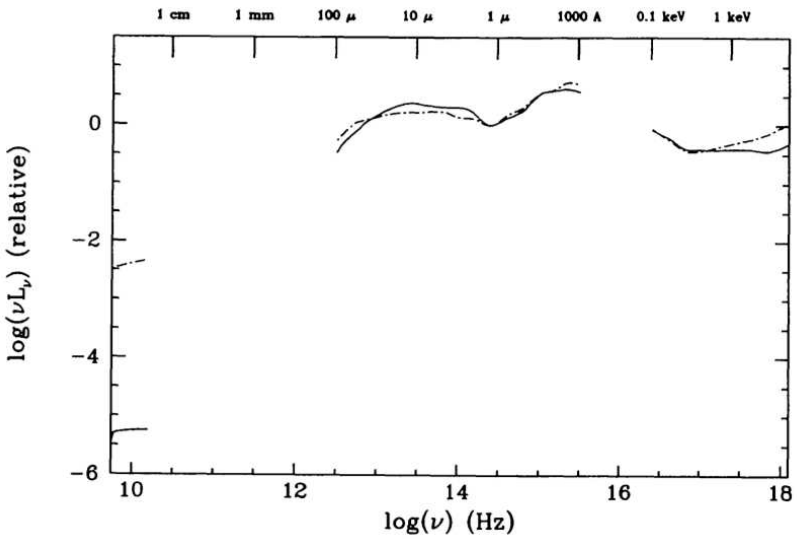

Figure 1.12: The mean quasar energy distribution from Elvis et al. (1994). This shows the normalised SEDs for both radio-loud (*dashed line*; sample size 18) and radio-quiet (*solid line*; sample size 29) quasars. The gaps highlight the regions where there is little or no available data.

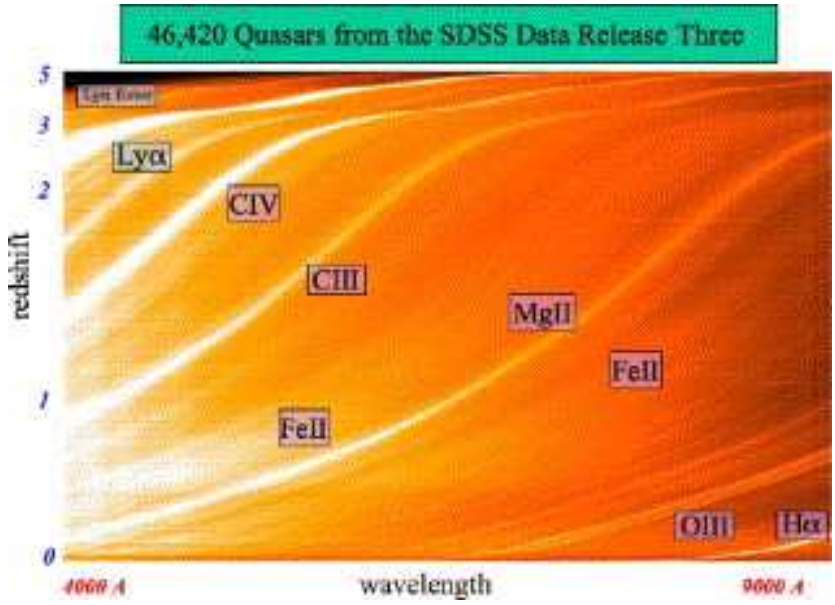

Figure 1.13: A two-dimensional composite optical spectrum of quasars from Fan (2006). The prominent emission lines are indicated on the figure.

1.8 AGN variability

It is thought that all AGN probably vary at all wavelengths, and this variability has been recognised for a long time. As it happens, optical variability was discovered before the true nature of AGN was known. Nearly 10 years before Schmidt identified the Balmer lines in the spectrum of 3C 273, Alexander Deutsch, working at the Pulkova observatory, reported that the nucleus of NGC 5548 appeared to vary by about one magnitude. At the time the continuous optical emission from the centre of galaxies was believed to be the combined emission from millions to billions of stars. Barring sporadic supernovae, this should have made detecting real optical fluctuations impossible and led to the majority of astronomers of the day rejecting Deutsch's results.

In the 1960s the first photometric catalogues of galaxies were being complied. During the compilation of electronic photometric measurements for the first Reference Catalog of Bright Galaxies (de Vaucouleurs & de Vaucouleurs, 1964), Antoinette de Vaucouleurs found that the fluctuations in the photometric magnitudes of NGC 3516, NGC 4051 and NGC 4151 obtained during 1958 considerably exceeded the normal photometric errors (see discussion in de Vaucouleurs & de Vaucouleurs, 1968).

As soon as AGN were identified and became a subject that astronomers could study, variability studies of these exotic objects began in earnest. A number of studies into the fluctuations of 3C 273 were in progress before Schmidt published his seminal paper. Based on previous searches for variability on plates from the Sternberg Astronomical Institute (SAI), Sharov and Efimov (1963) discovered that it varied by 0.7 magnitudes over the period 1896-1960, and by smaller variations with an amplitude of 0.2 - 0.3 magnitudes lasting several days, during a focused study carried out in the spring of 1962. Smith and Hoffleit (1963a, b) found evidence for a 10 year cycle with a peak-to-peak amplitude of 0.4 magnitudes with occasional flashes of larger variation lasting up to a week during a study of the Harvard plate archives from 1887-1963.

Shortly after these discoveries Dent (1965) found variations in the radio flux in flat-spectrum sources and, less than a decade after the discovery of optical variability of AGN, X-ray variability was discovered from observations taken from the OSO-7, *UHURU* and *Copernicus* satellites (Davidsen et al., 1975; Winkler and White, 1975).

1.8.1 Optical/UV variability

When looked at in greater detail the variability in the optical/UV region highlights some very interesting facts.

The optical/UV region varies enormously. Typically, in AGN the annual mean variability in the optical is in the region of $\sim$ tenths of a magnitude. On a physical scale the minimum variability seen (a few hundredths of a magnitude) means that for a 10^{45} erg s^{-1} AGN the energy equivalent of something in the region of 10^{10} solar luminosities is turning on and off, yet this is just the minimum amount of variability seen. The UV continuum of Fairall 9 was observed to vary by a factor of 30 in 180 days (Recondo-Gonzalez et al., 1997), and NGC 4151 was observed to vary by a similar amount over a few years (Ulrich et al., 1997). This shows that we must be observing a huge change in the fundamental energy production mechanisms, rather than just an additional superficial phenomenon.

Our knowledge of the timescales of the optical/UV variability is limited by how far back we have recorded images; 3C 273 has images back to the 1880s (Smith and Hoffleit 1963a, b), and observations of NGC 4151 go back to 1906 (Lyutyi and Oknyanskii, 1987).

Although X-rays are known to be variable on timescales down to an hour, constraining similar short-term variability optically in Seyfert galaxies has led to conflicting reports. We

often see that the largest amplitudes are seen on the longest timescales; detecting the shorter timescales with their smaller amplitudes is harder, and this is where the large sky surveys like the Catalina Sky Survey (CSS) and Pan-STARRS can contribute. With multiple nightly observations of the same area of sky over a period of years they should shed light on inter-night variability and help pave the way to understanding the focused studies that show intra-night variability. Studies of the optical light curves of AGN from Pan-STARRS has suggested that some of this variability could actually be due to stellar microlensing as the light from the AGN passes by a star within our own Galaxy, rather than a process intrinsic to the object (Lawrence, 2012).

1.8.2 X-ray variability

The X-ray flux of AGN is known to vary with very large amplitudes, on extremely short timescales. Variability on the scale of ~ 1 magnitude can be seen in the X-ray light curve of Cen A, going back to 1969 (Terrell, 1986). Flares are often seen, with one of the most extreme examples found during a 30 day monitoring campaign of IRAS 13224-3809, where Boller et al. (1997) found five giant amplitude flares, with the largest having an amplitude of 60. Further studies on this object found no evidence for a non-variable component (Gaskell & Klimek, 2003). As in the optical and UV variations, we can say that the variations represent changes in the fundamental energy mechanisms.

The variations in the X-ray region are more rapid than optical and UV variations of similar amplitudes. In IRAS 13224-3809 a factor of two variation in flux was found in just 20 minutes (Boller et al., 1997) and PHL 1092 has been observed to increase its flux output by a factor of four in less than an hour. If these variations are interpreted as changes in the isotropic flux, then they imply that the radiative efficiencies of these objects exceed the maximum than can be achieved from a rotating black hole.

The timescales involved in the variations give us an idea of where this variability can be coming from, as substantial variability cannot be observed from a source on timescales shorter than the light crossing time of the source (Terrell, 1967). The varying region is thought to be either within 15 R_S, or to originate from smaller regions further out (Gaskell & Klimek, 2003). The most important thing to come out of these studies is that the X-ray variations take place on a timescale equivalent to the light crossing time, rather than the viscous timescale expected by the accretion disc models of Shakura and Sunyaev (1973,

1976).

The greatest variability seen in the X-rays, such as the examples cited above, come from the soft X-ray region (soft-energies; < 2 keV). Possible interpretations for this feature are the presence of a softer continuum emission component that can vary more strongly than the harder (higher-energy; > 2 keV) component or a single component that is not constant and becomes softer as the source becomes brighter.

NLSy1s often exhibit the most spectacular cases of variability. Boller et al. (1996) was the first to show that, as a whole, NLSy1s have both a strong soft X-ray excess and a greater X-ray variability than is expected for their luminosity, although the first property can be partially explained by the fact that the hard X-ray component is particularly weak in NLSy1s. Leighly (1999) additionally highlights that the objects with the strongest soft excess also exhibit higher amplitude variability.

When looking at the X-ray power density spectrum (PDS), which gives a measure of the variability as a function of frequency, it is often noted that the PDS for AGN are very similar to those seen for Galactic BHBs, but on longer timescales. This similarity poses the possibility that there could be similarities in the processes causing the variability, especially as studies have suggested that the timescale scales with mass, but upscaling the accretion states seen in BHBs to AGN is difficult (Edelson & Nandra, 1999; and McHardy, 2010 for a review).

There is also evidence that the hard X-rays lag behind the soft X-rays (Reynolds, 2000; Vaughan et al., 2003). This lag is very small, with measurements of less than an hour for MCG-6-30-15, and has not been found in several well-studied objects including Ark 564 and Ton S180 (Edelson et al., 2002). It was also found by Edelson et al. (2002) that while there is a tight correlation on short timescales between the hard and soft X-ray bands, long-term changes could be seen in the ratio of the hard to soft X-rays.

1.8.3 The relationship between X-ray and Optical continua

Due to the large amplitude and rapid fluctuations of X-ray variability, it was for many years commonly assumed to be the driving variability of AGN.

In order to explain the AGN process that could produce the lags seen between the X-ray and optical variations two opposing models were developed. One model stated that the optical/UV bands observed were the result of reprocessed X-rays. In this scenario primary X-

rays heat cooler matter in the disc and torus, which then re-radiates the reprocessed emission. The prediction from this model was that the optical radiation would follow the X-rays. The second model produced X-ray emission from Comptonised, upscattered optical/UV photons. A corona of relativistic electrons Comptonises the optical/UV emission, producing X-rays. Here, the optical/UV emission would be followed by the X-rays.

Initial studies ruled in favour of the first model (Lyutyi, 1978) but multiple studies following this drew a range of conclusions: X-rays lagging behind optical emission, optical emission lagging behind X-rays and no significant correlation between the two (Done et al., 1990; Edelson et al., 1996, 2000; Nandra et al., 2000; Peterson et al., 2000). Even though these results have proved inconclusive so far, an alternate approach by both Uttley et al. (2003) and Gaskell & Klimek (2003) ruled out X-ray reprocessing as the source of the optical/X-ray correlation when they found that the fractional amplitude of the optical variability was greater than the X-ray fractional variability.

This conclusion forms the basis behind using upscattered, Comptonised optical/UV photons to produce the X-ray emission in the SED modelling in Chapter 3 of this thesis.

1.9 This Thesis

The optical and X-ray emission of AGN originates from the central region of the AGN, and studying this emission provides an insight into the processes that happen in the regions surrounding and containing the accretion disc and corona.

In the following chapters, we describe various studies that we conducted into improving our understanding of these regions. Chapter 2 is an exploration of the relationship of dust and gas in the central region of quasars conducted on a large sample of X-ray detected SDSS Type 1 quasars. In Chapter 3 we create a low redshift X-ray detected Seyfert 1 sample and model the resultant SEDs, constraining the physical processes behind this emission. Chapter 4 presents the results of a study on the optical and X-ray variability of a subset of the objects modelled in Chapter 3, utilising data from the Catalina Sky Survey and *XMM-Newton*. Chapters 5 and 6 both present the results of pilot variability studies with the Pan-STARRS telescope. Chapter 5 describes the result of a in-depth study into a single object, while Chapter 6 focuses on using Pan-STARRS to carry out large scale surveys. Finally, we summarise our main findings and discuss possible future work in Chapter 7.

Chapter 2 | *Gas and Dust in AGN*

In this chapter we use the 2XMMi Serendipitous Survey (Watson et al., 2009) and the SDSS DR5QSO Catalogue (Schneider et al., 2007) to produce a study of 1,201 quasars with in-depth optical and X-ray spectral analysis, producing composite spectra for gas absorbed quasars and dust reddened quasars, as well as investigating the dust-to-gas relationship seen in these subsamples and in the sample as a whole.

We present the construction of our sample in Section 2.2, our optical observations and data analysis in Section 2.3 and our X-ray observations and data analysis in Section 2.4. In Section 2.5 we discuss the results of the combined optical and X-ray analysis and look at the dust-to-gas relationship. The composite spectra of the samples are shown in Section 2.6 and we give our conclusions in Section 2.7.

2.1 Introduction

It is now understood that quasar catalogues are crucial when conducting a statistical study into the properties of quasars. There are known correlations between X-ray and optical properties that expose the relationship between the disc and the corona (Shakura & Sunyaev, 1973; Haardt & Maraschi, 1991). Although quasars were first discovered in radio surveys, today the majority of surveys for AGN (particularly quasars) are carried out in the optical/UV region, meaning our understanding of the evolution of these objects is biased toward the properties of optically luminous samples. The first slitless spectroscopic surveys were biased against weak emission line quasars and UV-based surveys were biased against 'red' sources, where the red colours were produced by high redshift, dust reddening or intrinsically reddened continua not related to dust. In recent years reddened and obscured quasars have been found by radio, IR and X-ray surveys, but optical/UV spectroscopy is still needed to confirm the central nucleus and determine the redshift.

Over the past 15 years there have been various studies into the relationship of gas and dust in AGN. While the dust-to-gas relationship for the Milky Way is well established, Maiolino et al. (2001a) found that AGN exhibit a broad range of values. Their study found that the dust-to-gas relationship in AGN ranges from ~ 3 up to ~ 100 times lower than the Galactic relationship for all subsets. This relationship has been explored for the nearest galaxies, and with new data for quasars this relationship is now being tested to higher redshifts. So far, only small sample studies have been carried out into the X-ray properties of dust reddened quasars due to the need for both high-quality X-ray and optical data (Hall et al., 2006; Wilkes et al., 2002; Green et al., 2009).

There have been limited studies of the X-ray properties of dust reddened and intrinsically red objects (Hall et al., 2006; Wilkes et al., 2002) which have progressed to catalogues of X-ray detected quasars. From these, the consensus is that there is significant dust reddening found in $\sim 6\%$ of all quasars, gas obscuration found in $\sim 10\%$ of quasars and that gas obscuration is found in $< 50\%$ of dust reddened selections.

The work in this chapter aims to test these findings by looking at the reddening and obscuration properties of a large sample of X-ray detected AGN. The sample contains objects across a wide redshift range and contains objects exhibiting all levels of obscuration from little/none to almost Compton-thick status.

2.2 Sample selection

We created a sample of 1,201 spectroscopically classified quasars that are X-ray detected by cross-matching the SDSS DR5QSO Catalogue (Schneider et al., 2007) with the 2XMMi-Netwon Serendipitous Survey (Watson et al., 2009). We need both optical and X-ray data to constrain the amounts of dust and gas, respectively, present in these systems.

2.2.1 SDSS DR5QSO Catalogue

The SDSS DR5QSO Catalogue (Schneider et al., 2007) is the fourth edition of the SDSS quasar catalogue, and is based on Data Release 5 (DR5). This catalogue covers an area of 5740 deg^2 (13.9% of the sky) and contains 77,429 objects. The quasar candidates are found

using a target selection algorithm. This selection algorithm selects objects that have an i band absolute magnitude brighter than M_i = -22 mag and that have at least one emission line with FWHM greater than 1000 km s^{-1}. Most of the quasars are identified by their position in the multi-dimensional SDSS colour space. The SDSS survey is magnitude limited in the i band (7461 Å), which means that it is more sensitive to dust reddened quasars than most optical surveys that are limited in the B band (4400 Å), as the spectral shapes of quasars are strong functions of wavelength, and the red end of the spectrum is less affected by dust reddening (Richards et al., 2003). In addition to this the SDSS survey is sensitive to quasars with non-standard colours, as it considers objects outside of the stellar locus in colour space to be possible quasar candidates. The SDSS quasar catalogue provides photometry in the *u, g, r, i* and *z* at wavelengths of 3541, 4653, 6147, 7461 and 8904 Å respectively, and spectroscopy is given for 3800 - 9200 Å.

2.2.2 2XMMi Serendipitous Survey Catalogue

The 2XMMi-Newton Serendipitous Survey (Watson et al., 2009) is the incremental second serendipitous X-ray source catalogue, consisting of both the targets and non-target source detections that are recorded in the field of view of the X-ray cameras. The catalogue contains information from 4,117 pointed observations taken between 2000-02-03 and 2008-03-28. It covers 560 deg^2, but due to field overlaps the total field coverage area is 420 deg^2. The total area contains over 290,000 detections, which reduces to $\approx$ 220,000 unique sources. The *XMM-Newton* imaging takes place on three European Photon Imaging Cameras (EPIC): MOS-1, MOS-2 (Turner et al., 2001) and the PN camera (Strüder et al., 2001). The MOS cameras have 33' x 33' field of view and the PN camera has a 27.5' x 27.5' field of view. The 2XMMi overlaps with 75 deg^2 of the SDSS DR5QSO catalogue (i.e. $\sim$ 1.5%)

2.2.3 Cross-correlating the catalogues

We initially created the X-ray detected quasar sample by selecting objects from the 2XMMi Serendipitous Survey that lay within 10" of an SDSS DR5 quasar; we made no cuts on where the sources could lie on the *XMM-Newton* observation fields. This initially yielded 2,013

objects. These objects were visually inspected in order to remove any spurious matches (multiple X-ray sources around one optical quasar), objects that lay on a chip gap or that were saturated by a nearby source. During this process it was found that 812 objects were contaminated in such a way to make them unsuitable for this study, reducing the sample to 1,201 unique sources, of which 79 were XMM targets. Figure 2.1 shows two examples of rejected objects. The object in Figure 2.1a was excluded from the sample because it was far off axis, on the edge of the EPIC field of view, and as a result is extended. Figure 2.1b shows an example of a source contaminated by a bright background.

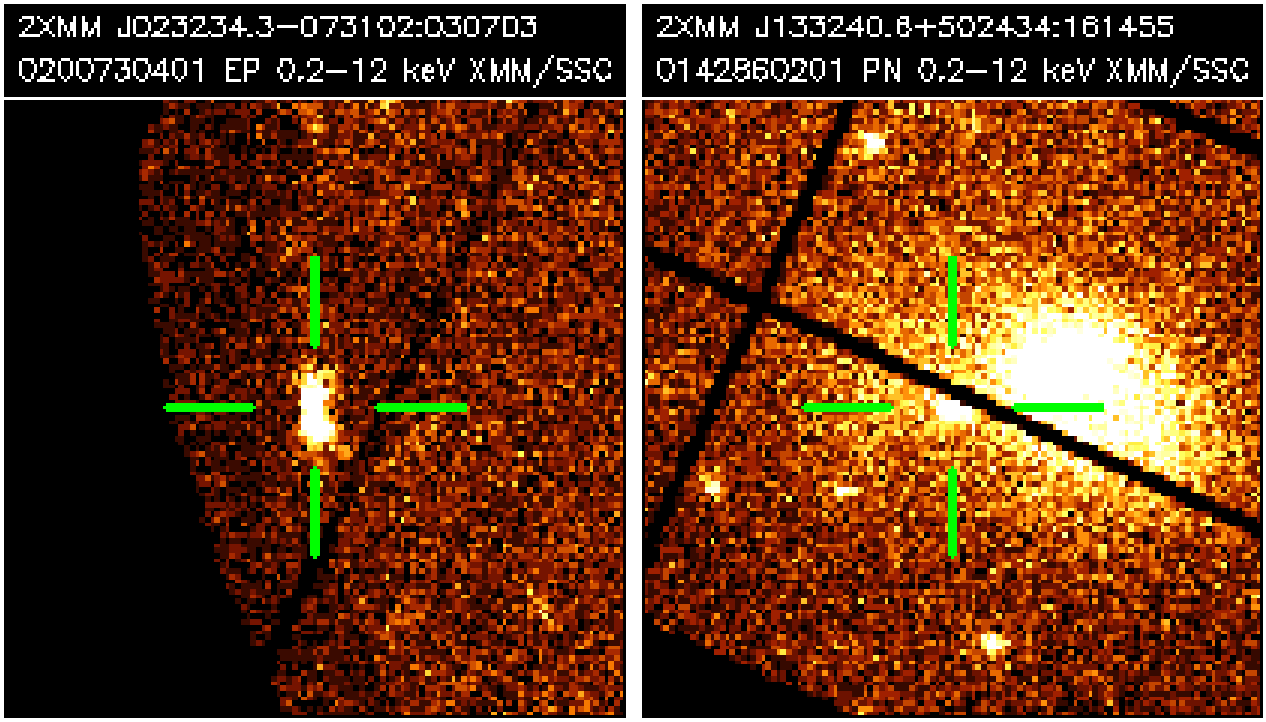

(a) Example of extended source.

(b) Example of bright source.

Figure 2.1: Rejected sources from XMM

The visual inspection and re-extraction of sources reaffirmed the decision to keep the search radius at 10", as many of the X-ray sources were found to be off-axis on the detector and it is known that the positional accuracy of *XMM-Newton* decreases with increasing off-axis angle (Pierre et al., 2007). The positional offset between the positions of the DR5 objects and the 2XMMi catalogue objects was analysed and it was found that 28 of the X-ray sources lay 5 - 10" from the SDSS source. These objects were later found to be objects that were extended due to being off-axis and all of these objects were excluded from the

X-ray analysis as they had too few counts to be modelled, but they were still included in the optical analysis. Figure 2.2 shows the positional offset, with histograms showing the relative frequency of the offset in both R.A. and dec shown above and to the right of the plot respectively. The median offset is found to be at (0.084", -0.085").

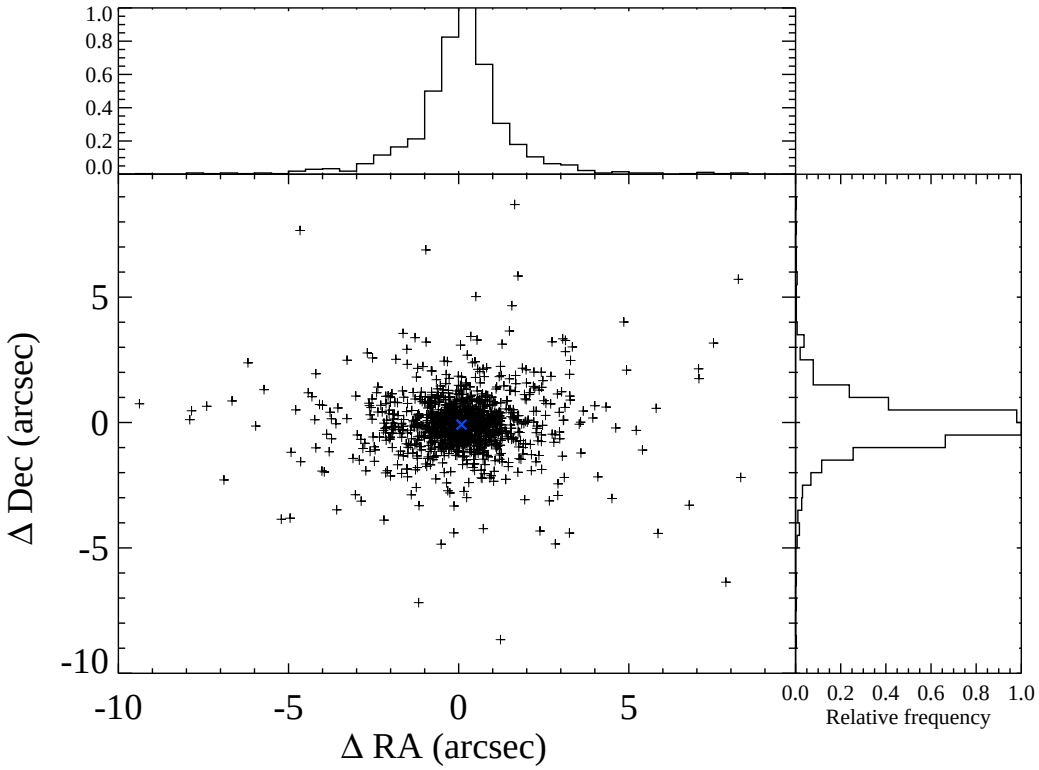

Figure 2.2: A scatter plot of the offset between the SDSS catalogue positions and the 2XMMi catalogue positions. The SDSS positions are used as the central point. Histograms showing the relative frequency of the offset in both R.A. and dec are shown above and to the right of the plot respectively. The median offset is at (0.084", -0.085"), and is well within the angular resolution of both telescopes.

2.2.4 X-ray data reduction

The data for the 1,201 objects was then re-extracted rather than using the catalogue data. The reason for this was that the data in the catalogue was found to be unreliable, with objects outside of the field of view of an EPIC pointing having positive detections, while others were blended with nearby objects. We extracted both the source and background,

making sure that the source radius was chosen to prevent blending and that the background was a true representation of the background at the position of the object.

The 1,201 X-ray observations were processed using the *XMM-Newton* Science Analysis System SAS v7.02.[1] The events were reprocessed to ensure that each observation had the same latest calibration and then filtered to remove time intervals containing high-energy background flaring events.

The source and background regions were defined with a semi-automatic process. The SAS task EREGIONANALYSE was used to optimise the source extraction radius for signal to noise, while visual checks were made to identify objects blended with nearby sources. The background extraction region was assessed by eye to make sure that it was not contaminated by other sources, chip gaps and saturation events. The regions were selected to lie at the same off-axis angle as the object and as close to the source as possible, without overlapping. Once source and background regions had been defined for all sources the X-ray spectra were extracted.

Where possible observations from all three *XMM-Newton* EPIC CCDs were reduced to be used in the analysis, but this was not always possible. A number of objects lie in a bad region in at least one camera, either in a chip gap or outside the field of view of the CCD, due to the different shapes of the MOS and PN cameras.

2.2.5 Upper limits

We calculate upper limits for quasars that appear in the DR5 catalogue whose positions overlap with the 2XMMi area coverage, but are not X-ray detected. We found 253 upper limit objects for which we have the maximum flux that the object could have in that band yet not be detected by the *XMM-Newton* cameras, based on the source positions from the DR5 catalogue. From this we found that due to the redshift of these objects the upper limits on their X-ray luminosity put them well within the distribution found for the rest of the sample, but due to the small count rates involved we could not do any further analysis on this sample, and so they were excluded from the rest of the study.

[1] http://xmm.esac.esa.int/sas

2.2.6 Characteristics of the sample

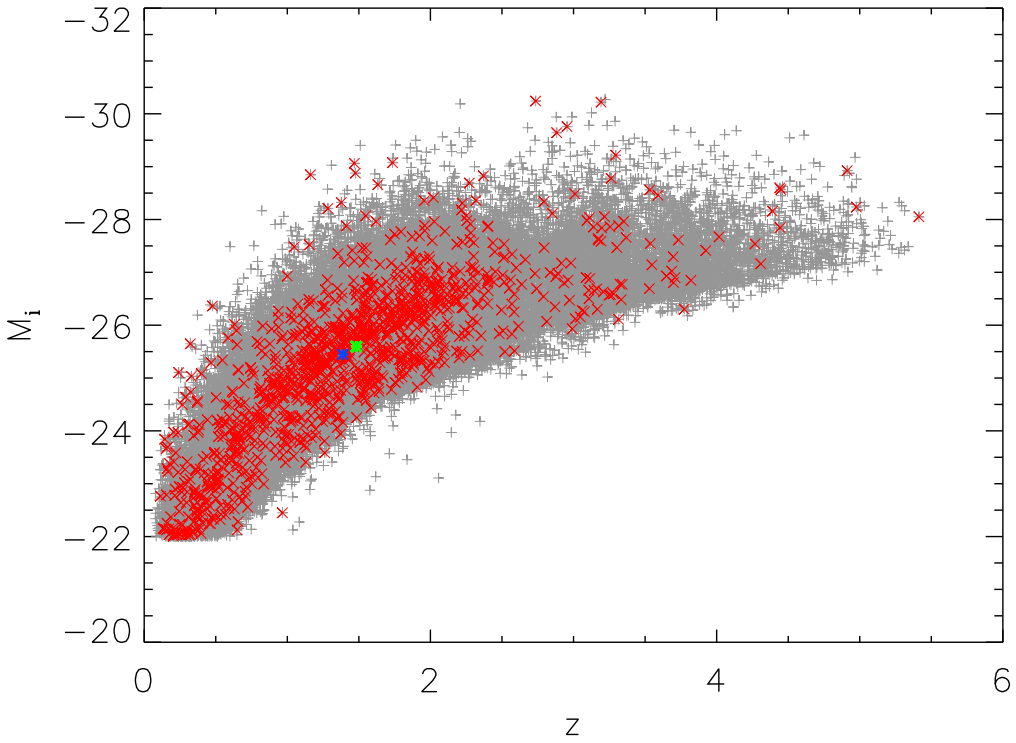

Figure 2.3: A comparison of the SDSS DR5 Quasar catalogue (shown in gray) with our X-ray detected subsample overplotted in red. The median value of the SDSS sample is shown in green and the median of our subsection is shown in blue.

The selection process outlined above ensures that we have selected 1,201 quasars with both an optical spectrum and the highest quality X-ray data that we could produce from the EPIC observations. This still produces a wide range in the data quality of our sample: 203 objects ($\sim$ 17% of sample) have fewer than 50 counts while 25 objects ($\sim$ 2% of the sample) have more than 10,000.

We have identified 1,201 optical quasars, which are formally detected in 2XMMi, to form our sample. In order to discern how representative the selected sample is against the SDSS DR5 parent sample two statistical tests were carried out on the absolute magnitude (M_i) and redshift distributions of the two samples. The first was a Kolmogorov-Smirnov test (K-S) test, which showed that the selected sample is representative of the parent sample.

Student's f-test was also carried out on randomly selected subsets of each sample; this also showed that the selected sample is representative of the parent sample.

The redshift against M_i distribution is shown in Figure 2.3, with the DR5 quasars shown as grey crosses and the sample population shown as red sideways crosses. The M_i < -22 cut-off point for the SDSS quasar definition can be clearly seen. The median values of the SDSS DR5QSO quasars are shown as a green cross and the median values for our subset are shown as a blue cross; while the values for our sample are slightly lower than the parent population, they are still shown to be in excellent agreement based on the statistical tests carried out above.

Figure 2.4 shows the redshift distribution of the sample. The range of the sample is 0.1136 < z < 5.413, and the median value is z = 1.39. It can be seen that the majority of the objects lie between z = 1 and z = 2, which is the peak of the quasar redshift distribution (Schneider et al., 2007).

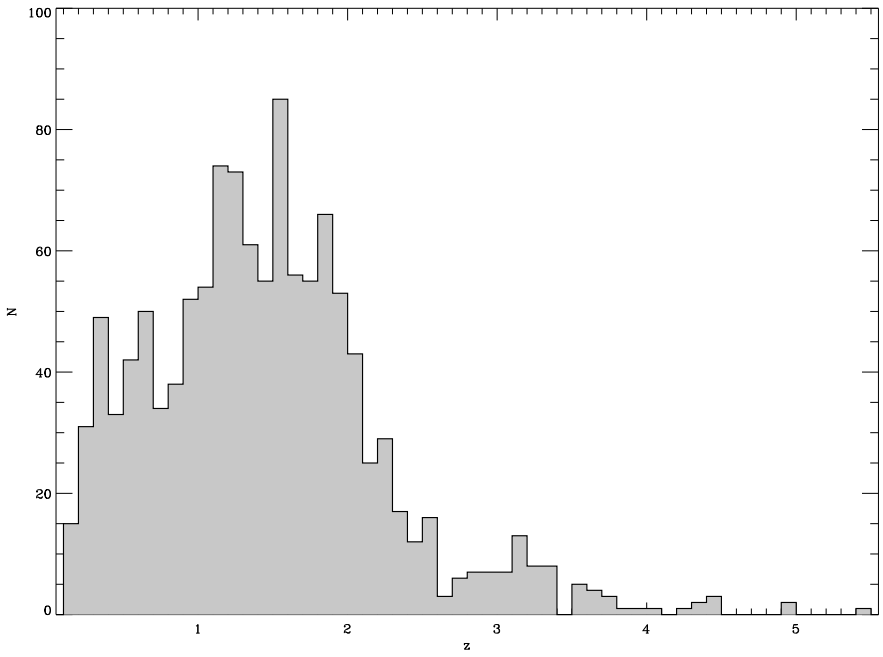

Figure 2.4: A histogram showing the redshift distribution of the quasar sample.

2.3 Optical Analysis

We used two different methods to identify dust reddened quasars in our sample. First the $\Delta(g-i)$ method championed by Richards et al., (2003), based upon relative colours as described below. The second method involves dereddening the optical continuum and comparing it to an average quasar continuum. The object's continuum is dereddened with an SMC-like extinction curve, which is used instead of a Galactic extinction curve due to the absence of the λ2175Å feature in AGN spectra (Calzetti et al., 2000).

In order to gather as much information about the optical properties of the 1,201 objects as possible, we also calculated the optical spectral index for each object, both before and after dereddening.

All spectral indices are a measure of the dependence of flux density on frequency and can be defined by:

$$f_\nu \propto \nu^{-\alpha} \tag{2.1}$$

where the flux at a given frequency f_ν is proportional to the frequency (ν) to the power of the negative spectral index (α). The optical spectral index is calculated by:

$$\alpha_{opt} = 4.960 \log\left(\frac{f_{7000\mathring{A}}}{f_{4400\mathring{A}}}\right) \tag{2.2}$$

Vanden Berk et al. (2001) found that there are two slopes in the composite optical spectrum of quasars. There is a slope running down from Lyα to Hβ ($\sim$ 1250 - 4250 Å) where α_{opt} = -0.46, and a steeped slope red-wards where α_{opt} = -1.58. With the redshift range of our sample we only measure one value for α_{opt} across the whole spectrum, but due to the findings given above we expect to find a range of values for the sample. All spectral indices are calculated from fluxes unaffected by absorption or emission lines that are measured in the rest frame as part of the continuum fitting processes used to determine the level of continuum reddening.

Fitting a continuum to such a large redshift range was difficult as a large range of emission line free wavelength ranges had to be established, which is essentially impossible in a quasar spectrum. We adopted a compromise by establishing regions where the contamination from emission lines is the weakest. The observed wavelength range for each object was corrected

to the rest wavelength range, then the continuum wavelengths bands were highlighted and visually inspected to ensure that the S/N in these regions was robust enough to fit the continuum and that there was no unusually strong non-continuum emission in the region. Once each object had a continuum range set, it was fitted. For high redshift objects ($z > 2.0$) a scaled, template continuum wavelength band was attached to the red wavelength end of each spectrum, in order to ensure that the continuum fit would follow the AGN continuum shape out to long wavelengths.

2.3.1 Relative colours

A major problem with trying to identify dust reddened quasars by colour alone is that quasar colours are a strong function of redshift. Following the work by Vanden Berk et al. (2004) and Richards et al. (2002; 2003) the quasar colour distribution has been characterised as a function of redshift, and these studies have presented their colour distribution. Previously used colour cuts such as $B - V > 5$ or $J - K > 2$ select quasars that are apparently red but fail to distinguish whether a quasar is intrinsically red due to an optically steep power law continuum, reddened due to dust extinction, or appears red due to an emission or absorption line in one of the bands (Hall et al., 2006). Following on from the work of Richards et al. (2002; 2003) it is now known that using relative colours allows a method of identifying redshift-independent red quasars. For each quasar a *relative colour* can be computed by subtracting the median colour of quasars at that redshift from the colour of the quasar (Vanden Berk et al., 2004). Relative colours are therefore more sensitive to reddened quasars at all redshifts. This is more advantageous than using an observed frame cut such as $J - K > 2$, as $\Delta(g - i)$ probes the shape of the optical/UV continuum at all redshifts, whereas $J - K$ measures different parts of the spectrum depending on the redshift of the object. In Richards et al. (2003) it is shown that the relative colours for quasars are easily fitted to a Gaussian distribution, but for several colours (including $\Delta(g - i)$) there are distinct red tails. Quasars are identified as being part of the red tail if $\Delta(g - i) > 0.2$. This value is then corrected for an SMC-like extinction curve with E(B - V) = 0.04, which is a value typical of high Galactic latitudes.

2.3.2 Photometric method

While using $\Delta(g-i)$ will give an indication of a reddened spectra, using this method alone will not distinguish between a dust reddened quasar and a quasar with a red power law continuum. In order to do so we compared relative colours from across the available spectrum, as relative colours can be used to give an idea of the shape of the continuum. As dust reddening affects the curvature of the blue end of the continuum more than the red, a dust reddened quasar will have $\Delta(u-r) > \Delta(g-i) > \Delta(r-z)$, but a quasar that has a power law continuum that is intrinsically redder than average will have $\Delta(u-r) < \Delta(g-i) > \Delta(r-z)$. For comparison a blue power law continuum will have $\Delta(u-r) \sim \Delta(g-i) \sim \Delta(r-z)$. In order to create accurate relative colours we used all of the objects in the SDSS DR5 catalogue and binned them into redshift bins of 0.01.

Our definition for dust reddened objects was taken to be those that were relative colour reddened with $\Delta(g-i) > 0.2$ when corrected to account for an SMC-like extinction curve, and which also showed evidence of spectral reddening, where $\Delta(u-r) > \Delta(g-i) > \Delta(r-z)$.

From this it was found that 106 of 995 quasars were reddened (i.e. $\Delta(g-i) > 0.2$); out of these 26 were found to be intrinsically red, with a red power law continuum, and 72 were found to have continuum curvature consistent with dust reddening (i.e with $\Delta(g-i) > 0.2$ and $\Delta(u-r) > \Delta(g-i) > \Delta(r-z)$). Hereafter, this sample of 72 is called the $\Delta(g-i)$ sample.

2.3.3 Continuum Reddening Method

As all of the 1,201 quasars in our sample have optical spectra from SDSS we also analysed the spectra to produce a different dust reddened subsample. With the large redshift range of our sample we had to impose a cut, as we could not reliably fit the continuum to the highest redshift objects; we only analysed objects with z < 4.

We use the Calzetti et al. (2000) dust reddening curves with the values for AGN. In order to calculate a value for A_V we compared each object to the composite spectrum of Vanden Berk et al. (2001). This value was then used to deredden the object's spectrum to force it to look like the composite spectrum of Vanden Berk et al. (2001). We used the

Vanden Berk et al. (2001) composite spectrum as our zero-reddening template because for the Hα - Hβ Balmer Decrement we calculated a value of $A_V = 0.08 \pm 0.07$. To calculate the A_V using this method we used the following formula from Ward et al. (1987):

$$A_V = 6.67 \log(\frac{H\alpha}{2.85 * H\beta}) \tag{2.3}$$

where Hα and Hβ are the respective fluxes of these emission lines.

Each object's spectrum was divided into bins of 1 Å. Each bin was then dereddened to match the composite value for that bin. A fitting routine was used to work out a best-fit value and error of A_V for the whole spectrum. This value was then used to redden the composite continuum and match it to the object's continuum. Finally the fitting routine was run again to see if the fit could be improved. Figure 2.5 shows an example of this process. The MJD, field and fibre number of the SDSS spectral observation, along with the R.A., dec and redshift of the object are given in the top left of the figure. The object's spectrum is shown in black and the emission free continuum regions are shown in red. The continuum fit to these bands is shown in blue and the continuum of the Vanden Berk et al. (2001) composite spectrum is shown in green. The thick black line represents the continuum after it has been dereddened by the best-fit A_V value. It can be seen that the resultant fit is a good match to the composite continuum. All the continua and the spectrum have been normalised to 8100 Å. Even though the fitting was done at rest wavelengths the observed wavelengths are shown in this plot as it was easier to visually assess the success of the fit of all the objects, particularly those at high redshift.

We defined objects that had a best-fit A_V of $0 < A_V < 1.5$ and produced spectra that were in good agreement with the composite in terms of continuum shape and strength, to have a good fitting result. Many objects in our sample have a bluer continuum than that of the Vanden Berk et al. (2001) composite, resulting in negative A_V values. In these cases the A_V is not a reddening term but rather, implies that the object's continuum is bluer than average. A possible cause for this is the Balmer continuum, which we did not model, but is known to produce a very blue continuum in some AGN (Jin et al., 2012).

Objects with $A_V > 1.5$ did not produce the composite continuum shape when dereddened, and no other value of A_V could be found to produce a better result. This indicates

that there are factors other than dust causing the reddening. While objects with a large A_V do have dust reddening, we were unable to categorise the amount present using this method, as the processes causing the intrinsic reddening are unknown.

Because of these caveats on the results of the analysis, we defined the quasars to be dust reddened if $0.5 < A_V < 1.5$. We found 61 objects that fit this criteria and are hereafter described as the A_V sample.

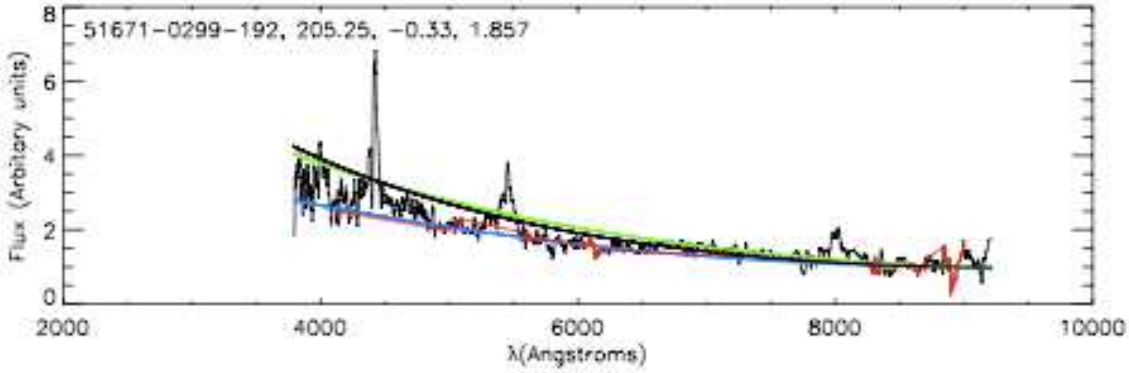

Figure 2.5: The continuum reddening fitting routine. The object's spectrum is shown in black, with its continuum overplotted in blue. The continuum of the Vanden Berk et al. (2001) composite spectrum is shown in green and the thick black line shows the best-fit dereddened continuum of the object. The red points indicate the continuum bands in the spectrum.

2.4 X-ray data Analysis

The spectra were fitted with **XSPEC** v11.3.2 (Arnaud, 1996). During this process the MOS+PN spectra, when available, were fit simultaneously over the 0.5 - 12 keV range with the same parameters, including normalisations.

We used three models during the fitting process: power law (*po*), absorbed power law (*apo*) and power law with a blackbody (either *po + bb* or *apo + bb*). No background model was used. Out of the 1,201 objects, 203 were detected but had too few counts (i.e. < 50 counts) for the modelling process, therefore a total of 998 objects were modelled. Each model

also includes an additional absorption component which is fixed to the value of the Galactic column density in the direction of the source, taken from the **nH** Ftool,[1] which uses the Dickey & Lockman (1990) map of the 21 cm H I.

The best fitting model was determined by an F-test at 99% significance. All 998 spectra were first fitted with the fixed power law, *po_fix*, model and then the absorbed fixed power law, *apo_fix*, model. For the 237 sources with 50 - 75 counts we assumed *po_fix* to be the correct model unless it required *apo_fix*.

When the fixed power law or fixed absorbed power law model was used, the power law photon index, Γ, was frozen at 1.9. This value was used as it agrees with most surveys that find an average of $\Gamma = 1.9$ - 2.0 (Mateos et al, 2010; Young et al., 2009; Mainieri et al., 2007; Mateos et al., 2005b, a; Page et al., 2006; Green et al., 2009). It was also frozen at $\Gamma = 1.9$ when there were less than 75 counts in total from all three cameras.

All 761 sources with > 75 counts were fitted with *po* and *apo*. The 680 sources with 100+ counts were also fitted with *po+bb* and *apo+bb*. For all 761 sources we assumed the correct model to be *po*, unless an F-test chose *apo* or *po+bb*. Once one of these models was chosen it was tested to see if *apo+bb* was required.

During the fitting routine, we noticed that 6 sources were classified as *apo_fix* but had a $\chi^2 = 0$ and dof $= 0$. This is because they have only ~ 60 counts and the *apo_fix* model cannot produce real fits in these cases. These sources were therefore classed as *po_fix* instead.

For the objects with constrainable gas absorption, we measured N_H values with a range of 0.01 - 58 x 10^{21} cm^{-2}, and for the rest of the sample we calculated upper limit values, which are all < 6.9 x 10^{22} cm^{-2}. Γ ranges from 0.42 to 3.34, in the cases when it is not fixed to $\Gamma = 1.9$. The value of Γ reported is dependent upon which spectral components are modelled in the spectra, and the quality of the spectra itself. If there is an unmodelled reflection component or a warm absorber present then they can produce a flatter slope than the true intrinsic value. For many of our sources the data quality was not good enough to recognize and model these additional components. Table 2.1 shows the breakdown of the different models.

[1] http://heasarc.gsfc.nasa.gov/docs/software/ftools/

Model	Number
apo	29
apo+bb	5
apo_fix	10
po	672
po+bb	55
po_fix	227

Table 2.1: The number of objects fitted to the different models, as determined by the F-test.

2.4.1 X-ray Obscured

Out of the 998 sources modelled, 50 objects were found to have constrainable values of N_H. Upper limits were calculated for the remaining 948 sources at the 90% limit.

We defined a source to be gas obscured it had a modelled N_H value > 1 x 10^{22} cm^{-2}. This gave us a gas obscured sample of 40 objects. A further 109 objects have an N_H upper limit value > 1 x 10^{22} cm^{-2}. Taking just the constrained sources gives $\sim 4.2\%$ absorbed sources. This value is lower that found in the literature, and is discussed in greater depth in the analysis of the X-ray properties of this sample in Scott et al. (2011). Figure 2.6 shows total X-ray counts against N_H. Objects with a constrained value of N_H are shown with their associated errors. Otherwise the upper limit for the object is shown as a grey arrow. The sample is subdivided into 3. Sample 1 is objects with $> 10^4$ counts, sample 2 is objects with $< 10^4$ and $> 10^3$ counts and sample 3 is objects with $< 10^3$ counts. 5 of the 20 sources in sample 1 have measured values of N_H which are greater than measured galactic absorption. This is less than the $\sim 30\%$ estimated by Scott et al. (2011) for objects with greater than 10^4 counts, in a simulation based on this sample, but is most likely due to small number statistics. Sample 2 has 8 of the 159 sources of this nature, which is in excellent agreement with the $\sim 5\%$ estimated by Scott et al. (2011) for objects with between 10^3 and 10^4 counts. For sample 3 we find 37 of 769 with constrained values of N_H, which is slightly higher than that predicted by Scott et al. (2011). It is worth noting that the data quality of several objects in this sample may mask any spectral complexities, making it easier than it

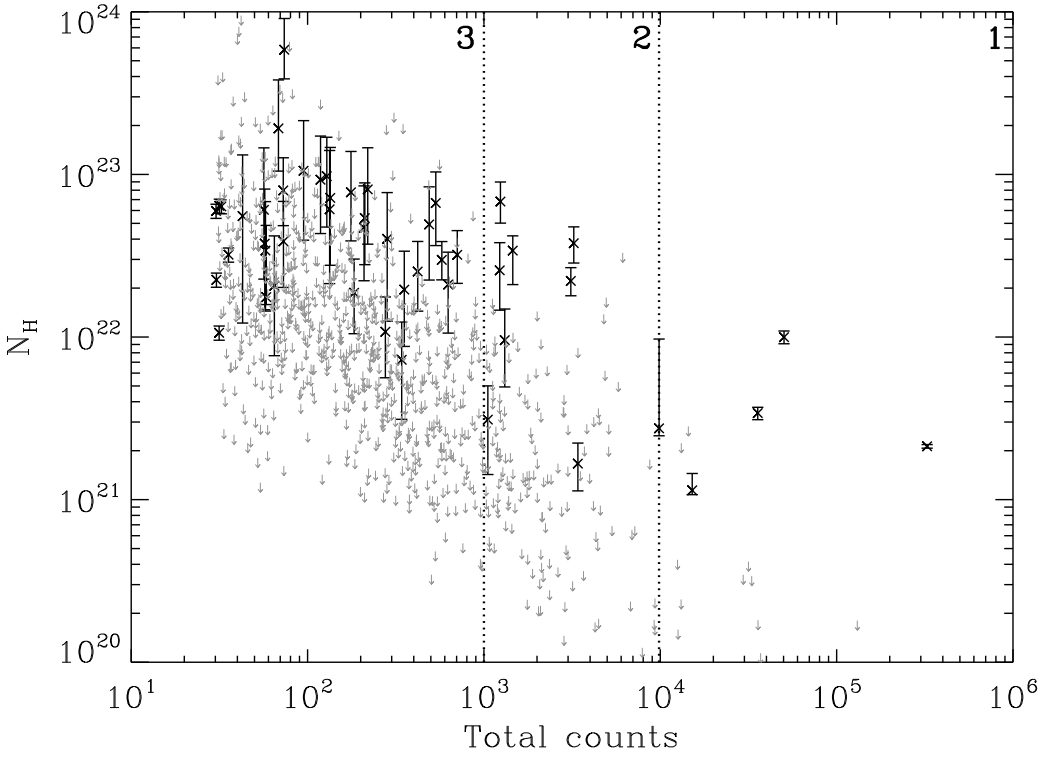

Figure 2.6: A plot of the total X-ray counts against N_H. Objects with a constrained value of N_H are shown with their associated errors. Otherwise upper limits are shown as grey arrows. The numbers refer to the subsamples based on number of counts: 1 is $> 10^4$ counts, 2 is between 10^3 and 10^4 counts and 3 is $< 10^3$ counts.

otherwise would be to constrain the N_H values, whereas in the objects with a high number of counts the spectra become too complex to be constrained by the models used.

2.4.2 X-ray model fitting

After defining the two dust reddened samples, it was found that only 3 objects in the A_V sample had a constrained value for N_H. In order to better constrain the value of N_H for these samples we used joint spectral fitting on both samples, where all spectra are fit independently with the same model and parameters, producing average parameter values. Initially 7 sources were removed from each of the A_V and the $\Delta(g-i)$ samples as they had less than 20 counts, which is the lowest number of counts able to be used in this method. Also one source (SRCID

211185) was removed due to pile up. This left 54 sources with 91 spectra in the A_V sample and 64 sources with 103 spectra in the $\Delta(g-i)$ sample, as some objects had multiple spectra from multiple observations. The spectra were rebinned to 10 cts/bin in order to retain as much information as possible for the low S/N sources and then both χ^2 and cash statistics were used, as well as binning the spectra to 1 ct/bin for comparison.

The joint spectral fitting used an absorbed power law model in which the power law photon index, Γ, was fixed at 1.9. the N_H value was tied for each spectrum to all of the other objects in the sample. This left only the power law normalisations free to vary. We chose to fix Γ, as when it was left as a tied parameter the model automatically produced a fit with a higher value of N_H and a flatter Γ, which was often not realistic fit to the spectra in the samples.

One of the major issues complicating this process is that of soft excess. The soft excess seems to be a ubiquitous feature in the sample, and in a joint fitting of low count spectra we are able to reproduce this feature. Therefore, we need to account for this component in the joint fittings we are doing here.

Firstly, we fit an absorbed power law with a blackbody to both samples. We could only do this with sources with greater than 30 counts; this dropped the samples to 50 sources with 78 spectra for the A_V sample, and 63 sources with 96 spectra for the $\Delta(g-i)$ sample. In these fits, Γ is fixed at 1.9, kT at 0.17, N_H is tied and both the power law and blackbody normalisations are free to vary. The spectra are still binned to a minimum of 10 cts/bin.

The fittings from this method showed a strong dependence between the N_H value obtained and the kT value used in the fit, because these components are both being fitted in the same parts of the spectrum. From this fitting procedure we found a value of $N_H = 5.8$ x 10^{21} cm^{-2} and $N_H = 5.65$ x 10^{21} cm^{-2} for the A_V and $\Delta(g-i)$ samples respectively. The values obtained from this fitting are shown as the right-hand red square in Figure 2.9. As both the A_V and N_H values are very similar for both of these samples, only the results of the A_V sample are shown for clarity.

Because of the dependence of the N_H value obtained on the value of kT used, a method was found to remove the necessity of having the blackbody component in the fit, and thus make the fit more reliable. A redshift cut is unlikely to help since Scott et al. (2011) show

that blackbody components can still be detected up to z = 2 and this would therefore remove too many sources from the samples.

Instead, we consider whether we can use a rest frame energy cut in order to remove the lowest energies where the blackbody component dominates, but retain enough of the spectra to allow the absorption signature to be measured.

We first considered the worst-case scenario of a source with a large blackbody component. We simulated a spectrum with $\sim$ 10,000 counts at z = 0 and use a high kT value = 0.23 keV and high blackbody/powerlaw normalisation ratio of 0.5. We then determined the ratio of the blackbody flux to the total flux when calculated over different energy ranges. The simulation shows that the blackbody goes from contributing 81% of the flux across the 0.5 - 12.0 keV range to only 4% of the flux across the 2.5 - 12.0 keV range. This shows that for a source with a large blackbody we are still heavily contaminated by this component up until $>$ 2 keV.

We also simulated a high count absorbed spectrum with different levels of N_H. We fit it with a simple power law model and an absorbed power law model and used the F-test to determine whether the measured absorption is significantly required in the fit. We did this for different energy ranges at each level of N_H.

For values of N_H in the region of 10^{21} cm^{-2} we can detect the absorption when we model over 0.9 - 12.0 keV. For values of N_H in the region of 5 x 10^{21} cm^{-2} we can detect the absorption when we model over 1.3 - 12.0 keV. For values of N_H in the region of 10^{22} cm^{-2} we can detect the absorption when we model over 1.6 - 12.0 keV.

Therefore, if we fit the spectra over 2.0 - 12.0 keV in order to remove the blackbody component we are not going to be able to detect absorption at the N_H levels that we might expect, whether it is there or not.

In order to combat this, if we consider a 'typical' size blackbody component rather than the largest (i.e. kT = 0.20 keV) and normalisation ratio of 0.04, we find that we can exclude most of the component by using only 1.0 - 12.0 keV, as over the 1.0 - 12.0 keV range the blackbody component only contributes 14% of the total flux. In this case we are unable to probe the very lowest absorption levels ($\sim$ 10^{21} cm^{-2}), but we will be able to detect everything else.

Fitting over this reduced energy range (i.e. fitting each spectrum over just 1.0 - 12.0 keV in its rest frame) we find N_H = 0.108 (0.087 - 0.130) x 10^{22} cm^{-2} for the A_V sample and $N_H = 0.097 \pm 0.020$ x 10^{22} cm^{-2} for the $\Delta(g-i)$ sample (with 90% errors). These results are shown as the left-hand red square in Figure 2.9, and again for clarity only the results from the A_V sample are shown.

We also considered how this analysis method would treat our 'typical' sources, as we would expect this to produce a result that is consistent with no reddening and no gas absorption, which is what we expect a 'typical' quasar to have. In order to select a sample of normal quasars, we began with the original sample of 1,201 objects. From 998 sources with spectra available, 597 have at least 1 spectrum with more than 100 counts, which is a requirement of this X-ray fitting process. 557 objects are free from lines and pile-up and 506 are not an *XMM-Newton* target.

It is from this subsample that we randomly selected 50 sources, with no cut based on redshift, X-ray model or inclusion in the reddening samples. This was done multiple times, and the A_V for the samples were calculated. The range in values for N_H for the samples is 2.5 - 3.0 x 10^{19} cm^{-2} and the range in A_V is -0.09 - 0.2. The average A_V, N_H and associated errors are shown as the purple diamond in Figure 2.9. It can be seen that the result is consistent with zero.

We also wanted to try this method with a sample of highly reddened sources, with an A_V cut at $A_V > 1.5$, but this left only 10 sources so it was not possible.

2.5 Discussion

As a result of our analysis we have defined three subsets from our overall sample. The properties of each of these subsamples as well as the overall sample are shown in Table 2.2. Below we outline the definitions of each sample:

1. $\Delta(g-i)$ dust reddened sample. This subset contains 72 objects with a corrected $\Delta(g-i) > 0.2$ and no evidence of continuum reddening where $\Delta(u-r) < \Delta(g-i) > \Delta(r-z)$.

2. A_V dust reddened sample. This subset contains 61 objects with a best-fit A_V in the

range of $0.5 < A_V < 1.5$ and a resultant continuum that is a good fit to the Vanden Berk et al. (2001) composite's continuum. While the analysis can be carried out on objects up to z = 4, the maximum redshift included in this subset is 3.31.

3. Gas absorbed sample. This subset has 40 objects, each with a well-constrained N_H value > 1 x 10^{22} cm^{-2}.

We also formed three subsamples based on the number of X-ray counts. Sample 1 contains 20 objects with $> 10^4$ counts, sample 2 contains 159 objects with between 10^3 and 10^4 counts and sample 3 contains 769 objects with $< 10^3$ counts.

2.5.1 The continuum slope - α_{opt}

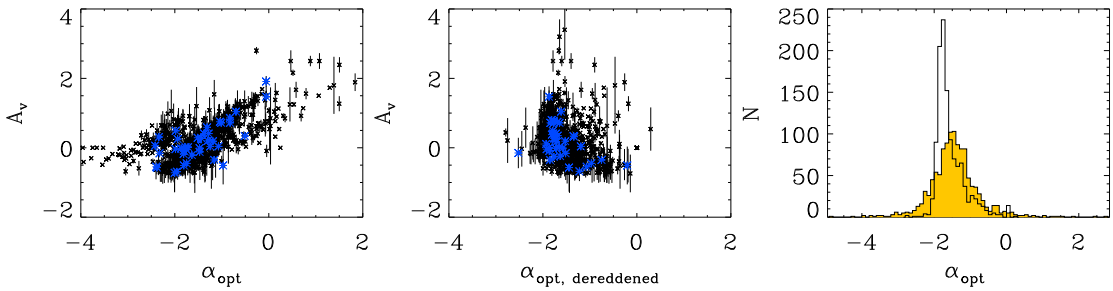

Figure 2.7: The properties of α_{opt}. *Left:* A_V against α_{opt} for all 1,201 objects in our sample. *Middle:* A_V against $\alpha_{opt,dereddened}$. *Right:* The distributions of α_{opt} (yellow sample) and $\alpha_{opt,dereddened}$. In the left two plots the blue points represent the gas absorbed sample.

We measured the slope of the continuum before and after it was dereddened for all 1,201 objects in our sample and show the results in Figure 2.7. The left-hand plot shows A_V against the reddened α_{opt}, the middle plot shows the values of A_V against the dereddened values and the right-hand plot shows the distribution of the two sets of values. The reddened values are shown in yellow, while the dereddened sample is shown unfilled. We show that the distribution for the reddened α_{opt} is diverse, but as the left-hand plot shows, as A_V increases so does α_{opt}, as expected. We find that the dereddened values have a much tighter distribution centred around the values expected from the Vanden Berk et al. (2001) study, which are α_{opt} = -0.46 (for 1250 - 4250 Å) and α_{opt} = -1.58 (4300 - 8000 Å).

The gas absorbed sample is shown overplotted in the two left-hand figures. It can be seen that the most heavily absorbed objects are not the most heavily reddened. However, any such conclusions must take into account the inherent bias of the sample, where high redshift, non-target objects will have far fewer counts than nearby targeted objects. Nearly all of the objects with significant reddening had too few X-ray counts to constrain their gas absorption. Figure 2.8 shows how A_V varies with the total counts in the X-rays. The $\Delta(g-i)$ subset is shown in red, and the A_V subset is shown in blue. It can clearly be seen that a majority of the objects in both of these subsets have less than 10^3 counts, but 3 objects from the $\Delta(g-i)$ subset have $> 10^4$ counts.

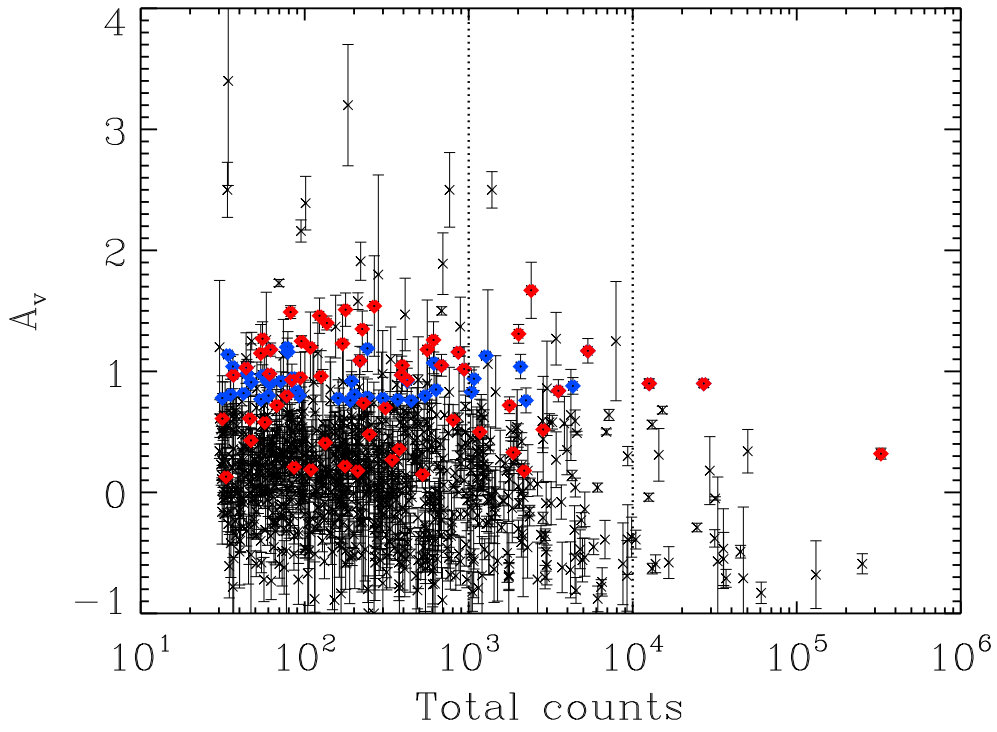

Figure 2.8: A plot of the total X-ray counts against A_V. The $\Delta(g-i)$ subset is shown in red, and the A_V subset is shown in blue.

2.5.2 Dust-to-gas ratio

As mentioned in Section 1.6.5.1 the dust-to-gas relationship in AGN is difficult to determine. The current view is that the dust-to-gas ratio for AGN is between $\sim$ 10 - 100 times lower than

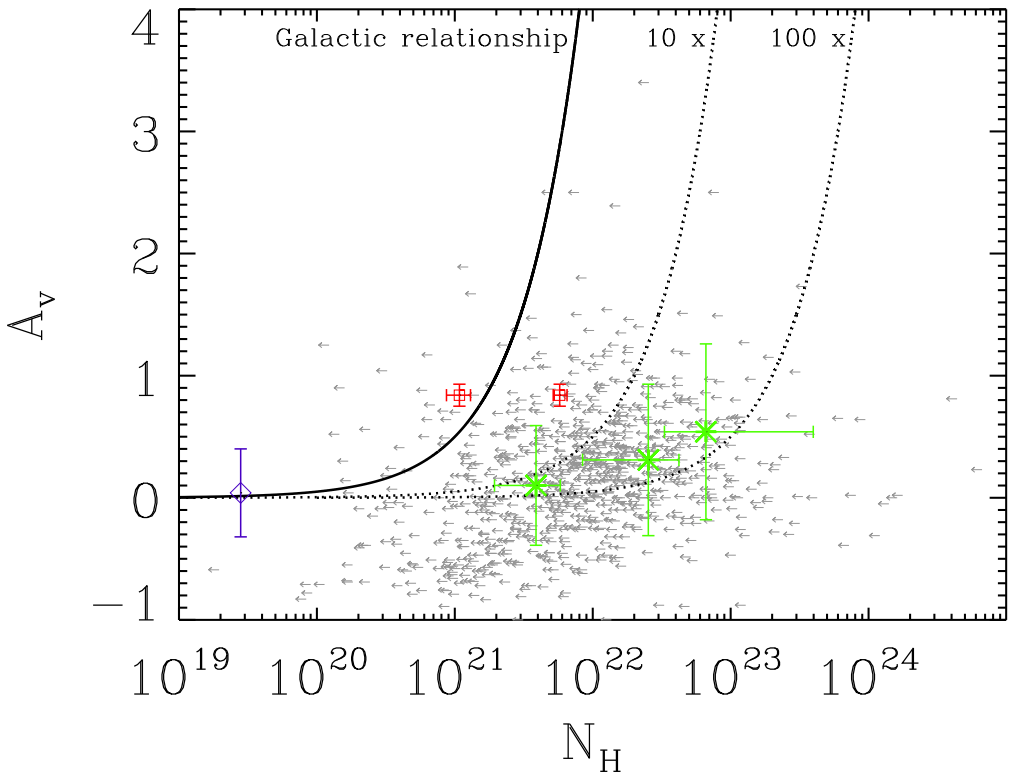

Figure 2.9: A_v against N_H. Upper limits for N_H are shown with grey arrows. The Galactic N_H/A_V relationship is shown by the thick black lines. The two dashed lines show 10 x and 100 x the relationship respectively, as predicted for quasars by Maiolino et al. (2001a). The averages of the constrained objects from samples 1, 2 and 3 from Figure 2.6 are shown in green from left to right respectively. The purple diamond indicates the average measured values of A_V and N_H from three random samples of 50 objects. The red squares show the decrease in measured N_H for the reddened samples if just an absorbed power component is used in the modelling process.

the ratio found for the Milky Way. Figures 2.9, 2.10 and 2.11 show how the different subsets defined above display different dust-to-gas relationships. In each figure we plot the Galactic relationship and 10 × and 100 × the Galactic relationship; the region where Maiolino et al. (2001a) found that most quasars reside, we define this to be the 'expected region'.

Figure 2.9 shows the relationship for the unconstrained objects. We have plotted the

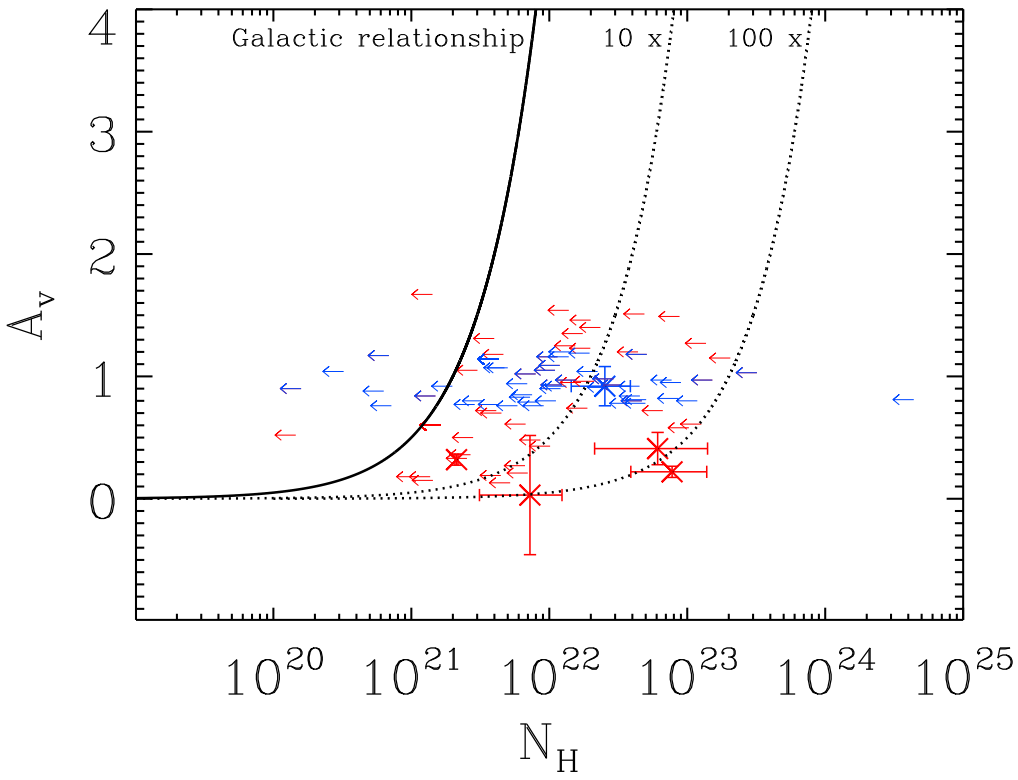

Figure 2.10: A_v against N_H. The $\Delta(g-i)$ reddened sample is shown in red and the A_V sample is shown in blue. Three objects in the A_V and one object in the $\Delta(g-i)$ sample are shown to have constrained N_H values. The relationship lines and green points are the same as Figure 2.9.

upper limits for the objects against their measured value of N_H. We can see that the objects cluster around the region where quasars are expected to lie from the Maiolino et al. (2001a) study. The purple diamond to the left of the plot shows the results of our 'typical sources' from Section 2.4.2 above. Here we stacked the X-ray spectra of multiple, randomly-selected groups of 50 objects in order to constrain the N_H value. We found that each subsample produced the expected result for a typical quasar, being consistent with zero gas obscuration and zero dust reddening. The green points lying between the two theoretical predictions represent the average values of the constrained objects from samples 1, 2, and 3 from left to right respectively. This shows that the level of absorption increases as the count

rate decreases, but still lies within the expected region. The red points indicate the results of the spectral fitting analysis in Section 2.4.2 carried out on the dust absorbed samples. The difference in the two points is brought about by the addition of a blackbody component in the fit which will increase the amount of absorption needed for a fit to work. It can be seen that the A_V values of these subsets raise the objects above the expected region and moving them closer to the expected Galactic relationship, indicated by the solid black line.

Figure 2.10 shows the relationship for the dust reddened samples. The $\Delta(g-i)$ reddened sample is shown in red and the A_V sample is shown in blue. It can be seen that these subsets mainly lie away from the expected region and do not follow the expected trend of increasing A_V with increasing N_H. However, it is worth noting that the 4 objects in these two subsets that have constrained values of N_H lie within the expected region, suggesting that if the other objects were able to be constrained then their values could also fall within the expected region. For the objects with a lower than expected upper limit we suggest that this limit could actually be higher if a soft excess component was actually present in the soft X-rays, but was not seen due to the current count rates. This would increase the amount of gas present and bring the objects into the expected relationship.

In Figure 2.11 we show the relationship for objects with constrained values of N_H. We show the averages for these objects divided up into samples 1, 2 and 3 based on their number of counts. Also shown are the results of the dust reddened sample for comparison. It can be seen that a majority of the constrained values lie within the predicted 10 $\times$ and 100 $\times$ of the Galactic relationship that is expected for quasars. However, it can be seen that the majority of the constrained objects have a very low measured reddening value, and it can also be seen that very few of the constrained objects lie near the values found for the dust reddened samples. Together, this indicates that the amount of gas and dust in the objects within these subsets may be more complex than the assumed dust-to-gas relationship suggests. Another reason for this result is that our method for constraining the value for N_H is introducing a selection bias towards those objects with little X-ray spectral complexity and may be not indicative of our sample as a whole.

Table 2.2: The median values of z, A_V, α_{opt}, $\alpha_{opt,dereddened}$, N_H, $L_{2-10keV}$ and $L_{0.2-2keV}$ for the overall selection and the subsets.

Type	N_{obj}	$< z >$	$< A_V >$ (mag)	$< \alpha_{opt} >$	$< \alpha_{opt,dered} >$	$< N_H >$ ($\times 10^{22}$cm^{-2})	$<\log(L_{2-10keV})>$ erg cm^{-2} s^{-1}	$<\log(L_{0.2-2keV}) >$ erg cm^{-2} s^{-1}
All	1201	1.394	0.14± 0.12	-1.47± 0.66	-1.69±0.38	0.54*	44.37	44.29
N_H constrained	49	1.353	0.34±0.09	-1.19±0.78	-1.67±0.51	3.40	44.54	44.41
Gas Obscured	40	1.468	0.48± 0.08	-0.72± 0.49	-1.68±0.47	4.70	44.54	44.34
Dust reddened (A_V)	61 (54[a])	1.538	0.91± 0.09	-0.75 ±0.54	-1.68±0.31	0.91 (1.76)*	44.60	44.47
Dust reddened (Δ(g-i))	72 (64[a])	1.226	0.84± 0.13	-0.71± 0.58	-1.52±0.41	0.67 (1.76)*	44.37	44.15

Notes : [a]Number of objects able to be X-ray modelled. * The upper limit values are used, bracket denotes mean of objects where N_H is constrained.

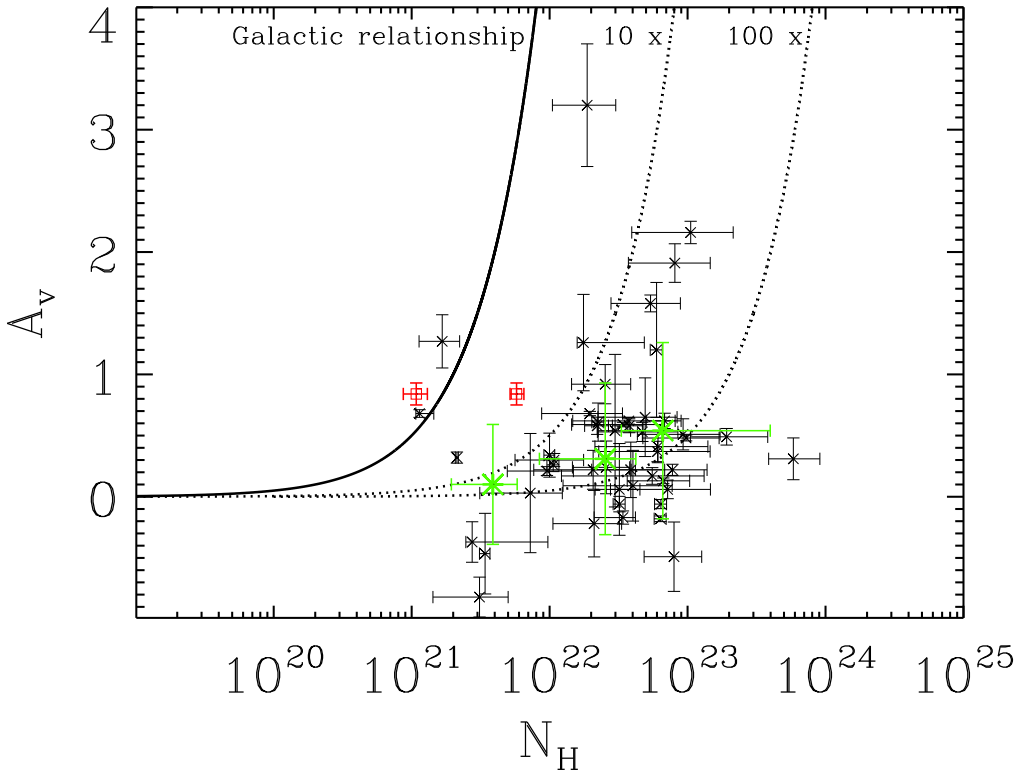

Figure 2.11: A_v against N_H. Objects with constrained values for N_H are shown with their associated errors as black points. The relationship lines, green points and red squares are as in Figures 2.9 and 2.10.

2.6 Composite Spectra

Following on from the seminal work of Vanden Berk et al. (2001) with the composite quasar spectrum, in the following section we make composite spectra for our three subsets and compare them to it. We follow the same fitting routine that we followed for all of the objects in the sample and characterise the optical properties of the different subsets.

2.6.1 Composite Spectra Construction

Creating composite spectra is a difficult process as the steps involve selecting the input spectra, determining confidence levels in the redshifts of the individual objects, rebinning

the spectra to their rest wavelengths, either scaling or normalising the spectra, before staking them into the final composite. In order to compare our sample and subsets to the Vanden Berk et al. (2001) composite we use their method to create our composites, with a few differences.

We have selected our input spectra, not on quality, but on whether they belong to one of the subsets defined in the previous sections, We make no quality cut on the objects that go into our sample composite, but we did exclude objects if they could not be normalised (due to continuum issues with high redshift objects) or if we could not reproduce a similar shape to the Vanden Berk et al. (2001) continuum when fitting the object. We use the redshifts given for each object in the SDSS DR5QSO catalogue.

For each sample the spectra were shifted to the rest frame using their redshifts, then rebinned onto a common wavelength scale at 1 Å per bin; roughly the same resolution as the observed spectra shifted to the rest frame, while flux was conserved. If the original flux values were held in pixels that covered more than one bin, the flux was distributed among the new bins according to the fraction of the original pixel width covering each bin. For each spectrum the number of quasar spectra that contribute to each bin is shown as a histogram above the figure of each composite spectrum.

In order to normalise each spectrum at the same point, the continuum fit for each object, described in Section 2.3, was extrapolated to the normalisation point at 7500 Å. These extrapolations were only used in the normalisation process, not for the spectra stacking. The spectra were ordered by redshift and the first spectrum was arbitrarily scaled. The other spectra were scaled in order of redshift to the average of the flux density in the common wavelength region of the mean spectrum of all the lower redshift spectra. The final spectrum was made by finding the median flux density in each wavelength bin of the scaled, shifted, rebinned spectra. The spectral region blueward of Lyα was ignored during the scaling procedures as the Lyα forest flux density can vary greatly between objects. Each resultant composite is discussed in greater detail below.

Unless stated otherwise, the A_V of the composite spectrum are from the continuum reddening method described in Section 2.3.3, and not using the Balmer Decrement method.

2.6.2 Composite Spectra Analysis

2.6.2.1 Overall sample

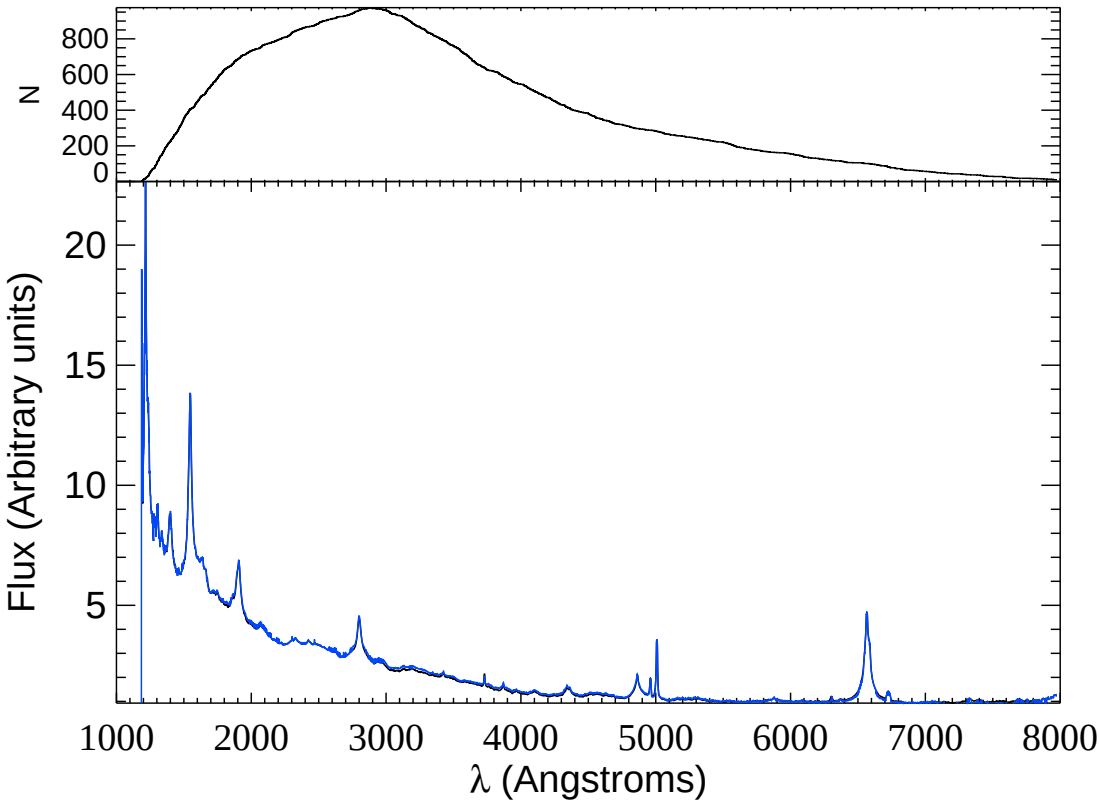

Figure 2.12: A comparison of the composite spectra of our sample in black and the composite spectra of Vanden Berk et al. (2001) in blue, with a histogram showing how many objects are in each redshift corrected wavelength bin.

In order to show that our selected sample was representative of the quasar population, we chose to recreate the Vanden Berk et al. (2001) composite spectrum using our objects. We have just over half the number of objects used in their study; 1,201 compared to 2,200. Figure 2.12 shows the comparison of these two composites, with our overall sample composite shown in black, and the Vanden Berk et al. (2001) composite spectrum overplotted in blue. It can clearly be seen that the two are in excellent agreement. This is further proof that the sample is representative of the parent sample and of quasars in general. The histogram shows that the number of objects peaks in the Mg II region, with the red end of the Hα region being poorly sampled with less than 50 objects in the bins redwards of 7500 Å. It can

be seen that both the continuum and emission line strengths of the sample are well matched to composite spectrum. We also make a cut at 1200 Å as the data quality of the objects in bins at lower wavelengths meant that the composite in this region was difficult to constrain. We find that the peak number of objects per bin occurs at 2950 Å, which is 150 Å redward of the peak in the Vanden Berk et al. (2001) composite. This difference can be explained by their slightly higher average redshift.

As we defined the Vanden Berk et al. (2001) composite continuum to be our benchmark for zero reddening, in order to estimate the reddening of our composite we used the Balmer Decrement technique described in Section 2.3 above and find a value of $A_V = 0.09 \pm 0.07$, which is in excellent agreement with the $A_V = 0.08 \pm 0.09$ for the Vanden Berk et al. (2001) and both are consistent with $A_V = 0$ within errors. We find that our sample composite has an α_{opt} = -1.47 ± 0.66, rising to -1.69±0.38 when it is dereddened.

2.6.2.2 $\Delta(g-i)$ dust reddened sample

The $\Delta(g-i)$ dust reddened composite, shown in Figure 2.13, is clearly much flatter that the overplotted, blue Vanden Berk et al. (2001) composite. The emission lines are weaker than the overall composite, but appear no narrower. Due to the redshift cut on this sample the objects in this subsample cover most of the optical region, with the peak of the distribution being centred around Mg II in good agreement with the parent sample. The dereddened continuum fit is shown overplotted on the Vanden Berk et al. (2001) composite. This fit shows that the continuum reddening method has produced a good estimation of the reddening in these objects, and shows that the underlying continuum is in good agreement with the composite continuum. The value of reddening for this sample is $A_V = 0.84 \pm 0.13$. The reddened value of α_{opt} is -0.71 ± 0.58 but does rise to lie within the range of the composite (α_{opt} = -0.46 - -1.58) when it is dereddened; while it is in agreement, it is the least constrained of the three subsets.

2.6.2.3 A_V dust reddened sample

The A_V dust reddened sample has a similar continuum to the $\Delta(g-i)$ dust reddened sample, however the emission lines are all considerably lower. The distribution of objects

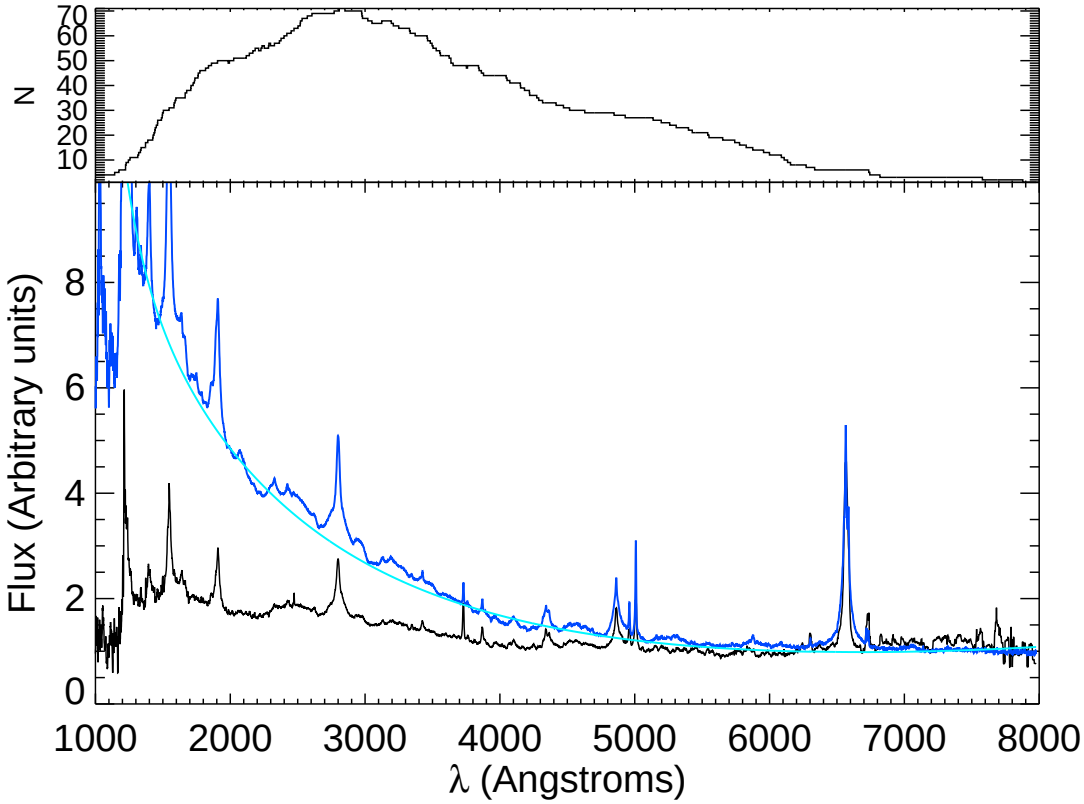

Figure 2.13: The composite spectrum of the $\Delta(g-i)$ sample, shown in black, with the Vanden Berk et al. (2001) composite shown over the top in dark blue. The dereddened continuum of the sample composite is shown in light blue. A histogram showing how many objects are in each wavelength bin is shown above the spectra.

in the wavelength bins is very different to the other composites, with very few objects at wavelengths longer than 4000 Å, but a flat maximum number of objects across the 2000 - 3000 Å range. This bias towards the shorter wavelengths in the dereddening process is shown in the plot. Figure 2.14 clearly shows that the dereddened sample continuum is not a good fit to the composite continuum. However, this is an effect of the normalisation process, as all the composites were normalised to the same point at 7000 Å, in keeping with the analysis of all the other samples. If an object in this sample did not cover this wavelength, the continuum and spectrum were extrapolated from the longest wavelength in the spectrum to 7000 Å for the normalisation. The value of reddening for this sample is $A_V = 0.91 \pm 0.09$. The dereddened value of α_{opt} changes from -0.75 $\pm$ 0.54 to -1.68 $\pm$ 0.31, which is in excellent

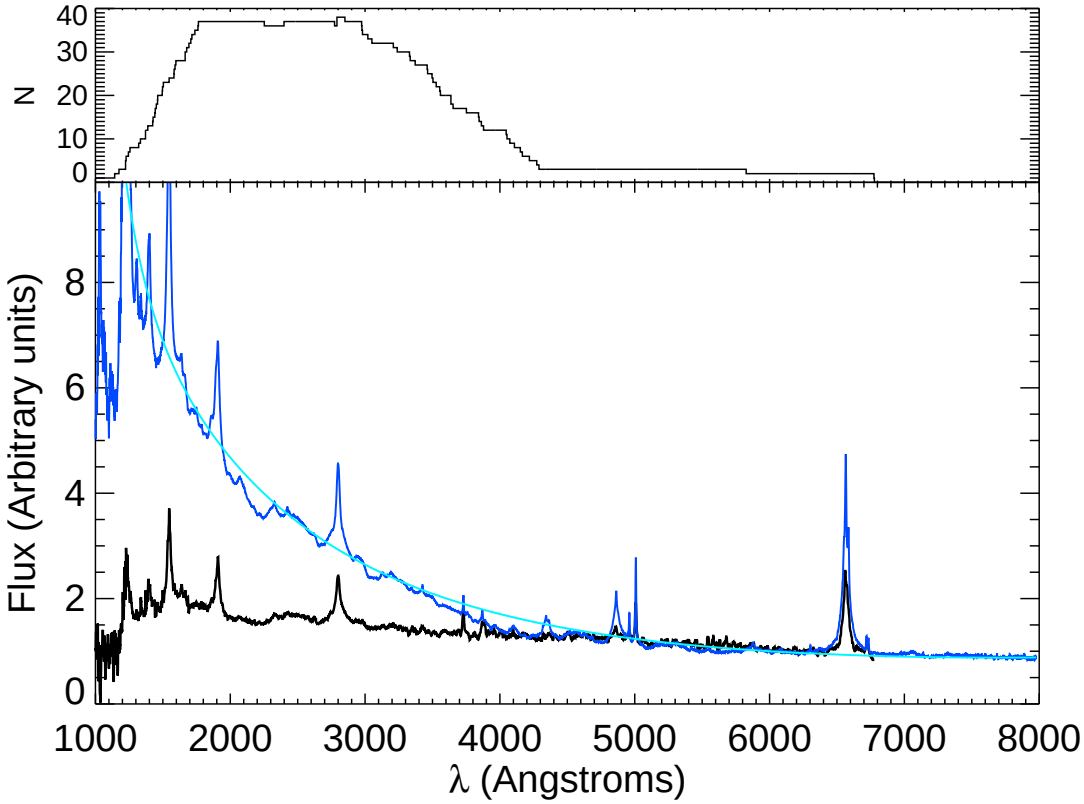

Figure 2.14: The composite spectrum of the A_V sample. The colours used are the same as in the previous plot.

agreement with the composite value. All of the emission lines in this sample are much weaker than the other samples and the parent sample, in particular the Hα, Hβ and [O III] region, yet the FWHM of the lines are in very good agreement with the $\Delta(g-i)$ sample. Further analysis on this was not possible as there are only 4 objects with data in this wavelength range in this sample.

2.6.2.4 Gas absorbed sample

The gas absorbed sample has the smallest number of objects out of our subsamples; however the redshift distribution is more representative of the overall sample and so the spectrum up to the Hα region is well sampled. The dereddened continuum shown in Figure 2.15 is in very good agreement with the composite continuum. The value obtained for the reddening for this sample is $A_V = 0.48 \pm 0.08$. This is the lowest value of reddening obtained for the

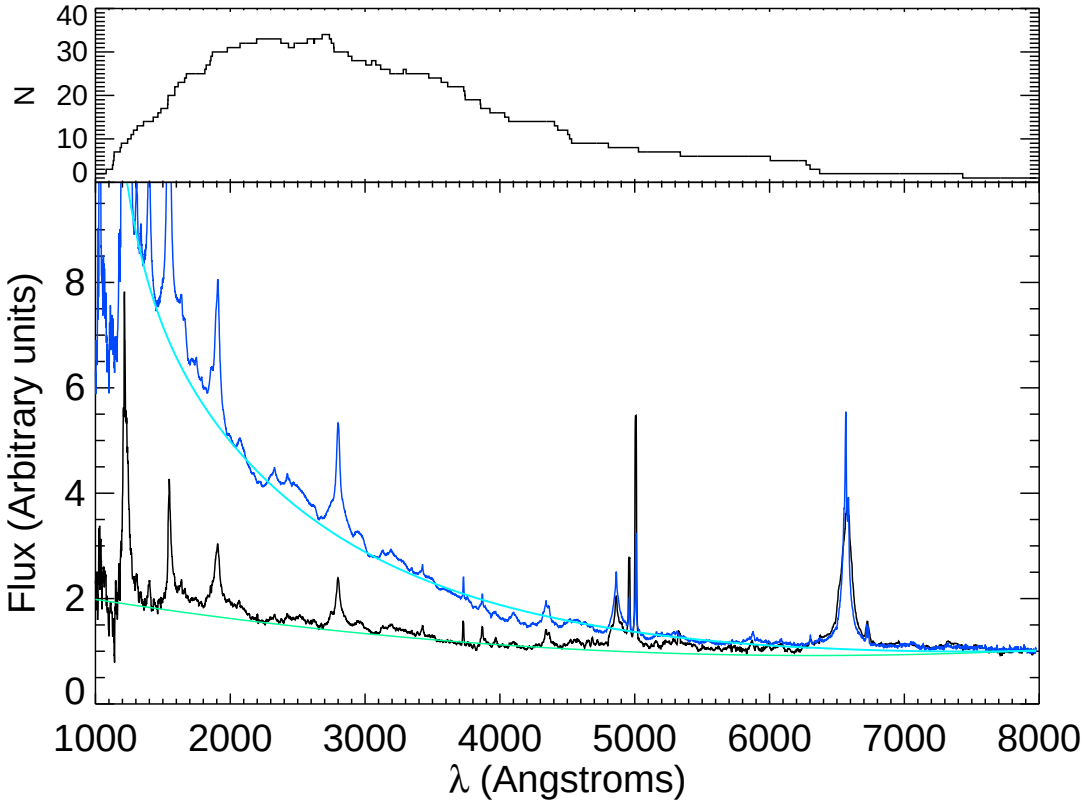

Figure 2.15: The composite spectrum of the gas absorbed sample. The same colours are used as in the previous two plots, with the addition of a green line showing the continuum fit to the sample spectra.

three subsamples, but does put the average sample results within the expected dust-to-gas relationship range for quasars as was indicated by the results for individual objects shown in Figure 2.11. Again we find that the dereddened value for α_{opt} is in excellent agreement with the composite spectra.

2.6.2.5 The Hβ/[O III] and Hα regions

The lower panel of Figure 2.16 shows the three subsample composite spectra overplotted with each other, normalised at 6000 Å. It can be seen that both of the dust absorbed samples have a similar spectral shape, but that the gas absorbed sample is steeper at $<$ 5000 Å. The upper left panel shows an enlargement of the Hβ and [O III] region and the upper right panel shows an enlargement of the Hα region. In both of these regions it can be seen that

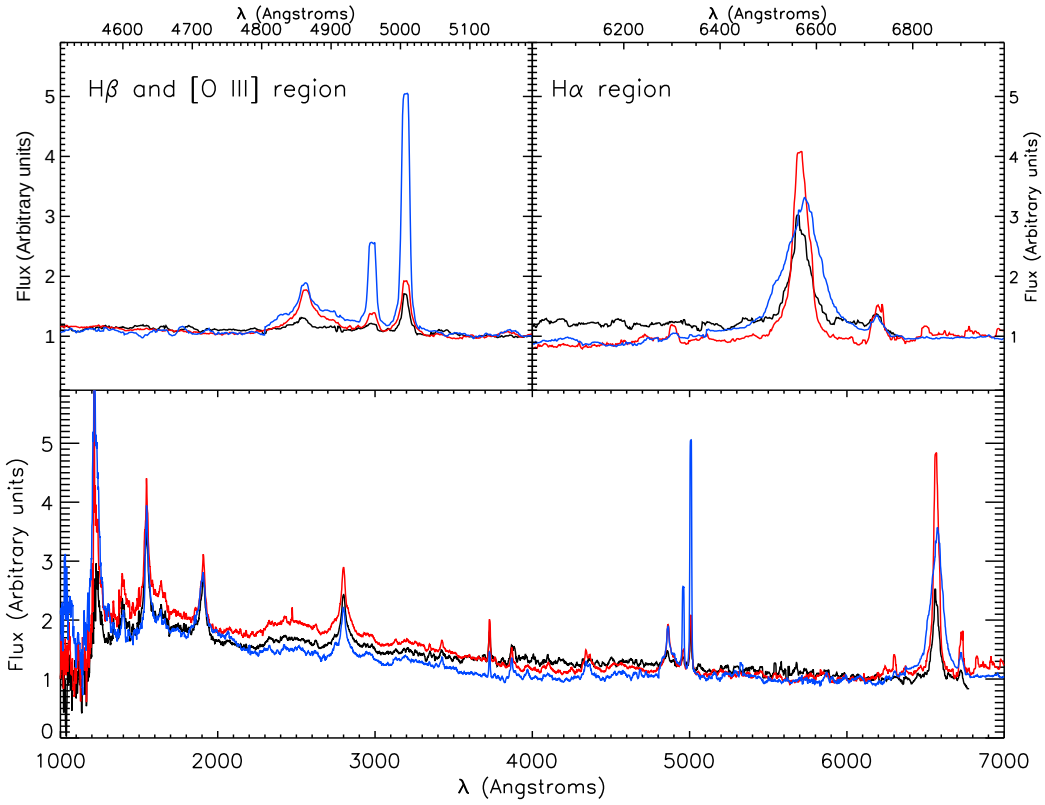

Figure 2.16: *Bottom:* A comparison of the composite spectra of the A_V reddened sample in black, $\Delta(g-i)$ sample in red, and gas absorbed sample in blue. The spectra are all normalised to 6000 Å. *Top Left:* A comparison of the Hβ/[O III] region with the same colours as the plot below. *Top Right:* A comparison of the Hα region, with the same colours.

the FWHM of the gas absorbed sample, shown in blue, is greater than the dust absorbed samples, and is in excellent agreement with the Vanden Berk et al. (2001) composite. For each of the samples a value of A_V was calculated from the Hα-Hβ Balmer Decrement, using the equation given in Section 2.3.

From this we find that the values obtained for the $\Delta(g-i)$ and gas absorbed sample show excellent agreement with those derived from the continuum fitting with $A_V = 0.90 \pm 0.13$ for the $\Delta(g-i)$ sample and $A_V = 0.42 \pm 0.11$ for the gas absorbed sample. The errors from this process are larger than from the continuum fitting due to the data quality in this region of the composites. In the A_V composite the Hβ region is very poorly constrained due to 2 out of the 4 objects in this region having very poor S/N, and a flux for Hα could not be

reliably constrained with the sole object that resides in this region. Due to these problems we considered that any value of A_V derived using the Balmer Decrement for this sample would be unsuitable for estimating the true A_V present in the system.

2.7 Conclusion

In this chapter we have a presented an in-depth optical and X-ray study of 1,201 quasars with a range of reddening and obscuration levels. We assembled data from the EPIC monitor onboard the *XMM-Newton* satellite and optical data from the SDSS DR7 after initially creating the sample by cross-correlating the 2XMMi Serendipitous Survey with the SDSS DR5QSO catalogue.

We began by carrying out statistical tests on the sample to see if it was representative of the parent sample, the DR5QSO catalogue. Once we were confident of our sample we created a detailed fitting routine to measure the continuum of the objects across the wavelength range of the sample. Due to the lack of completely emission line free regions in the quasar spectrum we used the ranges with the weakest emission known, and visually inspected all fits to ensure that no object had unusually strong emission lines in these bands. We measured the observed α_{opt} of all objects in the samples and found that the averages were within the range of those found by previous studies (Fan et al., 2001; Vanden Berk et al., 2001).

In order to determine the dust reddening of these samples we used two different methods. The standard Balmer Decrement determination of reddening could not be used for this sample as Hα is not covered in SDSS spectra beyond z $\sim$ 0.4 and we have objects in the sample up to z = 5.41. The first method was that used by Richards et al. (2003) and involves the relative colours of the quasar and its redshift. This produced a sample of 72 quasars and was called the $\Delta(g-i)$ subset.

The second method looked more directly at the continuum and used the dust reddening curves of Calzetti et al. (2000) to deredden the continuum to match the composite continuum of Vanden Berk et al. (2001), which through the Balmer Decrement was shown to have zero reddening. For this method we had problems dereddening the continua of the highest redshift objects, due to the small amount of data in the rest frame. We also found that many objects

displayed a continuum that was much bluer and steeper than the Vanden Berk et al. (2001) composite. We suggest that for several of these objects this could be due to the presence of the Balmer continuum, which can be strong in some AGN and will mask the true quasar continuum, while other objects may simply be intrinsically bluer. We also found objects that were far redder than could be explained by dust alone, as their dereddened continua shapes did not match the composite shape. We suggest that this could be due to processes other than dust and excluded them for our dust reddened sample. We defined an object to be dust reddened through this method if it had an A_V value between 0.5 and 1.5, which produced 61 objects for the A_V subset. We found that less than 10% of the objects overlapped between these two samples, but that they produced very similar composite spectra and have similar characteristics.

We modelled the X-ray spectra of 998 of the objects; as the remaining 203 had too few counts. We modelled each spectrum with 3 models: a power law, an absorbed power law and an absorbed power law with a blackbody component. The number of counts for the object dictated whether or not the third model was used and an F-test determined the best fit. From this it was found that 50 objects had constrainable levels of N_H, of which we defined the 40 with $N_H > 1 \times 10^{22}$ cm^{-2} to be obscured, and this became the gas obscured subset.

From there we examined the dust-to-gas relationship of the quasars in our different subsets. From Maiolino et al. (2001a) we expected most of our quasars to have a relationship between 10 - 100 times lower than the Galactic relationship. We found that the averages of the objects with constrained values of N_H and binned by number of counts fell within this region, as did most of the upper limits for the rest of the sample. On stacking the X-ray data of the dust reddened subsets, we found that both of these subsets lie far closer to the Galactic relationship, depending on what model is used, and they lie in a region where few of the obscuration constrained or gas obscured quasars lie. While there is a greater scatter in the $\Delta(g-i)$ subset, neither that nor the A_V subset show any indication of a relationship between the levels of gas and dust found in their systems. We note, however, that this may be a bias effect of the low number of counts available for this sample, as many objects in these subsets had too few counts to even be used in the spectral stacked routines. We also created stacks of 50 randomly selected objects to test whether they would display the zero

reddening and obscuration levels expected for a typical quasar. We found that all of the stacks created in this way were consistent with this hypothesis.

Finally we created spectral composites for our overall sample and three subsets following the method of Vanden Berk et al. (2001). We produced a composite of our overall sample that was an excellent match to the Vanden Berk et al. (2001) composite. Out of the three subsets we find that the reddening in the gas obscured subset is smaller than for the dust reddened subsets, and that the dereddened continuum of this composite is a much better fit to the overall composite than either of the dust reddened subsets.

For the $\Delta(g-i)$ and gas obscured subsets we also measured the reddening from the Balmer Decrement and found it to be in good agreement with that found from the continuum method, albeit with large errors due to the small number of objects in the wavelength bins in these regions of the composites.

In conclusion, we find that while our dust reddened subsets display levels of gas obscuration and our gas absorbed sample does have a small amount of dust reddening, they do not have the same characteristics. However, further work on objects with good X-ray data out to high redshifts will help determine whether this result is due to data quality bias in our sample or if the dust-to-gas relationship in quasars is even more diverse than previously thought.

Chapter 3

Optical-to-X-ray SED modelling: Models and bolometric corrections

In this chapter we describe and apply a new model of the emission across the optical, UV and X-ray range. We present modelling and interpretation of the emission lines for a sample of 192 Type 1 AGN with a range of obscuration levels. All of the objects in this study have both optical and X-ray spectra from SDSS and *XMM-Newton* respectively. When possible we additionally include optical and UV data from the *XMM-Newton* Optical Monitor (OM).

We constrain the black hole masses from spectral fits of the Balmer emission lines, and determine a best-fitting value from modelling the broadband spectral energy distributions (SEDs). Rather than use a generic template SED to model the emission, we created a broadband SED of each AGN and multi-component fit to model its emission. We examine how improvements to the models used in SED fitting are used to create robust fits, even when dealing with low-quality data.

The table of the SED fitting parameters and individual AGN SED fits are shown in Appendix A and B respectively.

3.1 Introduction

Since Elvis et al. (1994) produced robust multi-frequency template SEDs for AGN there has been an ongoing quest by astronomers to better constrain their shape with increasing complex modelling (Marconi et al., 2004; Hopkins et al., 2007). This process fits theoretical models for accretion onto super-massive black holes with multi-wavelength observations. While it has been established that the optical to X-ray SED can be relatively well described

by a blackbody disc spectrum peaking in the UV and a power law model extending into the hard X-rays, it is difficult to constrain lower luminosity objects as their luminosity peaks in the far UV and is therefore unobservable at low redshifts.

Black hole mass estimates combined with mass accretion rate are the fundamental properties of AGN. The black hole mass sets an upper limit on the energy released by the AGN at the Eddington limit, which is the maximum luminosity for an idealised case of spherical accretion. The Eddington ratio is used to estimate the mass accretion rate and to help understand the physical processes that are going on around the black hole.

The bolometric luminosity, L_{bol}, is the total luminosity emitted by an object across all wavelengths; in AGN it is often approximated as a fixed ratio of the optical luminosity (Kaspi et al., 2000). Ideally it is derived from integrating the entire AGN SED, which spans many decades in wavelength; this is hampered by the fact that data cannot be obtained for all wavelengths, and also by the fact that emission from AGN is known to vary over time. As such, bolometric luminosity is usually calculated by integrating an SED composed of all the flux points available. This method of estimating the bolometric luminosity is not dependent on the assumption that all SEDs are the same, and so it allows for a correlation between M_{BH} and L_{bol} to be induced.

3.1.1 Bolometric corrections and bolometric luminosity

The luminosity arising from any part of the EM spectrum is clearly just a fraction of the total accretion luminosity emerging from the AGN. The energy observed in X-rays is the high-energy part of the total intrinsic accretion emission emerging in the whole optical-to-X-ray region. Therefore, we need to apply a *bolometric correction*, $\kappa_{2-10keV}$, to use the $L_{2-10keV}$ to infer L_{bol}. The bolometric correction $\kappa_{2-10keV}$ is defined as:

$$\kappa_{2-10keV} = \frac{L_{bol}}{L_{2-10keV}} \tag{3.1}$$

for an individual AGN with bolometric and hard X-ray luminosities, L_{bol} and $L_{2-10keV}$ respectively.

Previously, bolometric corrections have been determined from the Elvis et al. (1994) mean quasar SED templates. One of the major problems with this method is that the Elvis

et al. (1994) templates include IR emission as part of the bolometric luminosity. If the IR emission is reprocessed, as in the paradigm of the Antonucci (1993) standard model, then these SED templates effectively double count part of the emission and the resulting bolometric corrections will be too high (Marconi et al., 2004). In order to recover the *intrinsic* accretion luminosity in AGN (that which emerges in the optical, UV and X-ray bands), the IR emission should be excluded when calculating bolometric corrections. As well as this, there is the additional issue of 'cosmic scatter': specific parameters of the AGN SED can vary strongly between AGN, despite apparent similarities in the SED shapes. Indeed, Elvis et al. (1994) cautioned against using the mean SED to determine global properties for all quasars and AGN, especially as the individual SEDs that were used to produce the mean template showed significant dispersion.

3.2 SED modelling

This section describes the development of a new broadband SED model, which can be used to replace the old multi-component models that were often inadequate for modelling the optical-to-X-ray region of the AGN SED.

We discuss the limitations of the previous models in accounting for the spectral properties of both high- and low- quality X-ray spectra, as well as the often unphysical solutions they produce. We will then introduce a new model 'OPTXAGN' and show how it combines aspects of the previously used models to create a more physically plausible and self-consistent solution.

3.2.1 Broadband SED Models

The standard interpretation of the broadband AGN SED is that the emission is dominated by a multi-temperature accretion disc component that peaks in the UV (e.g. Gierliński et al., 1999, XSPEC model: DISKPN). This provides the seed photons for Compton upscattering by a hot, optically thin electron population residing within a corona above the disc, which produces the power law component seen above 2 keV (e.g. Haart & Maraschi, 1991, XSPEC model:BKNPL). This two-component assumption has long been used in the creation

of broadband AGN SEDs, but there is often a third component seen rising below 1 keV in many objects, particularly those with a high mass accretion rate, which is left unaccounted for. In order to account for this a third component can be added to the modelling process. Below we describe the details of this multi-component model, its inability to model our sample and how it was adapted to produce a new model that we used to create SEDs for our sample.

Model: Diskpn+bknpl+comptt

Initially the whole sample was modelled using a multi-component model, where each component modelled a separate part of the SED. Previous studies (Vasudevan and Fabian, 2007, 2008; Middleton et al., 2009) just combine the DISKPN with a version of the BKNPOWER model to account for the total optical-to-X-ray emission. However, the X-ray data often exhibits an additional component at soft energies below 1 keV - termed the X-ray 'soft excess'. The best example of an object which has this feature is RE J1034+396 (Casebeer et al., 2006; Middleton et al., 2009). As this feature is not obviously ubiquitous in the AGN SED most studies exclude X-ray data below 1 keV, allowing the remaining data to be modelled with just the disc and power law components. While the origin of this component is still unknown (Gierliński & Done, 2004; Crummy et al., 2006; Turner et al., 2007; Miller et al., 2008), its effects can still be seen in the SED, and so in order not to exclude any data we must introduce a component that can account for it.

diskpn

DISKPN is the dominating component in this model. It accounts for the multi-temperature accretion disc component, which peaks in the UV and is described in Gierliński et al., (1999). The model takes the following parameters: T_{max}, the maximum temperature of the accretion disc; R_{in}, the inner radius of the accretion disc and K, the overall normalisation. Initially the inner radius, R_{in}, was frozen at 6.0 gravitational radii, which is appropriate for high accretion efficiencies following from the 'Soltan argument' discussed in Chapter 1. The temperature, T_{max}, was always seeded at 0.01 keV and allowed to be a free parameter. The normalisation, K, is defined as $K = M_{BH}^2 \cos(i)/D_L^2\beta^4$, where M_{BH} is the black hole mass, i is the inclination angle we are viewing the object at, D_L is the luminosity distance and β is the colour-to-effective temperature ratio.

bknpower

The BKNPOWER component is used to fit the hard X-ray tail. It is broken at low energies so that the power law cannot be extrapolated back to give spurious fluxes at energies lower than the thermal disc spectrum. The break energy is usually frozen to ~ 3 times the DISKPN T_{max} parameter.

comptt

In order to model the X-ray soft excess component we use a model that can phenomenologically fit the shape it produces: COMPTT (Titarchuk, 1994). It is an analytic model describing Comptonisation of soft photons in a hot plasma. It is a extension of the Sunyaev-Titarchuk Comptonisation model, the theory having been extended to include relativistic effects. It is best described as an analytical approximation to optically thick, low-temperature thermal Comptonisation where the seed photons for the Comptonisation are assumed to have a Wien spectrum.

Further, the approximations used in the model work well for both the optically thin and thick regimes. The Comptonised spectrum is determined completely by the plasma temperature and the optical depth, which is independent of geometry. In this model, the parameters that are frozen are the redshift of the object, the input soft photon temperature, which was fixed to be the same value as the maximum temperature of the accretion disc in the DISKPN model, and the object geometry, which is kept frozen at 0 to indicate a disc geometry.

3.2.2 Failure of the multi-component model

The main limitation of this model is that is made up of three separate components that, while linked together by some sub-components, can be moved to any part of the energy range studied in order to fit the data. The typical example of this involves the BKNPOWER and COMPTT components. Due to the low quality of data of some of the X-ray spectra the hard end of the X-ray spectrum occasionally has an additional feature centred at ~ 8 keV. There are physical reasons why this bump could be a real feature, including Fe emission lines in that region, but the model has no way of representing this. Instead the model will use the COMPTT component to fit the hard X-rays, as it can produce the required shape, leaving the

BKNPOWER component to fit the soft X-rays with unphysically soft spectral indices. With the setup of the multi-component model the only way to prevent this from happening is to manually constrain every free parameter for each component and to visually inspect the resultant model with each iteration, which negates the automated fitting routine we were trying to develop. Individually these components can produce the required shape of the AGN SED, they just need to be linked together in such a way that the energetics of the resultant SED are self-consistent and physically possible. To meet these requirements, a new model, OPTXAGN (Done et al., 2012), was developed.

Model: optxagn

The OPTXAGN model (Done et al., 2012), is a new model created in order to constrain the total energy produced by the AGN in the 0.001 - 10 keV range. The model uses the disc as a basis for the total energy available to the system and then upscatters photons into the X-ray region. OPTXAGN can model both objects with and without a soft excess in the soft X-ray region. Importantly it conserves energy as it is transferred between the components

For objects with a soft excess present there are 7 free parameters:

- M_{BH}: black hole mass. This can come from either line fitting, as is done in this study, or another of the methods outlined in Chapter 1.
- $\log(\dot{M})$: the total mass accretion rate.
- R_{cor}: corona truncation radius in units of gravitational radii (r_g). This is constrained to be between the values of 6 and 100.
- kT_e (keV): temperature of the electrons in the corona.
- τ: optical depth of the Comptonisation region.
- Γ_{pow}: the slope of the power law component.
- f_{pl}: the fraction of the power law component as part of the total reprocessed disc emission.

When there is no soft excess component present, the f_{pl} parameter is set to 1 and neither kT_e or τ are allowed to be free parameters.

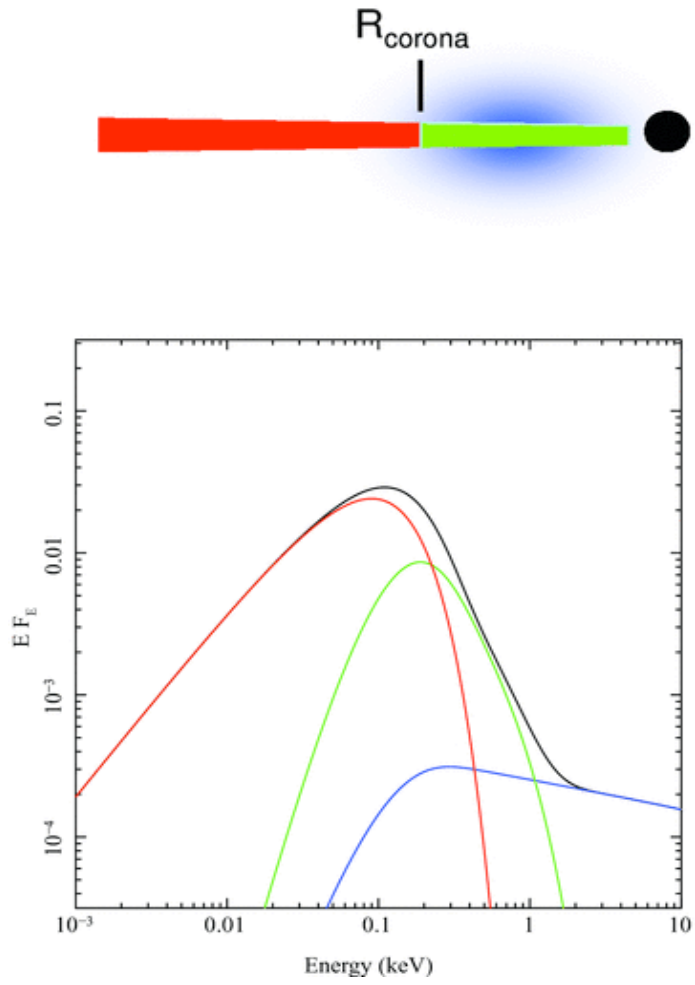

Figure 3.1: A schematic of the OPTXAGN model geometry and resultant spectrum from Done et al. (2012). The outer disc is shown in red and produces a colour-temperature corrected blackbody, an inner disc shown in green has its emission Compton upscattered and Compton upscattering emission from the corona that creates the power law tail seen to high energies is shown in blue.

Following on from the work of Vasudevan & Fabian (2008), we adopted a value of $i = 0°$

for the inclination angle; β was assumed to be unity after it was shown that changes to both of these values could only affect L_{bol} by up to 6%, which is smaller than the statistical error in the luminosities. This enabled the normalisation to be kept frozen as:

$$K = \frac{M_{BH}^2}{D_L^2} \tag{3.2}$$

Figure 3.1 (taken from Done et al., 2012; Figure 5) shows a schematic of the model geometry that goes into producing the OPTXAGN model. The resultant spectra is shown beneath it, with the outer disc shown in red producing a colour-temperature corrected blackbody, an inner disc shown in green, where the emission is Compton upscattered and finally the Compton upscattered emission from the corona is shown in blue and produces a power law tail out to high energies.

3.3 Sample selection and data assembly

To identify a sample of X-ray detected Type 1 AGN that had confirmed X-ray data and optical spectra we cross-correlated the initial 2XMMi catalogue and the SDSS DR7 catalogue. We filtered the resulting sample via the steps outlined below. The final sample used in the modelling process has 192 objects.

3.3.1 Cross-correlation of catalogues

The first step was to perform a cross-correlation between the 2XMMi and SDSS DR7 catalogues.

The 2XMMi Serendipitous Survey Catalogue (Watson et al., 2009) is the collection of all the sources detected in the 4,117 *XMM-Newton* EPIC camera observations taken between 2000-02-03 and 2008-03-28. The catalogue contains $\sim$ 289,000 source detections and covers an area of $\sim$ 420 deg^2.

The SDSS DR7 catalogue is the seventh data release by SDSS. This edition of the catalogue containing spectroscopic data has a sky coverage of $\sim$ 8200 deg^2 and covers the wavelength range 3800 - 9200 Å.

Our cross-correlation consisted of the following steps:

- We first searched for all SDSS/*XMM-Newton* position pairs that lie within 20" of each other. This resulted in 5,341 pairs.

- This sample was then cut down further. From the initial 20" spatial cut we reduced this to one of the two following conditions: the source positions are separated by no more than 3", or the sources are separated by no more than three times the positional uncertainty in *XMM-Newton* and no more than 7". This reduced the sample to 3,419 unique X-ray sources. The 3" cut was used to keep as many sources as possible at this stage. It is worth noting, however, that 114 pairs had a separation less than 3" but still greater than three times the *XMM-Newton* positional uncertainty. The 7" cut-off was used to mitigate spurious matches but still allow those off axis in *XMM-Newton*, with the associated positional uncertainty, to still be matched.

- We finally limited the sample to only those extragalactic objects with a spectroscopic classification cut. Only objects that had been classed as SPECCLASS = 2 (galaxy) or SPECCLASS = 3 (QSO) were selected. This cut the sample down to 3,342 pairs to be analysed further.

3.3.2 Selection of Type 1 AGN

In order to carry out SED modelling on the sources, the objects had to meet other requirements that reduced the sample size significantly. The steps used in this filtering process were as follows:

- In order to be able to measure and model the emission line profiles, which are required to estimate the black hole mass, we introduced a further criteria. The objects were required to have significant H β emission (defined as equivalent width (EW) > 0 Å to identify emission lines and $n_\sigma = EW/EW_{error} > 3.0$ to indicate 3σ significance from the SDSS data) and a redshift $z < 0.4$, in order to include Hα. This cut resulted in 888 SDSS/*XMM-Newton* pairs and 802 unique X-ray sources (some X-ray objects were matched to multiple SDSS sources).

- We then spectroscopically classified all of the SDSS sources, categorising them as

Seyferts (Type 1, 2, or intermediate), H II regions/star-forming galaxies, or LINERs. From this list we selected only Type 1 AGN (excluding those classed in the subtypes 1.8 and 1.9), which might be either NLSy1s or broad line AGN. We also excluded the most heavily reddened objects if either the disc emission or Hβ emission line was too badly affected, as this would result in being unable to fit the disc component in the SED modelling and hence being unable to derive a black hole mass estimate from the line fitting. Through visual inspection we then confirmed that the remaining pairs contained real X-ray sources; this resulted in 226 pairs that we considered to be X-ray detected AGN.

- Finally, during the Hα and Hβ line fitting process a further 34 objects were rejected as being either a Seyfert 2 galaxy with no broad emission lines or having no discernible broad component to either Hα or Hβ. This left a final sample size of 192 X-ray selected AGN that could used for modelling.

3.3.3 Characteristics of the sample

The sample selection procedure outlined above is only to ensure that we have selected AGN with both an optical spectrum and an X-ray detection. At this stage there are, deliberately, more stringent optical cuts in place than in the X-rays. This is because the 2XMMi Serendipitous Survey simply catalogues all of the objects detected during the observations. It covers a wide range in data quality, from objects with many thousands of counts to those that have just enough to permit detection. We wanted to test the limitations of the model used in the SED fitting. To this end we include objects in the sample that are heavily reddened in the optical (but not enough to preclude modelling and line fitting), have gas obscuration in the X-rays or have very poor X-ray data, but we also have objects that have thousands of counts with little/no reddening or obscuration. Testing how the model deals with the sample and the range of SED shapes produced will give us a good estimate of its robustness.

We were also able to supplement $\sim 1/3$ of the sample with additional data from the Optical Monitor (OM) attached to the *XMM-Newton* telescope. The OM, when available, provides optical and UV data taken simultaneously with the X-ray observations and will

allow additional constraints on the optical/UV region, which is important when modelling disc accretion.

As the sample has a range of reddening, the line profiles of those objects that are heavily reddened will be affected and their line widths will be difficult to model, affecting the black hole mass estimates. While we have excluded those that are most affected we expect that these remaining objects, even if they produce physically-plausible SEDs, will account for some of the poorest fits in the sample.

All of the sources are detected but not necessarily well-constrained in the 2 - 10 keV region, which is directly associated with the compact emitting region of the AGN. The range in X-ray quality will mean that some sources may contain a warm absorber that could result in the 2 - 10 keV slope being hardened due to absorption in the X-ray region. When the spectrum showed clear evidence of a warm absorber an additional component was added in order to prevent the absorption from this feature hindering the SED fitting process.

Our sample is covering a large parameter range for the physical properties of Type 1 AGN. Other studies such as Jin et al. (2012) have concentrated on defining the SED of AGN with high-quality spectral data, but this study will review the range of SEDs that can be produced by our chosen model; by comparing them to the well-constrained SED we will be able to test the robustness of the model and shed light on what SED modelling of poor quality data can tell us about AGN.

3.3.4 Additional data

All of the 192 AGN in our sample have SDSS survey-quality spectra (flagged as 'sciencePrimary' in the SDSS catalogue), including several objects that have multiple SDSS data measurements. When this is the case, we use the spectrum that was taken closest in date to the *XMM-Newton* observation.

Initially we used the 5 broadband count data sets for each object, but after modelling difficulties described in the next section we used all of the EPIC X-ray spectra (i.e. PN, MOS1 and MOS2) when available.

Additionally, we searched the *XMM-Newton* OM Serendipitous UV Source Survey (SUSS) catalogue for all the OM bands (*V, B, U, UVW2, UVM2* and *UVW1*), which were taken

simultaneously with EPIC spectra of our sources. This resulted in our sample of 192 objects consisting of 124 objects with optical and X-ray data and 68 objects with additional OM data available in at least one of the OM bands.

3.3.5 OM data corrections

When combining the SDSS spectra with the SDSS photometric and OM data points, it was noted that while the 'fiberMag' magnitudes from the SDSS photometric data were in good agreement with the SDSS spectrum, the OM points often displayed a discrepancy. The OM points are often brighter in the spectral plots than an extrapolation of the SDSS spectral shape would suggest. Figure 3.2 shows one example where the OM points lie above the expected extrapolated continuum and one where the SDSS point and OM points agree very well.

Occasionally in the optical bands the opposite case occurs; the OM points appear to lie beneath the spectral data. There are many reasons why this discrepancy could arise, from simple aperture effects to more complex reasons discussed in Section 3.6.3. The aperture effect is one of the most obvious reasons for a discrepancy. This is because, while the SDSS spectroscopic fibres and the 'fiberMag' photometric point use a 3" diameter aperture, the OM has a much large aperture, with a 12" diameter for the optical bands and 35" for the UV bands (Talavera, 2009). If the host galaxy is sufficiently extended (as is the case for many in our sample due to the low redshift cut) the larger aperture of the OM filter would include more emission from the host galaxy than is seen in the smaller SDSS apertures. In order to correct for this effects we carried out the following tests and procedures:

- We studied the combined SDSS and OM data plots, like those produced in Figure 3.2, to identify objects that have a brighter flux in the UV than the extrapolated SDSS continuum spectrum would suggest. We identified 47 out of the 68 sources with OM data where this was the case.

- Using this subsample of 47 sources we checked the catalogue flags to see if any of the sources had been flagged as extended in at least one OM filter. We found that 26 of the sources were extended.

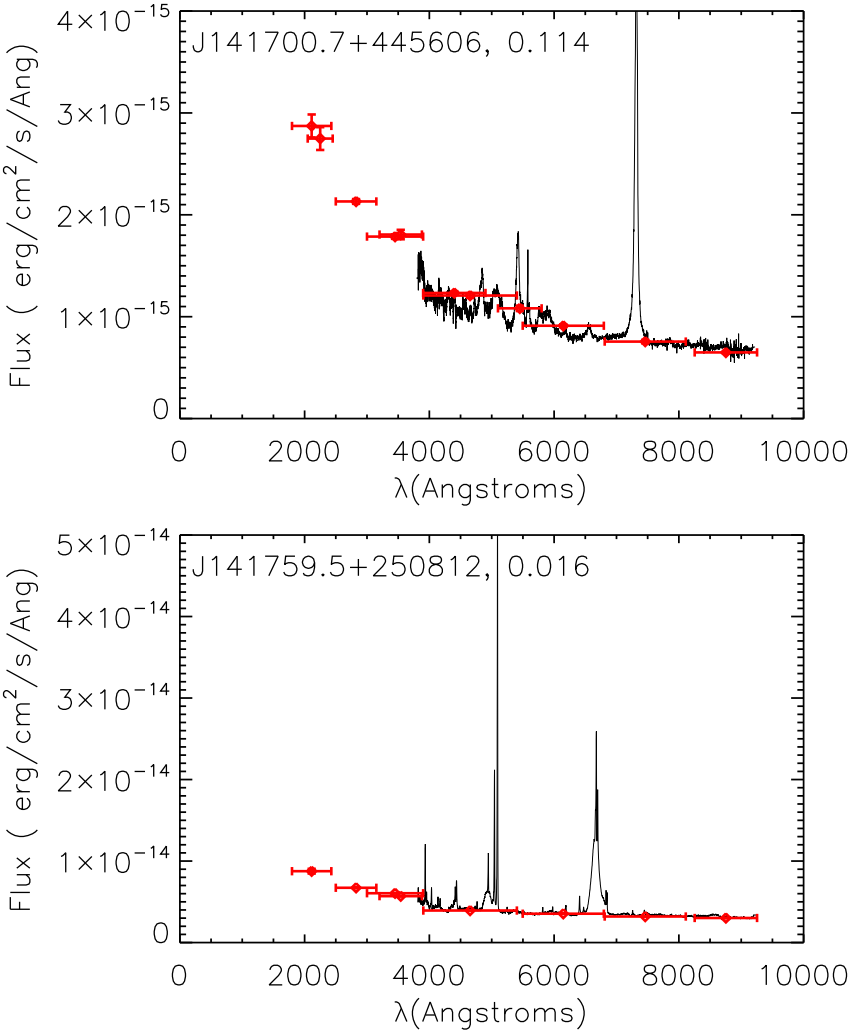

Figure 3.2: The SDSS spectrum, 'fiberMag' photometric data points and OM data points for two objects from our sample. *Top:* J141700.7+445606 is an example where the OM data points appear brighter than both sets of SDSS data. *Bottom:* J141759.5+250812 indicates that this isn't always the case as the OM points lie in the region expected from the extrapolated SDSS continuum.

- Next we checked the SDSS CCD images for all 47 of the objects to visually check if any appeared extended. From this we found 3 sources that appeared extended beyond the 3" diameter of the SDSS aperture, but did not have any OM flags indicating they

were extended. It is thought that for these 29 sources the aperture difference between the OM and SDSS apertures is responsible for the flux discrepancy seen.

- For each of these 29 objects we re-extracted the OM data on a smaller aperture scale. To do this, we downloaded all of the associated OM data files. In each OM image we used a 6" diameter aperture to extract the source flux. We then used the same sized aperture to extract a background region close to the object. Based on the point spread function (PSF) FWHM of the OM for the different filters, the adoption of a 6" diameter aperture is always at least 3 x PSF FWHM. This means that the aperture will have at least 90% of the flux from a UV point source that is detected by the OM.

The choice to adopt a 6" aperture was a compromise between reducing contaminating flux from the host galaxy and keeping any uncertainties and systematic effects caused by the PSF to a minimum.

In order to produce the new source count rate from the source+background flux files, we followed the method outlined in the OM instrument documentation[1]. This process requires three count rate calibrations. The first is a deadtime correction, required because for a small fraction of every exposure the CCD is in readout mode and is not recording data. The second calibration is to correct for coincidence losses, which is when more than one photon arrives on the CCD at the same place and within the same time-frame and results in only one photon being recorded. The final calibration is the OM time-sensitivity degradation correction.

Each of these calibrations were carried out according to the procedures outlined in the OM documentation and we performed each one on both the background file and the background+source file. Finally, the background count rate was subtracted from the background +source count rate to obtain the corrected source count rate. The results of these new source counts were lower than the previous flux levels for the 29 objects used. It also had the added effect of changing the shape of the OM continuum indicated by the points.

In the subsequent SED modelling we use the corrected OM data points.

[1] http://xmm2.esac.esa.int/docs/documents/CAL-TN-0019.ps.gz.

For further information see the *XMM-Newton* User Handbook:

http://xmm.esac.esa.int/external/xmm_user_support/documentation/uhb/index.html.

3.4 Optical spectral modelling: The emission lines

In order to generate black hole mass estimates we need to fit the Hβ line width, used in the estimation equation, as accurately as possible. As both the Hα and Hβ lines originate in the same region we use an optical spectral fitting routine that links the two line profiles together as well as fitting the surrounding spectral emission.

The code used was written in IDL, with the statistical analysis coming from the 'MPFITEXPR' program, which performs a Levenberg-Marquardt least-squares algorithm to obtain the optimal parameters. All of the spectral fitting was carried out on the SDSS DR7 spectra downloaded from the SDSS DR7 data archive. A detailed description of our spectral modelling is described in the following subsections.

Before any emission lines could be profiled, the underlying continuum emission was removed from each spectrum. This was done by fitting a continuum to specific wavelength bins where no emission lines are known to occur.

3.4.1 Profile fitting of the Hα and Hβ emission lines

Current AGN emission line models are based on the theory that there are stratified regions around the black hole that emit different lines. These regions are called the narrow line region (NLR) and the broad line region (BLR) with the possible addition of a third intermediate line region (ILR; Grupe et al., 1999; Hu et al., 2008; Zhu et al., 2009), although it must be stressed that while for some objects there are clear distinctions between at least the NLR and BLR line emission the regions are quite arbitrarily divided up and often appear in emission line profiles as blended emission. In order to account for these different regions we follow on from previous studies in adopting several Gaussian profiles for each emission line to fit the emission profile.

Both the Hα and Hβ line emission regions pose significant challenges for spectral analysis. In the case of Hβ, the permitted Fe II emission features (which can be strong in AGN, particularly NLSy1s) and the broad He II λ4686 Å line blend with the Hβ line, making it difficult to determine the true level of the underlying continuum and therefore the shape of the Hβ profile. This is most apparent when fitting the wings associated with the broad

component. The Hα emission region, the [N II] $\lambda\lambda$6584,6548 ÅÅ doublet blends into the broad Hα emission. If this is not subtracted properly it can distort the intrinsic profile of Hα.

Our approach to this is to fit Hα and Hβ simultaneously, using the same Gaussian profiles to represent each component of the line emission for both lines. Assuming that the intrinsic profiles of these two lines will be similar enables us to deblend these Balmer lines from the other nearby emission lines and results in a more reliable deconvolution for the separate components of their profiles.

3.4.2 Deconvolving the Balmer emission lines

The first stage in fitting the Hα and Hβ Balmer lines is to first fit the [O III] λ5007 Å line emission. Depending on the strength of this line either two or three Gaussian components are used. Once this has been done we move on to simultaneously fit the Hα and Hβ profiles. To do this we consider the simplified setup alluded to at the start of this section. We assume that the Balmer lines contain three components, each associated with a different region around the black hole: a narrow component from the NLR, an intermediate component from the ILR and a broad component from the BLR. These assumptions require us to make no guesses into the nature of the ILR, whether it is the transitory region between the NLR and BLR or the inner edge of the dusty torus (as in the case of Zhu et al., 2009), only that it exists and we account for it.

The broad and intermediate components are fitted with a Gaussian profile, but the narrow component is linked to the narrow component of [O III] λ5007 Å. As we do not know the level of reddening in each of the objects, or whether the Balmer decrements are constant across the different regions, we allow the relative strengths of the components to vary, only keeping the FWHM and relative velocities linked. The [O III] λ4959 Å line was defined to be 1/3rd of that measured for [O III] λ5007 Å from atomic physics while the [N II] $\lambda\lambda$6584,6548 ÅÅ doublet was also fixed to the [O III] λ5007 Å profile.

In order to separate out the narrow components of the Balmer lines from the other components as accurately as possible we set the following fitting method into practice:

- If the narrow component of the emission line was obvious then we matched the profile

of the narrow component to the [O III] λ5007 Å profile, but the normalisation of each component in the Hα and Hβ was left as a free parameter.

- If the narrow component was not obvious we determined the shape of the narrow component to be the same as the entire [O III] λ5007 Å profile, with the normalisation of the Hβ line narrow component set to be 10% of [O III] λ5007 Å (as this is the typical ratio for the NLR in Type 1 Seyfert galaxies; Osterbrock & Pogge, 1985).

After the line fitting profiles had been developed, we convolved the intermediate and broad components together to create a narrow component-subtracted Hβ profile. We then measured the FWHM of this resultant profile to use in the black hole mass estimations. We used this method, rather than take the FWHM directly from the Hβ line in the data, because the model profiles are not subject to localised noise in the data, which results in a low S/N line profile for many objects in our sample. The Hβ FWHM measured were deconvolved with the instrumental resolution of 69 km s^{-1}.

3.5 Black hole mass estimates

The BLR Size-Luminosity Relation first explored in Kaspi et al. (2000), was exploited by Woo & Urry (2002) which combines it with the equation for velocity ($\nu = f$ x FWHM, where $f = \sqrt{3}/2$; Netzer, 1990) and obtains the following equation for black hole mass:

$$\mathrm{M_{BH}} = 4.817 \left[\frac{\lambda L_{\lambda}(5100\mathring{A})}{10^{44}\mathrm{ergs\ s^{-1}}}\right]^{0.7} \mathrm{FWHM}^2 \tag{3.3}$$

where L_{λ}(5100Å) is the luminosity of the continuum at 5100 Å and the FWHM is the FWHM of the broad component of the Hβ emission line profile.

We adapted this equation to derive black hole mass estimates for our sample. In order to allow the SED model to have M_{BH} as a free parameter and due to the inherent errors arising from the definition of the 'broad component', we created a line profile that could be used to produce a range of FWHM and thus a range for the M_{BH} estimate for an object. We combined the broad and intermediate components from the Hβ fitting routine to produce a

narrow component-subtracted profile. We then used this profile to generate maximum and minimum FWHM, which were used in the equation above to produce a range for the M_{BH}. We took the measurements of $L_\lambda(5100\text{Å})$ directly from the SDSS spectra. From the line fitting profiles before the SED modelling we found that our M_{BH} estimates ranged from 2 x 10^5 to 3 x 10^9 $M_\odot$, which are in good agreement with the range of values found in literature (Bian & Zhao, 2004b; McLure & Dunlop, 2002).

3.6 SED Construction

3.6.1 Data preparation

Initially, in order to standardise the sample, only the broadband optical/UV and X-ray points were used in the modelling. This was in order to balance the number of data points with the number of free parameters, with the aim of having a similar number of optical and X-ray points (while in theory the maximum number of optical/UV data points available is 11 if both the SDSS and full OM range is used, the majority of the sample only has 5 SDSS bands available). We used the XSPEC package to carry out the modelling procedures as it is primarily an X-ray modelling package the optical and UV disc emission models are only accurate enough to model the underlying continuum emission and cannot account for the emission lines. Due to this fact we decided not to read the optical spectrum of the sources into XSPEC, so we used the PSF photometric magnitudes, 'PSF_mag', in the 5 different SDSS bands: *u, g, r, i* and *z*.

The data points could come from three different sources: SDSS, *XMM-Newton* and the OM. In order for the data to be read into XSPEC it all had to be in the same format, and therefore the data from each instrument had to be converted into the same units. The process for converting each data set is outlined below. Also outlined is the method used to extract the *XMM-Newton* spectral files that were used when the model used in the fitting was changed.

SDSS photometric data points

SDSS magnitudes are not given in the usual AB magnitude system, and so follow a different method to be converted into fluxes. The magnitudes given by SDSS are given as inverse

hyperbolic sine (or 'asinh') magnitudes, described in detail by Lupton, Gunn, & Szalay (1999). They are sometimes referred to informally as *luptitudes*. The transformation from linear flux measurements to asinh magnitudes was designed to be virtually identical to the standard astronomical magnitude at high S/N ratios, but to behave reasonably at low S/N ratios and even at negative values of flux, where the logarithm in the Pogson magnitude would fail. This allows SDSS to measure fluxes even when there is no formal detection, which means that there are no upper limit quotes in SDSS photometry.

The asinh magnitudes were converted into flux density by rearranging the following formulae:

$$mag = -\frac{2.5}{\ln(10)} * \left(\text{asinh}\left(\frac{f/f_0}{2b}\right) + \ln(b) \right) \tag{3.4}$$

$$S = 3631 \text{ Jy} * f/f_0 \tag{3.5}$$

where 1 Jy = 10^{-23} erg s^{-1} Hz^{-1} cm^{-2} and the constant b is a correction unique to each band and is taken from the SDSS DR7 website[1]. The units of flux were converted from erg s^{-1} Hz^{-1} cm^{-2} to photons cm^{-2} s^{-1} by integrating across the bandpass. These fluxes were then used in the FLX2XSP utility to produce data that could be used in XSPEC.

***XMM-Newton* broadband data points**

For the X-ray data points we used the broadband data, which divides up the total 0.2 - 12.5 keV range available into 5 energy bands (band 1: 0.2 - 0.5 keV, band 2: 0.5 - 1 keV, band 3: 1.0 - 2.0 keV, band 4: 2.0 - 4.5 keV and band 5: 4.5 - 12.5 keV). These were taken from the catalogue in the units photons cm^{-2} s^{-1}. As with the SDSS data, these fluxes were converted with FLX2XSP to be used in XSPEC.

The flx2xsp utility

The multi-wavelength fluxes were initially converted into photons cm^{-2} s^{-1} and then made into XSPEC spectral files using the FLX2XSP utility in the FTOOLS package. It creates PHA and RSP FITS files from a text file containing fluxes and errors. The response file created is a unit diagonal matrix of the appropriate size. In order for FLX2XSP to work the input file must be in a set format, with the fluxes given as photons cm^{-2} s^{-1} and the wavelength range given in keV. As the utility will only work when the wavelength ranges do not overlap each optical data point was made into its own file to prevent any rounding errors.

[1] http://www.sdss.org/dr7/algorithms/fluxcal.html#asinh_table

OM photometric data points

For 68 objects in the sample there was also *XMM-Newton* Optical Monitor (OM) data available; this allowed up to an extra 6 data points in the optical/UV region if all of the OM bands had data available. For the XMM-OM optical and UV data the band energies for the 6 different bands were based upon the crossing point between bands for all bands to prevent band overlap, apart from UVM2 and UVW2 which had an overlap of 25 Å at the upper end of the UVW2 band and bottom of the UVM2 that could not be avoided. To prepare the OM data for use the *om_filter_default.pi* file and all of the response files for the six OM filters were downloaded from the OM response file directory in the HEASARC Archive.[2] The OM source list was checked for each object to see if there were any available OM count rates. Each count rate and error was entered into the *om_filter_default.pi* file and combined with the response file of the corresponding OM filter, using the GRPPHA tool from the FTOOLS package, to produce OM data that could be used in XSPEC.

***XMM-Newton* Spectral data**

After the repeated failure of the model to fit an SED to the broadband data points as discussed in Section 3.2.2, we decided to replace the *XMM-Newton* broadband data points with the *XMM-Newton* spectral files to create more robust fits with the OPTXAGN model.

For each object we extracted the original data files and the pipeline products (PPS) from the *XMM-Newton* Science Archive.[3] As part of the data-reduction process, tasks from the *XMM-Newton* Science Operations Centre SAS v7.1.0 (Science Analysis System) software were used and we followed a different routine to that used in Chapter 2, due to the different nature of the samples. First the EPCHAIN/EMCHAIN task was used to extract events, unless the events files had already been extracted for each exposure by PPS. Then ESPFILT was used to define a selection of background good-time intervals, where there were no recorded flares. Each source region was extracted by a 45" radius aperture from the available EPIC images. The background was extracted from an annulus centred on the source with inner and outer radii set to 60" and 120" respectively. For other sources that were listed by the region files of PPS to be included in these regions, the extraction was carried out using the

[2]http://heasarc.gsfc.nasa.gov/FTP/xmm/data/reponses/om/

[3]http://xmm.esac.esa.int/external/xmm_data_acc/xsa/index.shtml

default radii generated by PPS, which scales with source brightness.

The GIT filter, source and background region filters were applied to the corresponding events files to produce a set of source and background events files. We only used photons with a 'quality_flag' = 0 and patter 0 - 4. The EPATPLOT function was then used to check for pile-up effects. In the few instances where pile-up was detected, the radii of the source and background extraction regions were scaled down until the pile-up disappeared. Source and background spectra were extracted from the events files for each EPIC exposure. RMFGEN/ARFGEN was used to produce both the response matrices and auxiliary files for the source spectra. The final spectra were grouped to a minimum of 25 counts per bin using the GRPPHA v3.0.1 tool for spectral fitting in XSPEC v11.3.2. In a few cases the data quality was so poor that there were not 25 counts for a bin. In these cases each object was binned in order to register counts throughout the X-ray bands. A spectrum was extracted for every object, but in some cases the resultant data was of such poor quality that no model could be fitted to it.

By combining the optical, UV and X-ray data, we created a broadband SED for each AGN. Due to the photoelectric absorption by Galactic gas there is a ubiquitous data gap between the near UV and the X-rays. Unfortunately, due to the redshift constraints of the line fitting process, this region is where we would expect the SEDs of low-redshift AGN to peak. This means that most of the bolometric output of these objects is concealed within an unobservable band. The attempt to fit emission in this invisible region with often poor constraints is what caused the multi-component models described above to fail. The next subsection describes how the SED fitting routine was optimized through improving the quality of the data by using the X-ray spectral data and by using an better integrated model OPTXAGN to create robust fits.

3.6.2 SED fitting

Initially the multi-component model DISKPN+BKNPL+COMPTT was used to fit the optical, UV and X-ray photometric points. This attempt was not successful as the data was unable to constrain the components, and the individual components are considered as being completely separate to each other and so can produce unphysical models. As a result we improve the

method in two ways. First we used X-ray spectral data instead of the broadband fluxes; this improved the data quality for the whole sample as we were able to extract a spectrum even for the objects with the poorest S/N. Secondly, we adopted the model OPTXAGN described in Section 3.1.2 above. The model is far superior to the previous model as it is energetically self-consistent and produces physically plausible parameters.

In the SED fitting, the optical/UV data constrains the mass accretion rate through the outer disc, using our black hole mass constraints derived in Section 3.5. As we want the model to fit the black hole mass as a free parameter, we make sure the limits of the model parameters are set so as to be consistent with the masses derived from the line fitting. When the black hole mass is constrained the model then uses the optical data to set the mass accretion rate, $\dot{\mathsf{M}}$, and from that the accretion efficiency will determine the total energy available.

The model assumes a stress-free emissivity for a Schwarzschild black hole, which gives an overall efficiency of 0.057 for $R_{in} = 6\ R_g$ (where $R_g = GM/c^2$). This gives the total luminosity of the soft excess and the power law as $0.057\ \dot{\mathsf{M}}c^2(1\text{-}\frac{R_{in}}{R_{corona}})$, and also will constrain the unobservable UV region. The parameter R_{corona} sets the model output for the luminosity ratio between the standard disc emission and Comptonisation components. The upper limit of R_{corona} is set to be 100 R_g, or the equivalent of 81% of the released disc energy. The other free parameters are as described in Section 3.1.2 above.

We also included corrections for dust reddening and gas obscuration. As there is intrinsic and Galactic attenuation, this resulted in four additional components. REDDENING and WABS was used for the Galactic attenuation and was fixed from Galactic dust reddening maps and known Galactic column densities respectively. The absorption intrinsic to each source was represented with the models ZRED and ZWABS, which behave as their Galactic counterparts with an additional redshift component. The intrinsic components were left as free parameters.

The results of the main fitting parameters are shown in Appendix A along with the luminosity for each of the main components from the model (disc, Comptonisation, power law and 2 - 10 keV band). The main uncertainty in these parameters, particularly the black hole mass, is dominated by systematic uncertainties arising from the observational data, the

model assumptions (a non-spinning black hole and a set observation angle) and the analysis methods involved. This means that the errors associated with individual parameters are not significant in comparison (often $< 10\%$) and so are not listed.

The resultant SED products for the whole sample are shown in Appendix B. In these figures the black line indicates the best unabsorbed model fit to the unabsorbed data. The absorbed model is indicated by the red dashed line. In several instances it can be seen that the obscuration is overestimated, producing a fit where the model is below the spectral data. Figure 3.3 shows the SEDs of 6 objects with good quality X-ray data. It can be seen that there is very little reddening or gas obscuration in these objects. In addition to the unabsorbed spectrum and model and the absorbed model the individual components of the model are plotted. The disc component is shown in red, the soft excess in green and the power law component in blue.

3.6.3 Modelling complications

After adopting the new data input method plus the new model and X-ray spectral data, we still had some other significant problems, which are discussed in greater detail below.

3.6.3.1 The discrepancy between the OM and SDSS photometry

Despite applying aperture corrections and correcting to the SDSS AGN continuum, there often remains a large discrepancy between the OM and SDSS data points. In most cases, the OM points appear to be brighter than an extrapolation of the SDSS continuum to the OM wavelengths would suggest. We suggest that there are three possible reasons for this:

1. **Remaining aperture effects:** There is an aperture difference between the SDSS fibres (3" diameter) and the OM apertures we used (6" diameter). Clearly the OM points will still include more host galaxy starlight than the SDSS points, and so will appear above the SDSS spectrum, even after correcting the OM points to the SDSS continuum.

2. **Contamination from emission lines:** The wavelength ranges for each OM filter (over which the effective transmission is greater than 10% of the peak effective trans-

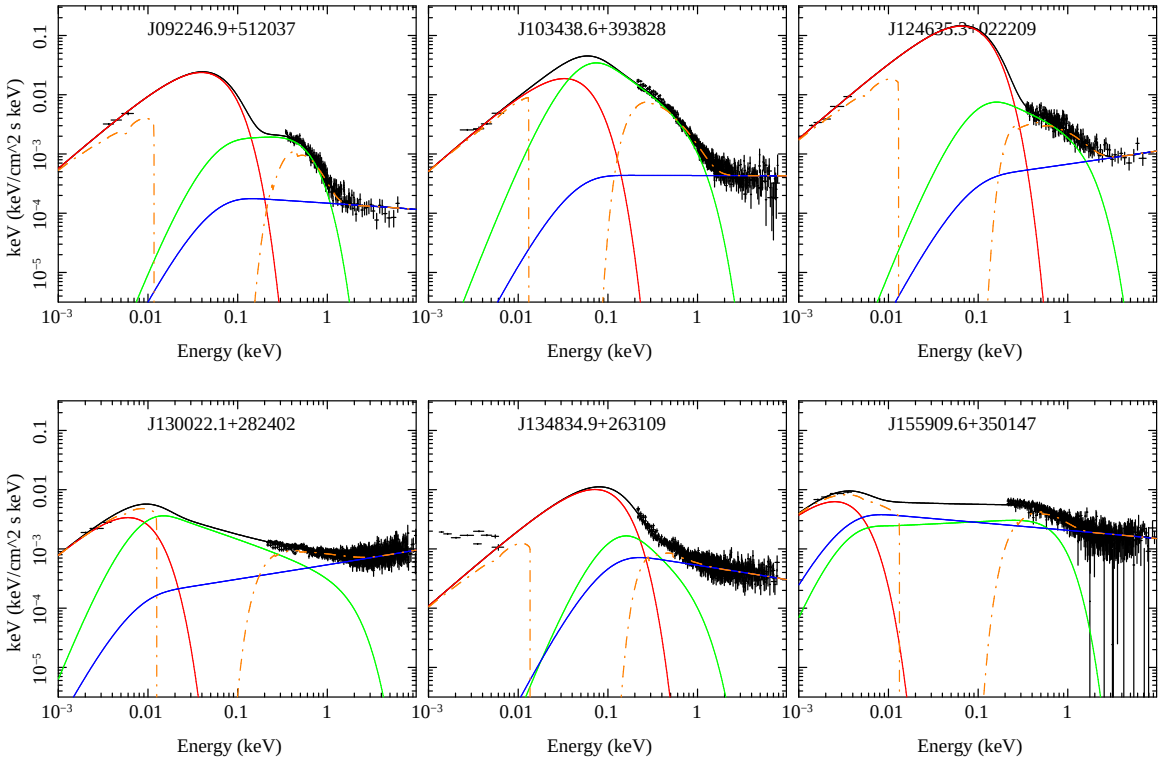

Figure 3.3: Six SEDs showing a range of model fits. In each SED the disc component is shown in red, the soft excess component in green, the power law component in blue and the resultant model in black. The unabsorbed spectrum is shown in black, while the absorbed model is indicated by the red dashed line. For these objects there is very little obscuration present and all have very good quality X-ray data.

mission) are as follows: UVW2 1805 - 2454 Å, UVM2 1970 - 2675 Å, UVW1 2410-3565 Å, U 3030 - 3890 Å, B 3815 - 4910 Å, V 5020 - 5870 Å. Unlike the SDSS *u, g, r, i* and *z* photometric bands there is no UV spectral data to compare the UVOT data to. Plotting the SDSS photometric points, the SDSS spectrum and the UVOT data allowed a standardised correction to bring the UVOT data in line with the AGN continuum seen in the optical, but did not correct for the emission lines that are known to be in the UV region. Inclusion of strong emission lines within these photometric data points would result in overestimation of the optical continuum, and so compromise our aim to study the shape of the optical underlying continuum. In many ways the UV continuum is more important than the optical continuum in constraining the SED, as the UV region is where we would expect to either see a flattening, turn-over

or continuation of emission depending on the extent of the disc component. We know that several strong emission lines lie within the UV bandpasses, such as Lyα, C IV λ1549 Å, C III λ1909 Å and Mg II λ2798 Å, the strength of which we are not able to judge from the SDSS spectra. In several cases we see that there is an apparent 'peak' in the OM UVM2 photometric point. This is probably due to strong emission in this region from lower wavelength lines, all of which would lie within this bandpass due to the redshift range used. Due to the strong emission lines contained within the UV region it is certain that many objects in the sample will have OM data points contaminated by this emission; this could be at least partially responsible for some of the discrepancies seen.

3. **Intrinsic source variability:** AGN variability is well known and is referred to throughout this thesis. While optical/UV variability is not as common on such short time-scales as X-ray variability, it is still observed. There is also often a significant time difference between the SDSS observations and the OM data. This means that a flare intrinsic to the AGN is a possibility on the timescales we are considering. In order to test the extent to which the variability could affect the SED we looked at all of the GALEX data available for our sample. Of over 100 objects covered by GALEX contained within the sample, we found that including this data into the SED only changed the total flux of the disc emission by $\sim 10\%$. Of course, there will be objects that have a considerably greater outburst than the low-level variability we expect to see from most AGN. One of these objects is J0925+5217: in this object the flux observed by the OM was ~ 30 times brighter than that recorded by SDSS. Unfortunately this object failed the fitting pipeline and so an SED could not be made; however, it does serve to highlight that non-simultaneous OM and SDSS data can cause problems during the modelling process.

   While the intrinsic source variability is very likely responsible for some of the discrepancy between the OM and SDSS data, it is unlikely that the non-simultaneity will cause major issues in the modelling process, as the errors due to the uncertainty in the true fluxes is less than the errors from the fitting parameters themselves.

In reality, all three of these factors will merge together to contribute to the observed discrepancy between the SDSS and OM data. Since the combined effects of the first two points will add flux and generally be greater than that caused by optical/UV variability, as shown by previous long-term reverberation mapping studies (Giveon et al. 1999; Kaspi et al. 2000), we should treat the OM points included in our SED modelling as upper limits when interpreting the results of our modelling. Indeed, the 90% confidence uncertainties in M_{BH} derived directly from the XSPEC fitting are almost certainly small compared with the systematic errors introduced by the above uncertainties.

3.6.3.2 Flat optical continuum

A problem that is related to the offset between the SDSS and OM data points is the shape of the SDSS continuum itself. We made the decision to use the photometric data points as they provide a good indication of the underlying continuum; however, this does cause some additional problems. One of the requirements of our sample was the presence of the Hα emission line in the spectral data. This means that for most objects the z band data points are brighter than the surrounding bands due to the additional Hα flux. While this does affect the shape of the disc component fitted to some extent, a greater problem lies with the red end of the optical data as a whole. While the blue end of the continuum is consistent with the SED shape predicted by the model, at longer wavelengths this is not the case, as the model underestimates the level of flux present. This suggests the presence of an additional component at these wavelengths extending through to the near IR region.

One obvious explanation for this excess is contribution from the host galaxy. In late-type elliptical or S0 host galaxies the emission from stellar populations in the galaxy is expected to peak in the near-IR. We investigated the stellar contribution to the optical continuum by fitting stellar templates of different morphological types, but we found that this did not work in most of the objects. Jin et al. (2012) showed that in a sample of high-quality SEDs the contamination from the host galaxy in the 3" diameter fibre is very small. It is more likely that this continuum is linked to the intrinsic activity of the AGN, but currently our models are unable to process it. In order to counter this the optical fitting was weighted to the bluer wavelengths, and providing a fit could be made to the u band data the fit was

allowed to stand.

3.7 Discussion

From the SED modelling process we measured fits for 170 of the 192 objects originally in our sample. The reason for the failure of the remaining 22 models was mainly due to poor data quality. In several cases there were too few counts in the X-ray region to provide an anchor for the fit and in others discrepancies between the optical and X-ray flux levels were such that no model could be made to fit. A further 13 objects produced fitting parameters, but only after considerable manipulation of the data to create the cleanest data possible. As a result we do not show the resultant SEDs or use them in the following analysis. However, for reference the parameters are shown in the list with the parameters of the entire sample.

From the sample we found that 37 objects have a $\lambda_{edd} > 1$ and these are therefore classed as super-Eddington. It was also found that 39 objects could not fit a soft excess component to the model. This was generally due to the data quality and the ambiguity of separating obscuration from a soft excess component in a poorly constrained spectrum.

93 objects from the sample were classed as have good fits with a reasonably low $N_H < 0.15 \times 10^{22}$ cm^{-2} and did not have all of the X-ray flux constrained to the power law component. While the parameter characteristics listed below use results from the 158 objects with fits unless otherwise stated, the analysis on the bolometric corrections and the SED types at the end of this chapter just use these 93 objects; these objects will be referred to as the well-defined sample.

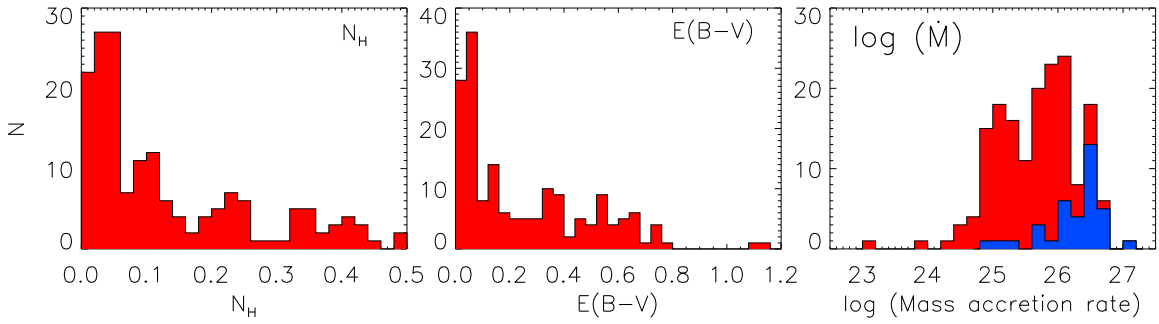

Figure 3.4: Distributions of our sample for N_H, E(B - V) and $\dot{M}$.

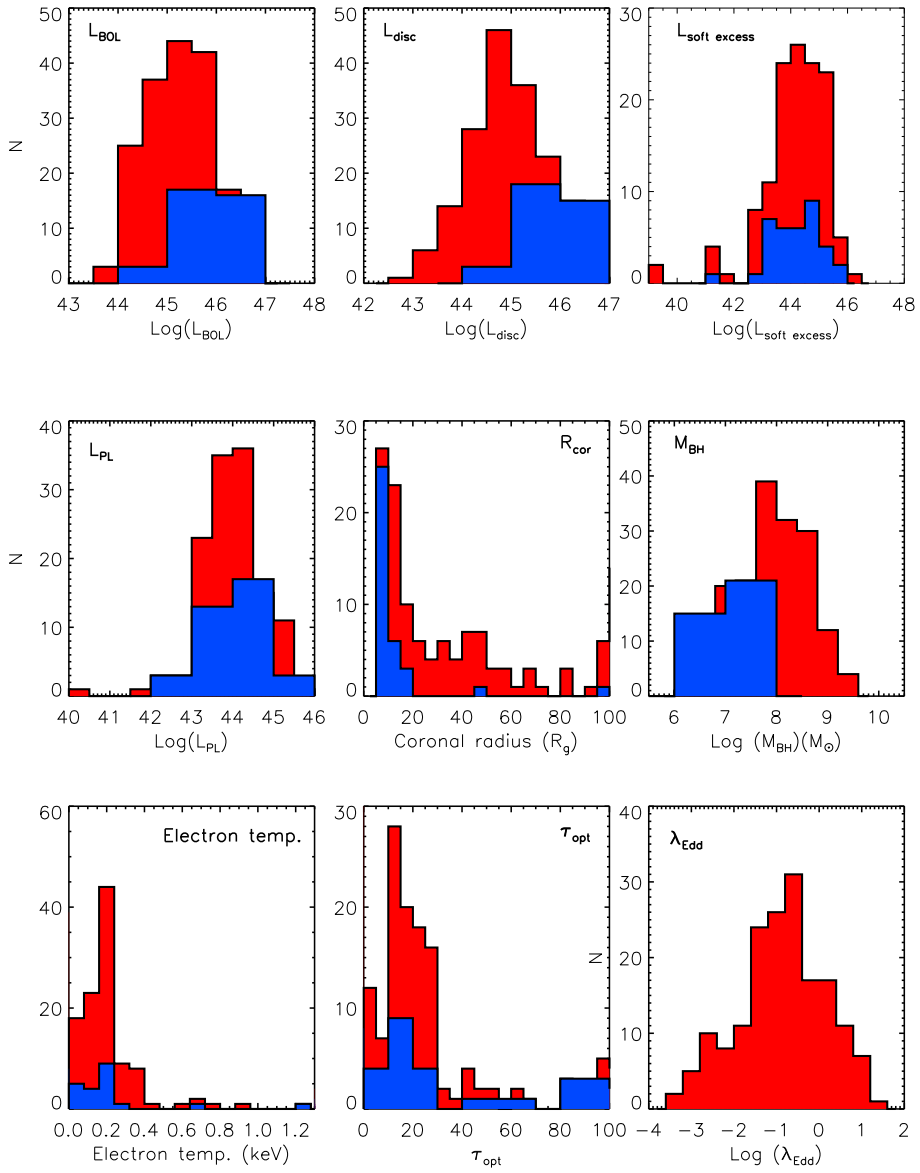

Figure 3.5: Distribution of model-dependent parameters from the SED fits. In each plot the red histogram represents the total sample while the blue histogram shows a scaled distribution of the 37 super-Eddington objects found in the sample. Each parameter is discussed in detail in Section 3.7.1.

In the left and middle plots shown in Figure 3.4 we show the distributions of the sample for the N_H and E(B - V) obscuration and reddening parameters. In the fitting process these were linked using the standard dust-to-gas conversion formula from Bessell (1991) of:

$$E(B-V) = 1.7 \times 10^{-22} N_H \tag{3.6}$$

However, as the work of Chapter 2 shows, this relationship does not hold true for a majority of AGN. In order to overcome this, the N_H and E(B - V) were initially fixed together, but if the model had difficulty fitting a mass accretion rate to the optical data then the parameters were untied but monitored and constrained to prevent the production of over-absorbed models. While some evidence of the overestimation of the obscuration in the soft X-rays can be seen in several models, the plots shown in Figure 3.4 show that the majority of the objects can be fitted by leaving the parameters tied together.

3.7.1 Results from the broadband SED modelling

Figure 3.5 shows the distribution of many different properties all derived from the SED fits; each one is discussed in turn below.

The bolometric luminosity

The bolometric luminosity ranges from 3.3 $\times 10^{42}$ (J092129.2+370103) to 4.0$\times 10^{46}$ (J135510.2 +383528) erg s^{-1}. The super-Eddington sample exists towards the higher end of the distribution, but there is no clear division between the complete sample and the subset. The average luminosity $\log(L_{bol}) = 45.56 \pm 0.64$, which is consistent with the value of 45.49±0.55 found by Jin et al. (2012) and the value of 45.19 ± 1.01 found by Vasudevan & Fabian (2007).

The mass accretion rate

The histogram showing the distribution of $\log(\dot{\mathsf{M}})$ is shown in the right-hand plot of Figure 3.4. The range is $23.0 < \log(\dot{\mathsf{M}}) < 27.1$, with a mean value of 25.7±0.4. From the figure it can clearly be seen that the super-Eddington objects cluster at the far right of the distribution. The mean of the super-Eddington sample is 26.2±0.5. This result is to be expected, as the super-Eddington objects must have a characteristic difference to make them more luminous

than their sub-Eddington counterparts; accreting mass at a higher rate would account for this difference.

The disc luminosity

The disc luminosity ranges from 3.3×10^{42} to 3.9×10^{46} erg s^{-1} and it is interesting to note that both of the objects with these values are classed as super-Eddington. The distribution of the overall sample is more Gaussian than the distribution of the super-Eddington sample, with the mean being centred in the middle of the distribution at $\log(L_{disc}) = 44.89\pm0.73$. The average of the super-Eddington sample is higher at 45.88 ± 0.92. This outcome is probably due to the high mass accretion rate seen in super-Eddington objects.

The soft excess luminosity

The soft excess Comptonisation luminosity ranges from 1.7×10^{39} to 1.2×10^{46} erg s^{-1}, with both the super-Eddington and the overall sample showing the same distribution. The mean of the overall sample is $\log(L_{comptt}) = 44.27\pm0.35$, and the mean of the super-Eddington sample is consistent with this at 44.03 ± 0.37. This result may seem surprising, as it is expected that NLSy1s have a large soft excess component, and 15 of the objects in the super-Eddington sample are classed as NLSy1s. However, as the other parameter plots show, the main difference between the super-Eddington sample and the overall sample lies in the disc luminosity and the mass accretion rate.

The power law luminosity

The power law luminosity ranges from 2.3×10^{40} to 5.6×10^{45} erg s^{-1}. The mean of the whole sample is $\log(L_{pl}) = 43.98\pm0.41$ and the mean of the super-Eddington sample is slightly higher but still consistent with this at 44.10 ± 0.48.

The coronal radius

For the overall sample the value of the coronal radius peaks between 8 - 15 R_g. There is also a much smaller but still significant peak between 40 - 50 R_g. The smaller group of objects clustered around 100 R_g is due to the fitting parameter limit of 100 R_g. In contrast the super-Eddington sample is consistent with just the first peak of the overall sample. This result is not as surprising as it appears, as the concentration of the soft excess temperatures at around 0.2 keV suggests that atomic processes may be significant (i.e. reflection and/or absorption from partially ionised material), which, if true, will influence our fits. The average coronal

radii are 21±19 R_g for the overall sample and 8±7 R_g for the super-Eddington sample. This supports the conclusions of both Jin et al. (2012) and Vasudevan & Fabian (2007) in showing that super-Eddington AGN have lower coronal fractions than those sub-Eddington.

The black hole mass

Taking the best-fitting black hole masses from the SED parameters we find that the sample peaks at $\sim 10^8$ $M_\odot$. The method used to calculate the range of black hole masses suggests that the mass is dependent on the FWHM of Hβ and $L_{5100\text{Å}}$, so those with the narrowest lines will have lower black hole masses. As λ_{Edd} is defined as L_{bol}/L_{Edd} the smaller the black hole mass the lower L_{Edd} will be, increasing the chances of an object being classed as super-Eddington. Our black hole mass size for the NLSy1 RE J1034+396 is $2.6\times10^6 M_\odot$, which is in excellent agreement with the values calculated from the quasi-periodic oscillation found by Gierliński et al. (2008). Our average $\log(M_{BH}) = 8.01\pm0.85$, while slightly higher than those found by Jin et al. (2012) and Vasudevan & Fabian (2007), is still in good agreement.

The electron temperature of the soft excess Comptonised component

When the f_{pl} was set to 1 there was no flux in the soft excess component and so these objects are not included in this plot. For the objects with a soft excess component the peak is concentrated at around 0.2 keV in all objects, which matches the trend seen in other studies for this component to exhibit a narrow range in peak energies (Czerny et al., 2003; Gierliński & Done, 2004). The peak is present in both the overall sample and the super-Eddington sample, suggesting that the origin of this component is the same for all AGN.

The optical depth of the soft excess Comptonised component

Again, objects with no flux in the soft excess Comptonised component are not included in this plot. It is clear that this component is always optically thick and most objects have $\tau \sim 10 - 30$, with a mean value of 19.7±17.3. The super-Eddington sample has a higher mean value due to the cluster of objects with $\tau \sim 80 - 100$, but the distribution broadly matches that seen for the overall sample.

The Eddington ratio

The mean λ_{Edd} for the super-Eddington sample is 4.35±3.23, with a large dispersion up to a maximum value of 14.15. For the objects with $M_{BH} > 10^8$ $M_\odot$ the average is 0.08±0.22.

The mean of the full sample is 1.07±1.09. For objects with $M_{BH} < 10^7$ $M_\odot$ the average is 4.15±3.70. This clearly shows that objects with smaller black hole mass and hence narrower Hβ FWHM measurements have a higher Eddington ratio. This is most likely due to the strong disc component from a high mass accretion rate which raises the bolometric luminosity, while the small black hole mass measurements lead to a lower Eddington luminosity, which results in a high λ_{Edd}.

3.7.2 Bolometric luminosity distributions

The fraction of the total luminosity contained in each component of the SED is shown in Figure 3.6. In each of the three plots red represents the disc component, green represents the soft excess Comptonisation component and blue represents the power law component. The bottom panel shows the sample arranged in order of increasing M_{BH} from left to right. The thicker lines represent super-Eddington objects. It is clearly shown that the super-Eddington objects are clustered around the lower end of this distribution. The objects to the far left of the distribution are classified as NLSy1s due to their FWHM Hβ measurements. The NLSy1s are also more likely to have a smaller fraction of their total luminosity emitted in the soft excess Comptonisation component than their BLSy1 counterparts, as can be clearly seen from the figure. The top panel shows the component distribution ordered by increasing λ_{Edd} from left to right. This shows that all bar two of the objects classed as super-Eddington are disc dominated and several have no discernible soft excess component.

It is worth noting that the BLSy1s with a large soft excess component could have alternative spectral fits that include reflection and/or absorption components that we do not model for. It can also be clearly seen that the lower limit for the disc fraction is 0.19, set by the upper limit on the R_{corona} parameter of 100 R_g.

3.7.3 Black hole mass

The black hole mass is one of the key parameters used in the SED fitting routine as it determines the shape of the continuum in the optical/UV region. As mentioned in Section 1.4.2 the most accurate method for determining black hole mass is believed to be reverberation

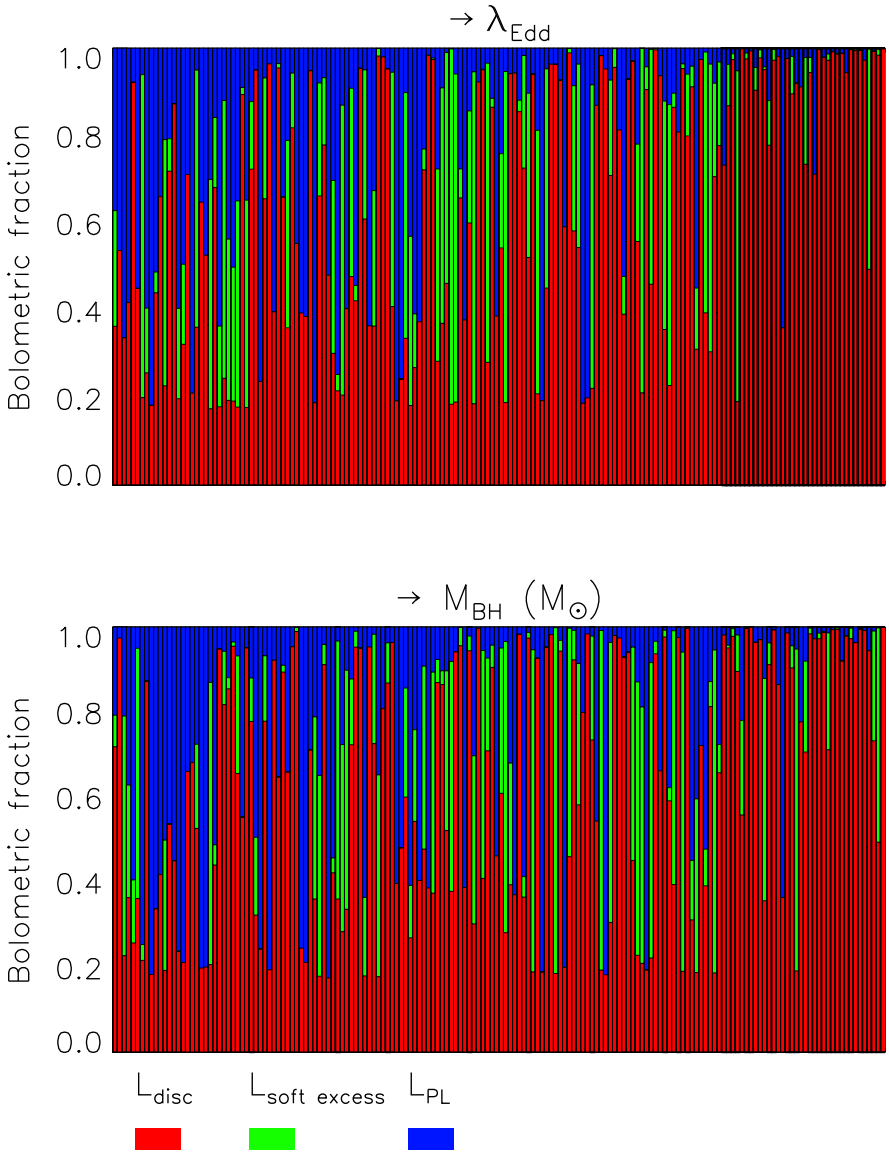

Figure 3.6: Luminosity plot showing the different luminosity components derived from the modelling process as a fraction of the bolometric luminosity. The disc component is shown in red, the power law component is shown in blue, and where present the soft X-ray excess component is shown in green. *Bottom panel:* The objects are arranged in increasing M_{BH} from left to right. *Top panel:* The objects are arranged in increasing λ_{edd} from left to right.

mapping, but this has only been done for a small sample of objects. The method that we have used in this study, exploiting the relationship between M_{BH}, the Hβ line width and $L_{5100\mathring{A}}$, is the most commonly used means of estimating the black hole mass.

The method of establishing the FWHM of Hβ varies from sample to sample, with some studies using just the intermediate component or just the broad component to produce their estimates. Both of these methods will result in errors due to difficulties in separating the components used from the narrow component and the broad wings respectively.

In our profile fitting routine we used the FWHM of the combined intermediate and broad component to derive a black hole mass, but also measured the FWHM of the intermediate and broad components to provide the lower and upper mass constraints in the SED fitting. In Figure 3.7 we show how the black hole masses from the SED fits ($M_{BH,SEDfit}$) differ from those derived from the profile fitting ($M_{BH,H\beta}$). It can clearly be seen that these two different estimates are not consistent with each other. The SED fitting often finds a higher mass than that found from the profile fitting. However, the opposite trend is found for the super-Eddington objects, resulting in them having a smaller black hole mass. We find that the mean for $M_{BH,SEDfit}$ is 0.21 dex higher than $M_{BH,H\beta}$ for the overall sample, but 0.18 dex lower for the super-Eddington sample. For the NLSy1s, the mean is 0.69 dex higher for $M_{BH,SEDfit}$ than for $M_{BH,H\beta}$. This is consistent with the results from Jin et al. (2012), Komossa (2008) and Grupe & Mathur (2004) in indicating that the masses derived from the profile fitting may not be true representations of the black hole mass of NLSy1s.

3.7.4 Bolometric corrections

We show the bolometric correction, $\kappa_{2-10keV}$, as a function of luminosity at the top of Figure 3.8. Only the 93 objects classed as well-defined were used for this analysis, as we wanted to investigate the relationship between $\kappa_{2-10keV}$ and $L_{2-10keV}$ in objects where the X-ray flux was not restricted to just the power law component. The red and blue lines show the theoretical models of Marconi et al. (2004; blue line) and Hopkins et al. (2007; red line). The difference between these two models is that Hopkins et al. (2007) employs a template SED and Marconi et al. (2004) does not. Hopkins et al. (2007) suggests that the intrinsic spread in AGN SEDs could give rise to a variation of a factor of ~ 2 in the bolometric correction, independent of the luminosity. We find a broadly similar spread to that of Vasudevan & Fabian (2007) although their sample does not contain a significant number of objects at $< 10^{43}$ erg s^{-1}.

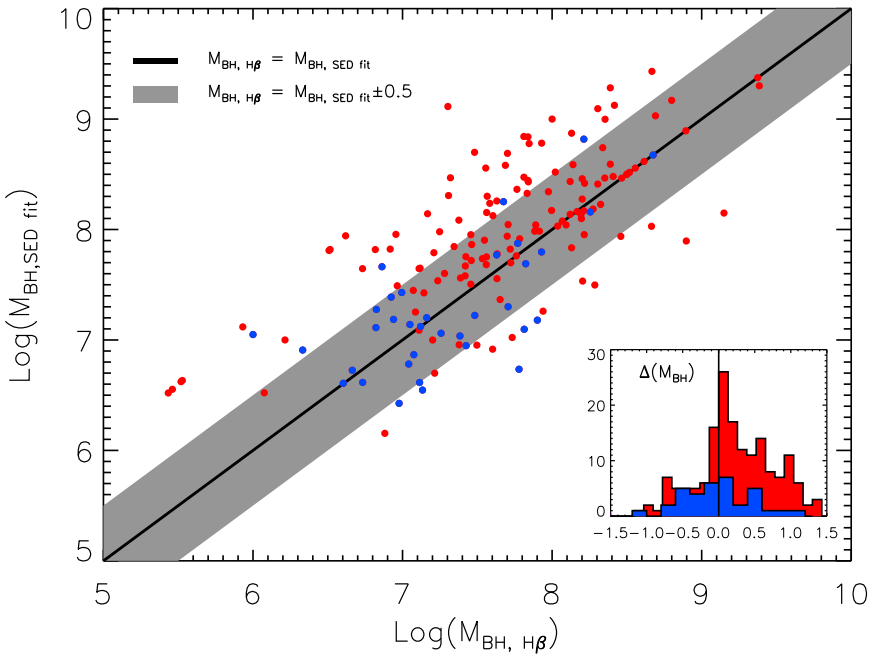

Figure 3.7: Correlation between the best fitting black hole mass from the Hβ FWHM ($M_{BH,H\beta}$) and from the SED fits ($M_{BH,SEDfit}$) . The blue points indicate the super-Eddington sample. The inset panel shows the distribution of ΔM_{BH} defined as $M_{BH,SEDfit}$ - $M_{BH,H\beta}$. The whole sample is shown in red and the super-Eddington sample is shown in blue.

The bottom plot of Figure 3.8 shows the objects binned by $L_{2-10keV}$ into groups of 14 with the top bin containing 9 objects, in order to produced the 7 bin spread of Vasudevan & Fabian (2007). The edges of the bins show the range in luminosity contained within that bin, and the $\kappa_{2-10keV}$ error is the standard deviation of each bin. As we do not have many objects with a luminosity $< 10^{42}$ erg s^{-1}, we compare our sample to that of Nemmen et al. (2011) shown in red. This study contains 21 low-luminosity AGN and we find that our results are in good agreement. From this study we find that there is no clear correlation between $\kappa_{2-10keV}$ and $L_{2-10keV}$, but that the values of $\kappa_{2-10keV}$ found from the SED fitting are in good agreement with that of other samples (Nemmen et al., 2011; Vasudevan et al., 2007).

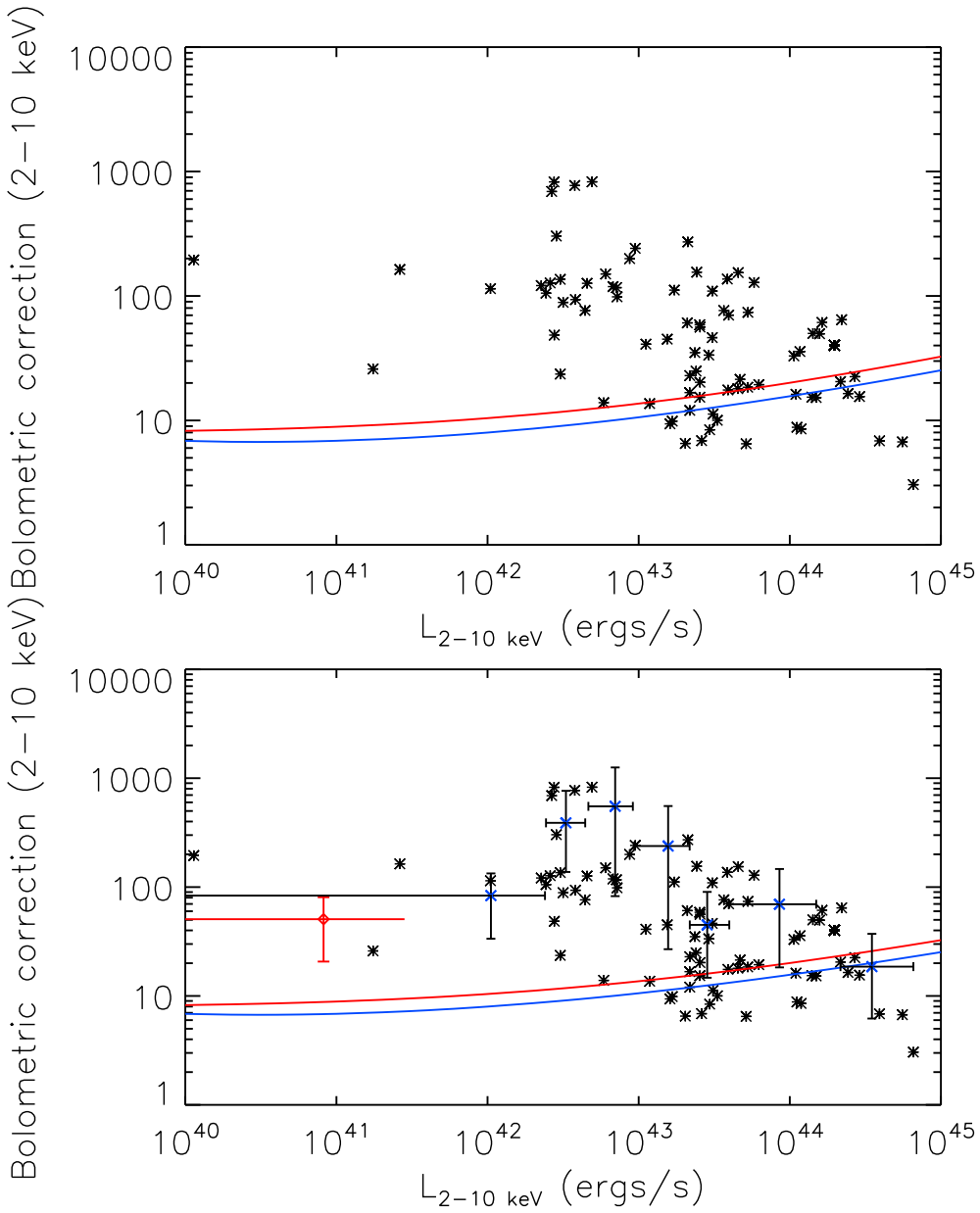

Figure 3.8: $\kappa_{2-10keV}$ against $L_{2-10keV}$, with theoretical predictions from Marconi et al. (2004) and Hopkins et al. (2007) shown in blue and red respectively. *Top:* The 93 objects in the well-defined sample. *Bottom:* The same 93 objects binned by $L_{2-10keV}$ in bins of 14 objects and 9 objects in the top bin. The average values of a sample of low-luminosity AGN from Nemmen et al. (2011) is shown in red to compare to the results of the low-luminosity end of our sample; we find that the two samples are in good agreement.

3.7.4.1 $\kappa_{2-10keV}$ as a function of Eddington ratio

We present the bolometric corrections for the well-fitted sample against Eddington ratio in the top panel of Figure 3.9. If we understand the Eddington ratio to be the luminosity scaled by the mass of the central black hole, then unlike the previous study of Vasudevan & Fabian (2007) we find no clear change in $\kappa_{2-10keV}$ as a function of λ_{Edd}. While the sample suggests a positive correlation in the top panel, the bottom panel of Figure 3.9 with the same binning as that used in the previous subsection suggests that most of this trend is consistent with the errors associated with the bins. Only between the highest and lowest two bins is there a trend that shows an increase of λ_{Edd} leading to an increase in $\kappa_{2-10keV}$. A comparison to the low-luminosity sample of Nemmen et al. (2011), shown in red, shows good agreement with our low λ_{Edd} bins. Previous studies have generally found a positive correlation between λ_{Edd} and $\kappa_{2-10keV}$ (e.g. Vasudevan & Fabian 2007; 2008) but with a very large scatter.

3.7.5 Trends in SED fitting

Elvis et al. (1994) constructed SED templates for both radio-loud and radio-quiet AGN from their sample of 47 quasars with a redshift distribution of 0.025 to 0.94. In Vasudevan & Fabian (2007), the study modelled the optical-to-X-ray SEDs of 54 AGN with a redshift distribution of 0.001 and 0.371 and found that the SED shape is related to the Eddington ratio; this result was reinforced by Vasudevan & Fabian (2008). Studies by Jin et al. (2012) and Lusso et al. (2010) have also investigated the shape of the SED against various parameters.

In Jin et al. (2011) average SEDs were created from subsets defined by their Hβ FWHM. Average SEDs were created for the 12 objects with the narrowest lines, the 12 objects with the broadest lines and 12 objects from the mid range of the sample. They produced 3 distinctly different SEDs. In order to test the robustness of the OPTXAGN model and our fitting parameters we decided to examine the average parameters of SEDs when grouped according to their shape. We defined three different shapes:

- *Category 1* - these objects have an SED with a large disc/soft excess component where there is no clear distinction between the two components. This category represents

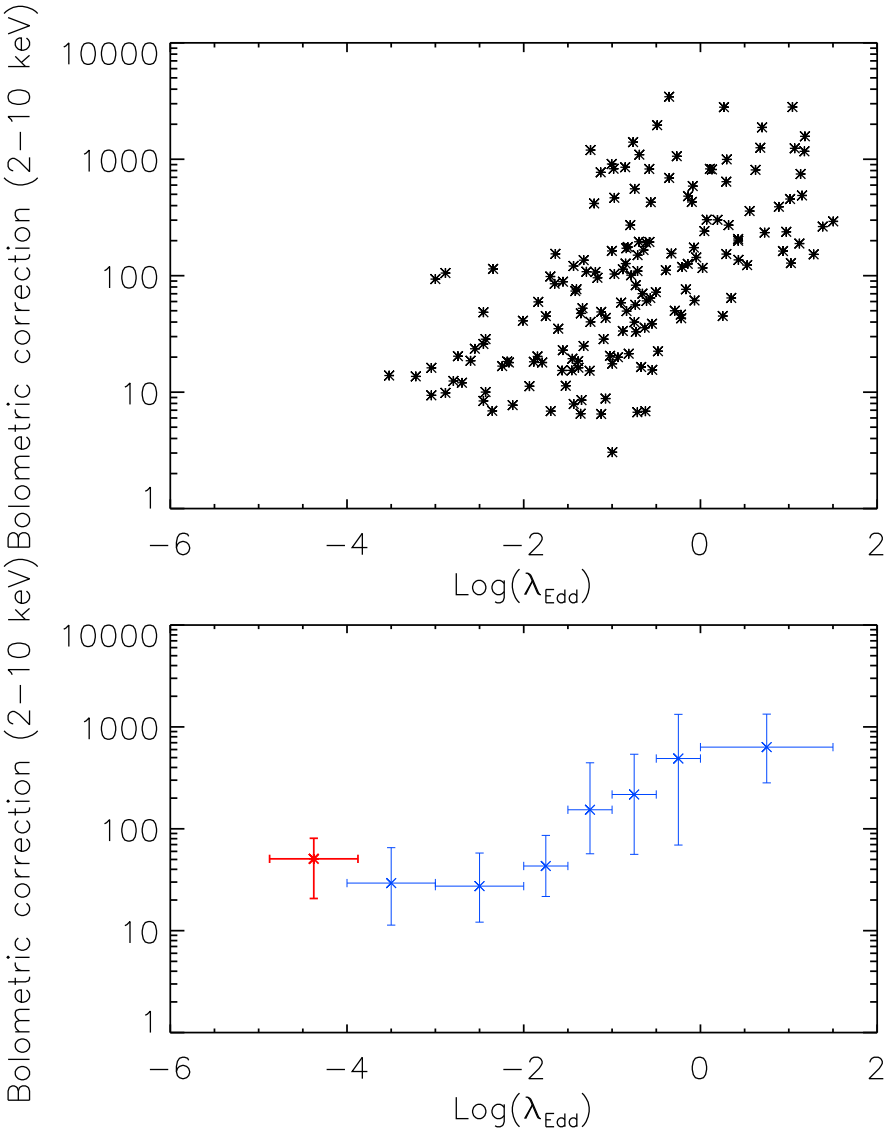

Figure 3.9: $\kappa_{2-10keV}$ against λ_{Edd}. *Top:* The sample of 93 well-fitted objects, showing a positive correlation but with a large scatter. *Bottom:* The same 93 objects binned by λ_{Edd} as in Figure 3.8. The sample from Nemmen et al. (2011) is shown in red and shows very good agreement with the low-λ_{Edd} end of our sample.

those objects with the same shape as those in the narrowest-linewidths sample of Jin et al. (2011).

- *Category 2* - these objects have an SED with the three components clearly visible, but with a distinct change between the disc and soft excess components. This category

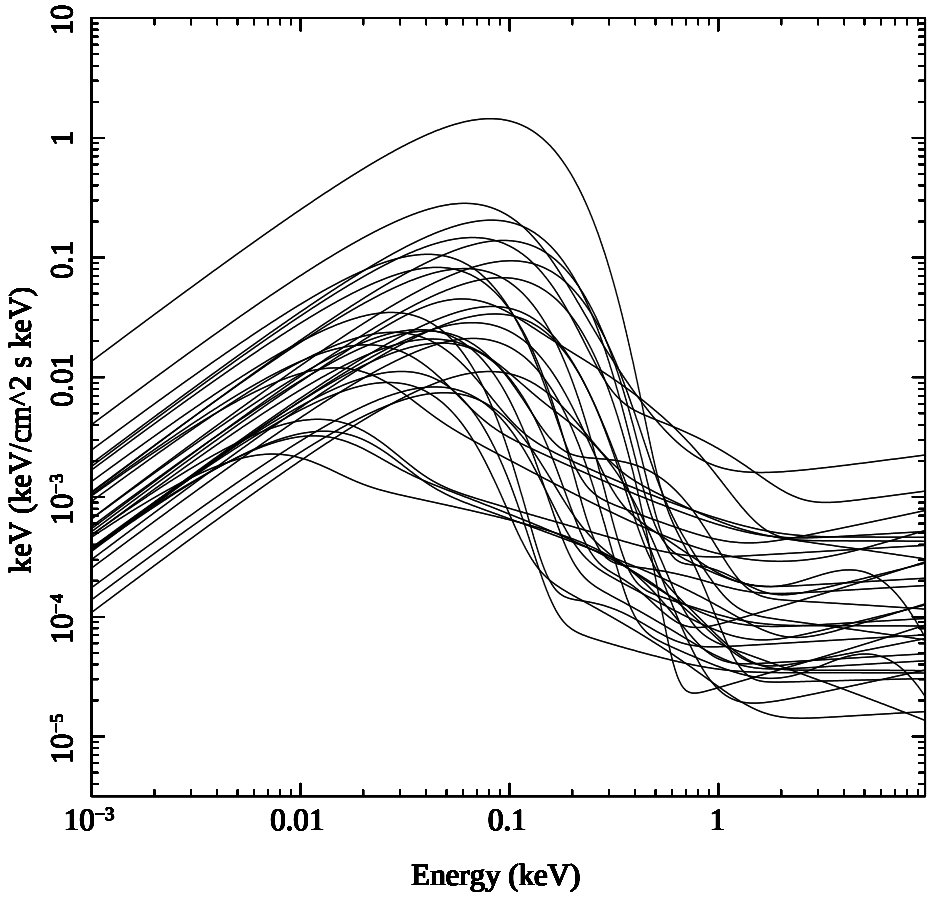

Figure 3.10: The 37 objects with SEDs defined to be Category 1.

represents those objects with the same shape as those in the mid-linewidths sample of Jin et al. (2011).

- *Category 3* - these objects have a similar luminosity in both the optical and X-ray regions, producing flat SEDs. This category represents those objects with the same shape as those in the broadest-linewidths sample of Jin et al. (2011).

The average parameters of these categories is shown in Table 3.1.

The SEDs of the 32 objects classed as Category 1 are shown in Figure 3.10. The overall shape produced by these SEDs is in excellent agreement with those produced by the NLSy1 sample in Jin et al. (2011). We find that the parameters produced by this sample are higher than those found by Jin et al. (2011), but they derived their parameters from a best fit model to the scaled SEDs of the individual objects, rather than the averages taken from the

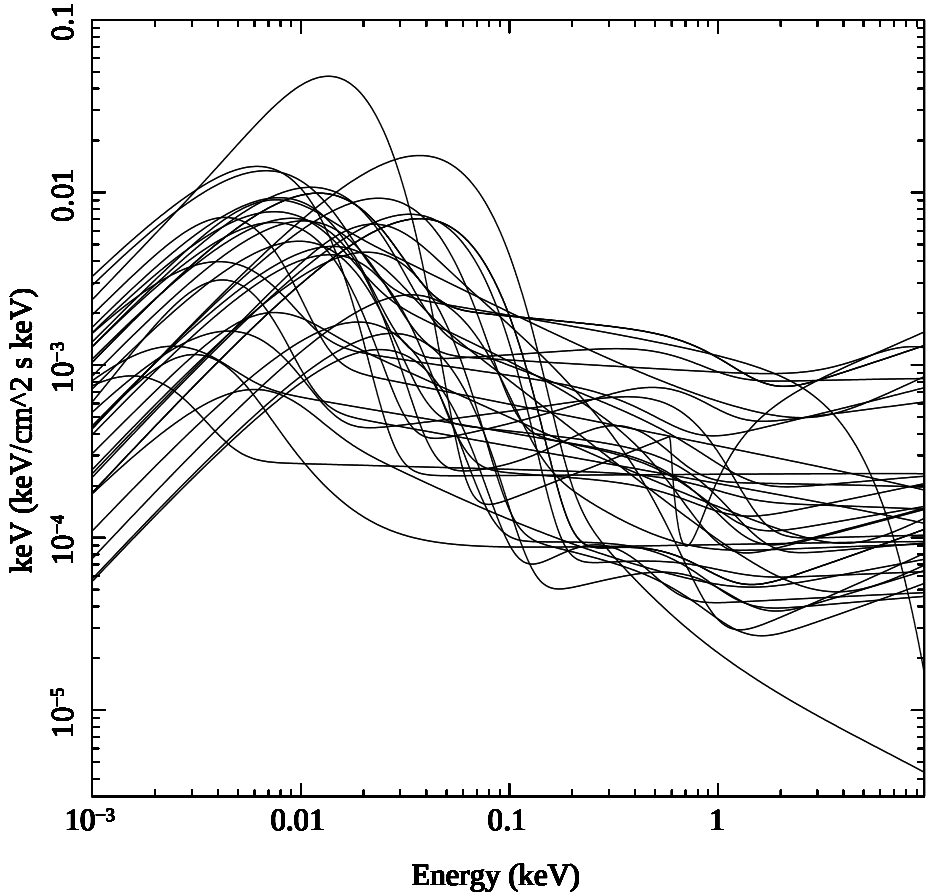

Figure 3.11: The SEDs of the 44 objects classified according to the shape outlined in Category 2 above.

individual SEDs. However, we do find that this shape does characterise the objects with the smallest black hole masses and highest λ_{Edd}. We also find that this category has the largest bolometric correction value out of the three subsamples.

The SEDs of the 44 objects sorted into Category 2 produce the poorest match to their Jin et al. (2011) counterparts. While the parameters do fit the general trend seen in Jin et al. (2011) the outline produced from our SEDs, shown in Figure 3.11, is not comparable to theirs. In particular the shape of the hard X-rays is very different as the objects in our subsample produce a much wider range of shapes.

The SEDs of the 17 objects sorted into Category 3 due to their flat SED shape are shown in Figure 3.12 and produce both similar parameters and a similar shape to that of the Jin

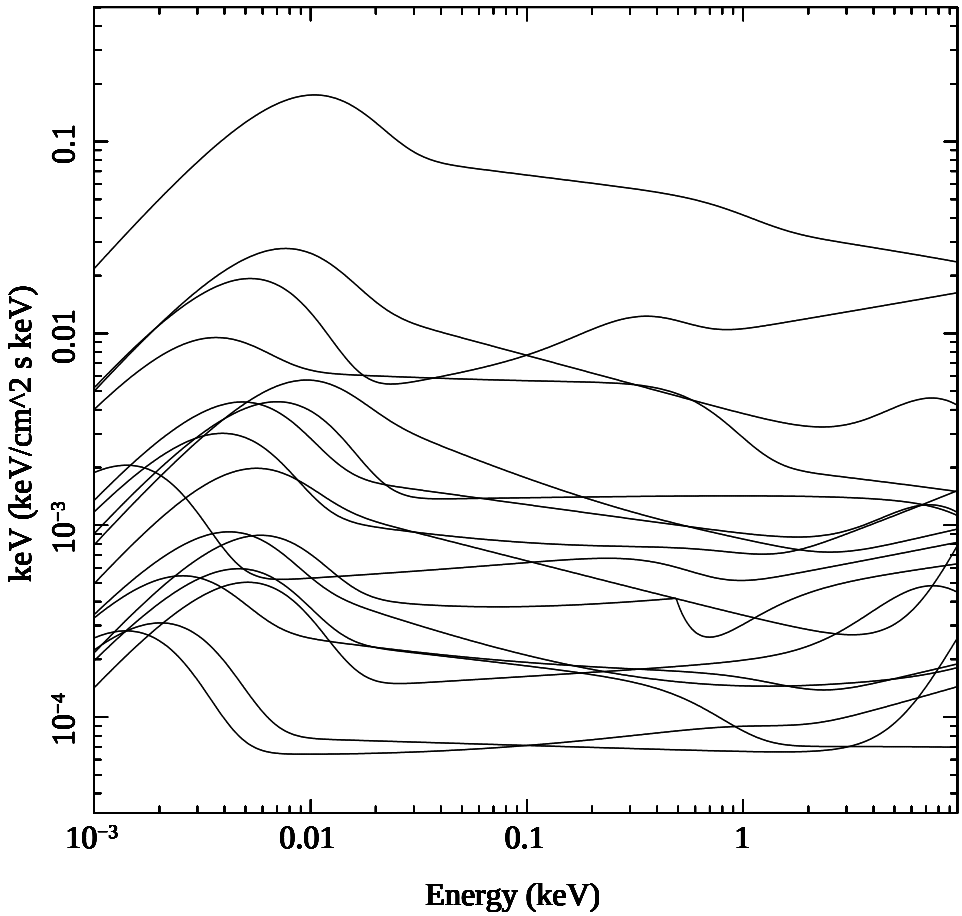

Figure 3.12: The SEDs of the 17 objects in Category 3 exhibit a very flat SED with comparable optical and X-ray luminosities.

et al. (2011) broad line subsample.

On the whole we find that by dividing up our sample by shape we recover similar SED properties to Jin et al. (2011) when they divided up their sample based on emission line FWHM. The biggest discrepancy arose in the middle band, as it covers a wide range of line widths and possible component parameters. This makes the resultant shape very dependent on the number and shape of the input SEDs. As we used far more objects than Jin et al. (2011) over a larger luminosity range it is understandable that our resultant product is more diverse; however, it does fit in the middle of the other two categories.

Like all previous studies into AGN SEDs we find that there is significant spectral diversity even when we attempt to divide up the sample by shape. If the SEDs are simply averaged

without taking into account their intrinsic properties the mean SED produced will contain very little information relevant to the actual properties of the AGN represented in the sample. Figure 3.13 shows how this can be the case. In this figure we show all 37 of the SEDs that had f_{pl} set to 1, with no flux in the X-ray soft excess component. It is clear that the outline produced bears little relation to any of the SEDs within it, and a mean SED produced from this would not be representative of the sample contained within it.

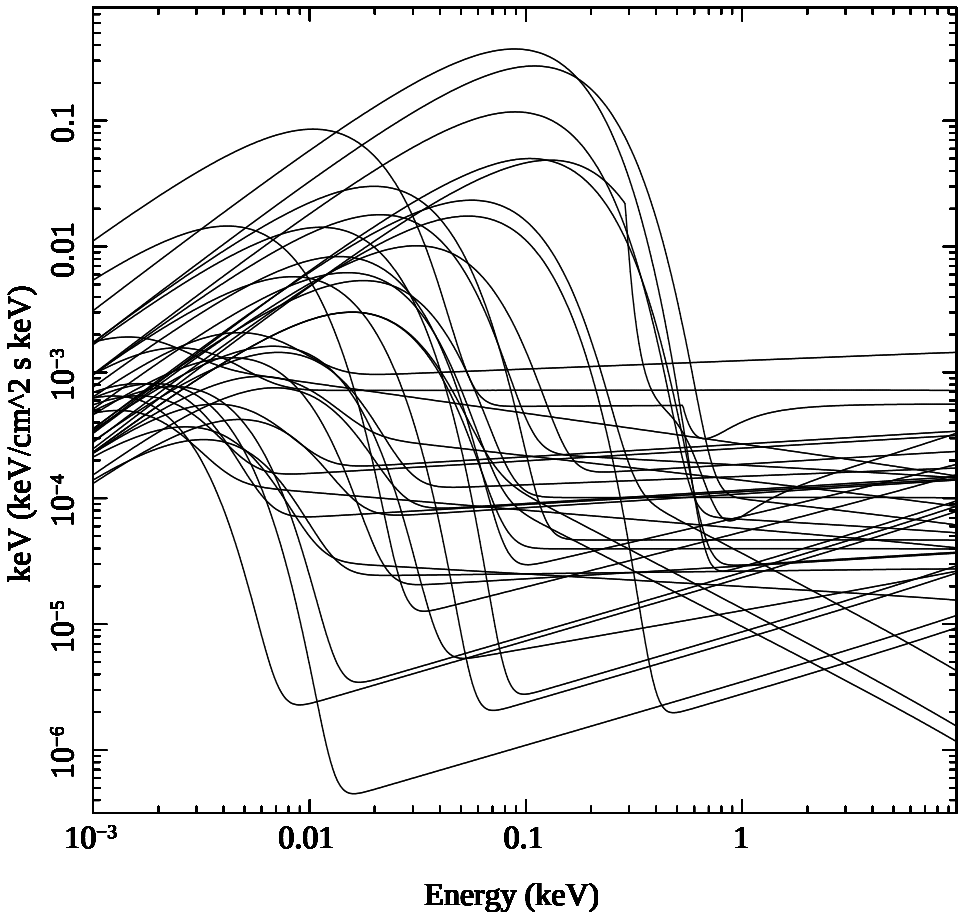

Figure 3.13: The SEDs of all 37 objects where $f_{pl} = 1$. This highlights the spectral diversity seen even when some basic parameters are the same.

We do find that spectral shape evolves with respect to Eddington ratio, with those in Category 1 having a much larger λ_{Edd} than those in Category 3. Previous studies link the shape of SEDs to those found for Galactic black hole binaries (BHBs). In this analogy, the low-λ_{Edd} AGN are likened to the low/hard state in BHBs, where there is a weak disc resulting in a strong high-energy tail, and the high λ_{Edd} AGN are analogous to the high/soft

state in which the accretion disc dominates. This result is unsurprising as the model used in this study is a scaled-up version of one based on BHB accretion, but the fact that it produces analogous results that match the expected parameters increases the relationship in the behaviour seen in BHBs and AGN: by understanding what is happening on the small scale we can understand what is happening on the large scale.

	No. of AGN	$< \lambda_{edd} >$	$< \log(M_{BH}) >$	$< \kappa_{2-10keV} >$	$< \Gamma_{int} >$	$< N_N >$
Category 1	32	4.211	7.53±0.21	512.3±43.6	1.92±0.08	0.147±0.014
Category 2	44	0.311	8.31±0.08	112.2±24.7	1.86±0.05	0.090±0.009
Category 3	17	0.0779	8.48±0.12	13.9±2.4	1.99±0.02	0.041±0.016

Table 3.1: Average SED parameters of the three subsamples

3.8 Conclusions

In this chapter we have presented a spectral study of 192 Type 1 AGN, with a range of obscuration and sub-classifications. We assembled data from the EPIC monitor onboard the *XMM-Newton* satellite and optical data from SDSS DR7. We also added optical/UV data from the *XMM-Newton* OM when it was available.

We use a detailed line fitting routine to measure the Hα and Hβ emission line profiles. The routine used multiple components representing the broad, intermediate and narrow emission to deblend the total line emission from the surrounding continuum and contaminating features through simultaneous fitting. We use the results from the Hβ profile fitting to constrain the black hole mass using the BLR size-luminosity relationship of Woo & Urry (2002). In order to determine a range for the black hole mass we use the FWHM of the broad and intermediate components to provide the upper and lower limits respectively. From this we found that NLSy1s by definition have lower black hole masses than their broader counterparts using this method, even if they have comparable optical luminosities.

The optical, UV and X-ray data points were combined into one SED and fitted using a new broadband SED model which is energetically self-consistent and places physical limitations on the unobservable UV region of the resultant fit. The model assumes that the

gravitational potential energy is emitted as optically thick blackbody emission as a function of radius down to a specific coronal radius. Between this radius and the last stable orbit, the remaining energy is divided up between a soft excess Comptonisation component and a hard X-ray tail.

We find that several problems arise from the fitting process, including the emergence of a flatter optical continuum than is expected from the standard accretion disc model. It is possible that some of this emission is due to the host galaxy. However, it is possible there may be an additional optical/IR component intrinsic to the nuclear AGN, which is not yet well understood or modelled for.

By breaking down the SEDs into their component parameters, we can draw some specific conclusions. We find that the contribution of each of the disc, soft excess and power law components to the bolometric luminosity varies dramatically from source to source, dependent on luminosity, Hβ linewidth and λ_{Edd}. We find that, on average, as L_{bol} and λ_{Edd} increase so does the contribution from the disc component. We also find a negative correlation between both Hβ linewidth and black hole mass with the contribution from the disc component. A larger study with higher quality X-ray data will help confirm this.

We also investigate the properties of super-Eddington objects with respect to the rest of the sample. We find that while the objects in this subsample have $L_{soft\,excess}$ and L_{pl} values similar to the parent population, they have larger than average L_{disc} values. They also have a smaller black hole mass, a higher mass accretion rate and smaller coronal radius than the overall sample. We also find that on average there is no discernible difference in the optical depth or electron temperature of the soft excess component in super- or sub-Eddington AGN.

We compare the black hole mass estimates from the Hβ line profiling and the best-fit result from the SED model. We find that the black hole masses derived from SED fitting are often higher than those obtained from the profile fitting. We find the opposite trend for super-Eddington objects, but the biggest discrepancy is found in the NLSy1s where we find that the SED fit produces a black hole mass over 5 times greater than that from the line profiling. This indicates that the black hole masses derived from the Hβ profile fitting alone may not be good proxies of the black hole mass of NLSy1s.

Finally we examine the SED produced and divide them into three subsamples based upon their shapes. We find that we can reproduce similar sample parameters to Jin et al. (2011), where they produced SED templates based on the FWHM of Hβ. While it must be stressed that there is substantial spectral diversity seen in these SEDs we can make analogous links to the spectral states observed in Galactic BHBs; this suggests that λ_{Edd} is a useful parameter for categorising the spectral state of AGN and that the energetic process taking place in AGN can be viewed as scaled up versions of the processes occurring in Galactic BHBs.

Chapter 4

Optical-to-X-ray SED modelling: Optical & X-ray variability studies

In this chapter we look in greater depth at a subset of 41 AGN from the sample created in Chapter 3. Here we look at the variability of these objects in both the optical and X-ray regions, combining data from the Catalina Sky Survey (CSS), SDSS and *XMM-Newton*. We calculate the excess variance of both the optical and X-ray light curves and relate them to several physical parameters. We also produce the RMS spectra of these objects to analyse the variability of the soft region of the X-ray spectrum and investigate the probability of it being a separate variable component.

We present the construction and data assembly of our sample in Section 4.4, our optical variability study in Section 4.5 and our X-ray variability study in Section 4.6. Our conclusions are given in Section 4.7.

4.1 Introduction

As discussed in Section 1.8 AGN are known to display flux variability in all wavebands and on timescales ranging from minutes to many years. Studies of this behaviour have been used to constrain the size and location of the emission regions and to infer the emission mechanisms as well as the processes that cause the variability.

As well as studying individual light curves, the average properties of statistical samples of AGN have been investigated in the optical/UV band (Vanden Berk et al., 2004) and in the X-rays through the analysis of fractional variability (Manners et al., 2002).

In general optical variability has been found to increase with decreasing luminosity and

black hole mass (Cristiani et al., 1996) and with increasing redshift (Giallongo et al., 1991). The latter relationship is expected because high redshift sources are observed at a higher rest-frame frequency, where the sources are more variable (di Clemente et al., 1996).

In the X-ray domain the variability occurs on much shorter timescales, and is thought to derive from the hot corona close to the central black hole. Previously most studies focused on the light curves of individual, low redshift Seyfert 1s (Uttley et al., 2003; Uttley & McHardy, 2005). As in the optical, low-luminosity AGN are more variable than those with high luminosities (Lawrence & Papadakis, 1993; Nandra et al., 1997; Vagnetti et al., 2011). Also the amplitude of variability is greater on long timescales than short ones (e.g. Markowitz & Edelson, 2004). Again, as in the optical, it has been suggested that variability increases with redshift (Paolillo et al., 2004).

The relationship between optical and X-ray variability has been interpreted in terms of is two main theories, which are outlined in Section 1.8.3. These two models predict opposite observable scenarios. One predicts the X-ray variability should lead the optical variability, while the other model predicts the optical should lead the X-ray variability. So far the results are inconclusive and display aspects predicted by both models.

4.2 Optical variability and transient searches

Since the discovery of AGN variability has been established as one of the main properties of the population, and is also one of the most carefully explored. Monitoring the optical variability can set physical constraints on many different aspects of the central region; the mass of the central black hole, the underlying structure and emission region sizes can all be deduced.

The light crossing time for a SMBH is very short, but the viscous timescale of the accretion disc constrains the typical optical variability to be of the order of years. While many previous studies of some single objects have been carried out for the past 100 years, well-sampled long timescale light curves are still comparatively rare. Static sky surveys have provided a great leap forward for this, as they cover large areas of sky on a regular basis. A further advance to the study of AGN variability is a by-product of supernovae searches.

Supernovae are very powerful cosmological probes and their systematic discovery outside the local Universe and to high redshifts has led to major scientific results (including the Noble Prize in Physics for 2011[1]). As such studies require well-sampled light curves and large statistical samples, this means monitoring large areas of sky to very faint limiting magnitudes, and the development of reliable quick-response data reduction pipelines. These surveys produce very large databases, which are suitable for many other scientific studies.

4.2.1 The Catalina Sky Survey

The Catalina Sky Survey (CSS) is a survey designed to detect near-Earth objects (NEOs) and potential planetary hazard asteroids (PHA), conducted by the University of Arizona.[2] CSS utilizes three wide-field telescopes:

- the 0.68 m Catalina Schmidt telescope based at Catalina Station, Arizona,
- the 0.5 m Uppsala Schmidt Telescope (also called the Siding Springs Survey; SSS, operated in collaboration with the Australian National University) at the Sliding Spring Observatory, NSW, Australia,
- the Mount Lemmon Survey (MLS), a 1.5 m telescope located on Mount Lemmon, Arizona.

Each telescope has a camera with a single, cooled, 4 k × 4 k back-illuminated, unfiltered CCD.

Between the three telescopes $\sim$ 2000 deg^2 of the sky can be covered per night up to a limiting magnitude of $V \sim 19 - 20$ mag. Each telescope operates for 23 nights per lunation (lunar month), meaning that the majority of the observable sky is covered between 1 and 4 times per lunation. The survey has been running in this format since 2004. Therefore, time baselines for objects in the survey now extend to $\sim$ 7 years, with up to $\sim$ 300 images per pointing over most of the surveyed area.

[1] http://www.nobelprize.org/nobel_prizes/physics/laureates/2011/

[2] http://www.lpl.arizona.edu/css/

Although all the survey is primarily to search the sky for NEOs and PHAs it is obviously imaging all background objects. The survey reduces and publishes the data for all of the objects covered by survey.

All the Catalina survey photometry used in the following study was measured using the SEXTRACTOR package with aperture-based photometry, which can be used for both point and extended sources. The resultant data is given as 'V band' magnitudes, where the unfiltered raw data is converted into Johnson 'V' band (5400 Å) photometry, and currently the reduced images cannot be downloaded in order to re-extract the data or check the image quality. The photometric uncertainties given in the data are determined via an empirical relationship between the source flux and the observed photometric scatter.

In crowded fields, where many sources are blended, aperture photometry is more inaccurate. This is a problem for our sample as the AGN are nearby and therefore blended with their visible host galaxy. The implications of this are discussed in Section 4.5. In order to mitigate this problem the CSS avoids dense fields near the Galactic plane, however other areas are still affected.

4.3 X-ray variability

As discussed in Section 1.8.2 AGN are known to exhibit large amplitude variability at X-ray energies on very short timescales. Unfortunately, as X-rays are difficult to observe and there are a limited number of satellites, large statistical studies of X-ray spectral variability are limited. As it is hard to create well-sampled light curves over a period of many years, as is possible in the optical domain, other techniques have been developed for the X-ray region. For this study we employ two slightly different methods for quantifying the statistically significant variability present in the X-ray light curves; the root mean square and normalised excess variance methods, which are outlined below.

4.3.1 Root Mean Square (RMS) spectra

The standard approach to investigating the energy dependence of X-ray spectral variability is to plot the fractional root mean square (RMS) variability amplitude, F_{var}, as a function

of energy. In this subsection we explain the basis for this analysis and what information it can provide.

Edelson et al. (2003) were amongst the first to use this technique, once X-ray satellites provided the back catalogue of data necessary for these studies. They define F_{var}, a measure of the intrinsic variability amplitude that includes the effects of measurement noise, to be:

$$F_{var} = \frac{1}{\langle X \rangle} \sqrt{S^2 - \langle \sigma_{err}^2 \rangle} \tag{4.1}$$

where S^2 is the total variance of the light curve, $\langle \sigma_{err}^2 \rangle$ is the mean error squared, and $\langle X \rangle$ is the mean count rate. The error on F_{var} is given by:

$$\sigma_{F_{var}} = \frac{1}{F_{var}} \sqrt{\frac{1}{2N}} \frac{S^2}{\langle X \rangle^2} \tag{4.2}$$

The derivation of this can be found in the Appendix of Edelson et al. (2003).

The method used to produce these spectra involves extracting a background-subtracted light curve in each energy band, then calculating the fractional RMS variability in each light curve and finally correcting the result for additional variance introduced by measurement errors. These techniques have been applied to data from all the major X-ray satellites: *RXTE* (3 - 20 keV), *ASCA* (0.7 - 10 keV; O'Neill et al., 2005) and *XMM-Newton* (0.3 - 12.5 keV; Ponti et al., 2012).

The resultant RMS spectrum for a given object is not necessarily unique, as it depends on the timescales over which the data sets are obtained. Different timescales probe different size scales. The *RXTE* has monitored multiple AGN on timescales between days and years (Markowitz et al., 2003), while both *ASCA* and *XMM-Newton* have covered timescales ranging from hundreds of seconds to days. As AGN variability is stochastic the RMS spectra can change in time. This was shown by Gallo et al. (2004), who demonstrated that dramatically different RMS spectra are produced depending on whether or not a strong flare is present in the light curve.

Therefore this method gives an indication of how much the flux varies about the mean, but it does not imply what timescales this occurs on, as one large deviation can give the same RMS value as many small ones.

4.3.2 Normalised excess variance

An alternate method used to quantify the amount of variability in the X-ray region is to calculate the normalised excess variance. The values calculated from this method are extremely similar to the RMS values above, but it has the advantage that it is better equipped to work over different time intervals. This method has been explored and developed by Nandra et al. (1997), Turner et al. (1999), Vaughan et al. (2003) and Ponti et al (2004, 2012). In order to utilise this method the light curve must already be binned and divided up into smaller time intervals. A popular practice is to use bin sizes of around 200 - 250 s and then to subdivide into 10, 20, 40 and 80 ks time intervals. The normalised excess variance for each light curve segment is given by the formula:

$$\sigma_{rms}^2 = \frac{1}{N\mu^2} \sum_{i=1}^{N} [(X_i - \mu)^2 - \sigma_i^2] \tag{4.3}$$

where N is the number of usable bins in the segment, μ is the unweighted arithmetic mean of the counting rates within the segment and X_i and σ_i are the counting rates and uncertainties, respectively, in each bin.

When more than one valid segment is available the normalised excess variance is determined by computing the unweighted mean of all the individual estimates following the method outlined by Ponti et al. (2012). This has the potential to reduce the large uncertainty which arises due to the stochastic nature of the excess variance.

4.3.2.1 Estimating the uncertainty on the normalised excess variance

The uncertainty on the normalised excess variance is comprised of two elements: the measurement uncertainties (e.g. Poisson noise) in the light curve, and the stochastic nature of the variability.

The measurement uncertainties were shown by Vaughan et al. (2003) and Ponti et al. (2004) to be approximated by the formula:

$$(\Delta\sigma_{rms}^2)_{meas} = \sqrt{\left(\sqrt{\frac{2}{N}}\frac{\langle\sigma_i^2\rangle}{\mu^2}\right)^2 + \left(\sqrt{\frac{\langle\sigma_i^2\rangle}{N}}\frac{2F_{var}}{\mu}\right)^2} \tag{4.4}$$

where $\langle\sigma_i^2\rangle$ is the mean of the uncertainties squared, and F_{var} is the fractional variability given in the section above.

The uncertainty due to the stochastic nature of the variability is much more difficult to estimate, and the method used to calculate it is dependent on the number of valid time segments available in the light curve. If there are less than 10 segments, then the 'red noise' scatter can be estimated using the method of Ponti et al. (2012; see Appendix A), which takes the results of Vaughan et al. (2003) and assumes a power density spectrum for each source. The power density spectra for AGN have been shown to have an almost ubiquitous shape, characterised by a steep power law above a characteristic break frequency, ν_{br}, and a flatter slope below it (Uttley & McHardy, 2005). This break frequency ν_{br} has been shown to scale with black hole mass and accretion rate (McHardy et al., 2006), and therefore we would expect to see different slopes for the power density spectra within the frequency range probed by the light curve based on the object's M_{BH} and mass accretion rate. Knowledge of the object's M_{BH} and mass accretion rate allows its ν_{br} to be calculated. By combining this with data from Table 1 of Vaughan et al. (2003) estimates of both the positive and negative error for the 'red noise' scatter can be made.

If there is more than one segment in the light curve, the final uncertainty on the 'red noise' scatter is equal to the square root of the sum of the squared 'error' of the individual segments, divided by the number of intervals (O'Neill et al., 2005). The final error on the normalised excess variance is equal to the stochastic scatter and the measurement uncertainties combined in quadrature.

4.3.3 Variable components: Origins of the X-ray Soft Excess

There is much debate on the physical origins of the soft X-ray excess. There is a strong argument that it derives from a combination of a variable continuum component and an absorption feature present at less than 1 keV. This argument comes from the fact that the soft excess is seen in many high mass accretion rate AGN, but always at the same characteristic energy despite significant differences in inferred temperature of the underlying accretion disc (Gierliński & Done, 2006). This constant energy suggests it is more likely to be associated with atomic processes, but with a continuing debate as to whether the soft

excess arises from extreme relativistic smearing of a reflection dominated spectrum (Crummy et al., 2006), extreme smearing of absorption in a relativistic wind, or absorption by clumpy material which only partially covers the source. X-ray spectral analysis alone cannot easily distinguish between these very different models (Middleton et al., 2007), but they can be defined on the basis of their patterns of variability.

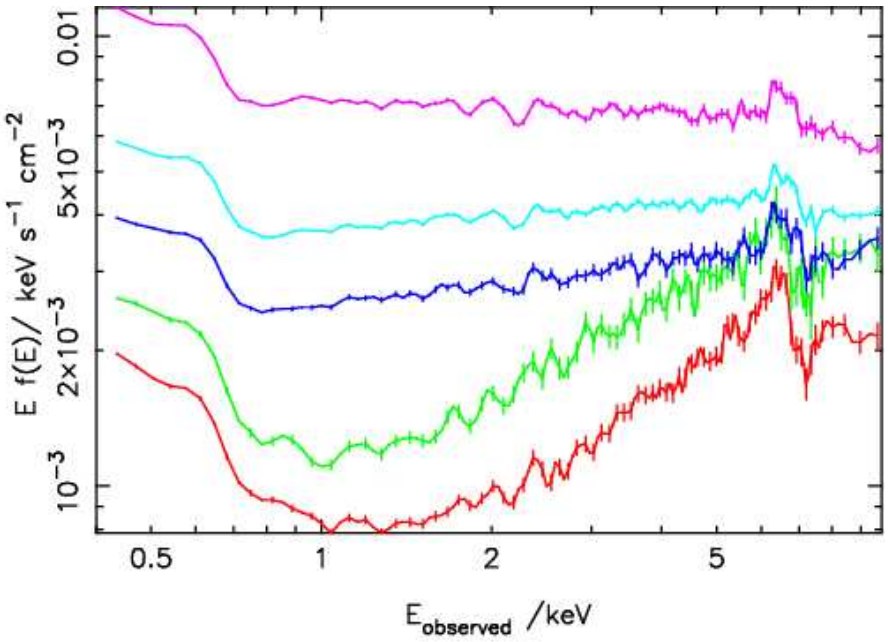

Figure 4.1: The different 0.4 - 10 keV flux states of Mrk 766. The data is averaged into five flux states. The variability seen here can be described by the domination of a variable component by a soft power law component of a constant power law index. This figure is reproduced from the top right panel of Figure 5 in Miller et al. (2007)

Figure 4.1, reproduced from Miller et al. (2007), shows the variation in the 0.4 - 10 keV X-ray flux from Mrk 766. It can clearly be seen that there is an absorption feature at less than 1 keV that dramatically changes the shape of the spectrum. The way in which this spectrum can be modelled changes from the top data set, where it is best fit with a hard power law and a slight soft excess, to the bottom data set, where it can be fit with either a very absorbed hard power law with a foreground soft excess feature, a soft power law and a strong soft excess, or a hard power law plus a strong absorption feature at $\sim$ 1 keV.

Only by making repeated observations over a long period would it be possible to define the correct model. Miller et al. (2007) draw the conclusions that there is a variable component in

the middle energy region, but it is dominated by a soft power law component with a constant power law index. However, the physical interpretation of this phenomenon is unclear.

In the case of RE J1034+396, which is included in this sample, the energy dependent excess variance (RMS spectrum: Edelson et al., 2002) shows an increase from soft through to hard energies, which was best fitted by a stable low-temperature, optically thick Compton component diluting a variable power law extending up to high energies (Middleton et al. 2009). This in turn suggests that the origin of the soft excess for *this* source is a separate continuum component. This is highly unlikely to be the source of the soft excess for other objects except perhaps for the most extreme NLS1s such as RX J0136.9-3510 (Jin et al. 2009), which also has the same RMS spectral shape, as very few objects have been shown to have a soft X-ray excess feature as strong as that seen in RE J1034+396.

4.4 Sample selection and data assembly

This study extends the work described in Chapter 3; the parent sample for this investigation consisted of the 192 objects defined as part of that previous study. The aim of that study was to test the robustness of the model used for the SED fitting, but many of the objects in that sample had very poor X-ray data, often with only a few hundred counts.

In order to perform an RMS spectral analysis on objects from that sample some initial X-ray data quality cuts needed to be made. We required more than 2,000 counts from all EPIC cameras over a continuous 2 ks observation with no signs of flaring. This resulted in the subsample of 41 objects shown in Table 4.1.

The data quality range was still quite large. The object with both the lowest number of counts and the shortest exposure is J020615.9-001730, with 2,056 counts over a 2 ks exposure. J124210.6+331703 has the largest number of counts with 604,165 over 78 ks. The longest observation is of J123054.1+110011 at almost 93 ks. One object from the sample is radio-loud (J150854.0-001148), with a further seven having radio detections but not enough flux to count as radio-loud. The radio-loudness parameter, $\mathcal{R}$, of AGN (Kellermann el al., 1989) is the ratio of the monochromatic radio luminosity to the monochromatic optical luminosity,

Table 4.1: The 41 objects in our sample.

2XMMi Catalogue IAU name	*XMM-Newton* Observation date	SDSS Observation date	z	FWHM$_{H\beta}$ (km s^{-1})	EPIC Counts	Exposure TIme (s)
J004319.7+005115	2002-01-05	2000-09-07	0.308	11022.989	19 126	20528
J020615.9-001730	2005-01-15	2000-09-25	0.042	4697.3999	2 056	2040
J030639.5+000343	2003-02-12	2001-12-15	0.107	3306.2959	35 651	52923
J083454.8+553422	2003-10-09	2005-01-16	0.241	612.33	7 248	9668
J092246.9+512037	2005-10-08	2001-12-04	0.159	538.04834	32 731	21725
J093922.9+370942	2006-11-01	2003-12-23	0.185	5929.0635	5 422	6619
J094057.1+032401	2005-10-30	2001-12-23	0.060	2211.0896	8 684	26565
J095048.3+392650	2001-11-04	2003-05-06	0.205	4897.2192	58 555	21357
J102147.8+131227	2003-05-05	2004-02-27	0.085	9978.3193	13 840	21090
J103059.0+310255	2000-12-07	2005-03-11	0.178	6009.292	69 434	26281
J103438.6+393828	2002-05-01	2003-12-29	0.043	2638.592	63 891	13083
J105143.8+335927	2002-05-13	2005-03-02	0.167	3945.051	47 858	31189
J111706.4+441333	2002-05-14	2004-02-27	0.143	5546.3081	48 524	42465
J112328.0+052823	2001-12-16	2002-04-12	0.101	2552.8386	10 098	30907
J115851.0+435048	2005-11-13	2004-03-25	0.287	4311.1069	6 679	63081
J120442.1+275412	2002-05-30	2006-03-25	0.165	5668.2856	66 550	17052
J123054.1+110011	2005-12-17	2003-04-02	0.235	5216.7061	165 823	92991
J124210.6+331703	2005-06-21	2005-03-02	0.043	3189.646	604 165	78021
J124319.9+025254	2001-01-05	2002-02-21	0.086	1789.525	5 902	60172
J124635.3+022209	2001-06-17	2001-04-25	0.048	3212.2771	8 509	2423
J125553.0+272405	2000-06-21	2006-03-29	0.315	5745.5288	7 591	18880
J130022.1+282402	2004-06-19	2005-05-09	0.091	3420.8311	209 458	77508
J131046.7+271645	2002-12-12	2006-02-28	0.301	7224.3184	8 416	43524
J131217.7+351521	2002-06-10	2006-03-05	0.182	5662.2109	20 778	27221
J132447.6+032431	2004-01-25	2002-03-09	0.305	4547.9609	6 305	17754
J134113.9-005314	2005-06-28	2000-05-07	0.237	3607.6572	18 007	14530
J134834.9+263109	2000-06-26	2006-04-23	0.058	2239.5725	71 985	44186
J135553.4+383428	2002-12-10	2005-03-31	0.050	5703.1616	13 974	7664
J140127.6+025606	2000-06-28	2001-04-29	0.264	3551.5945	7 525	32697
J141531.4+113156	2002-08-03	2006-04-23	0.256	5133.6743	5 349	29366
J141700.7+445606	2002-12-08	2003-03-30	0.113	5430.2695	55 786	24131
J141759.5+250812	2001-07-10	2006-05-04	0.016	6540.3081	493 650	73051
J142455.5+421408	2003-12-18	2003-07-05	0.316	4429.1196	5 313	7615
J142943.0+474726	2002-05-31	2005-04-02	0.220	3782.7085	70 995	37131
J143452.4+483943	2003-01-08	2003-04-04	0.036	4927.2129	18 885	7124
J144414.6+063306	2005-02-11	2005-05-04	0.208	4553.2212	37 568	16868
J150854.0-001148	2005-07-20	2001-03-22	0.054	9965.458	19 470	4958
J151600.9+000949	2004-07-23	2000-05-25	0.171	4781.7188	6 196	27958
J155829.4+271715	2002-09-10	2003-06-27	0.090	3919.6804	6 995	7899
J155909.6+350147	2003-01-16	2004-05-16	0.031	4051.6887	124 115	18338
J223607.6+134355	2003-05-28	2002-09-03	0.325	6436.8745	7 853	9027

where:

$$\mathcal{R} \equiv \frac{\nu_{radio} L_{radio}}{\nu_{opt} L_{opt}} \tag{4.5}$$

Historically, objects are considered to be radio-loud if $\mathcal{R} > 10$ and radio-quiet if $\mathcal{R} < 10$. This explains why seven objects have radio fluxes, but only one is classed as radio-loud.

As in the previous chapter we have a broad range of data quality from objects with a few thousand counts taken over a 1 ks exposure, to those with many thousands of counts taken over nearly 100 ks. This is sufficient to allow us to explore the variability of a selection of AGN that cover a large range in luminosity, black hole mass and SED characteristics.

Histograms showing the distribution of the M_{BH} and λ_{Edd} of the sample are shown in Figure 4.2. These distributions highlight the bias of our sample. As we are imposing both a time interval and count rate constraint on our sample, we are predisposed to select the brighter objects from the *XMM-Newton* Serendipitous Survey and targeted AGN. For a given luminosity an AGN can have a small mass but accrete at a significant fraction of the Eddington limit or above, or it can be a high mass black hole accreting at a low Eddington ratio. We find both types of objects in the sample, and due to the selection criteria our sample has a strong trend of increasing λ_{Edd} with decreasing M_{BH} as shown in the right panel of Figure 4.2.

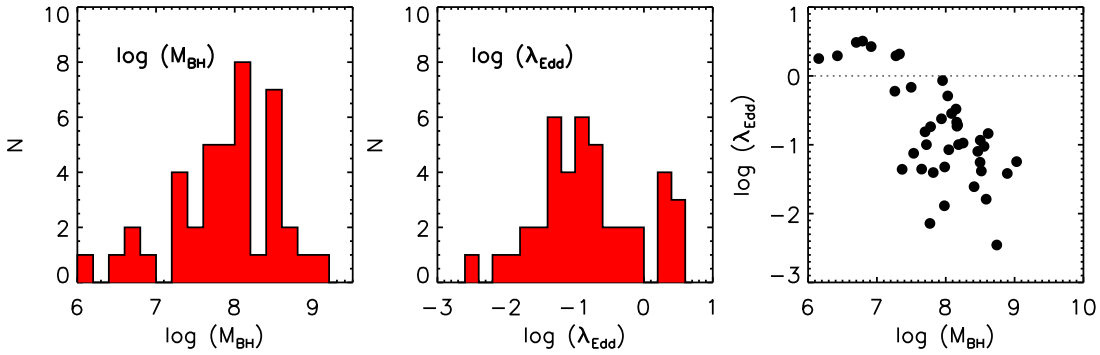

Figure 4.2: The distributions of $\log(M_{BH})$ (*left panel*), $\log(\lambda_{Edd})$ (*middle panel*) and $\log(M_{BH})$ against $\log(\lambda_{Edd})$ (*right panel*) of the 41 objects in the sample. The sample is composed of low mass, high Eddington ratio and high mass, middle/low Eddington ratio objects. The dotted line indicates $\lambda_{Edd} = 1$ and all objects above this line are classed as super-Eddington. It can be seen that all of the objects with a mass below 10^7 $M_\odot$ are classed as super-Eddington from the SED fitting of Chapter 3.

Table 4.2 shows the SED fitting parameters for the 41 objects in our sample. The objects are also shown as part of the larger sample in Appendix A, but are reproduced here for clarity. From these results it can be seen that three objects have no soft excess component but all are bright in the 2 - 10 keV range. The rest of the sample exhibit a large range of properties with no objects displaying a significant amount of reddening or extreme parameter values. A few objects to have R_{cor} values at the upper limit, where the corona is reprocessing as much of the disc emission as is possible, but the SED shapes produced are still considered to be good fits.

4.4.1 Optical light curve assembly

In order to examine the optical variability we used the Catalina Sky Surveys online records, which have observations that extend back over 7 years for 37 objects from our sample. The four remaining objects not covered by any of the CSS telescopes are J083454.8+553422, J092246.9+512037, J115851.0 +435048 and J142943.0+474726. As there are no other surveys that cover these objects over a similar time period as frequently as CSS, we omitted these 4 objects from our optical variability analysis, but they are still included in the sample for the X-ray variability study.

The optical light curves were downloaded from the Catalina Sky Surveys online database.[3] The initial search cone radius used was the default value of 0.1", which was extended up to the maximum of 3" if no object was found. Only in one case did extending the search radius reveal a previously unmatched object, and this was found to be within 0.5" of the SDSS co-ordinates and had no neighbours listed to be that close in SDSS.

One of the options in the Catalina online database is to search for a periodicity in the light curve data. While this option is mainly used for studying cataclysmic variables (CVs), it can also search over baselines of many years. Each light curve was searched with multiple periodicity fits, but none yielded a significant periodicity.

[3] http://nesssi.cacr.caltech.edu/cgi-bin/getcssconedb_release.cgi

4.4.2 Creating X-ray RMS spectra

For this sample we used data from *XMM-Newton* covering the energy range 0.3 - 12.5 keV. Data for each of the 41 objects in the sample were reduced in the same way.

The energy range 0.3 - 12.5 keV was split into three narrower bands: 0.3 - 1.5 keV, 1.5 - 3 keV and 3 - 12.5 keV. This was done in order to probe the three main energy ranges in which we would expect to encounter variability. The softest band is sensitive to fractional variation at low energies, i.e. the region that is associated with the soft excess. The hard band is sensitive to variability of the power law that is at high energies and the medium band samples the transition range between the two. By dividing up the complete energy range into three smaller bands we aim to study the energy dependence of the RMS spectrum, and search for evidence of different processes operating in each band. If this is the case we would expect to see a change in the slope across the RMS spectrum, but if the components are not distinct we would expect to see a continuous trend in the spectrum.

First the light curve data were downloaded from the *XMM-Newton Science Archive* (XSA) website[4]. During this process the 0.3 - 12.5 keV energy range was divided down into the three bands described above, so each object had data in each of the sub-bands. The data downloaded included the light curve of both the source and the background defined around the source.

In order to create a background-subtracted source spectrum the FTOOLS package LCMATH was used. This program extracts two binned light curves and, providing they cover the same time interval, calculates a resultant light curve by subtracting one from the other.

The utility LCURVE was used to produce the light curves. This uses the plot outputs to identify the best time interval in which to search for variability. The output of this utility is a FITS file containing the light curves, plots and analysis outputs.

Using the results from the LCURVE utility we calculated the RMS values for each object. The first part of this step is to bin the light curve according to pre-determined bin sizes. As mentioned in Section 4.3.1 above, different RMS spectra will result depending on both the timescale chosen and the time interval studied. In order to carry out a statistical study on our sample we used bin sizes that gave the best chance of constraining an RMS value even

[4]http://xmm.esac.esa.int/xsa/#tools

for the low-count objects. We chose two bin sizes of 100 s and 200 s.

A similar problem arises when deciding the time interval over which to search for variability. For most of the objects in the sample this was not a problem, as the total exposure time available was shorter than any of the intervals expected to make a significant difference to the RMS value (Middleton et al., 2009). Initially we only used the time interval defined by the usable exposure time.

In order to calculate the RMS values and errors we used the equations defined in Section 4.3.1. From this we often found that variability could not be constrained in either of the two timing bins selected. In order to estimate upper limits for these objects the utility LCSTATS was used. LCSTATS calculates statistical variables for a single input time series. The upper limits provided by this method are the 3-σ upper limits, which are calculated assuming the variance is not larger than the expected variance at a confidence level higher than 99.86%. This utility can also give the RMS value of a time series, and it was used to test the method based on the equations above.

As many of the longer exposures had unconstrained RMS values for their light curves we searched over different time intervals for all objects with an exposure time greater than 20 ks. For these 24 objects we used 20 ks and 10 ks intervals, and if neither interval produced constrained values we also searched other intervals that were determined from their light curves.

4.5 Optical variability study

The major difficulty in quantifying the variability of the CSS light curves arises from the data quality. The average uncertainties lie in the region of 0.05 - 0.1 magnitudes and in a few objects approach 0.2 magnitudes. This means that while apparent trends may be visible, they are not statistically significant. In order to quantify the level of variability we took several different approaches.

The first step was to check the CSS observations against archival SDSS photometric data. The 'V' band used by CSS lies between the SDSS g and r bands. During this check we found that the SDSS r band was the most similar to the CSS data, particularly the SDSS r model

Table 4.2: The broadband SED fitting parameters. The resultant fitting parameters from the SED model OPTXAGN for the 41 objects in this study. A description of each parameter and how they were calculated can be found at the beginning of Appendix 1.

2XMMi Catalogue IAU name	N_H $\times 10^{-22}$ cm^{-2}	log(M$_{BH}$) M$_\odot$	log($\dot{\mathrm{M}}$) g s^{-1}	R_{corona} r_g	τ	kT_e keV	Γ_{int}	f_{pl}	L$_{bol}$ erg cm^{-2}s^{-1}	λ_{Edd}	$\kappa_{2-10keV}$
J004319.7+005115	0.0404	8.15	26.313	25.83	19.34	0.138	1.90	0.51	6.05E+45	0.330	22
J020615.9-001730	0.0471	7.98	25.122	37.91	100.00	0.207	2.31	0.94	5.97E+44	0.048	25
J030639.5+000343	0.1332	7.78	25.558	30.85	7.56	0.650	1.53	0.30	1.43E+45	0.183	56
J083454.8+553422	0.1186	6.70	25.976	97.84	10.00	0.200	2.00	1.00	2.40E+45	3.068	8
J092246.9+512037	0.0598	7.33	26.175	11.04	28.97	0.141	2.10	0.18	5.75E+45	2.080	272
J093922.9+370942	0.0175	8.41	25.400	35.03	25.00	0.200	1.97	0.30	8.26E+44	0.025	35
J094057.1+032401	0.0491	7.82	24.882	14.98	16.42	0.214	1.90	0.31	3.38E+44	0.040	76
J095048.3+392650	0.0174	8.50	26.153	20.04	26.24	0.178	1.97	0.81	4.79E+45	0.116	20
J102147.8+131227	0.1400	8.74	25.050	100.00	28.80	0.120	1.79	0.77	2.48E+44	0.004	8
J103059.0+310255	0.0321	8.49	25.832	45.39	42.57	0.261	2.16	0.92	2.28E+45	0.056	15
J103438.6+393828	0.0131	6.42	25.141	46.78	14.64	0.196	2.00	0.05	6.80E+44	1.960	153
J105143.8+335927	0.0443	8.16	26.042	100.00	9.07	0.601	1.50	0.33	3.52E+45	0.186	33
J111706.4+441333	0.0271	8.03	26.284	50.35	7.92	0.032	1.53	0.26	7.11E+45	0.512	50
J112328.0+052823	0.0370	7.65	24.853	100.00	8.13	0.770	1.50	0.24	2.57E+44	0.044	47
J115851.0+435048	0.0127	7.26	25.669	12.76	23.00	0.250	1.66	0.80	1.42E+45	0.600	46
J120442.1+275412	0.0177	8.19	25.740	39.44	4.33	0.259	2.83	0.91	2.00E+45	0.101	3
J123054.1+110011	0.0234	8.56	26.148	17.79	34.08	0.181	1.85	0.84	4.44E+45	0.095	21
J124210.6+331703	0.0227	8.08	25.987	42.79	21.88	0.206	2.18	0.86	4.50E+45	0.285	16
J124319.9+025254	0.0192	7.28	26.044	7.49	20.00	0.200	1.90	0.73	4.81E+45	1.959	642
J124635.3+022209	0.0400	6.79	25.746	9.98	13.07	0.326	1.79	0.33	2.62E+45	3.252	214
J125553.0+272405	0.0098	8.52	25.855	58.84	5.71	0.645	1.70	0.47	1.78E+45	0.042	16
J130022.1+282402	0.0140	7.72	25.233	65.89	11.25	0.435	1.76	0.42	6.84E+44	0.100	18
J131046.7+271645	0.0437	7.94	25.987	100.00	15.00	0.250	1.85	0.90	2.68E+45	0.238	7
J131217.7+351521	0.0104	8.89	26.069	19.67	10.53	0.026	1.99	0.24	3.90E+45	0.038	74
J132447.6+032431	0.0525	8.47	26.071	100.00	0.10	0.010	2.22	0.53	3.05E+45	0.080	29
J134113.9-005314	0.0276	8.17	26.093	100.00	10.00	0.200	1.93	1.00	3.74E+45	0.193	7
J134834.9+263109	0.0350	6.15	24.802	14.90	13.79	0.203	2.23	0.54	3.32E+44	1.787	45
J135553.4+383428	0.0600	7.77	24.672	100.00	18.49	0.223	1.59	0.78	5.48E+43	0.007	1

2XMMi Catalogue IAU name	N_H ($\times 10^{-22}$ cm^{-2})	log(M_{BH}) ($M_\odot$)	log($\dot{M}$) (g s^{-1})	R_{corona} (r_g)	τ	kT_e (keV)	Γ_{int}	f_{pl}	L_{bol} (erg cm^{-2}s^{-1})	λ_{Edd}	$\kappa_{2-10keV}$
J140127.6+025606	0.4390	8.25	25.929	99.76	2.92	0.136	2.89	0.85	2.46E+45	0.106	47
J141531.4+113156	0.1000	8.59	25.541	100.00	10.00	0.200	1.98	0.43	8.14E+44	0.016	18
J141700.7+445606	0.0162	7.50	25.827	14.47	10.12	0.381	2.00	0.32	2.80E+45	0.684	76
J141759.5+250812	0.0251	7.37	24.496	100.00	99.95	0.085	1.81	0.96	1.33E+44	0.044	7
J142455.5+421408	0.0099	8.62	26.440	12.04	100.00	0.110	2.02	0.85	7.82E+45	0.146	50
J142943.0+474726	0.0491	7.95	26.463	17.78	10.70	0.359	1.90	0.28	1.00E+46	0.857	61
J143452.4+483943	0.1555	6.91	25.770	16.78	0.70	0.191	1.78	0.09	2.86E+45	2.669	27
J144414.6+063306	0.0287	8.16	26.063	23.80	60.17	0.686	2.07	0.93	3.99E+45	0.213	16
J150854.0-001148	0.0500	7.53	24.980	100.00	10.00	0.200	1.66	1.00	3.34E+44	0.075	6
J151600.9+000949	0.2369	8.04	25.535	45.52	36.96	0.090	1.79	0.19	1.22E+45	0.085	43
J155829.4+271715	0.0500	7.69	25.400	30.04	18.00	0.250	1.63	0.60	1.00E+45	0.154	21
J155909.6+350147	0.0211	7.98	24.622	100.00	26.17	0.160	2.13	0.62	1.61E+44	0.013	18
J223607.6+134355	0.0451	9.03	26.498	43.74	0.10	0.010	2.24	0.51	7.91E+45	0.057	40

magnitude. The SDSS model magnitudes are derived from a model fit to the image of the object. The model can fit both point sources and extended sources.

No attempt was made to correct the CSS data into a appropriate SDSS waveband range, as the SDSS data was only used to give an indication of a previous magnitude. Due to the size of the uncertainties on the data any correction would not have been justified.

For the majority of objects we found that the SDSS data was in good agreement with the CSS data. However, for a few objects including ones where the SDSS observation was taken during the CSS run, the SDSS magnitude is significantly fainter than the CSS magnitude. This may indicate that in these objects the CSS measured flux includes some contribution from the host galaxy as well as the AGN.

In order to quantify the variability we initially simply aimed to identify the largest rise and fall visible. However this only resulted in our ability to detect large changes and not the objects with smaller, continuous variability trends seen across the whole observation. Therefore, we adapted our method to account for this, and for the large uncertainties in the CSS data.

We binned the data into 5-day bins, and rejected any outlying bins that were greater than 2σ from its neighbours. We then used a technique similar to the normalised excess variance described in Section 4.3.2 above. We calculated the average excess variance per year for each object using the formula:

$$\sigma^2_{excess\,var} = \frac{1}{N}\sum_{i=1}^{N}[(X_i - \mu)^2 - \sigma_i^2] \tag{4.6}$$

where N is the number of bins per year, μ is the unweighted arithmetic mean magnitude for the year interval, and X_i and σ_i are the magnitudes and uncertainties, respectively, for each bin. The mean excess variance is determined by calculating the unweighted mean of all of the individual year-long segments for each object.

For the optical sample the uncertainties were completely dominated by Poisson noise, and therefore the Poisson noise on each result was used to approximate the uncertainty on the excess variance.

Detections of genuine variability are assumed when the excess variance is greater than zero. In order to see how the excess variance changes over the course of the light curve, the

cumulative excess variance for the whole light curve is shown in Figure 4.3. Here, only one time interval covering the whole light curve is used, and the excess variance is calculated for each bin. When the excess variance is greater than zero it contributes towards the cumulative excess variance. For clarity the resultant value for all objects is divided by the largest cumulative excess variance value. From Figure 4.3 it can be seen that the objects with the largest cumulative excess variance values show evidence of variability across their light curve, with constant increases present in the cumulative total. For several of the objects with lower values the rise is concentrated in a small section of the light curve, indicating that they only exhibit single variability events.

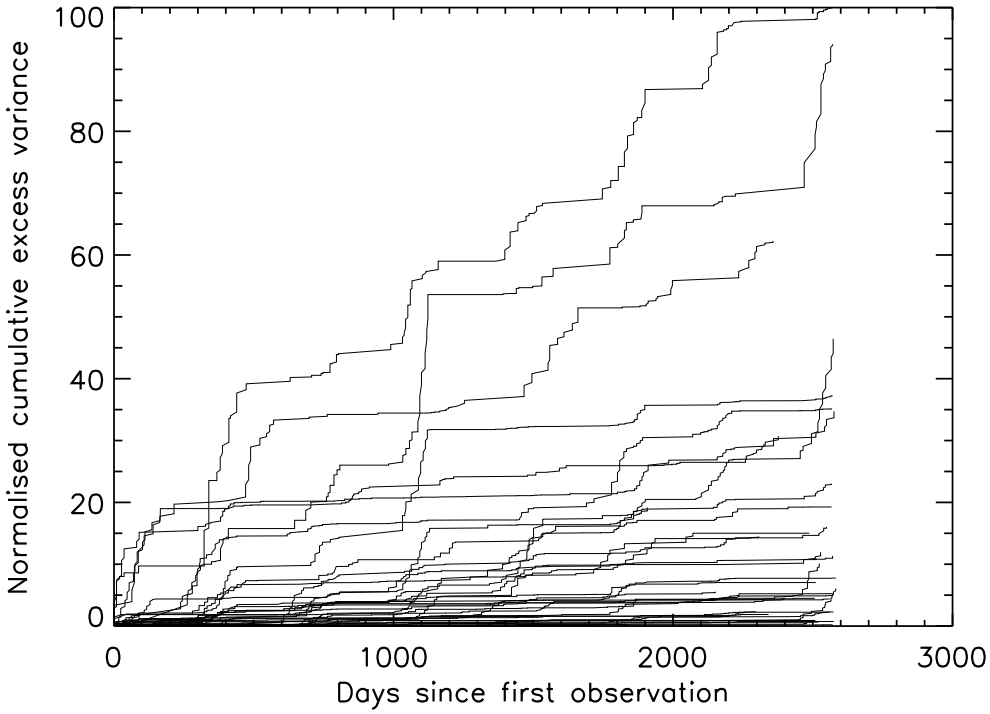

Figure 4.3: The normalised cumulative variability distribution of the 37 objects with CSS light curves. All objects are normalised to the object with the most variability in the sample - J134113.9-005314. The flat sections indicate either intervals where no data was recorded, or intervals where there was no significant amount of variability. The steepest sections of the graph indicate the most variable periods.

The light curve of the object with the largest rise and fall in our sample is shown in the right-hand panel of Figure 4.4. J004319.7+005115 rose by 0.65 magnitudes over 400 days.

The SDSS magnitude shown in blue on the left-hand side of the panel indicates that the object may have been stable at the lower magnitude before this outburst. From the optical spectra shown in the left-hand pane of Figure 4.4 it can be seen that the broad base of the Balmer lines of J004319.7+005115 are blueshifted and may even be double-peaked. This is thought such properties may be a result of outflows and winds from the AGN, and these may influence the variability seen in the light curve.

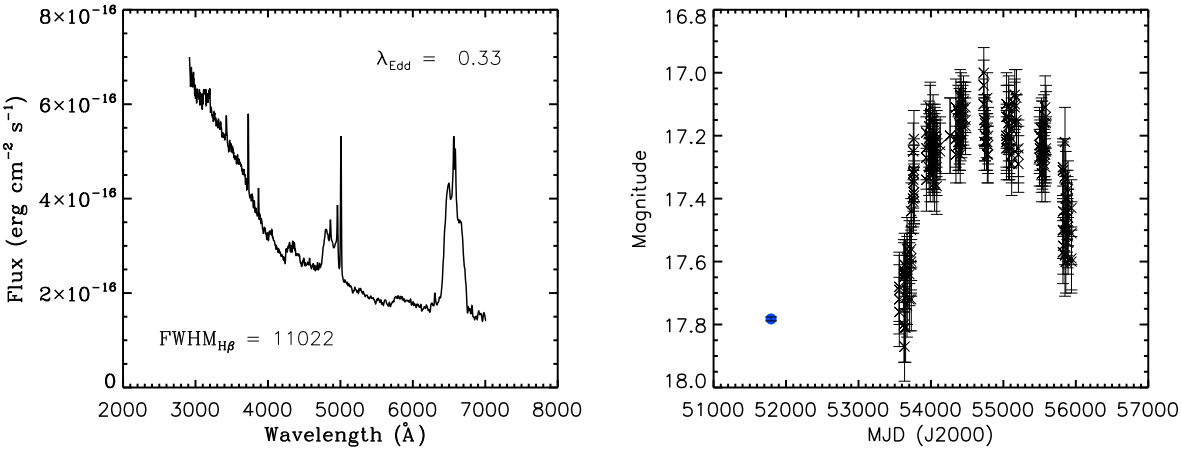

Figure 4.4: J004319.7+005115 displays the clearest outburst and subsequent dimming in the whole sample. The blue point denotes the SDSS r band model magnitude indicating that the object may have been at a constant luminosity for several years prior to its outburst.

An example of an object with a negative value for its excess variance is J094057.1+032401 shown in Figure 4.5. The light curve in the right-hand panel shows a large scatter in the data, but with large associated uncertainties. The optical spectra shows evidence of reddening, but no evidence of the blue excess associated with an accretion disc in the optical region.

J095048.3+392650 shown in Figure 4.6 is another interesting object, as it shows a slow decrease in luminosity over a period of several years, but the SDSS observation indicates that previously it had a similar magnitude to the final CSS observations. A possible explanation for this is that CSS observations of this object began just after it went into an outburst, and then monitored its decay back down to its pre-outburst levels. The optical spectrum does show a strong blue excess providing evidence of an accretion disc, but as it was taken at a similar time to the SDSS photometric data it offers no further insight into the variability

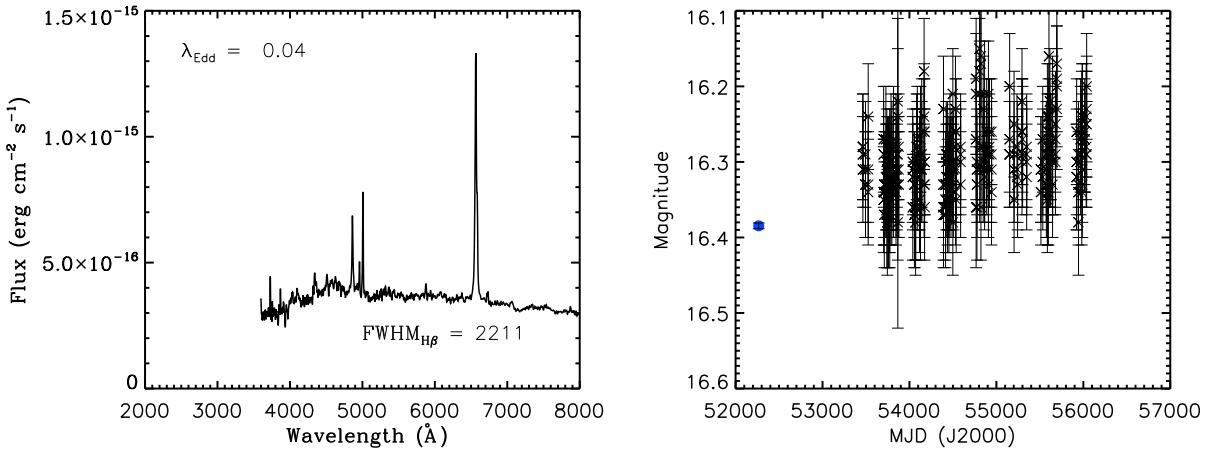

Figure 4.5: J094057.1+032401 is an example of an object with no statistically significant variability. All of the CSS data is in agreement and the SDSS r-band model magnitude from three years previous is at a similar level.

behaviour of this object.

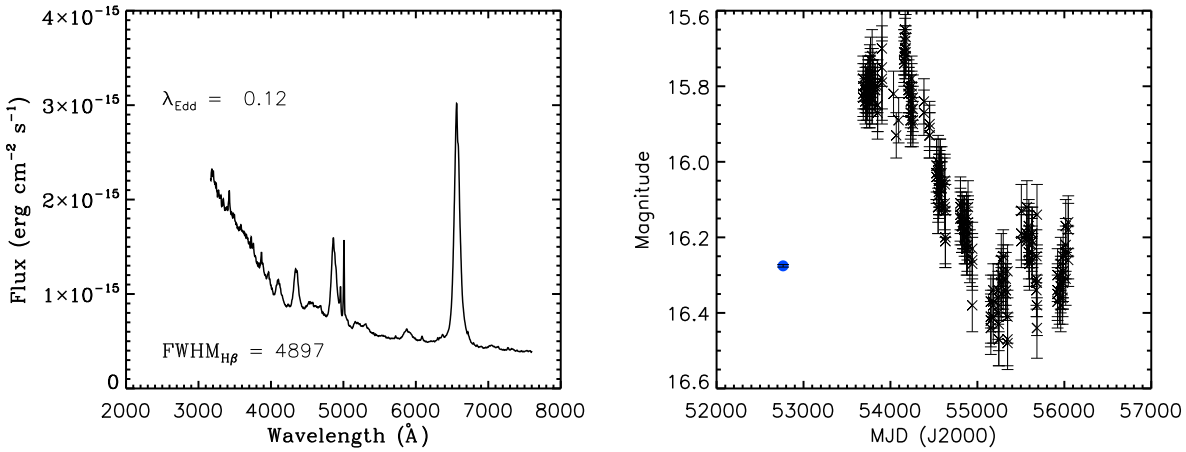

Figure 4.6: J095048.3+392650 is an example of an object dimming over a period of several years. The difference between the SDSS observation and the initial CSS observations indicates that during that time the object brightened by $\sim$ 1.5 magnitudes.

The object with the largest excess variance value is J134113.9-005314, shown in Figure 4.7. It can be seen that while there is no trend in the light curve there are a number of flares. The optical spectrum shows some evidence of an accretion disc in the blue half of the

spectrum, but due to its shape it is likely to be contaminated by a strong Balmer continuum, which is often seen in this region in unreddened objects (Jin et al. 2012).

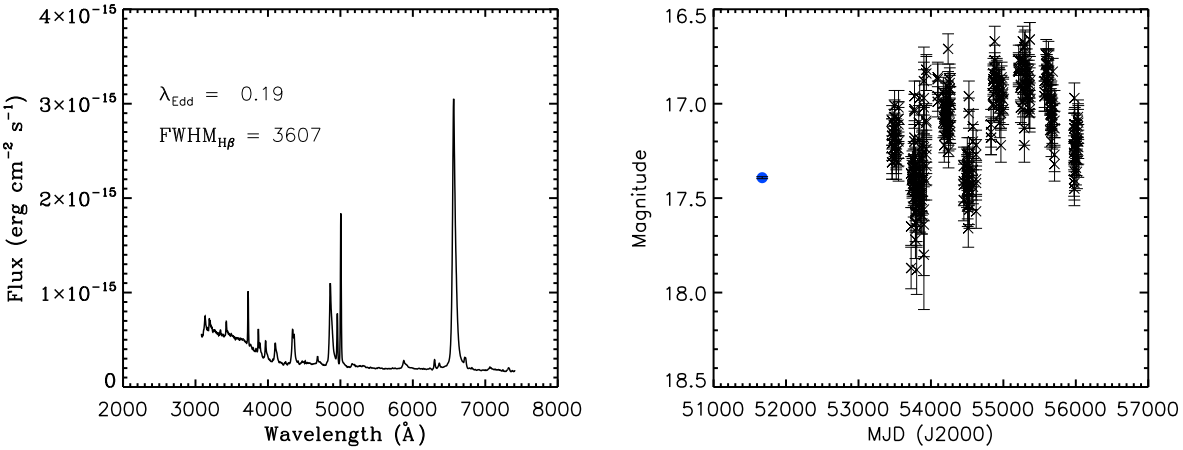

Figure 4.7: J134113.9-005314 is the object with the largest excess variance value due to the constant flaring seen across the CSS observation period. The rate of change per year over the entire 6 years of observations is 4.72 magnitudes/year, if all of the statistically significant variations are totalled.

RE J1034+396 (listed as J103438.6+393828 in the tables above) is the only known AGN with a convincing QPO, and it also displays a very rarely seen RMS spectrum (Jin et al, 2009; Middleton et al., 2009; and references therein). Its light curve and optical spectrum are shown in Figure 4.8. While displaying high levels of variability in the X-rays, it can be seen that within the errors RE J1034+396 does not vary in the optical. The Hβ linewidth shown in the left-hand plot of Figure 4.8 is the broadest value derived from the line fitting routines described in Chapter 3, and is mainly an indication of the FWHM of a broad base associated with the wings rather than a single Gaussian fit to the line. For the narrowest line objects, the broadest widths were used in the SED fitting. This was so as to provide the models with the greatest range of parameter spaces.

It is known that accretion discs do not stay as a fixed structure forever. There is no reason for the rate at which their fuel is supplied to stay constant or for them to stay stable. There are several characteristic timescales relevant to disc dynamics, and we describe two of them below.

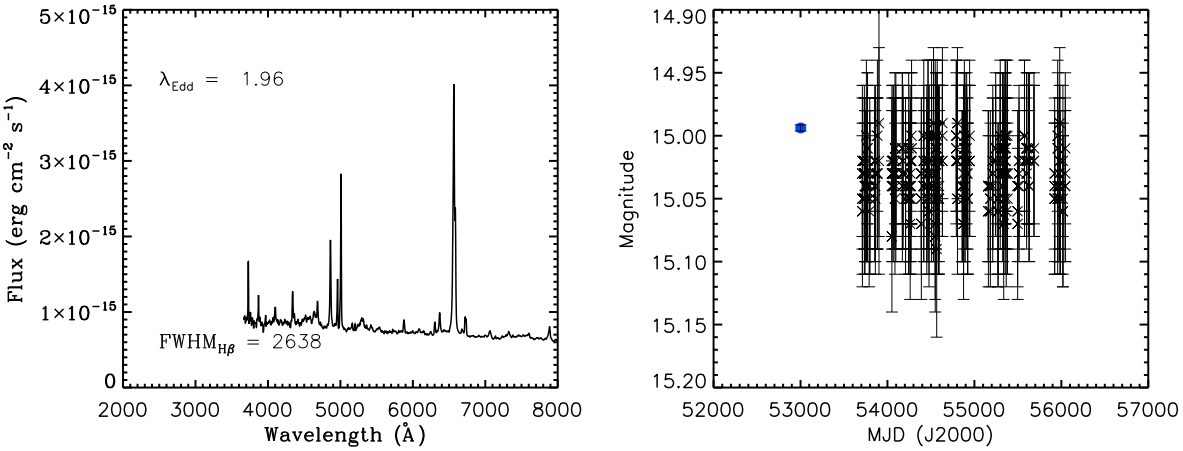

Figure 4.8: J103438.6+393828, or RE J1034+396. Despite its variability in the X-rays RE J1034+396 shows no signs of optical variability. The blue point indicates the SDSS r-band model magnitude.

For AGN the accretion timescale is the timescale over which the surface density of the disc changes significantly and is called the viscous timescale, t_{visc}. The viscous timescale is defined as:

$$t_{visc} = \alpha^{-1} \left(\frac{H}{R}\right)^{-2} t_{dyn} \tag{4.7}$$

where H is the vertical height of the disc, R is the radius, α has a value between 0 and 1, usually taken to be 0.1. We use a value of H/R = 0.1, as this represents a thick disc and will produce a lower limit to the viscosity timescale. The dynamical timescale, t_{dyn}, is the timescale associated with the response to gravitational forces in the radial direction, defined as:

$$t_{dyn} = \left(\frac{\mathrm{M}_{BH}}{10}\right) \left(\frac{r}{6}\right)^{3/2} * 4.5 \times 10^{-3}\mathrm{s} \tag{4.8}$$

where r is radius in terms of R_g (Czerny, 2004)

For AGN t_{visc} becomes:

$$\begin{aligned} t_{visc} &= \alpha^{-1} \left(\tfrac{H}{R}\right)^{-2} \left(\tfrac{\mathrm{M}_{BH}}{10^8}\right) \left(\tfrac{r}{6}\right)^{3/2} * 4.5 \times 10^4 \,\mathrm{s} \\ &\sim 4.5 \times 10^7 * \left(\tfrac{\mathrm{M}_{BH}}{10^8}\right) \left(\tfrac{r}{6}\right)^{3/2} \, s \\ &\sim \left(\tfrac{\mathrm{M}_{BH}}{10^8}\right) \left(\tfrac{r}{6}\right)^{3/2} \text{ years} \end{aligned} \tag{4.9}$$

For a 10^8 $\mathrm{M}_\odot$ mass black hole this is of the order of 2 years, reducing to $\sim$ 2 months for a

10^6 $M_\odot$ mass black hole. Due to the inherent assumptions in this method these times are considered to lower limit guidelines. There is also a relationship between temperature, T, black hole mass, M_{BH}, mass accretion rate, $\dot{\mathsf{M}}$ and radius, R:

$$T^4 \propto \frac{\mathsf{M}_{BH}\dot{\mathsf{M}}}{R^3} \tag{4.10}$$

using the substitution:

$$\dot{\mathsf{M}} \propto \frac{L}{L_{Edd}}\mathsf{M}_{BH} \tag{4.11}$$

and replacing R with $\mathrm{r}R_g$ this becomes:

$$T^4 \propto \frac{L/L_{Edd}}{r^3\mathsf{M}_{BH}} \tag{4.12}$$

If we assume a constant temperature then this rearranges to:

$$r^3 \propto \frac{L/L_{Edd}}{\mathsf{M}_{BH}} \tag{4.13}$$

as the region that produces the optical emission.

This result allows us to rewrite the viscous timescale as $t_{visc} \propto \mathrm{L}^{1/2}$. So we would expect the amount of variability to scale with $\sim 1/t_{visc}$ or $\mathrm{L}^{-1/2}$. We expect to see variability increasing with decreasing luminosity as found in previous studies.

In Figures 4.9 and 4.10 we plot both $\sigma^2_{excess\,var,year}$ and the largest magnitude change for each object, $\Delta\mathrm{var}_{opt}$, against various properties of the objects: $L^{1/2}_{disc}$, log (M_{BH}), log (λ_{Edd}) and $\mathrm{FWHM}_{H\beta}$. We found no significant trends with any of these parameters. We would expect to see variability increasing as luminosity, M_{BH} and $\mathrm{FWHM}_{H\beta}$ decrease, and as λ_{Edd} increases. In each case these correlations are predicted because of shorter light crossing time and viscous timescale, resulting in variability on shorter timescales.

While we expected to see correlations in the above parameters, the large scatter present can be explained for the two reasons outlined below:

1. **Host galaxy contamination**

   Due to the ~ 10 arcsec aperture used in the CSS data reduction in order to include all of the flux, we would expect there to be significant host galaxy contamination in the

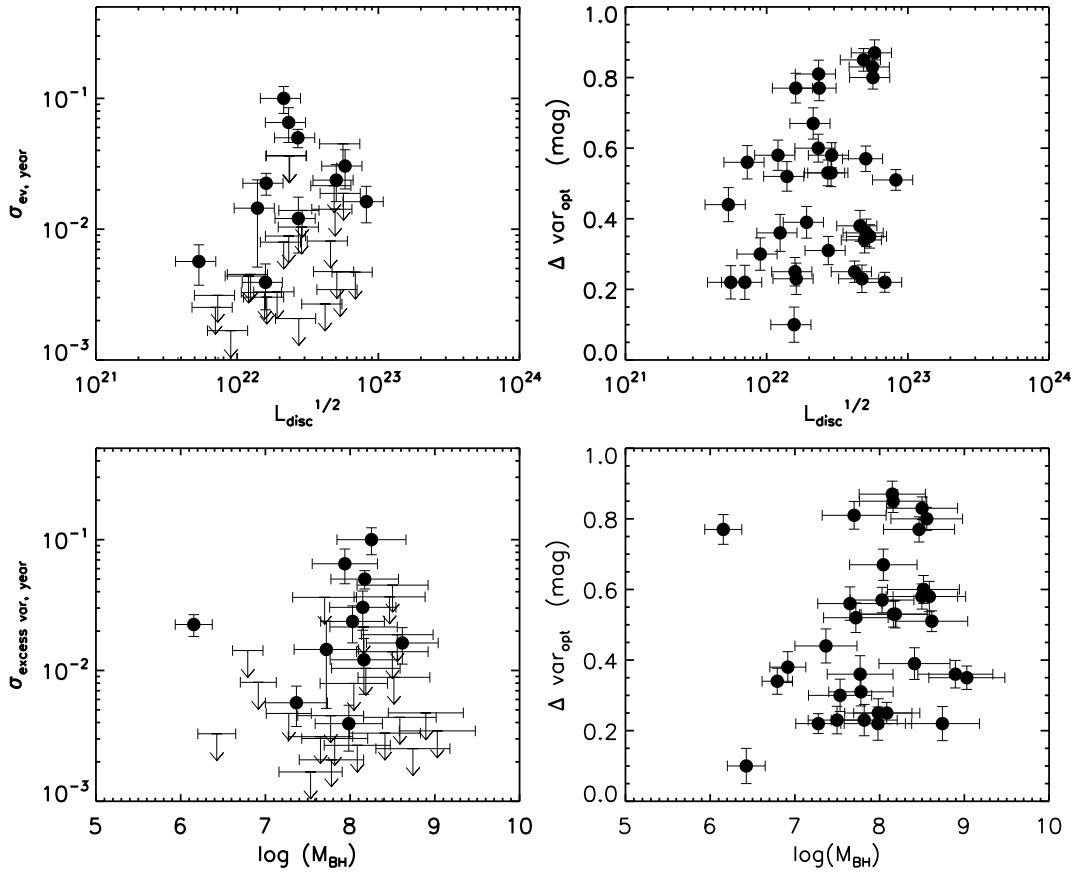

Figure 4.9: *Top left:* $L_{disc}^{1/2}$ against the excess variance in year-long intervals. Arrows represent the 3σ upper limit. *Top right:* $L_{disc}^{1/2}$ against the largest magnitude change per object. *Bottom left:* log (M_{BH}) against the excess variance in year-long intervals, with the arrows denoting the 3σ upper limits. *Bottom right:* log (M_{BH}) against the largest magnitude change per object. There is no trend between either measure of variability and the two different parameters.

light curves produced. We can define the ratio of the luminosities of the AGN to the host galaxy as:

$$\frac{L_{opt,AGN}}{L_{opt,stars}} \propto \frac{\dot{M}^{2/3}}{M_{BH}^{1/3}} \tag{4.14}$$

which, using the substitution for $\dot{M}$ shown above, becomes:

$$\frac{L_{opt,AGN}}{L_{opt,stars}} \propto M_{BH}^{1/3} \left(\frac{L}{L_{Edd}}\right)^{2/3} \tag{4.15}$$

This will make any trends between variability and optical luminosity of the black hole very difficult to see.

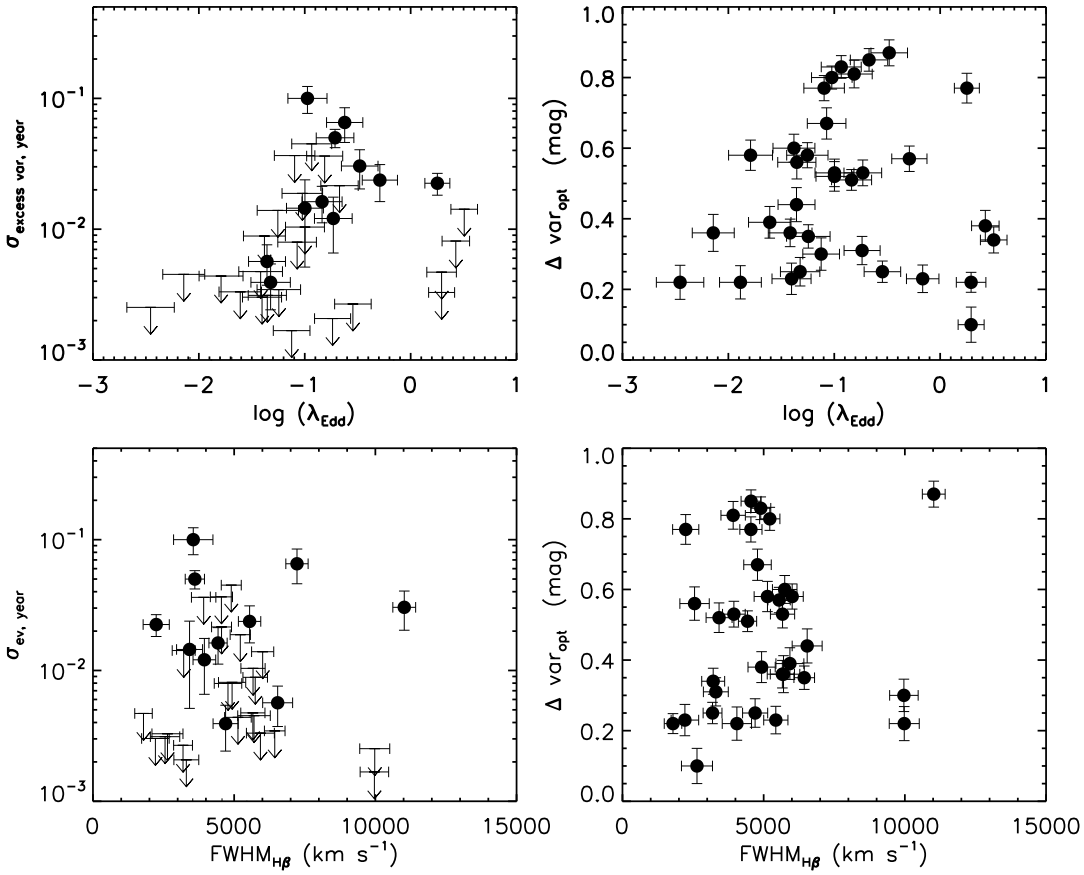

Figure 4.10: Top left: $\log(\lambda_{Edd})$ against $\sigma^2_{excess\,var,year}$. Arrows represent the 3σ upper limit. *Top right:* $\log(\lambda_{Edd})$ against the largest magnitude change per object. *Bottom left:* FWHM$_{H\beta}$ against $\sigma^2_{excess\,var,year}$, with the arrows denoting the 3σ upper limits. *Bottom right:* FWHM$_{H\beta}$ against the largest magnitude change per object.

2. **The accretion disc in the optical region**

Another point to consider when searching for optical variability is the behaviour and SED of the accretion disc in the optical region for the redshift range of our sample. Assuming that the accretion disc can be represented by a multi-component blackbody that we used in Chapter 3, the peak frequency of this blackbody is dependent on the black hole mass. The smaller the black hole mass the higher the temperature and the further the peak moves into the UV, leaving only the low energy tail in the optical region. Large black holes emit at a cooler temperature and peak in the optical.

We expect the peak frequency of the disc to be its most variable part, as this comes

from the smallest radii. We would also expect the smaller mass black holes to vary more rapidly than larger black holes, due to their shorter light crossing times. Therefore we would expect to see the peak of the accretion emission from small mass black holes to vary more rapidly than the accretion emission from large black holes. However, in the optical wavelength range we are using in this study, we are observing the peak of the accretion emission from large mass black holes and the low energy tail of the disc emission from smaller mass black holes. This means that while the small mass black holes may be more varying more rapidly, it will mainly be in the unobserved UV region, while the peak region of variability for the larger mass black holes is in the observed optical region. This significantly weakens any correlation between observed variability and black hole mass in the optical region.

Together, these two factors mean that detecting the correlations we might expect to see with the data quality of our sample is extremely difficult. We also have the inherent bias of our sample that in order to provide enough counts in the X-ray spectrum we are biased to select optically bright objects. This means that for a small range in L_{disc} our objects display a large range in the parameters we would expect the variability to correlate with, and weakens the presence of any underlying trend.

4.6 X-ray variability study

4.6.1 RMS Spectra

Our objective in creating the RMS spectra was to determine whether or not the soft excess is a separate component within the SED. This goal determined how we divided up the energy range of the *XMM-Newton* data, the time intervals we selected and the bin sizes used. Because of this we do not calculate the typical 2 - 10 keV values found in the literature.

Initially we calculated the RMS values over the whole observation, but we found that many of the values were unconstrained. In many cases this was due to too few counts, particularly at high energies. We were unable to constrain values for these objects and so we

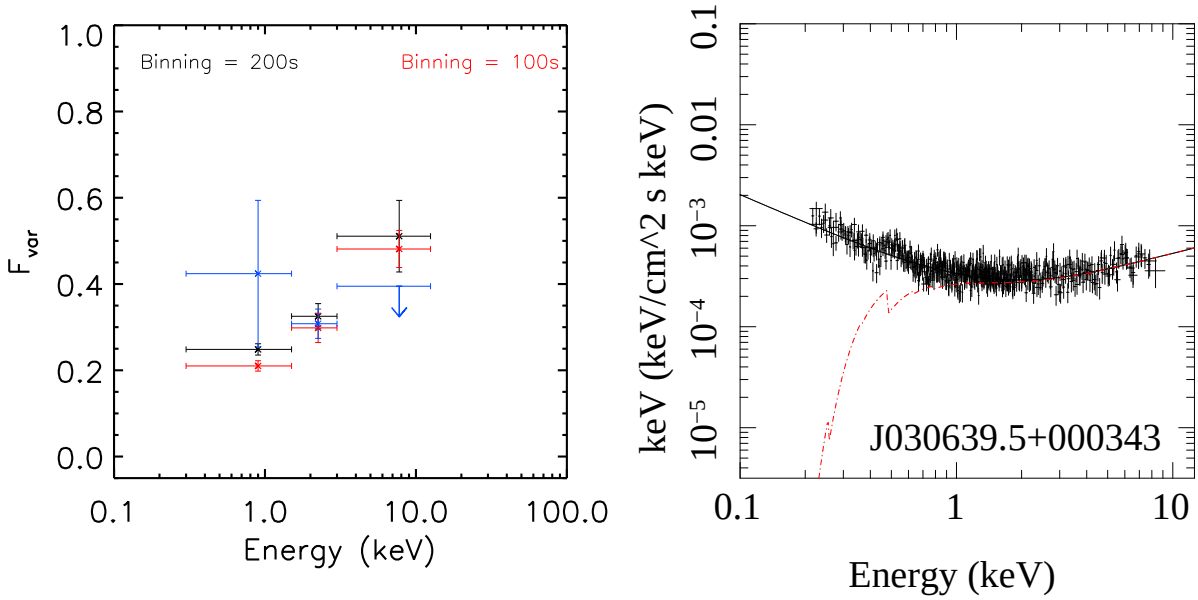

Figure 4.11: The RMS spectrum (*left*) and X-ray SED (*right*) of J030639.5+000343. The scatter in the RMS values for this object arise from a decreasing count rate at the start of the observation that is consistent with the tail end of a flare. The original RMS values for the whole observation are shown in blue. The RMS values for the observation excluding the first 20 ks are shown in red and black.

give conservative 3-σ upper limit values. Objects with observations longer than 20 ks were examined at different time intervals. We chose to focus on 10 ks and 20 ks intervals, as these intervals are the ones that produced the RMS spectrum for RE J1034+396 that indicate the presence of multiple variable components in the X-rays (Middleton et al., 2009).

We found that, while the RMS values for many objects were still unconstrained across most of the bands, especially the hardest band, others were constrained on shorter time intervals. For a select number of objects using shorter time intervals highlighted data quality problems, such as flares or poor background subtraction, which might falsely be taken as intrinsic variability of the object. 6 of the 24 objects with observations longer than 20 ks are shown in greater detail below, and give a representative view of the RMS spectral shapes created by the objects in the sample.

J030639.5+000343

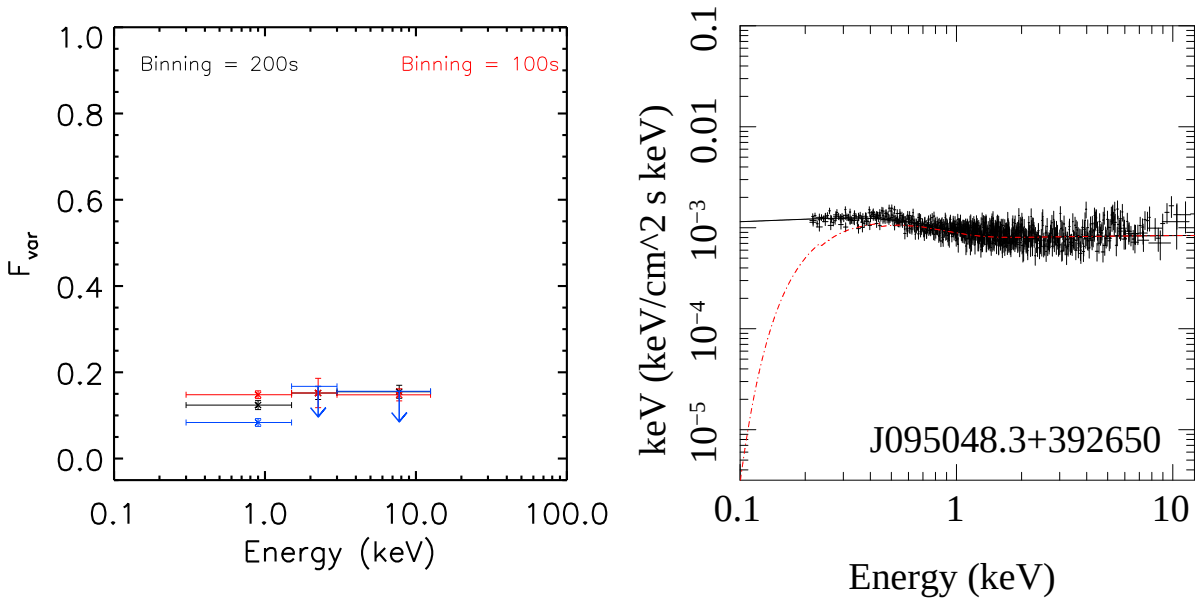

Figure 4.12: The RSM spectrum (*left*) and X-ray SED (*right*) of J095048.3+392650. The original RMS values are shown in blue, with the values for the RMS on 10 ks intervals shown in red and black. The resultant flat spectrum and flat X-ray SED indicates that there is only one variable component in the X-ray region.

J030639.5+000343 has RMS values across all bands when 200 s binning is used, but is unconstrained at higher energies with 100 s binning. When this is examined in greater detail, it is seen that these values arise from the variability during the first $\sim$ 20 ks of the observation. This resembles the end of a flare, particularly in the initial seconds of the observation, as the count rate is steadily decreasing and does not resemble the rest of the observation. It is most notable at higher energies, with a high constrained RMS value (1.46$\pm$0.34) on 10 ks time intervals and high upper limits for other intervals. In order to reduce the uncertainty on the lower energy bin and to constrain the higher energy bin, we excluded the first 20 ks in the subsequent calculations. The left panel of Figure 4.11 shows the RMS spectrum. The original RMS values using 100 s binning are shown in blue, and the values derived from the light curve if the first 20 ks are removed are overplotted in black for 200 s binning and red for 100 s binning. The right-hand panel of Figure 4.11 shows the X-ray region of the SED created in Chapter 3 for J030639.5+000343.

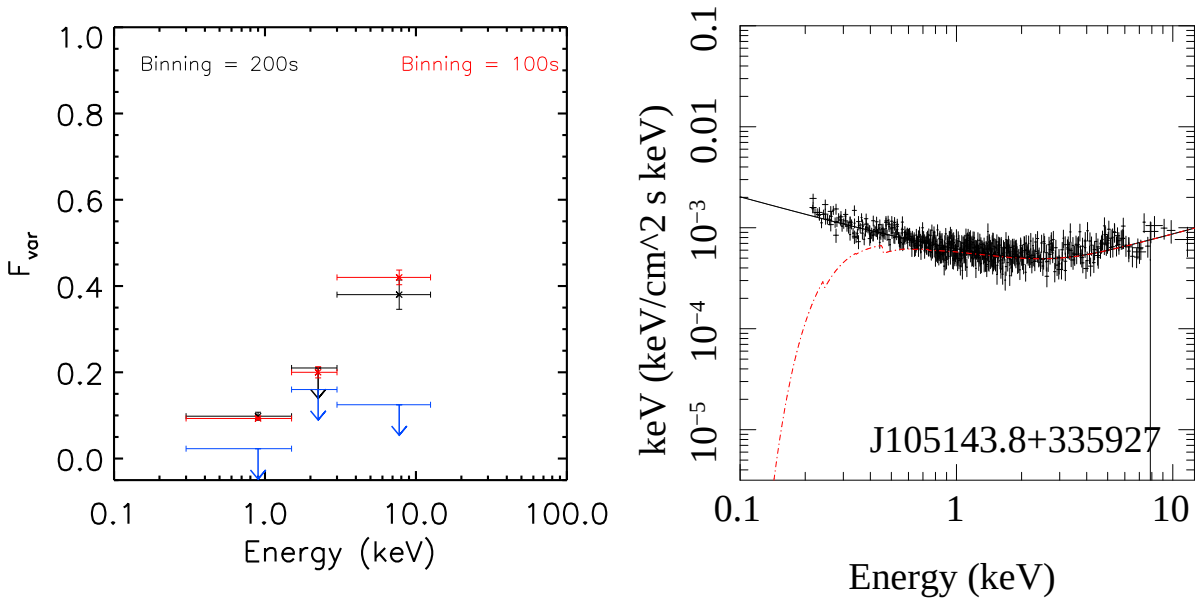

Figure 4.13: The RMS spectrum (*left*) and X-ray SED (*right*) of J105143.8+335927. The original RMS values for the entire observation are shown in blue and the constrained values for 10 ks intervals are shown in red. The resultant shape indicates that either there is only one variable component present in the X-ray region becoming more variable out to higher energies, or there are two components and the turn-over for the variability at higher energies is not seen in with this energy binning.

J095048.3+392650

J095048.3+392650 is only constrained in the soft energies over the whole observation, but if divided into 10 ks intervals, we find a flat RMS spectrum with values in the region of ~ 0.15 across all bands, shown in the left-hand panel of Figure 4.12. The original upper limits are shown in the blue with the resultant constrained values shown in black and red for 200 and 100 s binning respectively. The right panel of Figure 4.12 shows the X-ray SED.

J105143.8+335927

It can be seen by the blue points in the left panel of Figure 4.13 J105143.8+335927 is only constrained at the softest and hardest energies when a 200 s bin size is used across the whole 31 ks observation. It is completely unconstrained if a 100 s bin size is used. However, the object does exhibit signs of variability on a 10 ks timescale, with an RMS spectrum that

rises linearly from the soft to hard X-rays, shown in red in the left panel of Figure 4.13. The right panel of Figure 4.13 shows the X-ray SED.

J123054.1+110011

Over the whole observation, we find that if a 100 s bin size is used the RMS values increase

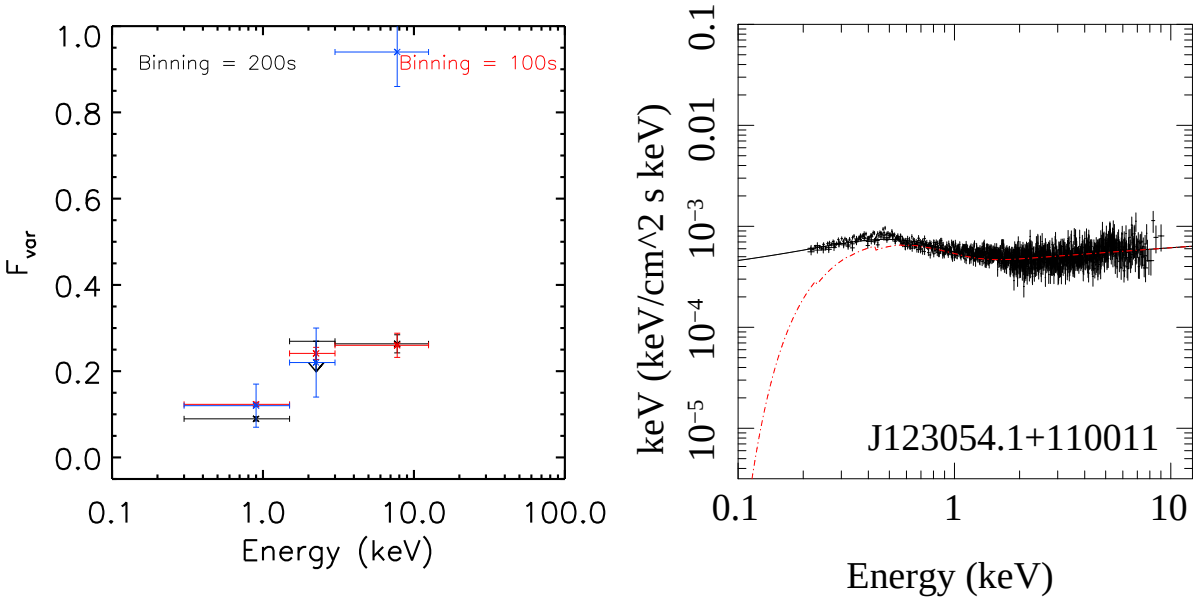

Figure 4.14: The RMS spectrum (*left*) and X-ray SED (*right*) of J123054.1+110011. The original RMS values are shown in blue and the corrected values are shown in red. The shape of the RMS spectrum is similar to that of RE J1034+396 and could indicate the presence of multiple variable components, with one in the soft X-rays and one in the hard X-rays. The blue points in the left panel show the RMS values when the spectrum had a badly subtracted background flare in the hard energies.

from the soft to the hard X-ray with a large value for the hardest band. With a 200 s bin size the RMS spectrum still rises from the soft to hard X-rays, but the middle band is unconstrained and the rise is not as pronounced.

In order to understand this phenomenon we divided the 93 ks observation into many different time intervals and applied many different bin sizes. We found a poorly subtracted hard X-ray background flare during the final 10 ks of the observation, which resulted in an over-subtraction and produced the RMS value that we found. With this contamination removed and using a larger bin size it was found that the harder X-rays were more variable

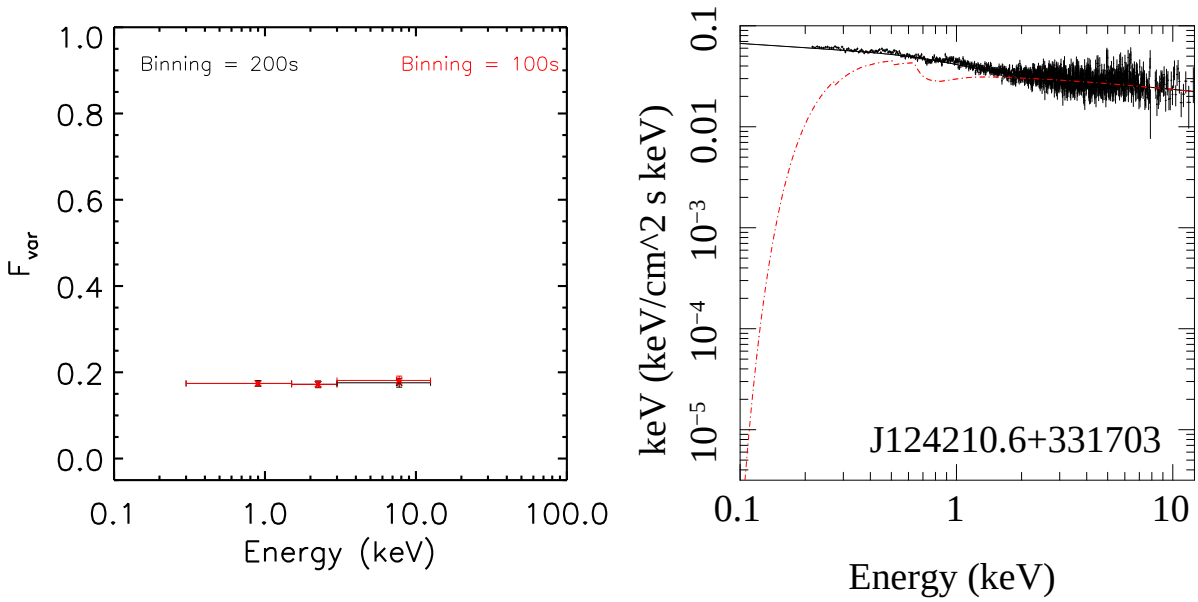

Figure 4.15: The flat RMS spectrum (*left*) and X-ray SED (*right*) of J124210.6+331703. This suggests only a single variable component is present in the X-ray region.

than the softer energies, with an RMS value of 0.26±0.02. Figure 4.14 shows the RMS and X-ray spectra of J123054.1+110011, with the original RMS values shown in blue in the left panel and the corrected value overplotted in red. This RMS shape is a close match to the RMS of RE J1034+396 shown in Figure 4.18, and could indicate the presence of more than one variable component.

J124210.6+331703

J124210.6+331703 is an object which has a flat RMS spectrum over its whole observation, as can be seen in the left-hand plot of Figure 4.15, as well as a flat X-ray SED shape, shown in the right panel of Figure 4.15. The light curves for the different energy bands map each other exactly. When divided into 10 ks intervals the RMS spectrum increases from the soft to the hard X-rays. The light curve across all three bands is shown in Figure 4.16. It shows that the events seen in the light curve of the softest band are replicated at the higher energies, just with an increased uncertainty. There is also no discernible time lag between the bands in this particular observation.

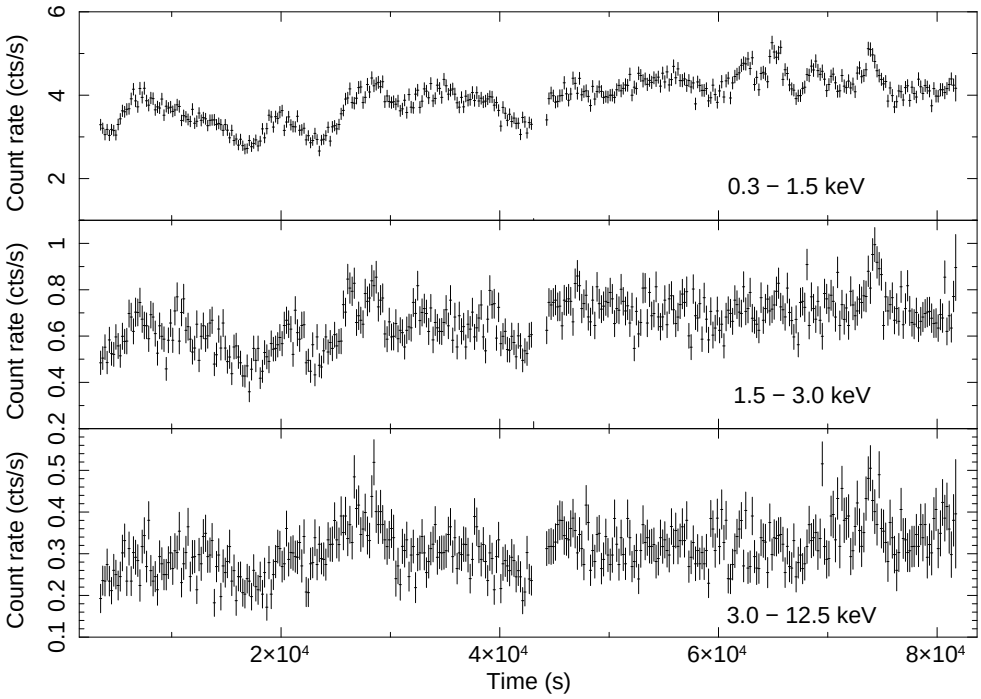

Figure 4.16: The X-ray light curve for J124210.6+331703 in the three different bands used in this study. It can be seen that the flickering seen clearly in the softest bands is replicated at higher energies, although with increased scatter.

J130022.1+282402

J130022.1+282402 is an interesting object, as its RMS spectrum, shown in blue in the left panel of Figure 4.17, appears to turn over in the middle. On closer inspection this turns out not to be the case. Breaking the light curve down into smaller time intervals we find 2 areas of constrainable variability on both 10 and 20 ks timescales. In the softest band the variability exists in two distinct parts: during the first $\sim$ 50 ks there is a constrainable small variability with an RMS value of $\sim$ 0.06 and during the last $\sim$ 12 ks there is far greater variability with an RMS value of $\sim$ 0.7. In the middle region only the latter variability is constrained, while at high energies the constrained variability comes from the first 20 ks and while the unconstrained upper limit for the last 12 ks is higher than for the rest of the observation it is not of the same scale as for lower energies. This suggests the presence of an X-ray flare during the last 12 ks of the observation, mainly composed of softer X-rays. The resultant RMS values with 100 s and 200 s binning and the flare removed are shown in red and black respectively, in Figure 4.17. The corrected RMS spectrum now matches other

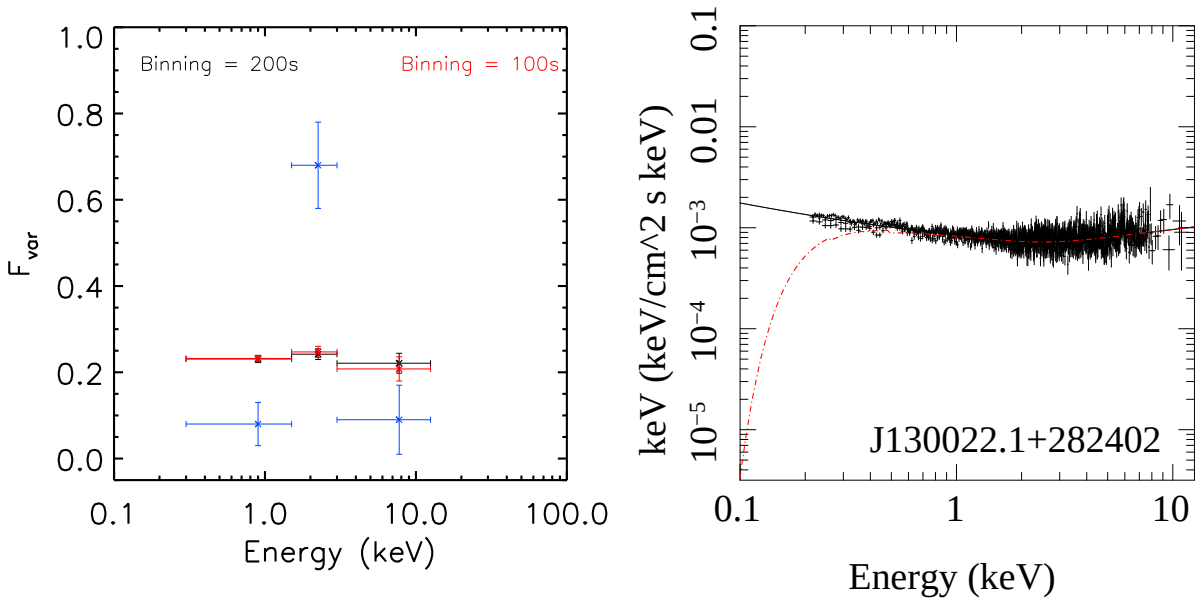

Figure 4.17: The original (blue) and corrected RMS spectra of J130022.1+282402 (*left*). The flat shape of the X-ray SED (*right*) combined with the flat RMS spectrum, indicates only one variable component present in the spectrum.

objects with a flat X-ray spectrum, such as J124210.6+331703 shown in Figure 4.15 above.

RE J1034+396

RE J1034+396 has been well-studied in recent years after it was discovered to display a ∼ 1 hour QPO (Gierliński et al., 2008). Its RMS spectrum is very unusual when compared to other well-studied AGN, and displays different values depending on the time interval used. The interval that displayed the most complex RMS spectrum was 10 ks and this produced a spectrum that rises through the soft energies to flatten off at energies greater than 2 keV (Middleton et al., 2009). While we do not reproduce the shape fully as we do not use as many energy bands, we do recover the appearance of tapering to higher energies as shown in the left panel of Figure 4.18.

J134113.9-005314

The final object we highlight in our RMS study is J134113.9-005314. This object was the most optically variable, but as can be seen in Figure 4.19 it is unconstrained across all bands.

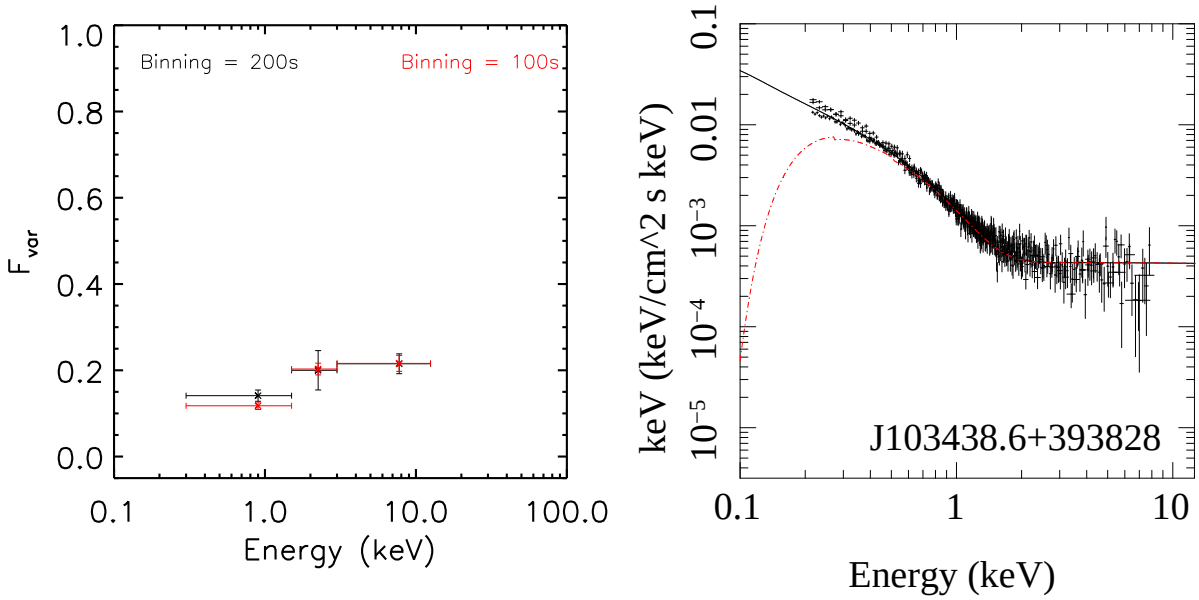

Figure 4.18: The RMS spectrum (*left*) and X-ray SED (*right*) of J103438.6+393828. There is evidence of the RMS slope flattening towards higher energies as found by Middleton et al. (2009), but as we are using larger bands and a shorter observation, we do not recover the same pronounced difference.

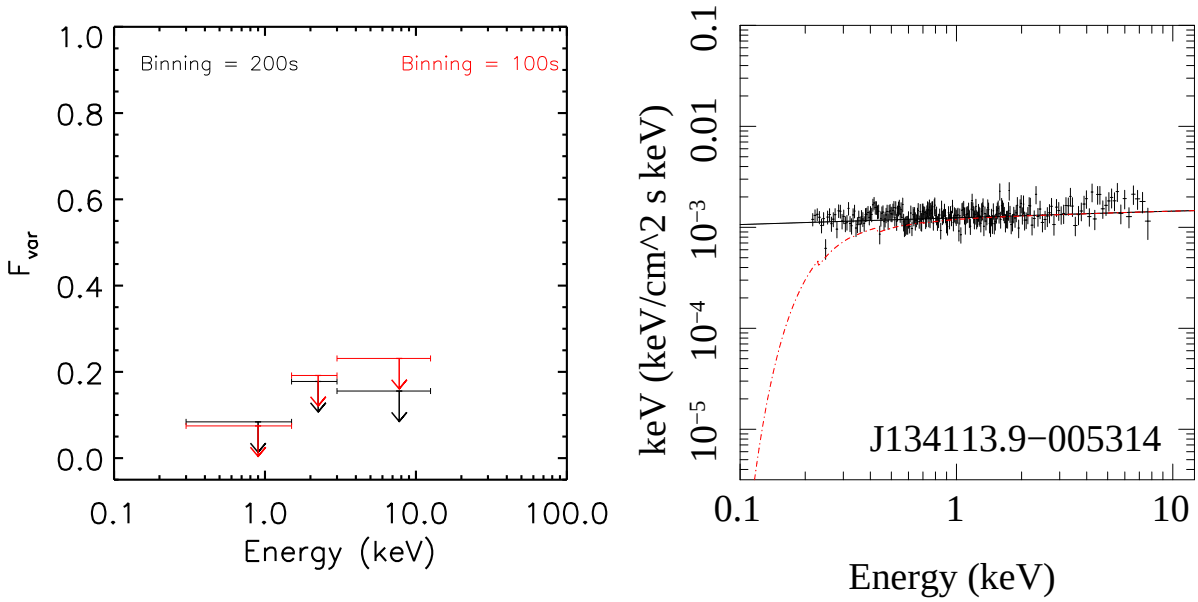

Figure 4.19: The RMS spectrum (*left*) and X-ray SED (*right*) for J134113.9-005314. Despite being the most optically variable object in our sample, the RMS spectrum was unconstrained in all bands, irrespective of the bin size of time interval used.

The X-ray SED in the right panel of the figure shows that the spectrum appears very flat, but is poorly sampled and has a large scatter at all energies.

4.6.2 Multi-component variability

Most objects were unconstrained in at least one band, resulting in an undetermined RMS shape. From the objects that could be constrained in all bands, we found that the predominant shape of the spectrum was a rise in the RMS values from soft to hard X-rays, or in a constant RMS value across all three energy bands. While the flat spectrum suggests only a single component, the rising shapes can either support a single component model or a two component model, where there is a low variability soft component and a more variable hard component, with the middle band blurring the two. With the broad bands and data quality of our sample, we have no clear way of differentiating between the two.

Figure 4.20 shows the ratios of the RMS values for the middle and softest bands on the x-axis and the hardest and middle bands on the y-axis. The black points indicate the objects that have fully constrained values across all three bands. The grey circles with arrows represent the ratios that can produce an upper limit in the direction of the arrow, while the green circles indicate the objects that have upper limits for RMS values and therefore have unconstrained ratios.

Studying the objects above we find that most objects that can be constrained (8/11) have similar values for both ratios. These objects lie along the line in Figure 4.20, and are indicative of having a single variable component in the X-ray region. The other 3 objects fall into one of two groups. REJ1034+38 and J123054.1+110011 lie close to each other beneath the relationship to the left side of the figure. They both have a ratio close to unity for the harder ratio, and a value closer to 2 for the softer ratio. The object that lies above the relationship is J141759.5+250812. This object has an RMS spectrum that shows a constant level of variability at lower energies and a much higher level of variability at higher energies.

While the unconstrained objects lie scattered across the parameter space, those that can be constrained in one direction lie close to the linear trend.

If there is only one variable component present we would expect to see a constant level of variability across the X-ray region, indicated by the red square on Figure 4.20, or a steady

rise from soft to hard X-rays to account for the increased scatter of the harder X-rays, which is what we see for many of our objects, shown by the grey shaded region of Figure 4.20.

Identifying multiple variable components is more difficult. Based on previous studies, it is believed that REJ1034+38 does have multiple variable components. There is a weakly variable soft component and a more variable harder component, with the middle region's variability determined by the overlap of these components. This can either produce the RMS shape that we see for RE J1034+396, or an almost linear trend which would overlap with the grey shaded region in Figure 4.20.

As J123054.1+110011 displays a very similar RMS spectral shape to RE J1034+396, it could also have similar components. However, this object is $\sim 100 \times$ more massive and is accreting at a much lower Eddington ratio. While objects of this type can still have an observable soft X-ray excess component, the RMS spectral shape could also indicate that the object could have a similar properties to Mrk 766 and hence an RMS spectral shape resulting from an absorption feature at low energies. A similar situation exists for J141759.5+250812, which, while it has a lower mass than J123054.1+110011, also has a low mass accretion rate and low Eddington ratio, and the spectral shape can be made to fit both multiple and single component models.

As a result we conclude that the objects that fall within the red shaded region of Figure 4.20 have a single variable component in their X-ray region. For the objects that lie outside this region, the case is far more complex. The difference in the physical parameters for RE J1034+396 and J123054.1+110011 make a similar energetic framework unlikely but they could still have same X-ray components, just with different intensities. Objects that lie on the linear trend, but away from a ratio of 1 could be comprised of either one or two components. This means that while this method highlights the difference in RMS spectral shapes for many different AGN it is not a useful tool for identifying objects with multiple variable components, due to the other factors that have to also be considered.

4.6.3 Normalised excess variance

In this section we study the correlations between the normalised excess variance, σ^2_{rms}, in various energy bands, and also between σ^2_{rms} and other source parameters. For this analysis

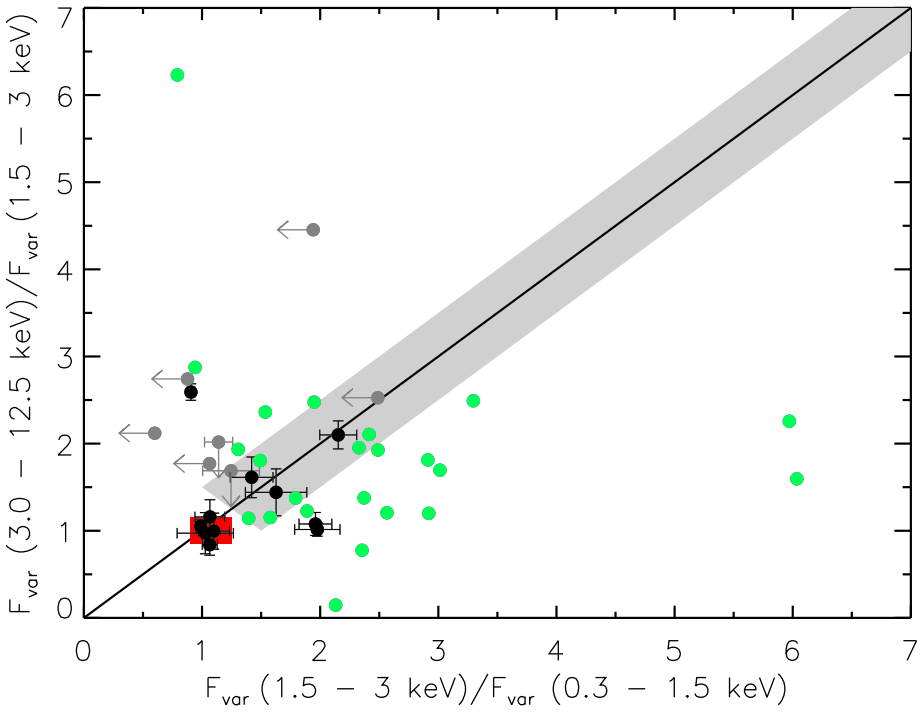

Figure 4.20: A ratio plot of F_{var}(1.5 - 3.0 keV)/F_{var}(0.3 - 1.5 keV) against F_{var}(3.0 - 12.5 keV)/F_{var}(1.5 - 3.0 keV). The black points indicate objects with fully constrained RMS values. The grey circles with arrows and error bars indicate those objects that can be constrained in on direction and have an upper in the other. The grey circles with arrows are completely unconstrained in one direction and only have an upper limit in the other. Finally the green circle indicate the objects that only have upper limits for all RMS values and so have unconstrained ratios.

we use 200 s binning.

Following the work of Nandra et al. (1997), O'Neill et al. (2005) and Ponti et al. (2012), in our correlation and resultant fits we only considered the excess variance of objects with at least one segment showing significant variations (even if the upper limits are also shown). To identify the 'variable' segments we performed a χ^2 test on each segment and source (i.e. all three energy bands and for 10, 20, 40 and 80 ks intervals), accepting a null hypothesis probability of less than 1% for evidence of 'significant' variability. We measured at least one 'variable' interval in 8, 10, 14 and 21 sources in the 80, 40, 20 and 10 ks intervals respectively.

In total there are 25 sources with at least one variable segment in at least one time interval. For the remaining 16 sources we do not detect any significant variability during any segment; the corresponding upper limits are indicated by arrows in the following figures. All of the objects with upper limits on σ^2_{rms} (i.e. those with non-detections) do not have a single variable segment in the observation examined.

4.6.3.1 Comparison of σ^2_{rms} in various energy bands

The three energy bands used in this study (0.3 - 1.5, 1.5 - 3 and 3 - 12.5 keV) were chosen to sample the different spectral components (especially the softest band), which introduces spectral variability in these bands. Therefore, a non-linear relationship between the measured σ^2_{rms} in these bands is possible if different spectral components are present.

The upper panels of Figure 4.21 show a plot of $\sigma^2_{0.3-1.5keV}$ vs. $\sigma^2_{3.0-12.5keV}$ (*left*) and $\sigma^2_{1.5-3.0keV}$ vs. $\sigma^2_{3.0-12.5keV}$ (*right*), when computed within 10 ks time intervals. Similarly the upper-middle, lower-middle and bottom panels show the same plots but calculated over 20, 40 and 80 ks time intervals respectively. It can be seen that the excess variance correlates best between the softest and hardest bands over the middle time intervals, with increasing scatter seen in the upper limit estimations over the 10 and 80 ks time intervals. The black solid line represents the line of best fit to the fully constrained objects in each plot. Each line has the general equation of the form log(y)=a+b*log(x), with the best fit values for a and b shown in the upper left corner of each plot. The dotted lines represent the combined 1-σ error on the best-fit slope and normalisation values, while the red dashed line shows the one-to-one relationship.

All of the best-fit slope parameters and normalisation estimates are consistent, within errors, with 1 and 0 respectively in the case of excess variance estimates that are calculated using the 80, 40, 20 and 10 ks light curves. This result implies that, on these timescales, the main driver of X-ray variability in these objects is the continuum normalisation variations, and that the variations of other spectral components must be of a much smaller amplitude.

While it is possible to integrate the signal over the broadest energy band (0.3 -12.5 keV) to gain better precision on the variability measurements, the correlation between the excess variance measurements in the three bands is not sufficient for our objects. As mentioned

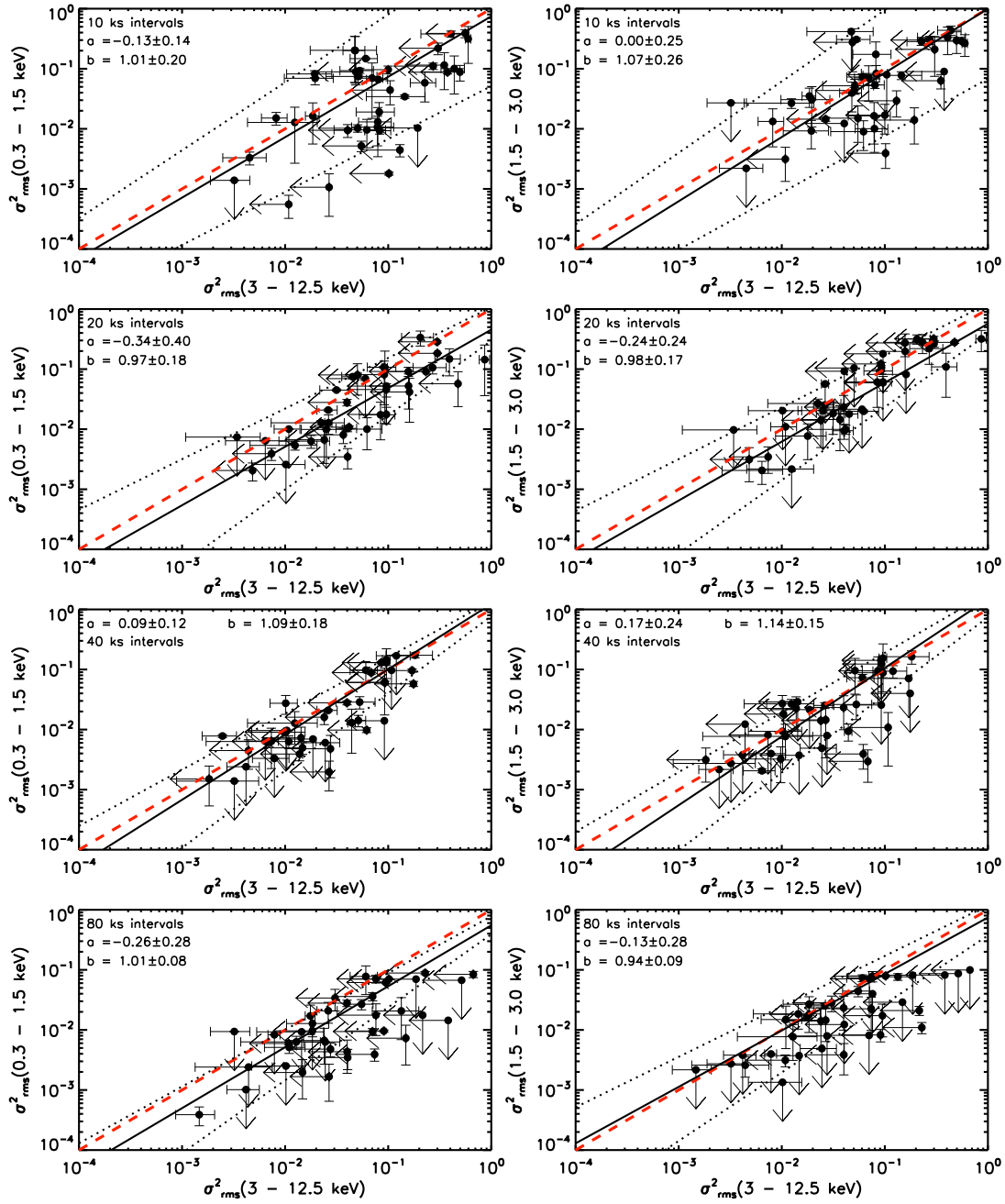

Figure 4.21: *Top panels:* soft (0.3 - 1.5 keV) vs. hard (3.0 - 12.5 keV) σ^2_{rms} (*left*) and middle (1.5 - 3.0 keV) vs hard (3.0 - 12.5 keV) σ^2_{rms} (*right*), computed within the 10 ks intervals. *Upper-middle, lower-middle and bottom panels:* similar plots calculated over 20, 40 and 80 ks intervals, respectively. The best fit curves are plotted with solid lines and the combined 1-σ error on the slope and normalisation with dotted lines. The red dashed lines represent the one-to-one relation expected in the case of achromatic variations. The normalisation and slope are given as a and b, respectively, in the top left corner of each panel. In each panel the best fit model is of the form log(y)=a+b*log(x).

above, the energy bands were chosen for the purpose of creating the RMS spectra above, and so cannot be directly compared with previous results in the literature. However, we can still explore the trends found in relation to the hard, medium and soft bands of the X-ray region.

4.6.3.2 Correlations between σ^2_{rms} and other source parameters

To investigate potential physical mechanisms which drive the X-ray variability in local AGN on the timescales covered by this study we look for correlations between the source variability amplitude (σ^2_{rms}) of the variable sources in our sample and various physical parameters of the sources: M_{BH}, $L_{2-10keV}$, and λ_{Edd}.

The σ^2_{rms} vs. M_{BH} relation

The correlation between X-ray variability and M_{BH} is already well established (Bian & Zhao, 2004a; O'Neill et al., 2005; Zhou et al., 2007,2010). For this comparison, we use the black hole mass derived from the SED modelling in Chapter 3.

We find that there is no significant trend in any of the bands, or any of the time intervals. This is due to the limited X-ray data quality of many of our objects, and also the conservative uncertainties we give to our M_{BH} estimates. As no correlation could be determined, we chose to see how our results compare with the 'case A' model estimates of González-Martin et al. (2011), as per the method of Ponti et al. (2012). This model is based on a detailed power spectral density (PSD) analysis of long X-ray light curves of several AGN. It assumes that the AGN PSD has a slope of -1 up to its break frequency, ν_{br}, above which it has a slope equal to -2. The break frequency decreases with increasing back hole mass and increases proportionally with the accretion rate, as shown by McHardy et al. (2006). The PSD amplitude, which is defined as the product of the PSD value at the break frequency multiplied by the break frequency itself, is assumed to be the same for all objects, with a value of 0.02, for the purposes of simplifying the model simulation.

We calculate the resultant model, based on Eqs. 7 from González-Martin et al. (2011), for three different accretion rates of 0.01, 0.1 and 1 times the Eddington accretion rate.

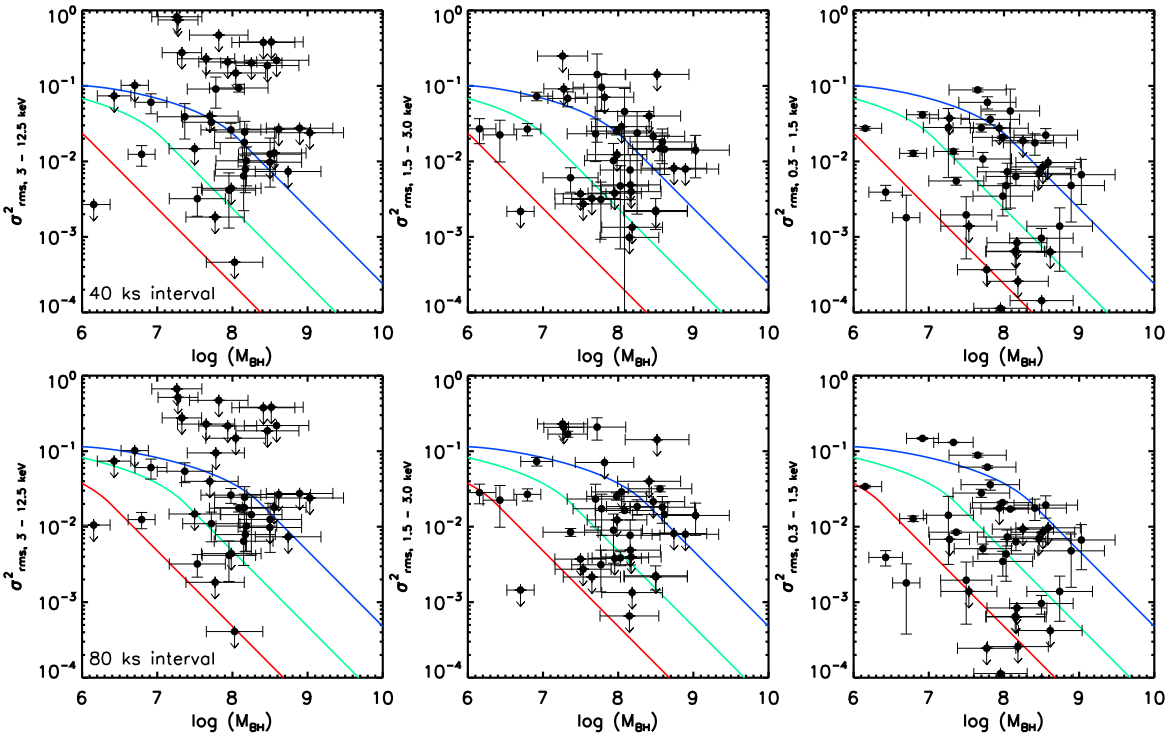

Figure 4.22: *Top panels:* hard (3.0 - 12.5 keV) (*left*), medium (1.5 - 3.0 keV) (*middle*) and soft (0.3 - 1.5 keV) (*right*) σ^2_{rms} vs. log (M_{BH}) in units of $M_\odot$ computed within the 40 ks intervals. *Bottom panels:* Similar but calculated over 80 ks intervals. The red, green and blue lines indicate the expected model relations for accretion rates of 0.01, 0.1 and 1 times the Eddington accretion rate, respectively, but our high-Eddington objects are found of the left side of this plot with the smallest black hole masses, while our low-Eddington objects appear in the region predicted to be highly super-Eddington.

Figure 4.22 shows M_{BH} vs. σ^2_{rms} for all three energy bands calculated over 40 (*top panels*) and 80 ks (*bottom panels*). The red, green and blue lines show the model predictions for accretion rates of 0.01, 0.1 and 1 times the Eddington accretion rate respectively. We do not find the expected anti-correlation predicted by the model, and in fact, find that our results display the opposite trend; the high-Eddington objects are clustered to the left side of the plot, while the low-Eddington objects lie where the objects with the highest Eddington ratios are expected to be found.

σ^2_{rms} vs. $L_{2-10keV}$

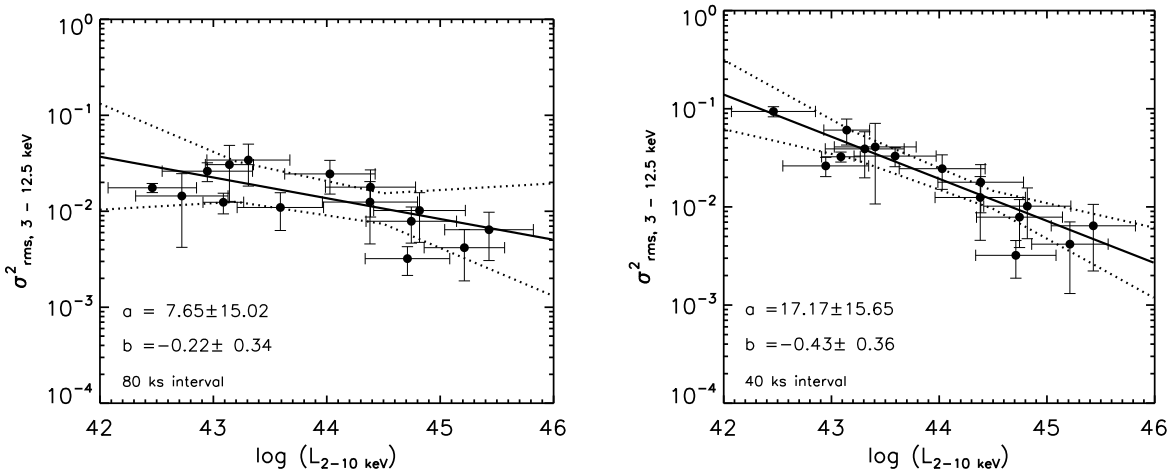

Figure 4.23: *Left:* $\sigma^2_{rms,3.0-12.5keV}$ vs. $L_{2-10keV}$ calculated over 80 ks intervals. *Right:* Similar, but calculated over 40 ks intervals. In each plot the best-fit relation is shown by the solid black line with the black dashed line representing the 1-σ error. The slope and normalisation parameters are listed as b and a respectively in the lower left corner of each plot.

The left-hand panel of Figure 4.23 shows the plot of $\sigma^2_{rms,3.0-12.5keV}$ vs. $L_{2-10keV}$ calculated over 80 ks intervals and the right-hand panel shows the same but over 40 ks intervals. Across all intervals the variability and luminosity are well correlated, with correlation probabilities greater than 99.8% in all cases. In both panels the slope and normalisation parameters for the best-fit relation, plotted in black, are listed as b and a respectively. The 1-σ error on these fits are shown by the black dotted lines.

It has been shown that the relationship between variability and luminosity is a by-product of the variability vs. M_{BH} relation (Papadakis, 2004; Ponti et al., 2012). If this is the case, then Figure 4.23 is tracing the variability vs. M_{BH} relationship of our sample as $L_{2-10keV}$ is well-correlated with M_{BH} for our sample.

σ^2_{rms} vs. λ_{Edd}

Figure 4.24 shows the variability $\sigma^2_{rms,80}$ vs. λ_{Edd} across the three energy bands for our sample. We find that there is no trend in any time interval, and no significant correlation between excess variance and Eddington ratio.

If the σ^2_{rms} vs. M_{BH} relationship holds and less massive black holes are intrinsically more

variable then they should populate the higher part of any σ^2_{rms} vs. λ_{Edd} plot at any given value of λ_{Edd}. This means that even if there is a correlation, there would still be significant scatter in the plots due to our large range of black hole masses.

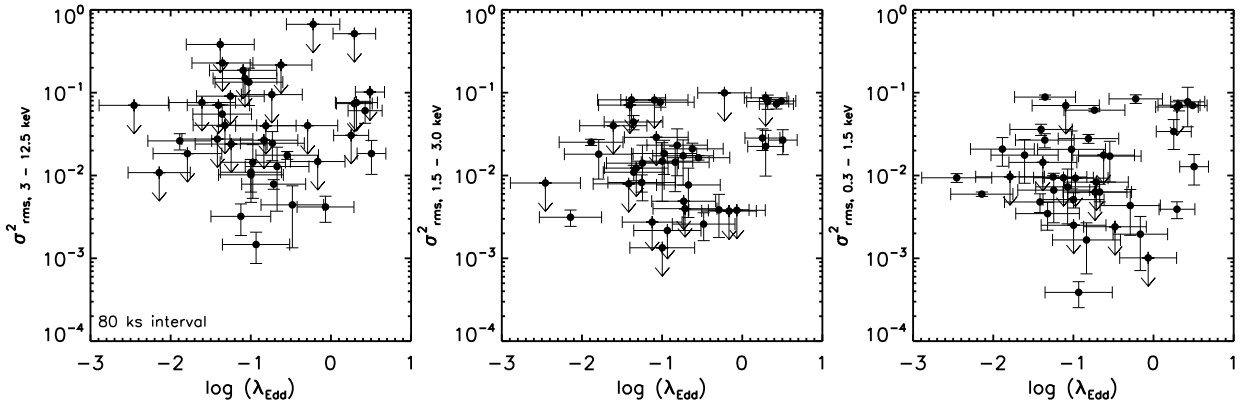

Figure 4.24: σ^2_{rms} vs. λ_{Edd} for the soft (0.3 - 1.5 keV) (*left*), medium (1.5 - 3.0 keV) (*middle*) and hard (3.0 - 12.5 keV) (*right*) calculated within 80 ks intervals. There is no statistically significant correlation between σ^2_{rms} and λ_{Edd} within any time interval.

4.7 Conclusions

We have studied the optical and X-ray variability properties of a subsample of 41 objects taken from our larger parent sample defined in Chapter 3. To create our sample we chose objects that had $>$ 2,000 counts during a minimum of a 2 ks *XMM-Newton* observation. We probed the optical variability over 1 year intervals and the X-ray variability down to either the observation length or 10 ks, whichever was shorter.

For our optical variability study we used data from the Catalina Sky Survey. We found that 37 of our objects were covered by the survey and in all bar 2 cases had 7 years of observations.

In our optical variability study we found that most objects exhibit continuous low- level variability throughout the interval they were observed by CSS. We found evidence of one object brightening and dimming by $\sim$ 1 magnitude over the course of the observed light curve, and several others exhibited flaring of a lesser magnitude. We found that a majority of the AGN with the smallest mass black holes showed no evidence for optical variability.

We calculated the excess variance for the sample using 1 year time intervals. We also

calculated the rate of change of the largest magnitude change during the light curve for each object. A relationship between luminosity and variability should be expected, but due to the data quality, the range of black hole masses in our sample and the properties of the accretion disc in the optical region our sample showed no evidence of a correlation.

The data quality of the light curves significantly hampered our efforts to constrain the variability in many objects and to reveal any correlations of variability with various physical parameters.

In the X-rays we used two different methods to attempt to constrain the variability. The first method we used was to create an RMS spectrum for each object. Our goal was to investigate whether or not the soft excess component could be proven to be a separate variable component, as in the case of RE J1034+396 (Middleton et al., 2009), or as an absorption feature on top of a single variable power law component as in the case of Mrk 766 (Miller et al., 2007). To this end we divided up the 0.3 - 12.5 keV energy range of *XMM-Newton* data into three bands: a soft band covering 0.3 - 1.5 keV, a medium band covering 1.5 - 3.0 keV and a hard band covering 3.0 - 12.5 keV.

Initially we calculated the RMS spectra over the entire observation for each object, but when that was unable to constrain values for most objects we divided up the observations longer than 20 ks into 10 and 20 ks intervals. Out of our sample of 41 objects we were able to constrain RMS values in the three bands for 11 objects, in one of 10 ks, 20 ks or observation-length time intervals. We calculated the ratio of the RMS value for the hard against medium and the medium against soft energy bands. From the 11 objects where the ratios could be fully constrained, we found that 5 objects had ratios consistent with having a single, underlying variable component in the X-ray region, with a flat RMS spectrum.

Three objects lie on the linearly increasing trend that can either be described through a single variable component, or two components with the middle energy band reflecting the change between the two levels of variability. Within the limits of our data quality and band selection, we are unable to separate the two scenarios.

Of the three objects that lie outside this relationship, one is the QPO AGN RE J1034+396. While another object has very similar ratio values, it has drastically different physical properties and it is unlikely that they have the same underlying physical mechanisms powering

the soft X-rays, but it could still have a real soft excess component that is not as strong or as pronounced as that found in RE J1034+396. The third object that lies outside of the relationship displays values consistent with an absorption feature affecting the 0.3 - 3.0 keV range before being dominated by a variable power law at high energies.

We conclude that 5 of the 11 constrained objects in this sample are dominated by a single variable component in the X-ray region, with the possible addition of a soft absorption feature. Objects that are seen to lie on the linear trend can either be comprised of one or two objects, but it is outside of the scope of this study to determine which is the case for the individual objects displaying these RMS spectral shapes. We also conclude that objects that fall below this relationship are likely to be comprised of two components, similar to the case predicted for the case of RE J1034+396. Objects lying above this trend are concluded to behave more like Mrk 766.

The second method we used was the excess variance method, σ^2_{rms}. For this study we followed several practices found in the literature, with the important difference that we used the energy bands as defined for the RMS study, rather than the ones typically found in literature. We calculated the σ^2_{rms} values for all three energy bands across 10, 20, 40 and 80 ks time intervals. We found the expected relationship between the values in the different bands in all time intervals. Finally we explored the relationship between σ^2_{rms} and various physical parameters. While we did not find the expected variability and black hole mass relationship, due to the large scatter of our sample, we did find a relationship between variability and 2 - 10 keV luminosity, which can be explained in terms of the relationship between $L_{2-10keV}$ and M_{BH} for our sample. We were unable to determine a correlation between σ^2_{rms} and λ_{Edd}, again due to the large scatter of our sample.

Previous studies of the optical and X-ray properties have concentrated on a few objects with excellent data quality, while recently a growing number of statistical studies are being carried out on large samples with low data quality. Our study covers the middle ground between these two approaches; for a few objects in our sample we have sufficient data to constrain the variability, but that is not the case for all objects in the sample. We have shown that preliminary variability studies such as ours can be undertaken using the current sky survey and serendipitous catalogues. Ongoing and future optical surveys, such as Pan-

STARRS and LSST will provide longer and better sampled databases. It is hoped that future X-ray satellites will be equipped for monitoring programmes, so that future studies of this nature will prove to be much more insightful.

Chapter 5

Pilot studies with Pan-STARRS: PS1-10adi

In this chapter we give an introduction to the Panoramic Survey Telescope and Rapid Response System (Pan-STARRS), before investigating an interesting object found by the survey, PS1-10adi.

We introduce the Pan-STARRS telescope in Section 5.2. In Sections 5.3 and 5.4 we discuss the two main extragalactic surveys to be carried out by the telescope, the 3π survey and the Medium Deep Survey (MDS). Section 5.5 shows how Pan-STARRS finds variable objects and proves that they are real events. The study of PS1-10adi is in Section 5.6 and covers the multi-wavelength observations of the object, its energetics and discussions on its true nature before finishing with our conclusions.

5.1 Introduction

With the rise of digital sky surveys where telescopes continuously sweep the sky and robotic telescopes can be brought online to respond to transient events, the exploration of the time domain is becoming an increasingly popular area of astrophysics (Paczyński, 2000). The discovery of transient astronomical objects is not new to the field of astronomy, as following on from mapping the star positions many ancient civilisations also recorded bright supernovae that appeared in the night sky (Zhao et al., 2006). The timescales of transient events range from a few seconds for gamma-ray bursts (GRBs; Klebesadel et al., 1973) to years for supernovae (Rest et al., 2011) and AGN (Ulrich et al., 1997).

Advances in technology are leading to the detection of new types of astronomical phenom-

ena that have previously only been predicted and theorized about. A systematic approach to the exploration of the time domain is very likely to lead to many new discoveries (Djorgovski at el., 2001a, 2001b, and references therein). While there are many types of transient events that have been theoretically predicted but not convincingly observed, such as GRB orphan afterglows, there has recently been a rise in the number of rare types of transients detected, such as supernova shock breakouts (Soderberg et al., 2008, Schawinski et al., 2008) and tidal disruption events[1] (TDEs; Gezari et al., 2009, van Velzen et al., 2011, Gezari et al., 2012). These recent discoveries show the abilities of the current large transient surveys and the promise of the future ones yet to come online.

Currently there are multiple optical surveys that are searching for transient phenomena including the Robotic Optical Transient Search Experiment (ROTSE; Akerlof et al., 2000), SDSS (Sesar et al., 2007), Palomar Quest (PQ: Djorgovski et al., 2008), the Catalina Real-time Transient Survey (CRTS; Drake et al., 2009: Djorgovski et al., 2011), Palomar Transient Factory (PTF; Rau et al., 2009) and the Panoramic Survey Telescope and Rapid Response System (Pan-STARRS; Hodapp et al., 2004). Shortly, additional surveys such as SkyMapper (Keller et al., 2007) and the Large Synoptic Survey Telescope (LSST; Ivezic et al., 2008) will join them. At longer wavelengths the LOw Frequency ARray (LOFAR; Röttgering, 2003) and the Allen Telescope Array (Croft et al., 2010) are studying the radio region. Finally, at high energies there are a number of ongoing searches of transients involving satellites. These include the *Fermi* Large Area Telescope (LAT; Atwood et al., 2009), *Swift* (Barthelmy et al., 2005), *Galaxy Evolution Explorer* (*GALEX*; Martin et al., 2005), the *Rossi X-ray Timing Explorer* (Jahoda et al., 1996) and the Monitor of All-Sky X-ray Image (MAXI; Ueno et al., 2008).

As both the spatial and temporal coverage of transient surveys increases there are increasingly exciting prospects for the discovery of rare transient events on short timescales. To this end, the new generation of transient searches work on real-time analysis and detection.

In late 2007 the CRTS (Drake et al., 2009) began simultaneous real-time analysis and notification of events in images taken by the Catalina Sky Survey NEO search (CSS; Larson

[1] A tidal disruption event is when a star is being ripped apart by gravitational forces as it falls onto a supermassive black hole.

et al 2003). Since then it has expanded and now the CRTS transient survey analyzes data from all three of the telescopes operated by CSS.

In May 2010 Pan-STARRS began a similar pursuit. Currently, it only has one telescope, PS1, but in the future it is planned that there will be 4 telescopes at the same site.

5.2 The Pan-STARRS telescope

Pan-STARRS1 (PS1) is the prototype telescope for the Pan-STARRS project. It is situated on the peak of Haleakala on the island of Maui in the Hawaiian island chain. The exact location of the PS1 telescope is: Longitude +203d44m38.740s E, Latitude +20d42m25.558s.

The telescope had first light in early summer 2009 and started its science mission in May 2010. The aim of PS1 is to produce five-band (g_{P1}, r_{P1}, i_{P1}, z_{P1} and y_{P1}) imaging for 3/4 of the sky that will be ~ 1 magnitude deeper than SDSS (York et al., 2000; Abazajian et al., 2009) after three years of observations. While its primary aim is to search for Near Earth Objects (NEOs), the science cases driving the PS1 are both Galactic and extragalactic.

The PS1 system has been optimised for survey observations. Its main surveys are a Near Earth Objects (NEO) survey, a Stellar Transit Survey, a Deep Survey of Andromeda, a Medium Deep Survey consisting of 11 PS1 footprints spaced around the sky and a 3π Survey which covers 3/4 of the sky. A complete description of the hardware and software components of the PS1 system is given by Kaiser et al. (2010). As the science goals for PS1 are extremely broad the observation time available is broken down to best service the science goals of each of the 12 key projects.

The PS1 optical design (Hodapp et al., 2004) utilises a 1.8 m diameter $f/4.4$ primary mirror with a 0.9 m secondary mirror. The converging beam that results from this is passed through two refractive correctors, a 48 cm x 48 cm interference filter and finally the dewar window (another refractive corrector). This allows the telescope to deliver an image with a diameter of 3.3° that has low distortion.

The PS1 imager (Tonry & Onaka, 2009) is unique. It is a 1.4 billion pixel camera comprising of a total of 60 4800 x 4800 pixel detectors, with 10 μm pixels that subtend 0.258 arcsec. This provides an instantaneous field of view of 7.1 deg^2. The detectors are

back-illuminated CCDs manufactured by Lincoln Laboratory. The detectors are read out using a StarGrasp CCD controller. This has a readout time of 7s for a full unbinned image.

The broadband filters for PS1 are designed to be similar to the filter system used in surveys such as SDSS, with a few notable differences. One is that the g_{P1} filter extends redward an extra 200 Å of g_{SDSS}, which makes it susceptible to the 5577 Å sky emission. However, this does give it greater sensitivity and lower systematics when used for photometric redshifts. Secondly, the z_{P1} filter is cut off at 9200 Å, giving it a different detector response to that of z_{SDSS}. Finally, SDSS has no corresponding y_{P1} filter. The details of the filters, including the wavelength ranges and zero-points, are given in Table 5.1.

The transmission functions for PS1 are shown in Figure 5.1. They were produced by Stubbs et al. (2010) by mapping the system response of the PS1 optics and camera across all bandpasses to create system throughput curves. These were then combined with estimates for the atmospheric transmission to compare the colours from synthetic photometry of spectrophotometric standards to the colours obtained from the PS1 system. The absolute filter transmission curves shown in Figure 5.1 were obtained by dividing the transmission curve obtained with a filter in the beam by one obtained with no filter.

The deep depletion detectors used in the PS1 camera have significant QE in the near infrared. This suppresses fringing compared to currently conventional CCDs. However, Figure 5.2 shows a full frame obtained in the z_{PS1} band at 9020 Å. It can clearly be seen that fringing is still present and poses an ongoing problem to image calibration. Measures have been put in place to create a fringe frame appropriate to each PS1 survey image.

Filter	Bandpass (nm)	ZP (mag)	Sky (mag/arcsec^2)
g_{P1}	405-550	24.90	21.90
r_{P1}	552-689	25.15	20.86
i_{P1}	691-815	25.00	20.15
z_{P1}	815-915	24.63	19.26
y_{P1}	967-1024	23.03	17.98

Table 5.1: Details of the PS1 filters.

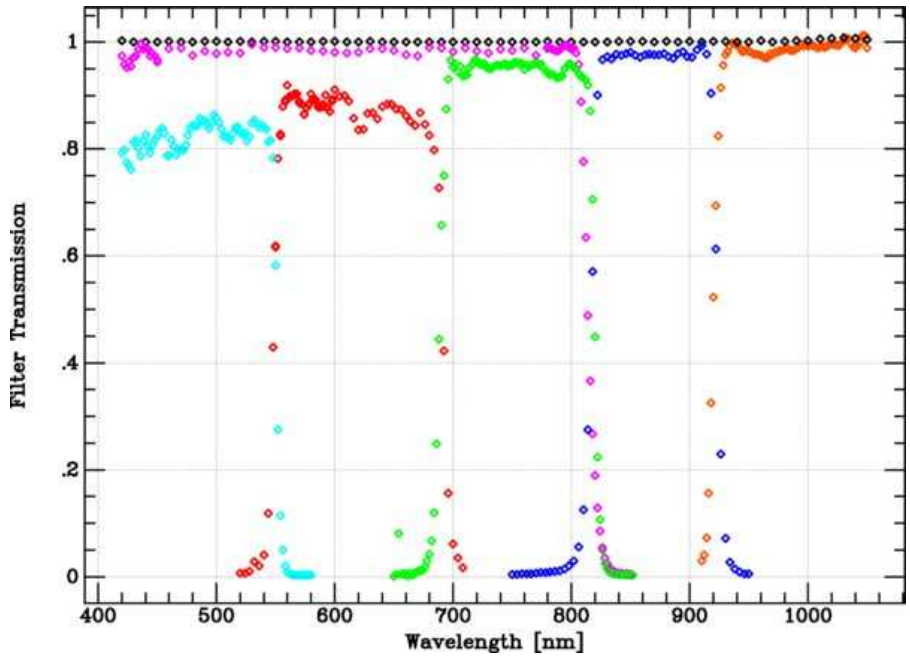

Figure 5.1: Pan-STARRS filter-only functions, for g_{P1} (cyan), r_{P1} (red), i_{P1} (green), z_{P1} (blue), y_{P1} (orange), w_{P1} (purple), and open (black). For this plot the vertical axis corresponds to the absolute filter transmission, since the data depicts the ratio between the measured sensitivity functions with and without the respective filters in the beam (reproduced from Stubbs et al., 2010).

5.2.1 Limiting Magnitudes and Saturation

The PS1 limiting magnitudes and exposure times for each filter are shown in the middle columns of Table 5.2. The limiting magnitude for each visit will be over a magnitude deeper than SDSS in all bands apart from r_{P1}, the limitations of the latter is due to its reduced exposure time in comparison to the g_{P1} and i_{P1} bands. After three years the survey is expected to be $\sim$ 2 magnitudes deeper than SDSS. However, it is important to note that this is compared to the current SDSS data release; the SDSS survey is ongoing and it is expected that their limiting magnitudes will also reduce in time.

The worst-case saturation limits for the 3π Survey are shown in the last column in Table 5.2. It is expected that many brighter stars will be obtained in guide-star video mode. Due to the multiple upgrades to the telescope, housing and optical set-up since the PS1 was

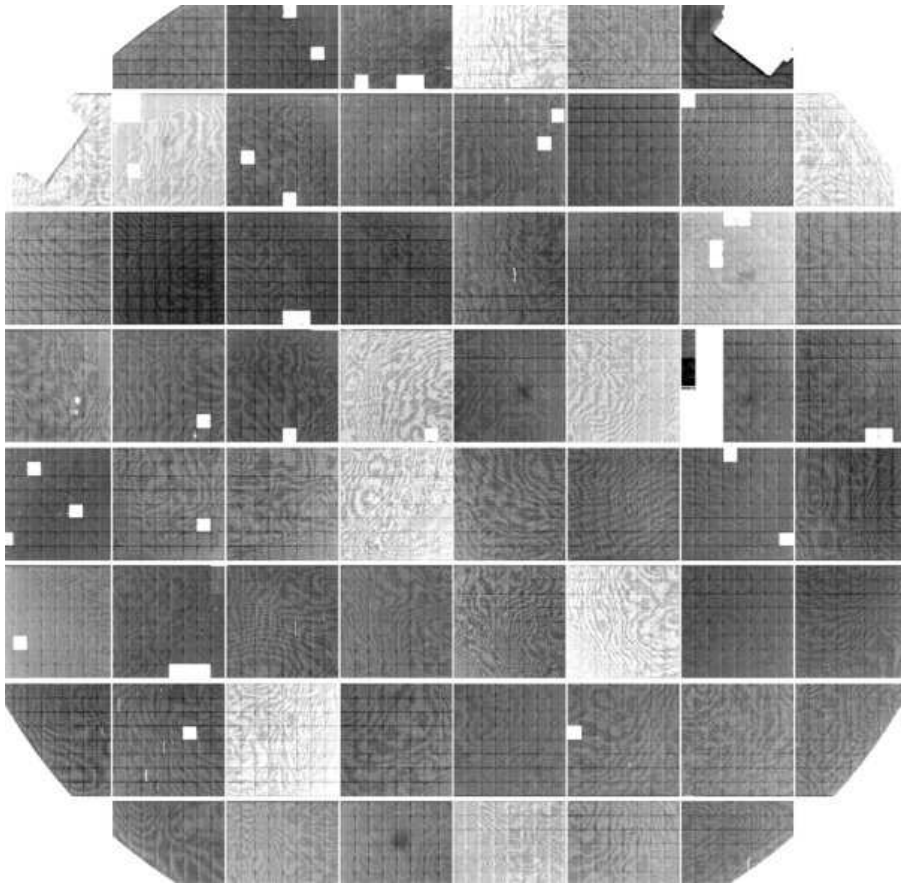

Figure 5.2: Fringing pattern in monochromatic light at 902 nm, in the z band, across the Pan-STARRS array. The peak-to-peak fringing amplitude at this wavelength is 5%. (The individual gains of the detectors have not been normalized, and that accounts for the chip-dependent variations.) This figure has been reproduced from Stubbs et al. (2010).

originally tested, it can be expected that the PS1 stellar catalogues will have a dynamic range from 6th magnitude to the limiting magnitude of the 3π Survey given in Table 5.2.

5.3 3π Survey

5.3.1 Coverage

The 3π survey will cover declinations between -30 and 90 degrees using all the photometric filters (g_{P1}, r_{P1}, i_{P1}, z_{P1} and y_{P1}). This corresponds to three quarters of the entire sky, or

Filter	Exposure/visit (sec)	Visit Limit (mag)	3 year limit (mag)	Saturation (mag)
g_{P1}	60	23.24	24.66	18.2
r_{P1}	38	22.71	24.11	17.9
i_{P1}	60	22.63	23.96	17.5
z_{P1}	30	21.59	22.98	17.3
y_{P1}	30	20.13	21.52	15.5

Table 5.2: Details of the PS1 imaging features including magnitude limits and saturation limits.

approximately 30,000 square degrees, and includes the Galactic Plane.

The survey uses an observing strategy designed to combine observations to create an all-sky photometry and astrometry catalogue with a search for solar system objects at opposition. For this reason the cadence is somewhat complicated and subject to last-minute change depending on weather and operating conditions. The basic plan behind the operation of the telescope, however, is to work in bands of R.A., each about 2 hours wide (equivalent to 30 degrees at the equator). This means that over the course of a month, providing the weather is good, the telescope will observe:

- two bands, twice each in g_{P1}, r_{P1} and i_{P1}, at opposition
- two bands, twice each in y_{P1}, adjacent to opposition
- two bands, twice each in z_{P1}, for 180 deg parallax measurements

The most important thing to note about this plan is that two bands will have been covered in each of g_{P1}, r_{P1} and i_{P1}, two different bands will have been covered in y_{P1}, and two further bands will have been covered in z_{P1}. This means that after a month no part of the sky will have coverage in all filters. The two bands covered in g_{P1}, r_{P1}, i_{P1} will have been completely covered by y_{P1} and z_{P1} after 5 months, given good weather.

Over the course of a year, each point within the 3π survey will receive 4 visits in g_{P1}, r_{P1}, i_{P1}, z_{P1} and y_{P1}. These visits are made in pairs to separate moving objects from stationary

transients. Each pair of visits is made in the same night, separated by a Transient Time Interval (TTI), which is of the order of 30 minutes.

The separation of the pairs is a function of the filter:

- g_{P1}, r_{P1}, i_{P1}: 1 month or 11 months
- z_{P1}: 6 months
- y_{P1}: 3 months or 9 months

5.4 Medium Deep Survey

The PS1 Medium Deep Survey (MDS) currently accounts for nearly 25% of observing time. It revisits 10 fields - each equivalent to a single PS1 imager footprint - on a near nightly basis in g_{P1}, r_{P1}, i_{P1}, z_{P1} and y_{P1} bands (Stubbs et al., 2010), reaching a typical 5σ limiting magnitude of $\sim$ 23.3 mag in one visit across the g_{P1}, r_{P1}, i_{P1} and z_{P1} bands and $\sim$21.7 mag in the y_{P1} band. The MDS fields are distributed across the sky, so only a small subset of the fields are being observed at any given time of the year. They are also subject to the weather conditions and phase of the Moon, so that on any given night, each field will only be being observed in a subset of bands.

The MDS fields are processed through the Image Processing Pipeline (IPP; Magnier, 2006) at the Maui High Performance Computer Center. The images then run through a succession of stages in the pipeline. These include flat fielding (termed 'detrending'), a flux-conserving warping to a sky-based image plane, masking and artifact removal and object detection and photometry. Difference images are produced from the stacked images by the PHOTPIPE pipeline (Rest et al., 2005). This flags up potential transients, which are then scanned by eye and can be promoted to become transient alerts. The IPP-PHOTPIPE pipeline flags up hundreds of possible transients per month, out of which a subset will be targeted for spectroscopic followup. The field name, position, overlapping surveys and the type of survey to be carried out in each field is given in Table 5.3.

Field	Name	Alt Name	RA (J2000)	Dec (J2000)	Comment
00	PS1MD00	M31	00 42 42	+41 16 00	M31
01	PS1MD01	XMM-LSS-DXS/VVDS-02h	02 23 30	-04 15 00	Multi-wavelength Survey Field
02	PS1MD02	CDFS/GOODS/GEMS	03 32 24	-27 48 00	Multi-wavelength Survey Field
03	PS1MD03	IFA/Lynx	08 42 22	+44 19 00	Radio Survey Field
04	PS1MD04	COSMOS	10 00 00	+02 12 00	Multi-wavelength Survey Field
05	PS1MD05	Lockman-DXS	10 47 40	+58 05 00	Multi-wavelength Survey Field
06	PS1MD06	NGC 4258	12 20 00	+47 07 00	H20 Maser
07	PS1MD07	DEEP2 Field 1	14 14 49	+53 05 00	Multi-wavelength Survey Field
08	PS1MD08	ELAIS-N1-DXS	16 11 09	+54 57 00	Multi-wavelength Survey Field
09	PS1MD09	SA22-DXS/VVDS-22h	22 16 45	+00 17 00	Multi-wavelength Survey Field
10	PS1MD10	DEEP2-Field3	23 29 15	-00 26 00	Multi-wavelength Survey Field

Table 5.3: Details of the 10 MDS fields.

5.5 Variable objects in 3π

In order to search for variable objects in 3π, difference imaging software was developed. As the survey is taking TTI pair images for the NEO search this reduces the complexity in the difference imaging. There is also the added advantage that for several fields there are TTI quad images available, where the same field is observed by two TTI pairs separated by a few hours. Over one month the survey covers 2000-3000 deg^2 (in three bands made up of g_{P1}, r_{P1} and i_{P1}) differenced with respect to a reference which would have been taken within ~ 5 - 6 days. This means that the survey can search for very young transients and can also pick up existing transients on the rise, providing the rise is large enough. The area covered by the survey is large enough to be competitive and interesting with respect to other transient searches.

5.5.1 Faint Galaxy Supernovae Survey

The Faint Galaxy Supernovae Survey (FDSS) is an extension of the transient pipeline, run out of Queen's University, Belfast, and was set up to search for transients associated with faint SDSS objects. The server will automatically cross-match 3π catalogued sources with SDSS and look for objects with greater than ~ 1.5 mag difference between the two. Additional checks to make sure that the detections are real are described in the next section; the

detectible magnitude range of transients is $\sim$ 16 - 19 mag.

The FGSS was originally set up as a method of probing for nearby supernovae in faint hosts, but has become useful in showing the breadth of transient events that can be found. As the FGSS has been running on and off for 18 months there have now been enough classification spectra taken to shown that the survey is successful at identifying variable QSOs, flare stars, CVs and supernovae in faint galaxies.

A few of the most interesting things to note about this survey is that if the transient is coincident with an object classified by SDSS as a faint galaxy, then it is nearly always ($>$ 95%) a supernova, while if the transient coincident with an SDSS point source (either QSO colours, or stellar colours) then $\sim$ 90% of time it will be a QSO, CV or flare star. However, examples of misclassification in SDSS have been found, as SN2010gx was coincident with an SDSS 'star' but turned out to be a galaxy. Detections of both supernovae and other point source objects are improving particularly as the cadence of the 3π survey improves.

5.5.1.1 Finding real transients in FGSS

The difficulty in finding real transients lies in separating what the transient pipeline can class as a transient and what is a real event. Initially all the data is processed through the main PS1 image processing software, IPP. The IPP can assign several flags to the reduced data, and the first check is to ensure the image is classed as a good detection. To be classed as a good detection, it must meet four standards: that the 'psf_mag' is finite, that the 'aperture_mag' is finite, that the detection does not have a 'bad detection' flag and, finally, that the detection *does* have a 'good detection' flag.

Once the image is classed as a good detection, the SDSS data that the object will be compared to is checked. The SDSS magnitudes used are 'modelMag', as they provide the best match to the aperture used in the IPP. Then the SDSS limiting magnitudes are considered and all of the data with magnitudes fainter than the limiting magnitude is excluded, but only in the band where the measured magnitude is fainter. These limits are $g_{SDSS} = 24.3$, $r_{SDSS} = 23$, $i_{SDSS} = 23.3$ and z_{SDSS} =21.8.

Once the data quality has been established, spacial cuts are made. Firstly, all PS1 detections that have an SDSS detection within 3" are considered. Usually only the closest

SDSS detection to the PS1 detection is used. However, if there is more than one SDSS detection within 3" of the PS1 detection then the second closest one will also be considered if the difference between the SDSS detection and the PS1 detection of both objects is less than 1". If either of these two objects used for comparison has another SDSS object within 1" of its position, the extra object is not compared to the PS1 detection. This is due to a subset of single objects that have double detections in SDSS when in reality there is only one object.

The final step is to compare the magnitudes of the SDSS objects that pass the spacial cut with the PSF magnitudes of the PS1 detection. If the PS1 magnitude is brighter than the matched SDSS object (or either of the objects, if there are two) by 1.5 magnitudes then a quality control flag is turn to 'ON' for a PS1 detection. Once an object has more than one detection where the quality control flag is 'ON' then the object is reported to the eyeball list for visual inspection. This means that for a detection to make it through to the eyeball list it has to have been observed at least twice and flagged either in two different bands, or from the same band twice.

Visual inspection is the first look at the data once it comes out of the transient detection pipeline. At this point there can be up to 100 detections flagged per day but around 95% of them will be rejected at this stage. The easiest detections to reject are ones where the image is a washout and no defined objects can be seen. Currently, the IPP has difficulty measuring extended sources, and will detect sources on bright/noisy backgrounds when none are present. Other detections are rejected when objects are too close together to be resolved separately, a nearby bright source has lead to over-subtraction of the background, or due to chip gaps and bad pixels. The US Air Force are also using PS1 to track satellites and in order to keep the locations of the satellites secret, they remove them from the data by removing large sections of the area affected. In order to prevent satellite tracking, other random areas of data are removed before the data is passed to the IPP for data reduction. This process is called MAGIC and at one point removed over 90% of the data before it could be processed; over time this amount has been reduced until in January 2012 it was announced that MAGIC would be no longer applied to any future data taken by PS1, but to date the previous images have not yet been corrected. Example of the effect that a bad

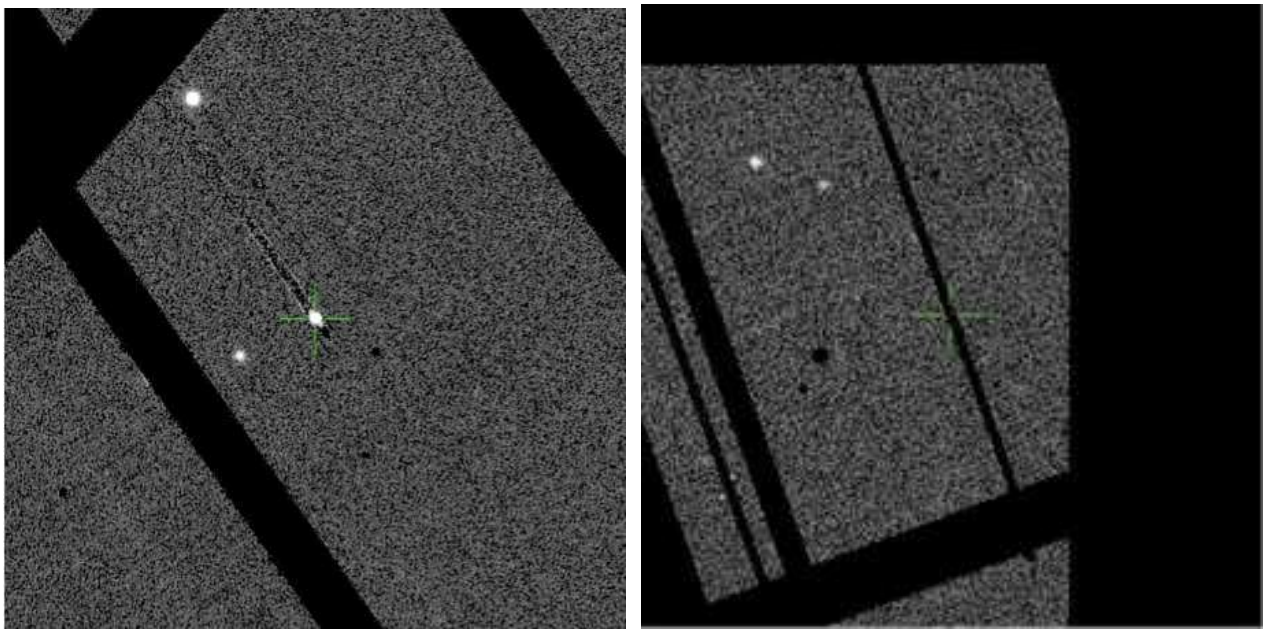

Figure 5.3: *Left panel:* A bad pixel causing a false transient detection. The solid black areas are where data has been removed by the magic software. *Right panel:* Data removed from the image by MAGIC causing a false transient detection. It can be seen that this process can black out a substantial fraction of the image.

pixel and MAGIC can have on images is shown in the left- and right-hand panels of Figure 5.3 respectively. It should be noted that a chip gap produces a very similar result to what is shown in the right-hand panel of Figure 5.3.

5.6 PS1-10adi

PS1-10adi was discovered by the PS1 FDSS at a J2000 location of R.A. = 20h:42m:44.73s (310.686358), decl. = 15d:30m:24.5s (15.506817) (uncertainty in position $\approx$ 0.05 arcsec). It was first detected on 2010-07-14, and on 2010-08-15 it was flagged by the FDSS transient database due to its rising flux in the PS1 g_{PS1} photometric observations. The image that caused the pipeline to flag the object is shown in Figure 5.4. It was seen to have brightened by 0.5 magnitudes in 2 months. This event was flagged for spectroscopic follow-up on the Nordic Optical Telescope (NOT), as no previous spectrum was available for it. Additionally, there was no detection in archival FIRST and NRAO VLA Sky Survey (NVSS) radio data

covering the object's location. The lack of any radio source suggests that the variability was not being powered by a jet, as is seen in the case of optically violent variable (OVV) quasars. The initial spectrum was taken by ALFOSC on the NOT on 2010-08-29. This spectrum, along with the best fit to a Type II supernova template and an AGN are shown in Figures 5.5 and 5.6 respectively. Both fits put the object at a redshift of z = 0.203. Figure 5.5 shows the fit to Type IIn supernova, SN1995G. The features that appear in the spectrum of a Type IIn supernova depend on how long after the initial event it was taken. The spectrum evolves quickly and the overall shape of the spectrum seen is highly dependent of the amount of host galaxy contamination. The AGN template used is a standard broad line Type I Seyfert spectrum, and while it is not in excellent agreement with the object's spectrum all of the main defining emission lines seen in an AGN are present in the spectrum. As the spectrum provides a good fit to both the AGN and SN template, with neither one providing an excellent fit, it was difficult to characterise the true nature of the object is and further follow-up observations were scheduled.

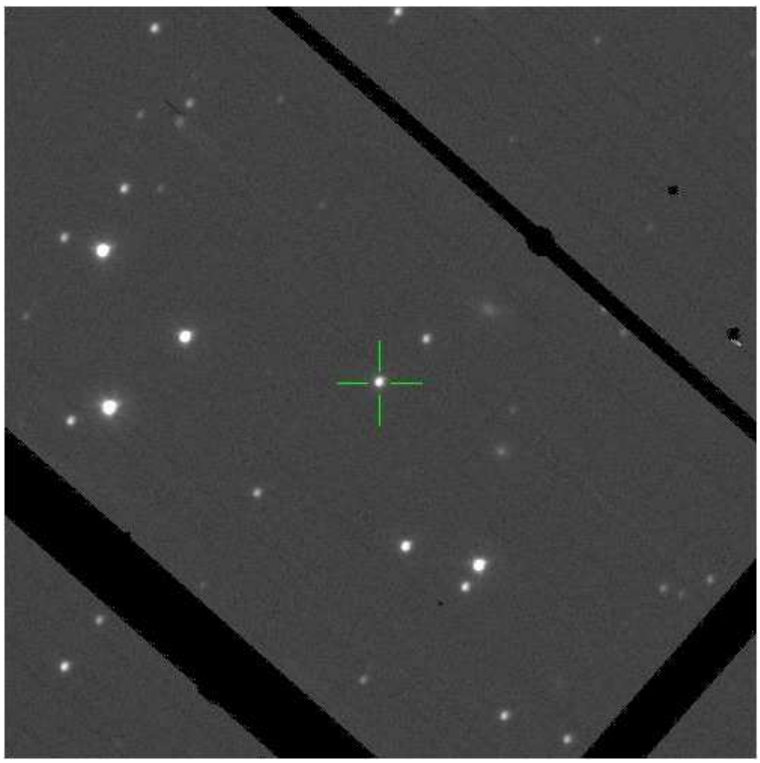

Figure 5.4: The i_{P1} band image of PS1-10adi taken on 2010-08-14 that provided the second detection needed to flag the object as a transient detection in FGSS.

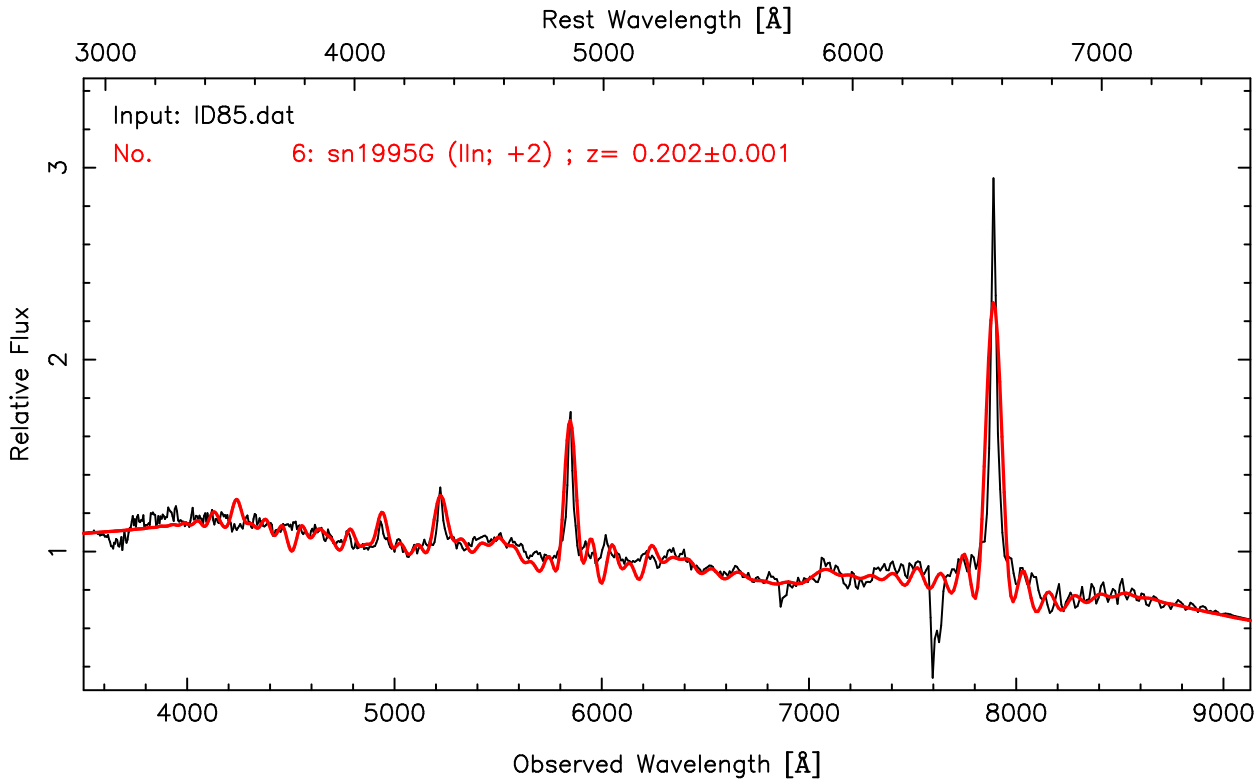

Figure 5.5: Initial spectrum of PS1-10adi taken on 2010-08-29 shown in black, fit to the template of Type IIn SN1995G, shown in red.

5.6.1 Multi-wavelength follow-up observations

Following the discovery of what was clearly an energetic event we undertook follow-up observations in the X-ray, UV, optical and near-IR wavelengths, as well as searching through archival γ-ray data. We also searched the Catalina Transient Survey, which has been running for 10 years, for archival data, but the survey does not cover the position. In Table 5.4 we present the sequence and nature of the follow-up observations we obtained. Table 5.5 presents the dates and values of all photometric observations of PS1-10adi. In the following section we will discuss the details of each set of observations. We will then combine the data to interpret the nature of the event in relation to known types of transient, and finally try to make some concluding remarks about the source.

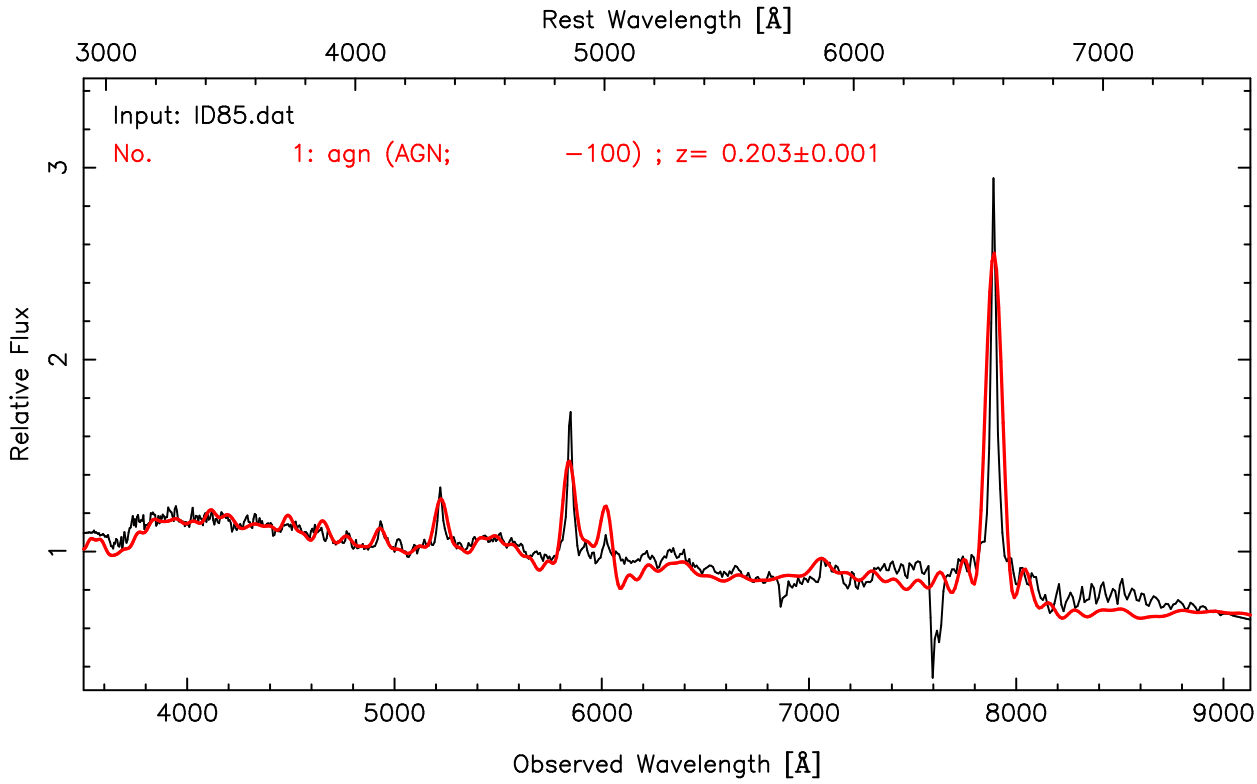

Figure 5.6: Initial spectrum of PS1-10adi taken on 2010-08-29 shown in black, fit to an AGN template, overplotted in red.

5.6.1.1 UV, Optical and Near-IR Photometry

Following the discovery of PS1-10adi a photometric monitoring campaign was set up on the Liverpool Telescope (LT) and the Nordic Optical telescope (NOT), to take photometric data when able and take a spectrum of the object approximately once a month.

The SDSS photometric observations taken in late 2004 exhibit g_{SDSS} and r_{SDSS} magnitudes of 20.41 and 19.65 respectively, and are given in Table 5.5. The SDSS classification of the object is as a galaxy due to its photometric colours, with a 'TARGET_QSO_FAINT' flag raised. An additional search through archival DSS data taken at the Palomar 48-inch Telescope in 1951 shows the object to be just above the detection limit of the telescope R = 20.3 (Harrington, 1952). This suggests that the object is either relatively stable on very long timescales, or exhibits quiescent outbursts that fade to a constant level.

Optical follow-up was taken soon after the PS1 trigger on the LT 2.0m telescope at La Palma, Spain in Sloan u', r' and i' filters and Bessel B and V filters. Data was also

Telescope + Instrument	Passbands	Observation Date (YYYY-MM-DD)
Photometry	**Filters**	
SDSS	u_{sdss}, g_{sdss}, r_{sdss}, i_{sdss}, z_{sdss}	2004-10-13
NOT	*U, B, V, R, I*	multi-epoc 2010-08/12, 2011-02/06
Pan-Starrs	g_{P1}, r_{P1}, i_{P1}	2010-07-14/2010-08-19
LT + RATcam	*B, V, u', r', i'*	2010-09-17,30, 2010-10-09,27, 2010-11-06
SWIFT + UVOT	*UVW1, UVM2, UVW2, U, B, V*	2010-10-06, 2010-12-09
NOT + NOTCAM	*J, H, K*	multi-epoc 2010-10/12, 2011-04/06
Spectra	**Wavelength Range (Å)**	
NOT + ALFOSC	3800-8300	2010-08-29, 10-06: 2011-02-03,05-10,06-08,08-24,11-08
WHT + ISIS	4000-7500	2011-05-06
X-ray	**Energy (keV)**	
SWIFT + XRT	0.2 - 10	2010-10-06, 2010-12-09

Table 5.4: Observations of PS1-10adi.

taken in Bessel *U, B, V, R* and *I* filters at the NOT 2.5m telescope, also on La Palma, Spain. The data was reduced and calibrated by the LT and NOT pipelines respectively. In order to both supplement the optical data and constrain the possibility that this event was a tidal disruption event (TDE: where a star near to a black hole is ripped apart by gravitational forces), we requested *Swift* Target of Opportunity (ToO) time to observe the object at optical, UV and X-ray wavelengths. These observations clearly showed that the object was very bright in the UV, but that the source was not detected in the X-rays.

In Figure 5.7 we show the photometry of PS1-10adi during the early phase of its decline. We show the ground-based optical filters *U, B, V, R* and *I* and the PS1 g_{P1} band. The *Swift* optical data is in good agreement with the ground-based observations, with the slight differences probably due to difference in the central wavelength and effective width of the filters, a difference that is the most pronounced in the *B* filters. There is a known offset between the *Swift* filters, and when $(U - V) < 0$ the difference is significant and the transformation to standard magnitudes is poorly constrained (Li et al., 2006). Due to this we did not convert the *Swift* magnitudes to the standard system.

From the PS1 photometry before the transient was flagged, we find that peak luminosity occurred on 2010-08-16. We fit three decline rates for each of the optical ground-based filters. The first decline rate is from the start of the photometric campaign to when the

MJD	Band 1	Band 2	Band 3	Band 4	Band 5	Band 6
SDSS	u_{sdss}	g_{sdss}	r_{sdss}	i_{sdss}	z_{sdss}	
53291.56	20.88±0.09	20.41±0.02	19.65±0.02	19.19±0.02	18.95±0.07	
PS1	g_{P1}	r_{P1}	i_{P1}	z_{P1}	y_{P1}	
55391.4	18.216±0.029	...	...	...	...	
55423.2	...	17.597±0.026	...	...	...	
55423.3	...	17.574±0.037	...	...	...	
55423.5	17.838±0.018	...	...	...	...	
55423.6	17.872±0.026	...	...	...	...	
55427.3	...	...	17.321±0.018	...	...	
NOT	*U*	*B*	*V*	*R*	*I*	
55442.40	17.071±0.020	17.679±0.009	...	...	...	
55450.57	17.130±0.017	17.756±0.010	17.447±0.006	17.154±0.007	16.732±0.011	
55476.32	17.282±0.018	17.829±0.011	17.497±0.006	17.228±0.007	16.749±0.007	
55491.38	17.288±0.022	17.854±0.013	17.525±0.009	17.250±0.006	16.759±0.009	
55648.75	18.008±0.027	18.629±0.019	18.134±0.011	17.860±0.014	17.221±0.011	
55661.73	18.020±0.021	18.705±0.014	18.212±0.009	17.907±0.012	17.276±0.013	
55718.62	18.272±0.026	18.880±0.017	18.455±0.014	18.151±0.015	17.412±0.019	
55774.47	18.393±0.037	19.097±0.017	18.604±0.012	18.283±0.013	17.580±0.026	
55809.37	18.505±0.042	19.196±0.017	18.770±0.015	18.450±0.017	17.741±0.013	
LT	*u'*	*B*	*V*	*r'*	*i'*	
55438.43	...	17.651±0.010	17.396±0.007	17.153±0.007	16.714±0.008	
55457.36	...	17.757±0.024	17.435±0.016	17.123±0.010	16.692±0.013	
55470.38	...	17.812±0.012	17.499±0.011	17.166±0.007	16.730±0.008	
55479.33	...	17.809±0.011	17.478±0.011	17.167±0.007	16.730±0.007	
55497.31	...	17.881±0.014	17.555±0.012	17.227±0.007	16.753±0.008	
55507.33	17.335±0.032	17.954±0.015	17.619±0.013	17.285±0.009	16.788±0.009	
55509.33	17.443±0.016	18.010±0.010	17.640±0.008	17.340±0.006	16.834±0.010	
55517.41	...	18.057±0.048	17.663±0.024	...	16.827±0.016	
Near-IR	*J*	*H*	*K*			
55469.38	16.068±0.019	15.319±0.018	14.486±0.011			
55498.37	15.886±0.020	15.052±0.021	14.122±0.048			
55519.35	16.081±0.062	15.323±0.057	14.191±0.044			
55543.34	16.027±0.038	15.194±0.040	14.039±0.044			
55666.72	16.395±0.122	15.458±0.069	14.130±0.040			
55697.70	16.246±0.022	15.242±0.021	14.315±0.025			
55723.61	16.255±0.042	15.312±0.051	14.118±0.053			
55787.64	16.526±0.041	15.502±0.035	14.351±0.031			
55818.53	16.537±0.042	15.545±0.026	14.443±0.040			
SWIFT	*UVW1*	*UVM2*	*UVW2*	*U*	*B*	*V*
55476.26	17.01±0.03	17.71±0.06	17.95±0.02	17.22±0.03	17.75±0.04	17.59±0.04
55477.34	...	...	...	17.26±0.04	...	...
55539.33	17.32±0.02	18.02±0.03	17.18±0.05	17.44±0.04	18.02±0.04	17.71±0.03

Table 5.5: Filtered Photometry of PS1-10adi.

object moved behind the Sun, the second is from when the object re-emerged to when the monitoring campaign ceased and the third is over the entire time the object was monitored. For the *Swift* filters only one decline rate was measured, as there were only two sets of observations. We find that the decline rates are the steepest in the bluest filters, with 0.006 mag day^{-1} in the U filter to 0.001 mag day^{-1} in I. The rapid decline at bluer wavelengths is consistent with an outburst that is cooling over time. The rates of decline of the *Swift* bands were higher than the redder filters, but as the ToO observation was not done until $\sim$ 2 months after the initial optical observations had taken place this is not a good reflection of the decline rate in the UV. We find that after the object reappears the rate has dropped to 0.003 mag day^{-1}in both the U and I filters.

The decline rates seen in the optical are consistent with the lower range observed for Type IIn supernovae (Trundle et al., 2009); however if this was a supernova then the true decline rate of the transient would be much greater than what is quoted above as the photometry would include both the transient and the host galaxy. When comparing to a similar object discovered by the Catalina Transient Survey, CSS100217 (Drake et al., 2011), we find that the latter's decay rate is much more rapid and follow the decline rates of Type IIn supernovae more closely than PS1-10adi does.

The foreground Galactic extinction for this object is $A_V = 0.25$, based on the Schlegel et al. (1998) reddening maps. We do not see any evidence for host galaxy extinction in the spectra of the object, suggesting that this is a small effect. If we apply a V-band reddening correction and a K-correction of 0.1 mag, to account for the effective rest-frame bandwidth, we find that the peak luminosity is $M_V = -23.6$.

The near-IR observations were all carried out with the NOTCAM on the NOT, and the data was reduced using the standard NOT pipelines. The processed magnitudes are shown in Figure 5.8. Unlike the optical data there is little clear evidence for a decline in luminosity. Instead, for the first 4 months of observations the flux was rising. Initially all three bands show a magnitude increase ranging from 0.0006 mag day $^{-1}$ in the J band, to 0.006 mag day^{-1} in the K band. This effect may be attributed to the cooling of expanding material. The object is brighter than 2MASS in the follow-up observations by $\Delta J \sim 1.2$, $\Delta H \sim 1.4$ and $\Delta K \sim 1.6$ mag. While strong near-IR excess has been observed in many Type IIn

supernovae, interpreted as thermal emission from dust in a pre-existing circumstellar nebula, it can also be consistent with thermal reprocessing by dust, which would allow the event to be an outburst from an AGN if the dust is close to the black hole. If PS1-10adi is a Type IIn SNe, then the near-IR emission would be expected to increase initially and then gradually decline over a period of years (Dwek, 1985; Pozzo et al., 2004).

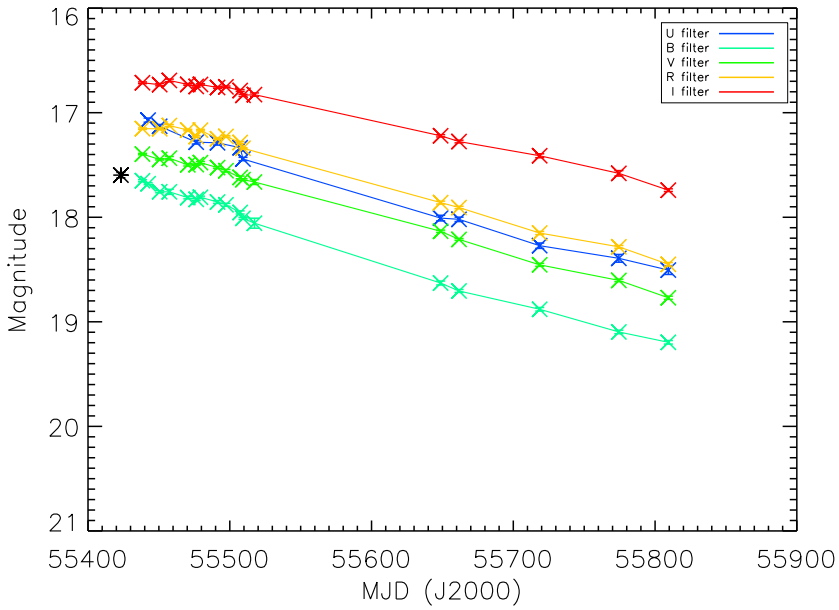

Figure 5.7: The multi-colour evolution of PS1-10adi, showing the black point from the PS1 g band that triggered the observation and subsequent LT and NOT follow-on observations. The LT magnitudes were corrected so that all observations show Bessel *U, B, V, R* and *I* filters. For the distance of this object, an absolute magnitude of -21 is equal to an apparent magnitude of 19, -22 = 18, -23 = 17 and -24 = 16.

In order to determine whether PS1-10adi was due to an event in the nucleus, as in the case of AGN variability or a TDE, we needed to investigate the location of the event. Due to the process by which the transient server looks for supernovae and the need to determine their position in the host galaxy, there is already a difference imaging pipeline available. We used this pipeline to determine the location of the flux of PS1-10adi relative to the location of the SDSS source. This pixel by pixel mapping showed that the event is within ~ 0.2" of the SDSS source, which is the limit that this process can resolve to. If the object is at z =

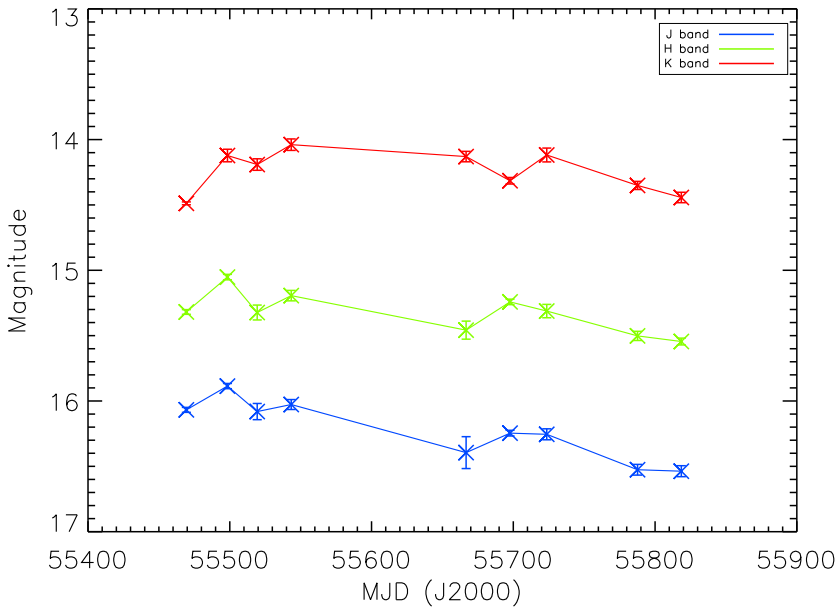

Figure 5.8: The near-IR light curves for PS1-10adi in *J, H* and *K* bands. For the distance of this object, an absolute magnitude of -23 is equal to an apparent magnitude of 17, -24 = 16 and -25 = 15.

0.203 this gives an angular size distance, D_A, of 681.9 Mpc, which gives a scale of 3.306 kpc arcsec^{-1}. This means that PS1-10adi is within 660 pc of the nucleus of the SDSS source.

5.6.1.2 Optical Spectra

When PS1-10adi was discovered and the initial spectrum was taken by the WHT it was immediately recognised as an unusual object. There was no archival optical spectral data for the object, but SDSS had classed it to be a galaxy based on its photometric colours and there was no evidence of any previous outbursts. In Figure 5.10 we present the evolving spectrum of PS1-10adi taken between August 2010 and October 2011. The spectrum is very similar to an AGN with clear Balmer (Hα, Hβ and Hγ), [O III], and Fe II emission lines. The Balmer emission places the event at a redshift of z = 0.203, and there is no indication of a separate similar event along the same line of sight but at a different redshift.

As there is no pre-outburst spectrum available we cannot make any clear distinctions between the spectral features that are due to the outburst event and those that can be

attributed to the host galaxy itself. Instead, we can only look at how the spectrum evolves over time, studying in depth the changes between initial and final spectra taken. This covers a period of 14 months, and the intermittent spectra taken on an approximately monthly basis when the object was visible give an indication as to when the features began to evolve.

The initial spectrum was taken by ALFOSC on the NOT on 29 August 2010 and we used that as the basis for our subsequent analysis. The emission line features observed in the spectrum are similar to those seen in a NLSy1, except for Hα having a broad component at its base. When these lines were deconvolved using the same method as used in Chapter 3 we find that we can easily fit a broad and narrow component to Hα, while a three component fit with an extra intermediate component is more difficult. We found that the broad base of Hα was not as obviously present in Hβ, as simultaneous fitting of the Hα and Hβ lines produced unsatisfactory results. Due to the quality of the spectrum and the ambiguity of the strength of the [O III] lines we overestimate the width of the broad Hβ component. The [N II] lines were poorly modelled as they are convolved with the Hα line and line widths could not be established. For the [O III] we found that we could only model the stronger line from the doublet, as the weaker component, if present, was convolved with the wings of Hβ. The results from the line fitting analysis for this spectrum are shown in the first column of Table 5.6.

Various studies have been carried out into objects that lie around the starburst/AGN dividing line in the standard BPT emission line diagrams, and it has been found that while usually NLSy1s lie towards the upper right of the AGN region on a BPT diagram, they can also be found close to the dividing line. Mao et al. (2009) studied three of these objects, one of which was in the star-burst region while the other two were in the dividing composite region. They concluded that the objects were AGN that were buried in an H II region where the galaxy is transitioning from a star-burst dominated phase to an AGN dominated one. As we could not take measurements for the [N II] and [O II] lines and the [O I] line was lost due to an spectrograph fault at that wavelength, we cannot carry out the usual BPT analysis. The only line ratio that we can resolve is the [O III]/Hβ ratio. This places PS1-10adi along the bottom of a BPT diagram, far from where NLSy1 usually reside. However as we know from the line fitting routine that we underestimated the flux of [O III] and overestimated

the flux of Hβ, if the ratio changes so that [O III]/Hβ = 0.5 then PS1-10adi would fall into the range of known NLSy1s (Mao et al., 2009). To highlight the spectral similarities of PS1-10adi with NLSy1, Figure 5.12 shows three spectra from PS1-10adi compared to the spectrum of a NLSy1 at a similar redshift.

It is the discernible detection of the broad components of the Balmer lines that indicates the presence of an AGN, however it is also known that core-collapse Type II supernovae produce lines of a similar breadth to those seen. In Izotov et al. (2007) they discuss the possibility of this arising from multiple supernova events and massive star-forming regions, but the probability of these events occurring is not large and over time the spectrum of the object will show these features fading as the event that caused them fades.

A further spectral emission feature that supports the NLSy1 hypothesis is the abundance of strong Fe II. While the spectra does show this, it is known that Type IIn supernovae also show strong Fe II emission features as they evolve. This is discussed in more detail in the next section.

The evolving spectrum of PS1-10adi

Over 14 months between August 2010 and October 2011 eight spectra were taken, of which six were of good quality where we were sure of the flux calibration. Of these five were taken by ALFOSC on the NOT and one was taken by ISIS on the WHT. Over the course of the year the continuum level is seen to drop steadily, and the strength of both the Hα and Hβ emission increases.

One test for whether the outburst of PS1-10adi is due to AGN activity can be derived from emission line characteristics. Again, we are limited in our analysis as there is no pre-outburst spectra, and so we cannot subtract the host galaxy contribution from the emission lines. Figure 5.9 shows the Hα and Hβ line fits, using the method outlined in Chapter 3, for the August 2010, November 2010 and October 2011 spectra, at the top, middle and bottom of the figure respectively. The major problem that arose during this process was that the broad base of Hα is not found in Hβ and the two lines do not show the same component widths, as we expect them to. In each spectrum the broad component of Hβ is convolved

with emission that can be associated with weaker line of the [O III] doublet. This is especially true in the October 2011 spectrum where the line has a large velocity associated with it which moves the line from under Hβ towards [O III]. The results of the fitting routines are shown in Table 5.6.

From the line fits it can be seen that in the case of Hα the final fit with three components is the better one, as both of the other two spectra show that the narrow top of the emission is not modelled.

A possible interpretation of these fits is that the true narrow component of Hα is not modelled in the first two spectra, only the intermediate component. This component increases in width between November 2010 and October 2011, by which point a single component cannot be made to fit both features. If we consider the Hα broad base is actually blended with other spectral features we do not account for, we would always overestimate the width of the broad component. By forcing the broad component to be so broad, it forces the intermediate and narrow components to model flux that should be included in the broad component and could account for the poor fits seen. The substantial decrease in the width of the broad component would provide a much better fit to the broad component of Hβ and also would fall within the definition of a NLSy1.

5.6.1.3 X-ray observations

Two sets of X-ray observations were taken, both with the *Swift* X-ray Telescope (0.2 - 10 keV), to detect whether there was X-ray emission from the object and to rule out events such as a TDE that would have a strong soft excess component in the soft X-rays. The initial observation was taken on 2010-10-06 and comprised of 5 x 5 ks exposures. The object was undetected, so we derived upper limits for both the full XRT energy range (0.3 - 10 keV) and the hard band (2 - 10 keV). The upper limits for the source counts as a function of confidence level are shown at the top of Table 5.7. The limits were calculated by combining all three observations, to yield a mean exposure time at the source position of 10,265 s. We then followed the methodology of Kraft et al. (1991). The inputs we used were the measured number of counts in a reasonable source extraction region and the expected background count rate for this same region. The region was a 1.5' diameter circle centred on the coordinates

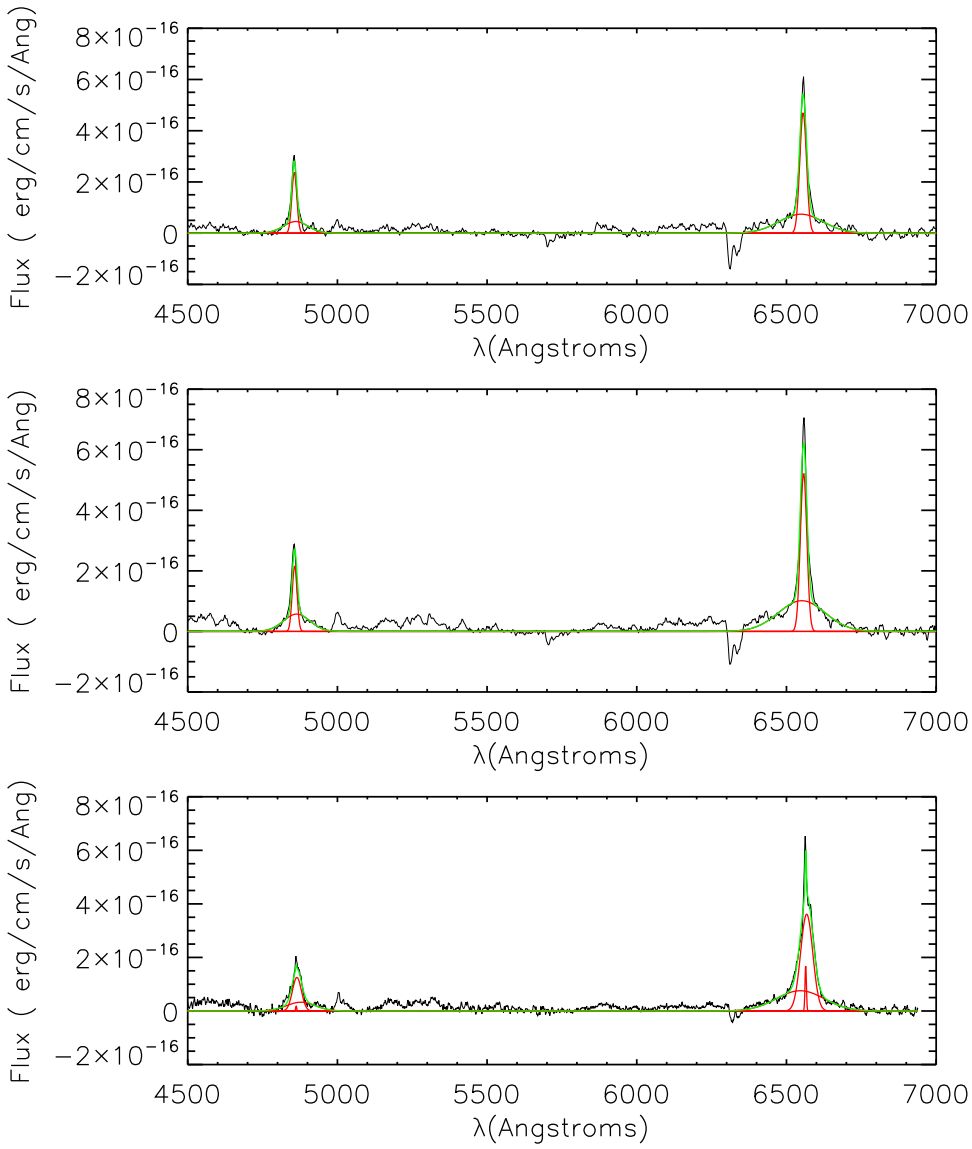

Figure 5.9: *Top panel:* August 2010 - Hβ - Hα region showing the results of the fitting routines used to measure the line profiles. Only two components are fit to each line, and it can be seen that the broad emission of Hβ is convolved with the weaker emission from the [O III] doublet. *Middle panel:* November 2010 - As above. *Bottom panel:* October 2011 - As above, but this time the emission is fitted with three components as the intermediate component is significantly wider than was seen previously, allowing for an additional component to fit the narrowest emission.

of PS1-10adi. The measured number of counts in this region is 5 in the 0.3 - 10 keV band and 2 in the 2 - 10 keV band. The estimated background count rates are 7.121 and 3.114

MJD	August 2010	November 2010	October 2011
Hα - 6564.61Å			
Broad component			
FWHM (km s^{-1})	8000±250	8410±280	8640±360
Velocity (km s^{-1})	-740±140	-620±160	-850±140
Flux (erg cm^{-2} s^{-1}Å^{-1})	$1.36 \pm 0.02 \times 10^{-14}$	$1.98 \pm 0.03 \times 10^{-14}$	$1.52 \pm 0.04 \times 10^{-14}$
Intermediate component			
FWHM (km s^{-1})	0	0	2180± 130
Velocity (km s^{-1})	0	0	130±15
Flux (erg cm^{-2} s^{-1}Å^{-1})	0	0	$1.83 \pm 0.02 \times 10^{-14}$
Narrow component			
FWHM (km s^{-1})	1200±150	1160±140	250±50
Velocity (km s^{-1})	-410±130	-340±80	-20±30
Flux (erg cm^{-2} s^{-1}Å^{-1})	$1.31 \pm 0.01 \times 10^{-14}$	$1.41 \pm 0.01 \times 10^{-14}$	$1.01 \pm 0.06 \times 10^{-15}$
Total Hα Flux (erg cm^{-2} s^{-1}Å^{-1})	$2.67 \pm 0.02 \times 10^{-14}$	$3.39 \pm 0.04 \times 10^{-14}$	$3.45 \pm 0.06 \times 10^{-14}$
Hβ - 4862.68Å			
Broad component			
FWHM (km s^{-1})	5960±140	6430±320	7150±230
Velocity (km s^{-1})	-120±20	80±30	960±460
Flux (erg cm^{-2} s^{-1}Å^{-1})	$4.68 \pm 0.16 \times 10^{-15}$	$6.34 \pm 0.17 \times 10^{-15}$	$3.96 \pm 0.20 \times 10^{-15}$
Intermediate component			
FWHM (km s^{-1})	0	0	2180±130
Velocity (km s^{-1})	0	0	130±15
Flux (erg cm^{-2} s^{-1}Å^{-1})	0	0	$4.70 \pm 0.05 \times 10^{-15}$
Narrow component			
FWHM (km s^{-1})	1199±160	1160±140	250±50
Velocity (km s^{-1})	-410±130	-340±80	-20±30
Flux (erg cm^{-2} s^{-1}Å^{-1})	$4.90 \pm 0.08 \times 10^{-15}$	$4.33 \pm 0.08 \times 10^{-15}$	$8.02 \pm 0.05 \times 10^{-17}$
Total Hβ Flux (erg cm^{-2} s^{-1}Å^{-1})	$9.58 \pm 0.20 \times 10^{-15}$	$1.67 \pm 0.03 \times 10^{-14}$	$8.74 \pm 0.21 \times 10^{-14}$
[O III] - 5008.24Å			
Flux (erg cm^{-2} s^{-1}Å^{-1})	$1.1 \pm 0.3 \times 10^{-15}$	$1.92 \pm 0.05 \times 10^{-15}$	$1.94 \pm 0.03 \times 10^{-15}$

Table 5.6: Line width measurements of PS1-10adi from three epochs

counts per second in the full and hard bands, respectively.

To convert these XRT count rates to limiting fluxes we had to assume a spectral model. We then used the WebPIMMS tool provided by *HEASARC*.[2] In order to determine the 2.0 - 10.0 keV (observed) hard band flux limit at the 95% confidence level we used an absorbed power law model with $\Gamma = 1.7$ with a Galactic $N_H = 6.48$ x 10^{20} cm^{-2}. This gave an observed 2 - 10 keV flux upper limit of 3.6 x 10^{-14} erg cm^{-2} s^{-1}, or an intrinsic 2 - 10 keV flux of 3.6 x

[2]http://heasarc.gsfc.nasa.gov/Tools/w3pimms.html

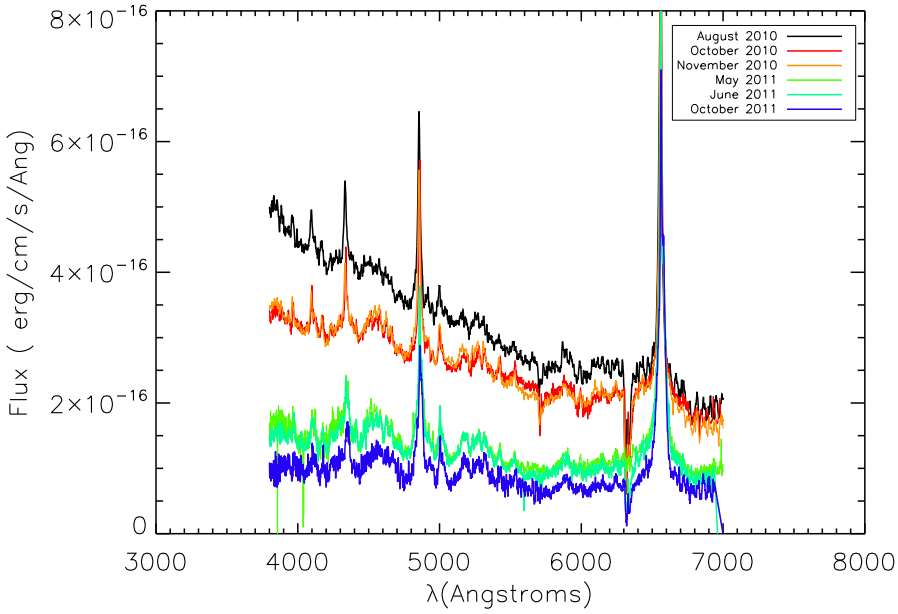

Figure 5.10: The complete evolving spectrum of PS1-10adi. This figure shows 6 spectra taken over 14 months. It can be seen that during the first 4 months only the blue end of the spectrum is decreasing in brightness. After 6 months the underlying continuum has decreased in brightness and there is no longer a blue bump present. Over the next 5 months, there is a slight decrease in the continuum luminosity across the optical spectrum.

10^{-14} erg cm^{-2} s^{-1}, where in this case it is intrinsic as it has been corrected for absorption, but the flux given is still in the observed 2 - 10 keV energy band without accounting for redshift.

A second observation with *Swift* on 2010-12-09 resulted in 3.7 ks of usable data; the limiting count rates were obtained by the same method as discussed previously and are shown at the bottom of Table 5.7. These new count rates gave an observed 2 - 10 keV flux limit of 9.8 x 10^{-14} erg cm^{-2} s^{-1}, or an intrinsic 2 - 10 keV flux of 9.8 x 10^{-14} erg cm^{-2} s^{-1}.

Converting the upper limit flux from the second observation to luminosity gives $L_{2-10keV} < 1.1 \times 10^{43}$ erg s^{-1}. This is well within the range of AGN X-ray luminosities (see Section 3.6) and therefore a none-detection cannot rule out that PS1-10adi may be an AGN.

Observation 1		
Energy band:	Full (0.3-10 keV)	Hard (2.0-10 keV)
99% conf UL:	7.64×10^{-4} cts s^{-1}	6.28×10^{-4} cts s^{-1}
95% conf UL:	5.30×10^{-4} cts s^{-1}	4.30×10^{-4} cts s^{-1}
90% conf UL:	4.22×10^{-4} cts s^{-1}	3.40×10^{-4} cts s^{-1}
Observation 2		
Energy band:	Full (0.3-10 keV)	Hard (2.0-10 keV)
99% conf UL:	1.4651×10^{-3} cts s^{-1}	1.5811×10^{-3} cts s^{-1}
90% conf UL:	0.7651×10^{-3} cts s^{-1}	0.8618×10^{-3} cts s^{-1}

Table 5.7: Formal limits for the X-ray count rates as a function of confidence level for the two *Swift* observations.

5.6.2 The Energetics of PS1-10adi

The extreme luminosity that we have seen in PS1-10adi makes it obvious that there is a great deal of energy powering this event. In order to determine the bolometric output from this object we modelled the SED of the object in the optical to X-ray region using the OPTXAGN model described in Section 3.2. In order to model the SED we first had to estimate the black hole mass from Hβ line fitting; this gave a black hole mass of $\sim 10^7$ $M_\odot$. We combined this with the X-ray upper limit and the first set of *Swift* UVOT data to constrain the X-ray and optical sides of the UV gap respectively.

As only an upper limit was available in the X-rays many parameters were frozen so that the model could match them. The soft component part of the model was left in, as we could not rule out the presence of the component. It was also needed because removing the component and putting all of the upscattered disc photons into the power law produced a 2 - 10 keV flux that was several orders of magnitude above the upper limit derived above. We allowed some flexibility in the black hole mass, because from the evolution of the optical spectra it is clear that there is a broad component to the Balmer lines, though it is difficult to separate it from the underlying continuum around Hβ. While the data restrictions imply

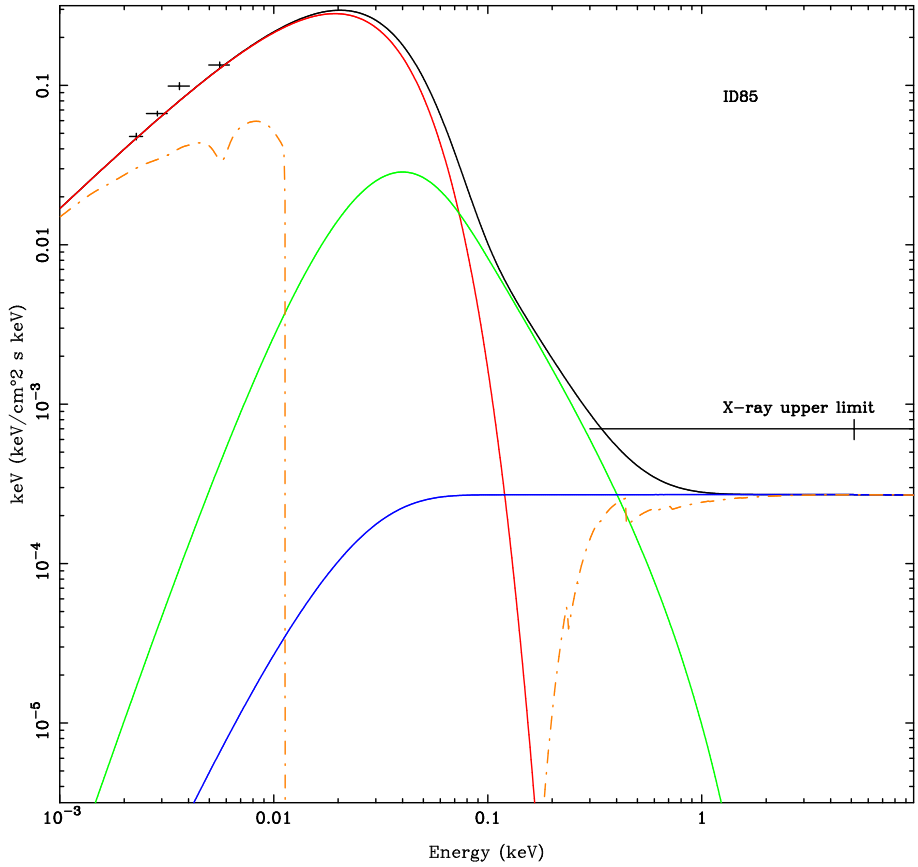

Figure 5.11: The optical to X-ray SED of PS1-10adi, with its alternate name ID85. The model used is OPTXAGN, with the red line showing the disc component, the green line showing the soft excess component and the blue line showing the power law component. The resultant fit is shown in black. This SED uses the UVOT data taken on 2010-10-06.

that the physical parameters produced by the model may not be correct the model never over-predicts the flux constraints we applied, and as the model produced is physically possible for an AGN the total flux values calculated from it can be used as a good estimate for the bolometric flux of the object. It is also worth noting that the model was deliberately restricted to the least amount of gas and dust obscuration, to prevent an overestimation of the flux. The result of the SED fitting is shown in Figure 5.11, where the red line shows the disc component, the green line shows the soft excess component and the blue line shows the power law component. The resultant fit is shown in black. It is clear from the SED that most of the bolometric luminosity for this object will be emitted in the UV. While this is

difficult to model with no soft excess to guide the X-ray tail of the UV output, the work done in Chapter 3 indicates that these objects do exist and are usually NLSy1s. The fluxes derived from the model are 1.0×10^{-9} erg cm^{-2} s^{-1} across 0.001 - 100 keV and 8.2 $\times10^{-14}$ erg cm^{-2} s^{-1} across the 2 - 10 keV range. This gives $L_{Bol} \sim 1 \times 10^{47}$ erg s^{-1}.

During the second set of UVOT observations it was apparent that the source had dimmed by $\sim$ 20%, so we decided to remodel the SED to estimate the change in the bolometric flux. Using the same model, parameters and X-ray upper limit as the first SED, we replaced only the UVOT points with the newer data. This time we derived a bolometric flux of 7.1×10^{-10} erg cm^{-2} s^{-1} across 0.001 - 100 keV and 7.8 $\times10^{-14}$ erg cm^{-2} s^{-1} across the 2 - 10 keV range. This gives a new bolometric luminosity of $L_{Bol} \sim 8 \times 10^{46}$ erg s^{-1}.

From these two measurements we can determine an estimate for the total power output of the object. The two *Swift* observations were taken 63 days apart; this translates to 5.443×10^{6} s. Taking the lower of the two bolometric estimates, the power output is luminosity multiplied by time, $E_{Bol} \sim 2 \times 10^{53}$ erg. If this result is real, it makes PS1-10adi an extremely powerful object, which is more consistent with the output observed from AGN than SNe. It must be noted that the model does produce most of the flux in the invisible UV region but, as stated above, the work on a large sample of AGN in Chapter 3 shows that this model is physically possible, particularly if the object in question is a NLSy1. A more conservative estimate would be to model the flux just across the known UVOT data points with a blackbody peaking in the near UV at 0.0017 keV (2.0 $\times10^{4}$ K). Again using the conservative estimate that the object has been emitting at the lower luminosity for the whole 63 days between the two observations we get a reduced total power output of $E_{Bol} \sim 4 \times 10^{52}$ erg. This is still extremely luminous and puts PS1-10adi above the power output of known Type IIn supernovae. In comparison, Drake et al. (2011) found that CSS100217 expended $\sim 1 \times 10^{52}$ erg, while Rest et al. (2011) found that SN2203ma had a value of 4×10^{51} erg. Finally, Drake et al. (2010) obtained a value of $> 1.4\times10^{51}$ erg for the Type IIn supernova SN 2008fz without any bolometric corrections.

5.6.3 PS1-10adi as a Supernova

The smooth rise and decay of the light curve of PS1-10adi could match the general shape observed for supernovae and even for Type IIn supernovae, particularly if we could separate the host galaxy contamination. The spectroscopic follow-up of the object showed that there were strong narrow Balmer features on top of broader features (most obviously the Hα emission line in the October 2011 spectrum), which are required for the object to be classed as a Type IIn supernova. The emergence of a strong broad component of Hα as the spectrum evolves, especially as the outburst itself is fading, is a feature that is not generally associated with NLSy1s. The strong Fe II lines are also a feature that are associated with Type IIn supernovae.

The temperature derived from the blackbody modelling of the UVOT data ($T = 2.0 \times 10^4$ K) is broadly consistent with supernovae in general (Drake et al., 2011), while the absolute magnitude of this event ($M_V = -23.6$) is brighter than previously known Type IIn supernovae. However, currently the peak luminosity of Type IIn supernovae has a range of 5 magnitudes and the most luminous ones have only been discovered recently as surveys like Pan-STARRS begin to focus on looking for transients in intrinsically faint galaxies (Drake et al., 2009).

The scenario of a luminous supernova near to the core of an AGN is thought to be a rare occurrence. However, if the host galaxy has significant star formation, particularly close to its centre, then this would enhance the rate of all types of supernovae including Type II. Additionally, it was found by Strubbe & Quartaert (2010) that the rate of Type II nuclear supernovae would exceed the rate of TDEs by a factor of ~ 3 at 0.05 arcsec resolution for a 10^7 $M_\odot$ black hole.

While there have been X-ray detections of Type IIn supernovae, such as SN 2006gy (Smith et al., 2007), these objects tend to be the exception rather than the established norm. This means that the lack of detection in the *Swift* observations is consistent with PS1-10adi being a Type IIn supernova.

The energy output of PS1-10adi is difficult to relate to an supernova hypothesis. One of the progenitors of Type IIn supernovae are massive η Carinae-like LBVs. These stars undergo large outbursts and can deposit material into the inter-stellar medium, which will

be illuminated when the star explodes. In these cases, much of the kinetic energy released in the explosion is converted into luminosity, and the brightness limit of these events are constrained by the amount and distribution of the material around the star interacting with the shockwave of the supernova. If there is a series of dense shells around the star, or if the surrounding material is particularly dense, it can give rise to such an extreme luminosity that the explosion appears as a supermassive star. Drake et al. (2011) uses this explanation to explain how CSS100217 is more luminous than previous Type IIn supernovae. In order for this process to explain what is happening in PS1-10adi it would need to cover a further factor of 4 increase in the bolometric output over what is needed to provide the 1×10^{52} erg output of CSS100217.

5.6.4 PS1-10adi as a NLSy1

NLSy1s are known to be optically variable. The AGN standard model allows for outbursts in luminosity due to an accretion event or disc instabilities. As we do not know the time it took the object to rise to the peak luminosity seen in the PS1 data from the levels seen the in SDSS data, we cannot comment on the nature of such an accretion event. However, while we do know that AGN tend to vary on long timescales at optical wavelengths, we also know that these events can produce light curves that vary over a period of $\sim$ 100 - 1000 days, which is what we are seeing in PS1-10adi as it dims. For the light curve to originate from a Type IIn supernova, the event would represent an uncharacteristically lengthy decay.

Figure 5.12 shows the main evolution stages seen in the optical spectrum of PS1-10adi, with a typical NLSy1 spectrum from SDSS shown underneath. This clearly shows that by the end of the observation period PS1-10adi appears very similar to the NLSy1. The Fe II emission is of comparable strength, and the shape of the Hβ/[O III] region is very similar in both objects. Both objects show very little reddening both in the continuum and from the Balmer decrement. However, the PS1-10adi spectrum does vary from that of NLSy1s in several interesting areas. The emergence of the broad Hα base, particularly as it is blueshifted with regards to the narrow line emission, is something that is not seen in NLSy1s by definition. We see that over the interval of 14 months the flux at 5100 Å halves and is reduced more at bluer wavelengths than at the longer wavelengths. This suggests that

the event was very luminous in the blue/UV region, particularly just following the outburst, which would support our SED modelling that had the disc emission peaking in the far UV.

The X-ray non-detection by *Swift* does not exclude PS1-10adi from being an AGN as the derived upper limit falls well within the range for AGN X-ray luminosities. While NLSy1s are known for having a strong soft X-ray excess it is not a ubiquitous feature of the subclass, but as shown in the SED in Figure 5.11, PS1-10adi could have a considerable soft excess component and yet still fall beneath luminosities needed for a *Swift* detection.

It is the energy output that makes the most convincing case for PS1-10adi being a NLSy1. Even just looking at the integrated bolometric output constrained by the fainter UVOT data over the time between the two observations, it is ~ 10 times more luminous than the next most luminous Type IIn supernova known, SN 2006gy (Smith et al., 2010). If we use the output predicted by the SED modelling then it would be ~ 100 times brighter.

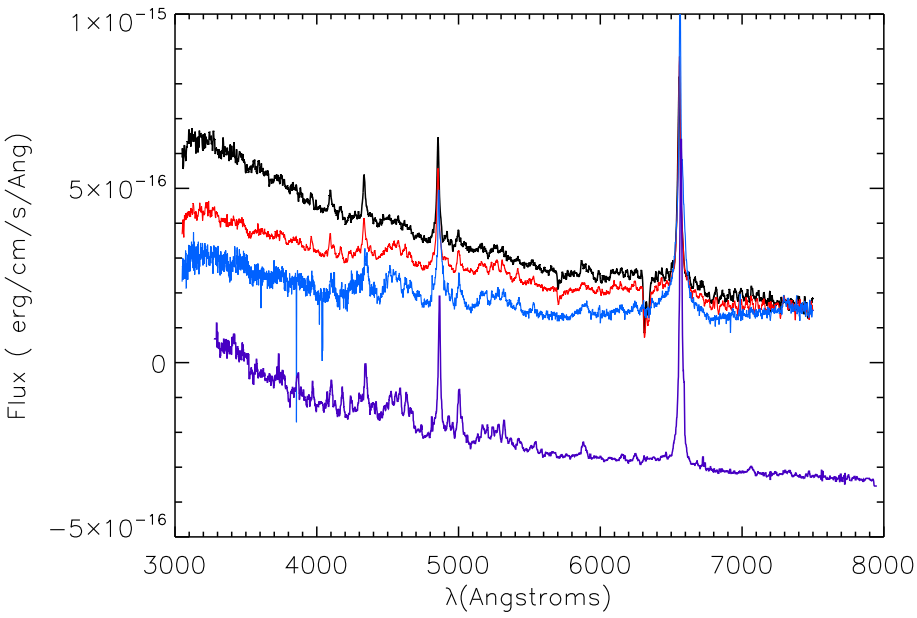

Figure 5.12: The evolving spectrum of PS1-10adi compared to the spectrum of a NLSy1. This figure shows 3 observations taken in August (black) and October (red) 2010 and May (blue) 2011. It can clearly be seen that the line widths stay consistent during this time as the blue continuum decreases. There is little evolution in the red end of the spectrum. The comparison spectrum of an SDSS NLSy1 is shown in purple.

5.6.5 A Supernova/AGN connection?

While Peterson & Ferland (1986) interpreted the flare of NGC 5548 to be the first observational evidence of an accretion event onto the central object, Terlevich & Melnick (1988) took a different view. They interpret the event as an extreme Type II supernova in the intensely star-forming region at the centre of the galaxy. Here the AGN is not matter accreting onto the black hole, but rather a very luminous star-forming region. The scenario can explain the optical emission and the variability seen in AGN, but it fell from use when it failed to explain the hard X-rays seen in these objects.

We now have the unified model to explain AGN (Section 1.5.2) but that doesn't exclude supernovae from the picture completely. One of the interesting pieces of information to come out of this study and that of Drake et al. (2011) is the proximity of the events to the nucleus. In Drake et al. (2011), Hubble Space Telescope imaging was used to place CSS100217 within ~ 150 pc of the AGN.

One possible explanation is a chance alignment along the line of sight, and while the probability of this happening in both objects is extremely small it cannot be discounted. NLSy1s are expected to reside in spiral galaxies (Crenshaw et al., 2003), which have a typical half-light radius in the region of a few kpc. This means the chance of an alignment along the line of sight far from the AGN is very small, particularly as we do not see the event emission redshifted from the AGN emission. It is also known that the narrow line region of Seyfert 1 galaxies have been measured to extend anywhere between 700 and 1500 pc (Bennert et al., 2006), so PS1-10adi occurred within the limits of the narrow line region.

Imanishi & Wada (2004) presented evidence to support the fact that significant star formation could be detected in the nucleus of Seyfert 1 galaxies and could predict nuclear starbursts within their dusty tori. If such rapid star formation was happening in the nucleus then Type II supernovae would be produced in the region. Nevertheless, we do not detect any morphological evidence of either dusty lanes or star-forming regions around the nucleus, nor do we detect any of the spectral or photometric reddening signatures that indicate a star-forming region hidden by dust. If the star-forming region is precluded from existing in the vicinity of the AGN, then there is the possibility that it may be within the region dominated by the AGN itself.

Closer to the AGN the effects of the strong *UVX* radiation field surrounding it would prevent any star formation from occurring unless it was adequately shielded. This leads to the possibility that PS1-10adi is a Type II supernova within the outer edges of the accretion disc, where it could be shielded from the AGN emission. The theory that the violently unstable region of the accretion disc can lead to it fragmenting and the formation of star-forming regions was first put forward by Shlosman & Begelman (1987, 1989). Since then it has been developed by numerical methods and semi-analytical models (see Jiang & Goodman, 2011 and references therein). An interesting point to note about these models is that they predict the formation of extremely massive stars. This would allow PS1-10adi to be a hyperluminous supernova, and make it, along with CSS100217, the first detection of supernovae from within an AGN accretion disc.

This could also offer an interpretation of the line emissions seen. If PS1-10adi is a Type IIn SNe in the vicinity of a NLSy1 then the broad component seen in Hα could be related to the supernova itself, or changes in disc accretion due to shockwaves from the explosion. As this event would have occurred recently the perturbations to the systems should be seen for years, and as the shockwaves travel out from the central region it could be expected that they would have some effect on the NLR and would result in variability in the narrow components of the emission lines.

5.6.6 Conclusions

PS1-10adi is an extremely energetic transient event. The confusion over the origins of the event is compounded as there is no pre-outburst spectrum to compare the evolving spectrum to. As it stands there are arguments to support PS1-10adi as a NLSy1 and a Type IIn supernova. Similarities in the spectral properties of these two objects allow for the spectrum to substantiate both hypotheses.

The main divergence in the scenarios can be found in the energetics of the event. For PS1-10adi to be a Type IIn supernova it would have to be between $\sim$ 10 - 100 more energetic that the current most energetic Type IIn supernova. However, if PS1-10adi was an AGN then this strength of output would be expected.

The discovery of a similar transient CSS100217 (Drake et al., 2011), which has identi-

cal issues with identification (though it does have the added advantage of a pre-outburst spectrum) suggests that these are not extremely rare events. In both cases the light curve appears to rise quite sharply (for PS1-10adi we see a g_{P1} band increase of 0.35 magnitudes in 32 days) and fade very slowly, looking more regular than most AGN variability seen in previous chapters. In both of these cases the light decay is slower than expected for a Type IIn supernova, but if they happen within the disc then the resultant shockwaves would produce disc instabilities that could affect the AGN accretion rate and therefore the observed luminosity of the AGN.

If these two events are truly supernovae within an AGN accretion disc then it raises the question of why this type of object hasn't been discovered before. The simplest answer to that would be that all supernova searches are deliberately biased against AGN, so any variability detected is assumed to be from the AGN if the spectrum of the object classifies it as such. Indeed, the reason behind the interest in PS1-10adi was due to the fact that it had no previous spectrum and the initial post-outburst spectrum was ambiguous. Another issue is that AGN astronomers have previously had very little interest in supernova searches and vice versa. This has lead to a divergence in method and analysis by the two different groups.

In Pan-STARRS both supernova and AGN astronomers are working together on the transient data, as shown by the TDE found by PS1 data (Gezari et al., 2012). If data from surveys such as Pan-STARRS can be combined with the longer running transient searches such as CSS it is hoped that we will be able to separate the long timescales due to AGN variation from the short timescales associated with TDEs and supernovae. PS1-10adi does not display typical AGN variability, but as this is the first of its kind to be discovered with Pan-STARRS it is hoped that similar objects will be found as the telescope continues its operations.

Chapter 6

Pilot Studies with Pan-STARRS: Large scale surveys

One of the major advances in astronomy over recent years has been the development of online catalogues. The SDSS project is undoubtedly one of the most well known of these. It provides an advanced user interface and direct access to summary pages for astronomical objects identified through a variety of means. The advantage of this construct is that samples can be created, defined and refined with high efficiency. The Pan-STARRS project is currently producing vast quantities of data and developing resources to exploit it. This chapter reports faults from some pilot studies and investigates the current limitations of the PS1 environment for dealing with survey studies.

We perform a variability study on BALQSOs in the Medium Deep Survey (MDS). We create subsamples extracted from a much larger spectroscopic survey to probe the differences in the nature of the optical variability seen in BALQSOs and non-BALQSOs. We present the sample selection and data assembly in Section 6.2 and the light curve analysis in Section 6.3. We then investigate the properties of two particularly interesting objects to emerge from this study in Sections 6.4 and 6.5. In Section 6.6 we present a short study on Seyfert 2 AGN, in which we created a sample in SDSS and cross-matched it to the available 3π catalogue. Section 6.7 presents the conclusions of both studies.

The light curves and spectra for each of the 39 objects in the BALQSO study are shown in Appendix C.

6.1 Introduction

In this thesis we have already shown how exploring the time domain can be a powerful tool to aid our understanding of the mechanisms and structure of the region surrounding supermassive black holes, providing that the data is of sufficient quality. The Pan-STARRS extragalactic surveys are the MDS and the 3π survey. The MDS aims to create a database of data of similar to if not better quality than that available in the SDSS in Stripe 82. Whereas the 3π Survey will be much shallower, but cover 3/4 of the observable sky.

In order to investigate the best way of conducting large scale surveys with Pan-STARRS, this chapter considers two distinct methods, producing different results. The first study creates a sample from data taken by Pan-STARRS supplemented by targeted optical spectra. This study exploits the good time sampling of the MDS fields and examines how the survey compares to other current static sky surveys that overlap with it. The second study takes an AGN sample defined using SDSS data and cross-matches it to the 3π catalogue data.

6.1.1 BAL variability

Broad absorption line quasars (BALQSOs) display characteristic broad, ultraviolet line absorption troughs that span between 1000 and 10000 km s^{-1}. By studying the evolution of these features we can learn about the structure and dynamics of absorbing material in AGN.

It is now thought that BAL outflows are seen when QSOs are observed at large inclination angles with respect to the accretion disc. In this scenario the line of sight to the central engine passes through an equatorial disc wind, which imprints a broad absorption signature onto the continuum. This implies that BAL outflows are present in all QSOs, but will only be seen from $\sim 20\%$ of the available orientations, which is close to the fraction of BALs found in the overall QSO population (Hewett & Foltz, 2003, Allen et al., 2011).

Recent spectroscopic studies by Filiz Ak et al. (2012) into the nature of BAL troughs have found that ~ 3.5 % of BALQSOs show evidence for a disappearing absorption trough on rest-frame timescales of 1 - 4 years. They also suggest the average trough rest-frame lifetime to be 100 - 200 years, and that if a trough disappears all other troughs in the spectrum will also weaken. This supports the hypothesis that BALQSOs will exhibit a higher degree of

variability in their colours (differences between photometric bands) than non-BALQSOs as a result of changes in their absorption troughs. Preliminary results of Rogerson et al. (2012) based on SDSS Stripe 82 suggest that this holds true if the BALs are at the correct redshift for troughs to fully fall within one photometric band but not the others. This effect could also be expected from individual bands as well as relative colours.

Stripe 82 is the closest comparison to the PS1 MDS project, with data extending back 8 years, with nearly 10,000 spectroscopically confirmed quasars. Currently the MDS fields have 2 years of data along with targeted campaigns to spectroscopically identify quasars. This provides an ideal basis to carry out a pilot study into light curve variability. It should be noted that any sample created at this stage will be incomplete but will provide an insight into the data quality, availability and reduction that we can expect from the final MDS products.

6.2 Sample selection and data assembly

Our study is based on a subgroup of a sample created by Fine et al. (2012). We use this sample of 504 spectroscopically confirmed QSOs to identify 3 subsamples: a BAL subsample, a possible BAL subsample and a control subsample.

6.2.1 PS1 light curves

To produce the PS1 light curves we use the nightly stacks from the telescope that are formed from eight dithered, individual exposures (see Kaiser et al., 2010 and Tonry et al., 2012 for more details on the PS1 observing strategy and data processing). These nightly stacks are reduced by PSPhot, which is part of the standard PS1 IPP system, to extract PSF photometry for the objects. Each stacked image for every field is divided up into ~ 70 skycells and each one of these is calibrated separately using SDSS photometry (York et al., 2000) of moderately bright point sources (i.e. $16.0 < \text{mag} < 18.5$ and defined as having $type = 6$ in the SDSS database). The bright magnitude cut is used because the brightest objects have been shown to create artifacts in the PS1 images. The lower boundary is set in order to produce the largest number of calibration objects possible in each skycell, while still

ensuring high-precision photometry for each object (95% have errors < 0.01 magnitudes).

In some cases the flux calibration was found to be unstable due to artifacts around the object that were used in the flux calibration in the PS1 imaging. The average offset between the PS1 and SDSS photometry was measured to calibrate the data, and the RMS around this average was recorded. We only accepted skycells with an RMS < 0.1 magnitudes; a cut that removed $\sim 5\%$ of the stacked skycells from the overall sample.

6.2.2 Hectospec spectra

The Fine et al. (2012) sample is part of a larger project to study the variability of QSOs in the MDS fields using spectra obtained with the MMT. The QSO candidates are selected for spectroscopy using current photometric databases of QSOs based on SDSS photometry (Richards et al., 2009; Bovy et al., 2011). Additional candidates are comprised of point sources that correspond to X-ray sources, variability selected objects and UVX selected objects.

The MDS fields are being observed with the Hectospec spectrometer on the MMT, situated on Mount Hopkins, Arizona. Each MDS field is tiled with seven MMT pointings. Each exposure is ~ 1.5 hours, meaning that each MDS field (containing ~ 500 QSOs) can be observed during the course of one clear night of observing time.

The spectra are extracted and reduced using standard Hectospec pipelines (Mink et al., 2007) and then flux calibrated using observations of F stars in the same fields. These stars are compared to a grid of model stellar spectra created using the spectral code SPECTRUM (Gray et al., 2001) with models from Castelli & Kurucz (2004), to correct for the efficiency response of the Hectospec instrument. The absolute flux calibration is made by scaling to the r-band SDSS magnitudes of the stars. Errors in the response curve calibration are usually $\lesssim 10\%$ over the main body of the spectrum (4000 - 8500 Å).

6.2.3 BALQSO sample selection

The entire parent sample comprises of ~ 1200 objects spanning a redshift range of 0.01 - 4.5, with $g < 22$ mag, located primarily in MDS fields MD03 and MD07. As we are looking for

BALQSOs with absorption troughs that appear in the rest-frame wavelength range of 1200 - 2000 Å, we imposed a redshift cut of z = 1.45 in order to place the required lines in the observed wavelength range. This reduced the initial sample to 504 objects.

The MMT spectrum for each of these objects was visually inspected to classify the quasar. From this inspection we produced two BAL subsamples. One subsample is composed of 12 objects that could firmly be classed as BALQSOs, with absorption troughs present in the profile of Si IV λ1400 Å and the C IV λ1549 Å emission lines. The sample will be hereafter referred to as the BAL subsample. The second subsample is composed of 10 objects that show evidence of absorption features/troughs in the region of at least one emission line, but which cannot securely be defined as BALs. This sample is hereafter referred to as the possible BAL subsample.

Out of the remaining 482 objects we selected a sample of broad line AGN, spanning a similar redshift range to our two subsamples, with the best-quality spectra available to form a control, comparison subsample. This subsample is composed of 17 objects and is hereafter referred to as the control subsample.

Initially we carried out statistical K-S tests on the redshift and absolute magnitude $M_{sdss,i}$ of the different subsamples and the parent sample to test if they were consistent with coming from the same population. Using the full parent sample, we found that the subsamples were not representative of the parent sample in redshift space; however, we found that if we increased the redshift cut to z = 1.50 for the parent sample (we did not identify any BALs or possible BALs at a lower redshift), so reducing the sample size to 465, then the all of the subsamples have a p-value great enough to accept the null hypothesis i.e. there is no difference between the samples. One possible reason for the rejection of the null hypothesis if the entire parent sample is used is that while that sample is relatively complete at $z \lesssim 2$, in the interval $2 \lesssim z \lesssim 3$ it is highly incomplete due to the nature of optical/UV selected QSO surveys (Richards et al., 2002). This results in weighting the mean of the parent sample to lower redshifts, while BALQSOs are predominately found at higher redshifts in optical surveys. We find no statistical difference in the SDSS photometry or the absolute magnitude between any of the subsamples and the parent sample or between the subsamples. It does not appear that our BAL and possible BAL subsamples are actually taken from a sample

different to that of the parent sample as a whole, particularly since the photometric method used above to select the quasar candidates is not biased against BALQSOs (Allen et al., 2011). To confirm that any trends found are not due to population selection effects we ensured that our control subsample is both representative of the parent sample and of the other two subsamples.

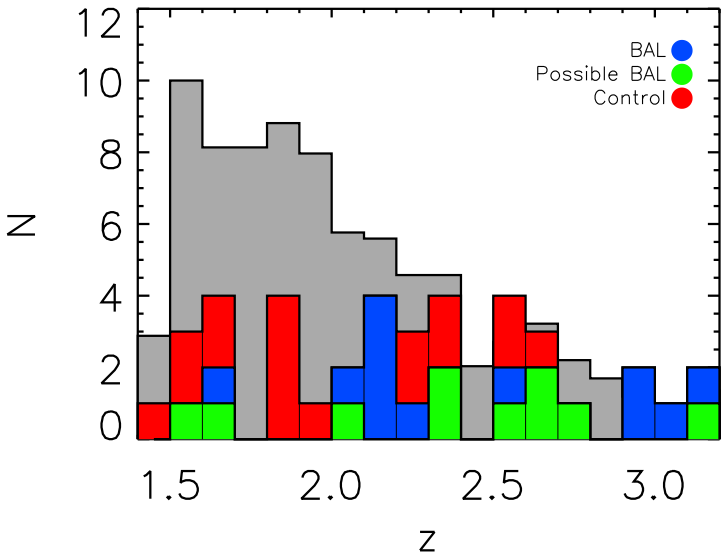

Figure 6.1: Redshift distribution of the objects in all of the subsamples. The distribution shows the total number of objects in each bin, broken down into each subsample. Blue represents the BAL subsample, green represents the possible BAL subsample and red represents the control subsample. The normalised distribution of the parent sample is shown in grey.

Traditionally, BAL troughs are observed in ∼15% of quasars (Reichard et al., 2003; Hewett & Foltz, 2003), but even if we combine both the BAL and possible BAL subsamples, we appear to have only identified 4.3% of the whole parent sample to be BALQSOs. This is not completely unexpected, as only 1 - 8% of SDSS QSOs are found to contain BALs if steps are not taken to correct for incomplete identification. In many cases BALs are unidentified due to a combination of low S/N and shallow troughs. As we are mainly identifying C IV absorption troughs a detection fraction of $\sim 4\%$ is unsurprising (Allen et al., 2011).

Figure 6.1 shows the redshift distribution of all the objects in the subsamples, broken

down into subsamples. Blue indicates the BAL subsample, green indicates the possible BAL subsample and red indicates the control subsample. A normalised distribution of the parent sample is shown in grey, and it can be seen that the parent sample has a steep drop-off at z $\sim$ 2, indicating the incompleteness of the sample at higher redshifts.

None of the sources in our sample are identified as radio-loud, using the standard definition in Section 4.4.

6.3 Light curve analysis

Our sample is composed of 39 objects divided into 3 subgroups, 12 in the BAL subsample, 10 in the possible BAL subsample and 17 in the control subsample. All of the objects have r band light curves, 32 objects have g band light curves and 26 have i band light curves. In the BAL subsample 8 objects have g, r and i band data and 4 objects have only r band data. In the possible BAL subsample, 5 objects have g, r and i band data, a further 3 have g and r band data and the remaining 2 have only r band data. The control subsample is the most complete out of the 3 subsamples with 13 out of the 17 objects having data in all three bands, a further 3 having g and r band data and only one object having only r band data.

We conducted a visual inspection of each light curve, and stacks displaying a deviation of $> 2\sigma$ from the mean were investigated. During this study we found that image artifacts and chip gaps were responsible for all large deviations from the mean; large errors were a direct result of poor seeing. We also extracted the light curves of standard stars in each skycell using the same method outlined above, to check that there was no inherent variability in the skycell due to telescope operating procedures.

After the removal of points affected by chip gaps and image artifacts, the light curves could be analysed. The light curves for each object along with the Hectospec spectra are shown in Appendix C. The BAL subsample is shown first, followed by the possible BAL subsample, with the control subsample at the end of the section. For each object the available light curves are colour coded (g - blue, r - green, i - red) in the left-hand plot. Along the left edge of the light curve plot the appropriate SDSS magnitudes are displayed. As all of

the SDSS photometric observations of our objects were taken between MJD $\sim$ 52200 - 52300 they all lie beyond the left side of the plot. Upper and lower limit arrows indicate that the SDSS points lie outside of the magnitude range displayed. The right-hand plot shows the observed spectrum with the wavelength range of the available light curves overplotted.

From the light curves it can be seen that all of the objects show evidence of variability at some level over the course of the observations. The predominant trend is for objects to decrease in luminosity, with only one object in the sample displaying a significant rise in luminosity. In the cases of the objects that do not display a general trend, they can be seen to either display evidence for long timescale (longer than the observation period), low-level variability or have a single significant variation during the course of the observation period. For objects displaying long timescale trends an attempt was made to fit a basic periodicity template to the data, but in each case the observation length was insufficient to constrain a fit.

In order to quantify the variability we took a similar approach to the method used in Chapter 4. The first study was to quantify the statistically significant variability over the course of the light curve. To do this we defined Δvar to be:

$$\Delta\mathrm{var} = \sum_{i=1}^{N}[(X_i - \mu)^2 - \sigma_i^2] \tag{6.1}$$

where N is the number of good points in the light curve, μ is the unweighted arithmetic mean of the magnitude of the object, and X_i and σ_i are the magnitudes and uncertainties respectively, for each data point.

Figure 6.2 shows the distribution of this significant variability in g, r and i in the left-hand, middle and right-hand plots respectively. The subsamples are colour-coded the same as in Figure 6.1. It can be seen that most light curves display < 0.3 magnitudes of significant variability over the 2 year light curves. The i band light curves display the least amount of variability with all bar 3 objects displaying < 0.3 magnitudes of variability. The r band light curves show the largest range in variability; however this is also to be expected as all objects have r band light curves, but not necessarily g or i band light curves.

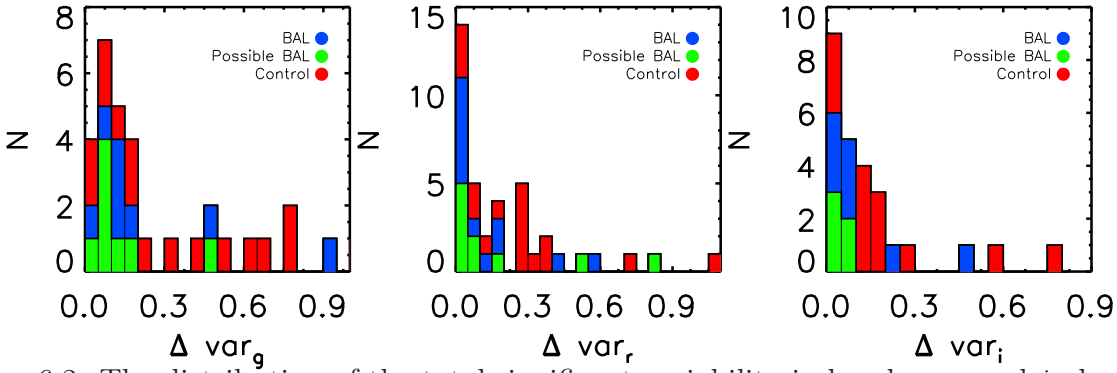

Figure 6.2: The distribution of the total significant variability in bands g, r and i, shown in the *left, middle* and *right* panels respectively. The colours indicate the different subsamples as defined in Figure 6.1.

6.3.1 Uncertainties in the PS1 data

In most objects in our sample we detect evidence for flickering outside of the uncertainty estimates given on the magnitude values. While this effect could be real, there is also the possibility that the uncertainty calculation from PSPhot is too conservative. The uncertainties are calculated using Poisson statistics, and only take into account the read noise and image gain variations present, as well as the saturation levels. In addition, errors in the zero-point calibration, sky noise and flat fielding are not taken into account. If these factors are included in the results then the uncertainties would be significantly increased.

All PS1 data is currently awaiting re-calibration, and upgrades to the PSPhot pipelines should produce results that better represent the true uncertainties present in the data.

6.3.2 Multi-epoch spectra

In order to investigate this further, we examined the 5 objects out of our subsamples that have an SDSS spectrum as well as the Hectospec spectrum. These five objects are; J083612.35+451458.4, J141123.68+532845.7, J142015.64+523718.8, J142039.47+521928.4 and J142129.40+522751.9. Two objects are from the BAL subsample, two are from the control subsample and one is from the possible BAL subsample. All of the objects apart from J142129.40+522751.9, which is discussed separately in Section 6.4, are discussed below. All of the SDSS spectra were taken between 2001-11-19 and 2003-05-05, while the Hectospec

spectra were taken between 2010-10-14 and 2011-04-03, giving a time interval of 8 - 9 years between observations.

6.3.2.1 J083612.35+451458.4

J083612.35+451458.4 is in the possible BAL subsample. It has absorption features associated with the Si IV λ1400 Å and C IV λ1549 Å emission lines, but no clear absorption trough. The separation between the SDSS and Hectospec spectra is 9 years, and the spectra show no evidence of spectral change over this time. There are only g and r band light curves available for this object and both display a low-level of variability ~ 0.05 magnitudes. While the SDSS PSF photometry is ~ 0.4 magnitudes brighter than the PS1 photometry, the SDSS fibre magnitudes are in excellent agreement with the PS1 data.

6.3.2.2 J141123.68+532845.7

J141123.68+532845.7 is in the BAL subsample. There is no evolution between the SDSS and PS1 PSF magnitudes, and the variability decreases from 0.09 magnitudes in the g band to 0.04 magnitudes in the i band. The spectra show evidence of continuum brightening since the SDSS observation, but there is no evolution in the trough shapes.

6.3.2.3 J142015.64+523718.8

J142015.64+523718.8 is in the control subsample. The light curves indicate considerable flickering activity in all bands, with no significant trends, but the spectrum shows an increase in the continuum flux of the object of $\sim 20\%$. There are no additional features in the spectrum to indicate that there is contamination from another object, however, the SDSS image shows the object to have extended red features that are not identified as a separate object. If this is a separate object then the overlap with our object would cause problems when extracting the photometry, particularly in less-than-optimum seeing.

6.3.2.4 J142039.47+521928.4

J142039.47+521928.4 is also in the control subsample. The r and i band light curves show no significant trends either over the course of the PS1 observations or in comparison to the SDSS photometry. The only difference is that the SDSS g band is always brighter than the PS1 data, and the light curve suggests a slight downwards trend. When comparing the spectra it was found that while the continuum emission was constant between the two epochs, the emission line flux decreased, on average by $\sim 5\%$. The effect of this is most noticeable in the g band which has a wing of C IV and Al III within its wavelength range.

6.3.3 Excess variance study

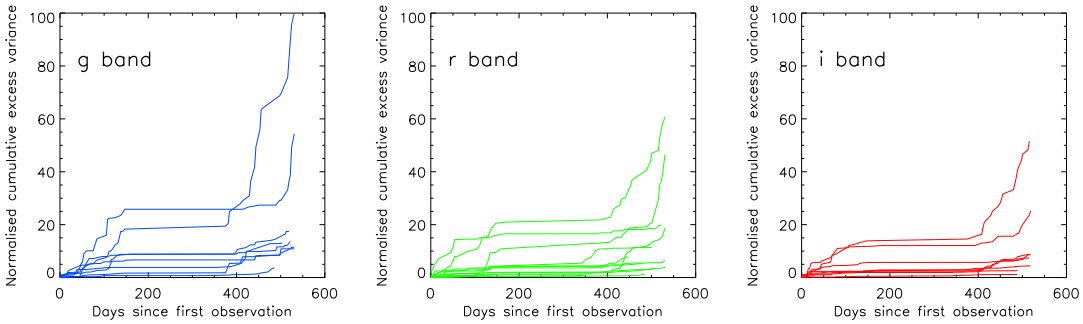

Figure 6.3: The normalised cumulative variability distribution of the 12 objects in the BAL subsample. All objects and bands are normalised to the largest value obtained in any band for the subsample. The flat sections indicate either periods where no data was recorded, or intervals where there was no significant amount of variability. The steepest sections of the graph indicate the most variable intervals.

As is the case for the CSS light curves in Chapter 4 we also calculate the excess variance, using the same method. While the photometric accuracy of Pan-STARRS far exceeds that of CSS (see Figure 6.9 for an example), this sample cover a much larger redshift range, and as a result the bands are probing different parts of the optical continuum and lines for each object. While the i band is usually probing the coolest visible edge of the accretion disc, the g band is probing towards the peak of the accretion disc emission for low redshift objects, and the Lyα forest for higher redshift objects. Unlike the study in Chapter 4, we found that all of our objects had a constrainable, 'real' excess variance in all the bands

studied, where 'real' detections of variability are claimed when the excess variance is greater than zero. In order to show how the excess variance changes over the course of the light curve, the cumulative excess variance for each band across the whole light curve is shown in Figures 6.3, 6.4 and 6.5 for the BAL, possible BAL and control subsample respectively. In this calculation only one time interval covering the whole light curve is used, and the excess variance is calculated for each bin. When the excess variance is greater than zero it contributed to the cumulative excess variance. For clarity, the resultant value for an object is divided by the largest cumulative excess variance value across all three bands for each subsample.

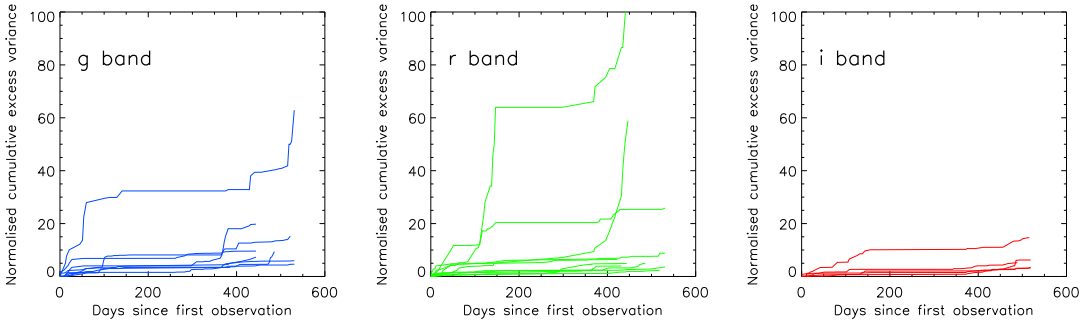

Figure 6.4: The normalised cumulative variability distribution of the 10 objects in the possible BAL subsample. All objects and bands are normalised to the largest value obtained in any band for the subsample. The flat sections indicate either intervals where no data was recorded, or intervals where there was no significant amount of variability. The steepest sections of the graph indicate the most variable intervals.

In general it can be seen that the g and r bands show more variability that the i band. The objects that have the largest values often have steep increases in several sections indicating that they either experience extended rises or falls or spend a significant amount of time at a constant magnitude away from the mean.

In the BAL subsample shown in Figure 6.3 it can be seen that the majority of the objects in the sample display a continuous low-level of variability across their light curves, indicated by the small continuous increments in the cumulative totals. However, in each band there are two objects that display much higher variability than the rest of the sample, and they are the same objects in each band.

J141955.26+522741.2 displays the largest cumulative variability. From the light curves

it can be seen that there is a similar trend in all three bands: they show an initial dip then rise in the first season of observations, followed by a rise and flattening during the second season. There is also a large scatter in the data points, particularly the first season's g band data. This is likely to be due to image processing and telescope issues during the first season rather than flickering in the object itself, as this scatter is significantly reduced in the second season's observations. While there is clear evidence of variability, the true degree of this is likely to be less than our measured values once the data is reprocessed. The second object to display a high level of cumulative variability is J140716.82+531236.6. This object is one of the lowest luminosity objects in our sample and sits on the magnitude limit of $g < 22$ that we imposed on the sample. There is a large scatter in all bands that is larger in the first season than the second; again this is likely to be a result of image quality than the object flickering. The SDSS magnitudes are of a similar level to the final observations, indicating that the downwards trend of the light curve may be real if there was an outburst between the SDSS and PS1 observations.

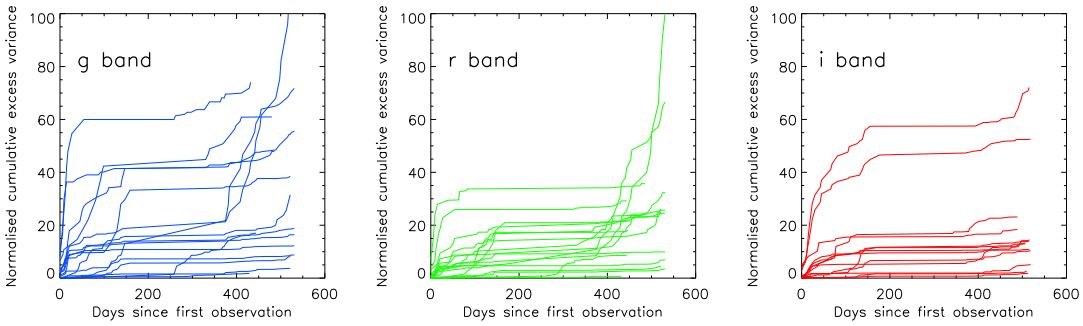

Figure 6.5: The normalised cumulative variability distribution of the 17 objects in the control subsample. All objects and bands are normalised to the largest value obtained in any band for the subsample. The flat sections indicate either intervals where no data was recorded, or intervals where there was no significant amount of variability. The steepest sections of the graph indicate the most variable intervals.

In the possible BAL subsample shown in Figure 6.4 it can be seen that again some objects display a much higher level of cumulative variability than the rest of the sample. The object with the largest total variance is J160948.66+541644.0 and it only has r band data. This object has very poor data, with large uncertainties and a large scatter. It is very faint and the points with the smallest uncertainties appear to be in good agreement with the previous

SDSS photometric observation. Therefore it is probable that any underlying variability is lost in the associated uncertainties. The object with the largest excess variance total in the g band is J141422.46+540344.2. This object is also very faint and has a large scatter, but when compared to the SDSS points it has dimmed by ~ 1 magnitude in the g and r bands and by ~ 0.5 magnitudes in the i band.

The control sample is shown in Figure 6.5 and again we analyse the two objects with the largest total variance in greater detail. J140849.41+534051.2 displays the largest values in all three bands. From the light curve in Appendix D it can be seen that there is a strong downwards trend across the light curve with a similar degree in all bands. Interestingly it can be seen from Figure 6.5 that the end of the light curve in the g and r bands is the most variable part of the curve, and it is more variable in these bands than in the i band. This can be seen in the light curves, as the slope of the i band in the second season is not as steep as that seen in the other bands. J140616.09+533926.0 shows the second largest excess variance totals and is an object that appears to have complex variability trends. The light curves show little scatter and small uncertainties, but with different trends seen in each season of the light curve. During the first season all bands show a short rise followed by a fall, with a small increase at the end. In the second season there is a brief decrease, followed by a long rise, ending with a short decrease. Each trend has a similar amplitude, but the second season is ~ 0.2 magnitudes dimmer. The second season is also consistent with the SDSS photometric bands, but the current curve is too short to constrain any periodicity if it is present.

As in Chapter 4 we examined the excess variance over three different timescales: 1 year, 6 months and 1 month. Figure 6.6 shows the relationship with the excess variability in different bands, on these three timescales. The top panels show the relationship between the g and i bands, the middle panels show the relationship between the r and i bands, and the bottom panels show the relationship between the g and r bands. The left column has excess variance values calculated with year-long intervals, the middle column uses 6 month intervals and the right column uses month-long intervals. We find that there is a positive correlation for all bands on all timescales, however, the scatter increases for the shorter intervals. Each plot is fit with a line of the general form log(y) = a + b*log(x) where a and b are the

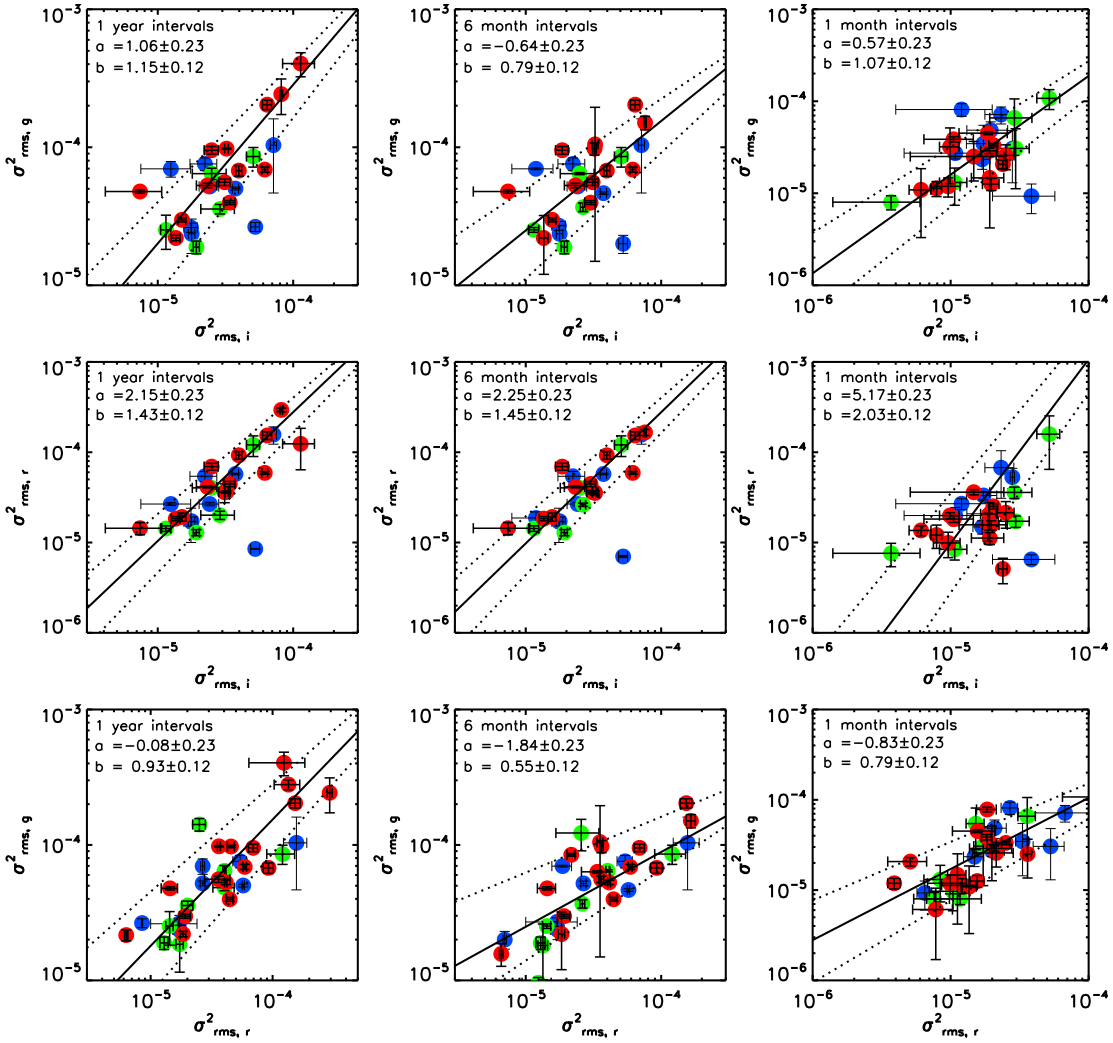

Figure 6.6: *Top panels:* The normalised excess variance calculated over 1 year (*left panel*), 6 month (*middle panel*) and 1 month (*right panel*) time intervals for the i band on the x axis and the g band on the y axis. *Middle panels:* Similar but with the r band values on the y axis. *Bottom panels:* Similar but with r band values on the x axis and g band values on the y axis. The line of best fit to all of the objects in the sample (excluding J142129.40+522751.9, which always appears below and to the right of the general trend) is shown in black, with the dotted lines showing the 1-σ uncertainties on the line. The values of the normalisation and slope of the best-fit line with the 1-σ uncertainties are given as a and b, respectively at the top left of each panel. The general equation for the line of best fit in each panel is log(y) = a + b*log(x), where a and b are the values defined above. The blue points indicate the BAL subsample, the green points indicate the possible BAL subsample and the red points indicate the control subsample.

normalisation and slope parameters respectively and are given in the top left corner of each plot. The thick black line indicates the best-fit line and the dotted lines show the combined 1-σ error on the normalisation and slope parameters. In the top two rows of Figure 6.6 there is an object from the BAL subsample that is always below this relationship. This object is J142129.40+522751.9 and is examined in greater detail in the next section. For the purpose of constraining the relationships, this object is removed.

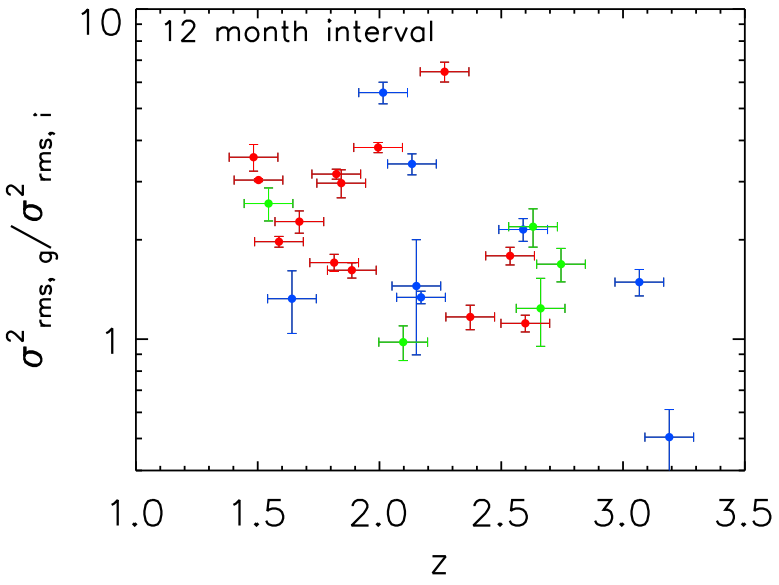

Figure 6.7: The ratio of the excess variance in the g to the excess variance in the i band over a 12 month time interval against redshift. A trend of decreasing ratio with increasing redshift can be seen, but with a large scatter.

In general we find that the g and r bands are more variable than the i band, and over year-long intervals have a normalisation value consistent with 0 and a slope of 1, within errors. We expect the excess variance to decrease with increasing wavelength, as the shorter wavelengths are observing more towards the peak of the disc emission. However, we find that the r band is more variable with respect to the i than the g band but this most likely results from the redshift range of the sample. For the higher redshift objects we observe emission from the accretion disc in the r band, but emission from the Lyα forest in the g band. For the low redshift objects we observe emission from the accretion disc in both the

g and r bands. As the Lyα forest is not created by accretion disc emission from the AGN we can expect the relationship between the g and i to evolve with redshift as they trace different components at different redshifts.

Figure 6.7 shows the ratio of the excess variance in the g and i bands over the 12 month time interval against redshift. It can be seen that the ratio decreases with increasing redshift, but with a large scatter. This indicates that objects where the Lyα forest is a large contributor to the g band observed emission will show different variability relationships to those where it is not, but other factors such as the luminosity of the object and the S/N of the detection will also affect what is seen.

6.3.4 Summary of the light curve analysis

From the optical light curves we used three different methods to quantify the variability. All of the methods calculate the excess variance of the light curve but are used for the interpretation in different ways.

1. **Δvar method**

   The Δvar method adds up the statistically significant variability over the course of the light curve and divides it by the number of bins. We found that all objects had at least a small but statistically significant amount of variability in all of the observed bands. All samples displayed a large scatter in values across all bands, with the total amount of variability measured decreasing from the g to the i band.

2. **Cumulative excess variance**

   The cumulative excess variance is the excess variance built up over the course of the light curve. It shows how the light curves behave on a point-to-point basis with respect to the mean. We find that each sample behaves in the same way, with a few objects, usually those having poor-quality data or at the magnitude limit of our sample, displaying the largest totals. In general, it was found that the final total variance decreases from the g to the i band. We also find that this representation of the variability helps us to understand how the object is varying. The majority of objects show small, steady increases throughout their observed interval, with little change in the

slope of the rise, but others have clear episodes of brightening and dimming where the slope becomes increasingly steep until the trend changes or fades away.

3. **Normalised excess variance**

   The normalised excess variance is the same method as was used in Chapter 4. We find that there is a positive correlation between all bands on all three of the timescales investigated (12 months, 6 months and 1 month). The g and r band are shown to display the closest one-to-one correlation in log space and are more variable than the i band. We expect that the g band would be more variable with respect to the i band, than the r band is. However we actually find that this is not the case. If we look at the ratio of the excess variance in the g and i bands against redshift, we find that there is an anti-correlation, with the higher redshift objects having more similar levels of variability in the g and i bands. We suggest that this is an effect of the Lyα break and subsequent forest that appears in the g band at higher redshifts and means that the g band is tracing different components at different redshifts, just as any wavelength range used would, providing the appropriate redshift was reached.

From these studies we find that there is no significant difference in the three subsamples, but as we only have a small number of objects further work needs to be done to see if this holds for large samples.

6.4 J142129.40+522751.9

J142129.40+522751.9 is an interesting object, as it occupies a unique space in the normalised excess variance plots shown in Figure 6.6. In every plot of the top two rows it lies below and to the right of the general trend on all timescales. This indicates that the excess variance of the i band is greater than both the g and r bands. On further investigation, the i light curve (shown in red in the top panel of Figure 6.8) does show larger variations than the g and r band light curves and always has small uncertainties. It is possible that this is not a correct uncertainty estimate, but rather is an example of the problems described in Section 6.3.1. The first half of the i band light curve has fewer points than either of the g and r bands and yet shows a similar level of flickering. If the uncertainty calculations used in

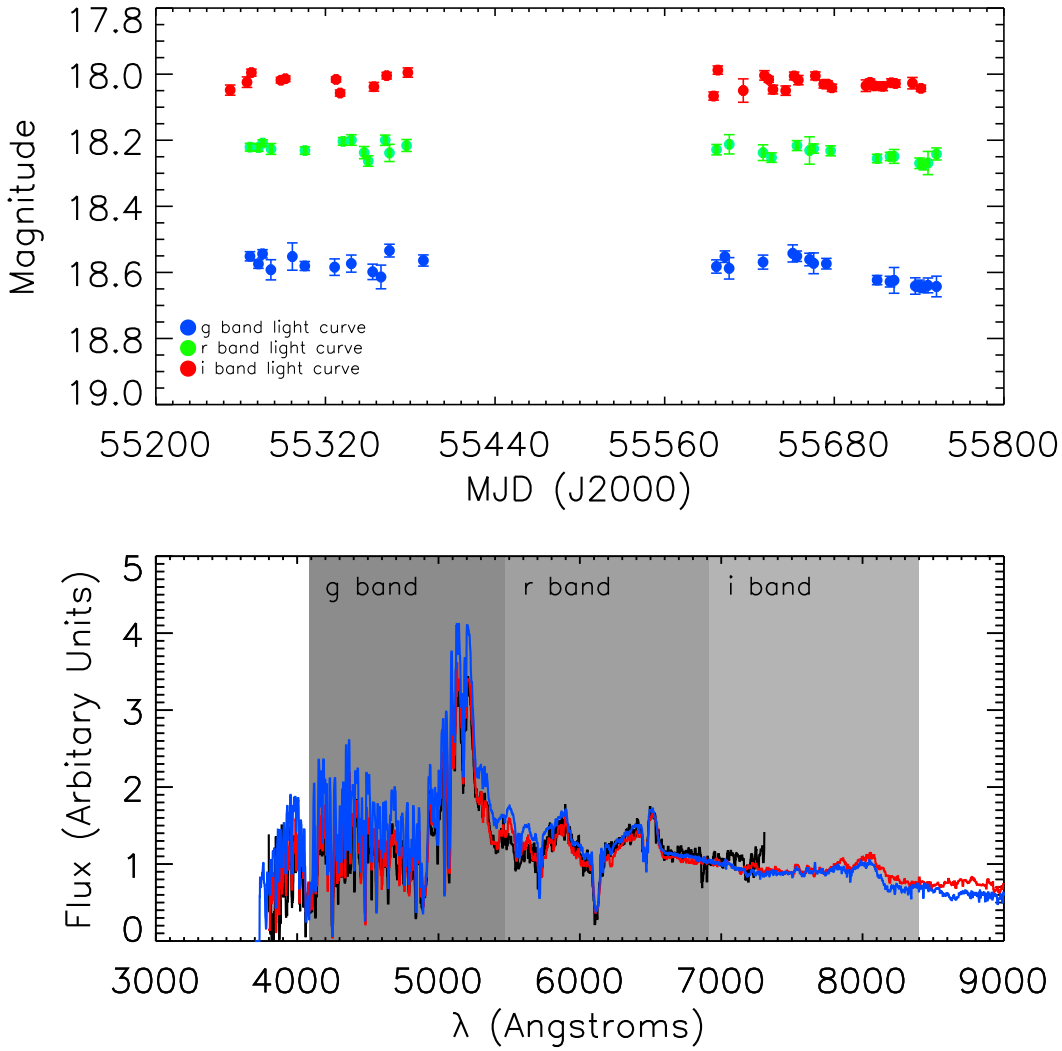

Figure 6.8: *Top panel:* g, r and i band light curves for J142129.40+522751.9 shown in blue, green and red, respectively. *Bottom panel:* Three spectra of J142129.40+ 522751.9 taken over a period of 9 years. The SDSS spectrum, shown in red, was taken on 2003-05-05, the MMT spectrum, shown in blue, was taken on 2011-04-03 and the OHP spectrum, shown in black, was taken on 2012-02-05.

PSPhot do not take into account flat fielding errors and zero-point uncertainties then the true uncertainty on these points could be larger than shown. Another possible reason is that the reduced number of data points in the i band results in a more statistically significant level

of variability as the sampling perhaps coincides with the maximum and minimum flickering levels.

For this object we also have spectra from three different epochs; they are shown in the bottom panel of Figure 6.8. The first one was taken by SDSS on 2003-05-05 and is shown in red on the plot. The second was taken by Hectospec on the MMT on 2011-04-03 and is shown in blue, while the final spectrum was taken by the Observatoire de Haute-Provence on 2012-02-05 and is shown in black.

The spectra are normalised to 7000 Å, and it can be seen that there is no spectral evolution during this time. The apparent changes in the depth of the BAL troughs are due to data smoothing.

6.5 J104516.6+573137

J104516.6+573137 is unique in our sample. It displays a transient-like dip in the light curve, with little scatter around the prevailing trend, but the crucial segment of the light curve, the bottom of the dip, was unobservable, as the object was behind the Sun during this time. Only r band data is currently available for this object, though we were able to extend the light curve to include more recent data from the third season's observations.

We find that the SDSS r band magnitude is 19.55, which is ~ 0.2 magnitudes higher than the initial Pan-STARRS observation, but it was taken 6 years previously. The top panel of Figure 6.9 shows all of the photometric data available for J104516.6+573137, consisting of 7 years of r band corrected CSS observations, shown in red, the SDSS observation, taken 3 years before the first CSS image and indicated by the purple point with the arrow, and the Pan-STARRS MDS data, shown in blue.

The improvement of the PS1 data over that from the CSS is instantly obvious. The uncertainties of the CSS data are larger than the variability of the object, and so there is no indication from the CSS points of any unusual behaviour during the interval of the Pan-STARRS observations.

The middle panel of Figure 6.9 is an enlarged plot of the Pan-STARRS light curve with additional data from the start of the third year of observations. The curve is reminiscent

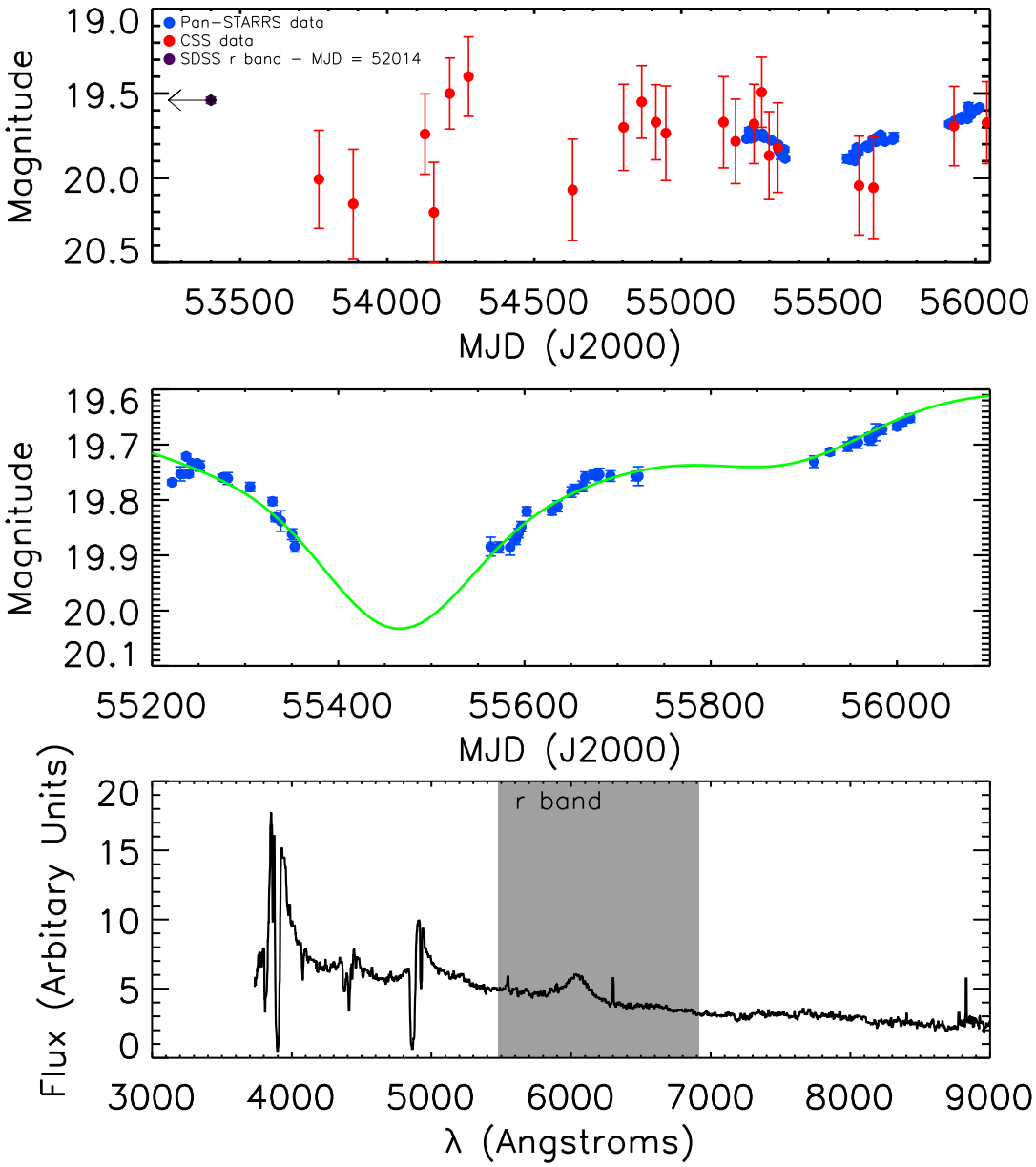

Figure 6.9: *Top panel:* CSS (red) and PS1 r band (blue) light curves for J104516.6+573137. The CSS data is binned into 1 day bins, whereas the PS1 photometry is taken from nightly stacks. *Middle panel:* PS1 light curve with a Gaussian fit. While the main dip between 55300 and 55500 is well fitted by the curve it is currently unclear if the rise seen in the most recent data is a continuation of the same trend. *Bottom panel:* Hectospec spectrum of J104516.6+573137 taken on 2011-05-20, highlighting the region of the spectrum covered in the PS1 r band photometry.

of planetary transit light curves, but as crucial information on the slope and depth of the event is missing we could not fit a reliable transient event to the curve. Instead we show the

best fit curve to the data. As we do not know how this feature fits in with the long-term variability of the object we could not establish a base continuum level, so instead we took the SDSS magnitude as the base level, as it is brighter than any point of the Pan-STARRS light curve. The main dip was fit with three components in order to keep the amplitude down to realistic levels, as using fewer components resulted in a predicted dip of ~ 2 magnitudes. The FWHM of the overall fit is 220 days and the amplitude of the dip is 0.54 magnitudes. The feature at the end of the light curve was modelled to be an additional dip peaking 380 days after the initial dip. These fits are crude estimates and the assumption that the trends seen are a reduction from the original brightness of the object. We also attempted fits with varying continuum levels, but when the continuum was placed at ~ 19.7 mag, the fits failed as there were insufficient data points to constrain the edges of the curves.

The Hectospec spectrum is shown in the bottom panel of Figure 6.9, with the range covered by the r band photometry indicated by the shaded region. This spectrum was taken on 2011-05-20 or MJD 55701, which places it at the end of the initial dip. From the plot it can be seen that the wavelength range covered by the r band contains the Mg II emission line and continuum emission. The variability in the observed light curve could result from either the continuum flux level decreasing by at least 25% or the complete disappearance of the Mg II emission line.

6.5.1 A toy model for J104516.6+573137

We have developed a possible explanation for this light curve which builds on the similarities between this event and observed planetary transit events. We investigated the idea that this dip was not caused by an accretion event in the disc or a change in the behaviour of the AGN, but rather by another object passing relatively close to the AGN and blocking some of the emission for the length of time it took to pass in front of the accretion disc.

Using the results of the curve fitting we start the transient event at 55254 and end it at 55654, spanning 400 days. The emitting region that the transient is covering is the accretion disc, which, if we assume $M_{BH} = 10^8$ $M_\odot$, has a diameter ~ 3 x 10^{14} m. From this we can estimate the velocity of the transiting object, which is $\sim 10^7$ m s^{-1}.

In order to locate this object with respect to the accretion disc we assume a Keplerian

orbit, which results in a distance of $\sim$ 5 x 10^{14} m. This is of a similar scale to our accretion disc size, which would place the transiting object very close to the nucleus of the quasar.

A possible candidate for such a transiting object based on these calculations is the broad absorption line region. If these clouds actually orbit the black hole, then one may occasionally block the line of sight to the centre of the quasar, creating large absorption troughs in the spectrum. It would then pass on and the troughs would disappear. It has been shown that BAL troughs can indeed disappear (Filiz Ak et al., 2012) and, as mentioned in the introduction to this chapter, can vary in equivalent width and/or shape on timescales from months to years. For this to work in our example the outflow stream would have to pass across the line-of-sight to the accretion disc. The observed event causes a decrease in magnitude of $\sim$ 0.25 - 0.54 magnitudes (based on the observed decrease and the amplitude of the curve fitting), which can only be caused by extremely dense material. Capellupo et al. (2011) estimated that the broad line absorption region could only produce a 10% decrease in observed luminosity, which is less than half of our minimum required level and makes the broad line absorption region an unlikely candidate for this transient object.

Another possible candidate is a BLR cloud, which are located at the distance required. However, we encounter a different problem, as a BLR cloud could be dense enough, but is unlikely to be large enough to create a projected area on the accretion disc of the size required to produce the decrease in flux observed.

A final candidate for the transitory object is a star. A star could produce the required area and opacity at wavelengths shorter than the mid-IR due to the presence of H^- ions in its atmosphere. If we assume that the flux decrease seen is caused by a transiting star, we can estimate an approximate size for the star. If we take the flux decrease as 30% since a 0.3 magnitude range is a conservative lower limit for the total decrease, than this translates into the percentage of the accretion disc that is covered (i.e. 30% of the projected area of the disc).

Using the diameter of the accretion disc to be $\sim$ 3 x 10^{14} m, this gives a radius for the star of 8.21 x 10^{13} m. While this is larger than even the largest supergiants, it has been confirmed that the gas envelope of red supergiants can extend up to $\sim$ 200 times further than the radius of the star (Lobel, 2005). If the object was a star in the vicinity of a

supermassive black hole, then we would expect radiation from the quasar to heat up and bloat the atmosphere of the star and tidal forces to draw out the envelope into a tail, so this scenario is plausible. If we use a smaller black hole mass, this would result in a smaller accretion disc and correspondingly a smaller radius for the star.

An interesting prediction from this is that if the event is a transit event caused by a star, then the calculations show that it would orbit at a distance of $\sim 10^{14}$ m with a velocity of $\sim 10^{7}$ m s^{-1}, which translates into an orbital period of 8 years. The orbital period will decrease for smaller black holes. There is also a chance that this scenario could result from a star in a plunging orbit, where the material of the star will eventually accrete into the black hole as it is ripped apart by the tidal forces. If this is the case then we may speculate that our object could be a progenitor of a tidal disruption event.

However, based on only one object displaying these features we must be cautious identifying the cause of a transit-like event in a light curve. As the Pan-STARRS project progresses, this will provide a plethora of objects that can be studied in detail and will provide valuable insights into the long- and short-term variability properties of both quasars and lower luminosity AGN.

6.6 A search for Transitions of Seyfert 2 to Seyfert 1

A short pilot study was conducted focusing on cross-matching the SDSS and PS1 3π catalogues to look for AGN with extremely large (> 2 magnitudes) increases between the two sets of photometry. The motivation behind this project was to identify AGN changing state from Type 2 to Type 1, as predicted by clumpy torus models (Nenkova et al., 2008). In these models the torus consists of many optically thick, dusty, molecular clouds orbiting the nucleus. In this scenario an object would be classed as a Seyfert 2 if a cloud lies in front of the line-of-sight to the central region, but might evolve into a Seyfert 1, if by chance the motions of the clouds provided a clear view of the nucleus. Figure 6.10 is a reproduction of Figure 8 from Thompson et al. (2009). It illustrates the clumpy torus and indicates how the probability of unobscured views of the nucleus increases as the viewing angle, i, decreases. The statistics of such transition events, if detected, could give constraints on the number

and the physical properties of the dusty molecular clouds within the torus.

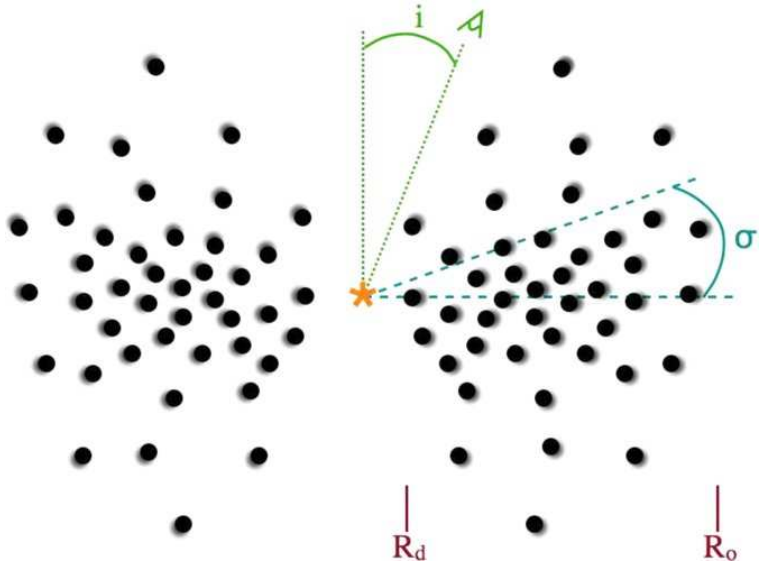

Figure 6.10: A cartoon of the clumpy torus, reproduced from Figure 8 of Thompson et al. (2009). The emission and obscuration of the nucleus are functions of the viewing angle i. R_d is the dust sublimation radius and R_0 is the outer radius. σ indicates the scale height of the distribution.

We decided to only investigate the cases where the objects brighten as looking for large decreases would necessitate us probing the magnitude limit of Pan-STARRS for all but the brightest objects.

We created a sample of Seyfert 2 AGN from the SDSS DR7 catalogue (Abazajian et al., 2009) using the CASJOBS, the SDSS Catalog Archive Server Jobs System[1]. In order to select Type 2 AGN we followed the same line width selection criteria as Barth et al. (2008), which use the following two criteria:

$$\log\left(\frac{[\mathrm{O\,III}]}{\mathrm{H}\beta}\right) > \frac{0.61}{\log([\mathrm{N\,II}]/\mathrm{H}\alpha) - 0.47} + 1.19 \tag{6.2}$$

and

$$\frac{[\mathrm{O\,III}]}{\mathrm{H}\beta} > 3 \tag{6.3}$$

We also used a redshift cut of < 0.40, so that Hα is covered by the SDSS spectrum. Finally the object had to be spectroscopically classed as a galaxy (SpecClass = 'Galaxy') and have

[1] http://casjobs.sdss.org/CasJobs/

no quality control flags raised. In order to ensure that we had selected Type 2 AGN we visually inspected the spectra and produced a final sample of 2,834 objects.

We then crossmatched this sample with the PS1 3π catalogue, using internal search algorithms and a 5 arcsec matching radius. We found 2,624 objects in the 3π catalogue, although at the time of searching the 3π catalogue was not complete in any of the g, r or i bands required to match to the SDSS data.

Using this sample we searched for objects where the PS1 magnitudes were at least 2 magnitudes brighter in at least one band, and we found 6 objects: 3 that brightened in the i band, 1 that brightened in the g band and 2 that brightened in the g and i bands.

From analysing these 6 objects in greater detail it was found that none of the photometric differences were due to intrinsic variability of the source. We found that 3 of the objects were affected by artifacts in the image covering the object, 1 was due to the object falling on a noisy chip gap, creating a spurious detection, and 2 were due to background brightness problems.

In order to check the likelihood of all of our extremely variable objects being due to PS1 data quality problems, we looked at objects that decreased in magnitude between the SDSS and PS1 observations, and also drew a random sample of 10 objects from the whole sample. We found that the reason for the largest decreases were also due to PS1 data quality problems, and similar issues affected 3 out of the randomly selected sample of 10 objects to some degree.

This study therefore proved to be inconclusive as none of the sample were found to have either significantly increased or decreased between the SDSS and PS1 observations. However, the data quality concerns raised indicated that if such an event was to take place the current PS1 reduction pipeline could potentially have difficulty in identifying it.

This study was completed before the FGSS survey described in Section 5.5.1 was initiated. The FGSS survey would be an ideal tool for this type of search, as it makes difference images between the SDSS and PS1 data and flags significant changes. Now that the pipeline has been optimised for supernovae detection it is being developed to make it more flexible and allowing for directed sample searching through the 3π images. This type of study will also be able to be completed using the Published Science Products Subsystem (PSPS) database

once all of the data has been reprocessed. The main disadvantage of this method over the FGSS one is that of timescale, as the recalibration is expected to be ongoing until Spring 2013, while the FGSS pipeline is expected to be enhanced before the end of 2012.

6.7 Conclusions

From an initial sample of 504 spectroscopically identified quasars with z $>$ 1.45 we formed three subsamples to investigate the variability properties of BALQSOs compared with non-BALQSOs. We found 12 BALQSOs in the parent sample, which form the BAL subsample, 10 objects were found to have BAL-like features, but did not have the absorption trough definition needed for classification as a BAL. These objects form the possible BAL subsample. Finally, a control subsample of broad line Type 1 quasars was formed from the remaining objects in the sample. We chose 17 objects with classical quasar spectra, and which matched the redshift distribution of the other two subsamples.

We created light curves for the objects from the PS1 MDS images using the Pan-STARRS IPP software. Data points that were found to deviate by more than 2-σ from their neighbours were investigated, and rejected if problems were found with the input images. From this we recovered *g, r* and *i* data for 8 out of the 12 objects in the BAL subsample, 5 of the 10 objects in the possible BAL subsample and 13 of the 17 sources in the control subsample. A further 3 objects in both the possible BAL and control subsamples have g and r band data, and all remaining objects have r band data.

From the optical light curves we used three different methods to quantify the variability. All of the methods calculate the excess variance of the light curve but are used for the interpretation in different ways.

From these studies we find that there is no significant difference in the three subsamples, but as we only have a small number of objects further work needs to be done to see if this holds for large samples.

As a part of this study two interesting objects emerged. One, J142129.40+522751.9 is a BALQSO that occupied a unique position on the excess variance correlations, proving to have a much higher level of variability in the i band when compared to the other bands than

all the other objects. We obtained spectra from three different epochs spanning 9 years and during that time there is no evidence of spectral evolution, either in the emission lines or the continuum. However, we do find that the first season's worth of observation has a high level of flickering in all bands, but there are far fewer points in the i than the other two. As the sample points appear to fall close to the maximum and minimum levels of the flickering, this would produce a higher level of variability in this band and may account for the results seen.

The second interesting object is J104516.6+573137, which is also part of the BAL sub-sample. J104516.6+573137 was flagged during the initial visual inspection of the light curves as it has an unusual transit-like dip. Unfortunately the crucial segment showing the bottom of the dip was unobservable due to object/Sun constraints. This object also highlights the improvement that Pan-STARRS provides over other surveys such as the CSS. The CSS light curve for this object has a large degree of scatter and so the trend visible in the PS1 data is undetectable due to the uncertainties associated with the CSS data. It also highlights the difference in the observing frequency of the two surveys. However it should be noted that the MDS fields are visited more frequently than the 3π fields and will have $\sim$ 10x more exposures per year by the time the survey is complete.

We propose several possible scenarios to explain the origins of this event, based on its transit-like properties. We find that the a broad line absorption outflow and a BLR cloud are not likely causes, because of opacity and occulting area required. However, a large high mass star is a possible candidate. We show that, using basic assumptions of the mass of the black hole and scale of the accretion disc, the size of the object needed to produce the event is comparable to the gas envelopes of red supergiants currently known. If this event is indeed an orbiting star then we predict a orbital period of $\sim$ 8 years. An alternative is that the star may be on a plunging orbit. In this scenario we cannot predict the fast decaying orbital period, and the star could be a progenitor for a TDE.

Finally we presented a pilot statistical study based on SDSS classified Seyfert 2 AGN. We created a sample of 2834 nearby Seyfert 2 based on optical spectra, and cross-matched the sample to PS1 3π catalogue data. As the 3π survey has only just achieved complete base coverage, at the time of the study it was incomplete and only 2624 objects were matched.

The motivation behind the project was to discover Seyfert 2s changing into Seyfert 1s, characterised by a large (> 2) magnitude rise. We found 6 objects that fitted this criteria, but on closer inspection of the data all were rejected as data artifacts, and not intrinsic to the AGN.

This study proved inconclusive, and the limited data quality of the 3π catalogue data suggests that if such events were present they might not be observable in the current data. After PS1 completes the grand reprocessing, plus improvements to the 3π survey, this study could be redone and the results should be markedly more robust than those of this study.

This chapter has demonstrated that Pan-STARRS offers considerable potential to investigate AGN variability with large data sets, but at the moment is hindered by data processing limitations. The future work section of the next chapter summarises the current abilities of Pan-STARRS, and reports how it is being improved and on what timescales, before considering the type of future studies that could be undertaken.

Chapter 7 | *Conclusions*

In this thesis we have seen how the observable properties of AGN are affected by the presence of gas and dust and key parameters such as black hole mass and mass accretion rate. In the first science chapter we used a large sample of X-ray detected quasars to study correlations between the amounts of gas and dust present in the objects. In Chapter 3 we used a low redshift X-ray detected sample of Type 1 AGN to produce constrained SEDs, and investigated how the presence of gas and dust can affect the model parameters. Chapter 4 extended this study to examine the optical and X-ray variability of this sample using the Catalina Sky Survey optical data and *XMM-Newton* X-ray data. Finally, Chapters 5 and 6 focused on variability studies using data from the Pan-STARRS telescope. Chapter 5 described an in-depth study of a single interesting object, while Chapter 6 investigated the potential of using Pan-STARRS data from large scale surveys. In this concluding chapter we provide a summary of the major findings and suggest possible lines of future work that would build on the studies presented here.

7.1 Gas and dust in AGN

In Chapter 2 we presented an in-depth optical and X-ray study of 1,201 quasars with a range of reddening and obscuration levels. We assembled data from the EPIC monitor onboard the *XMM-Newton* satellite and optical data from the SDSS DR7 after initially creating the sample by cross-correlating the 2XMMi Serendipitous Survey with the SDSS DR5QSO catalogue.

In order to determine the dust reddening of the sample, we used two different methods. The first method was that used by Richards et al. (2003) and involves the relative colours of the quasar and its redshift. This produced a sample of 72 quasars. The second method was

to deredden the continuum to match the composite continuum of Vanden Berk et al. (2001). We found that many objects displayed a continuum that was much bluer and steeper than the Vanden Berk et al. (2001) composite. We suggest that for several of these objects this could be due to the presence of the Balmer continuum, which can be strong in all AGN and will mask the true quasar continuum. We also found objects that had more reddening than could be explained by dust alone, as their dereddened continua shapes did not match the composite shape. We suggest that this could be due an intrinsically redder continuum and excluded these objects from our dust reddened sample. This method created a sample of 61 objects. We found that less than 10% of the objects overlapped between these two samples, but that they produced very similar composite spectra and have similar characteristics.

We modelled the X-ray spectra of 998 of the objects and we found that 50 objects had constrainable levels of N_H, of which we identified the 40 with $N_H > 1 \times 10^{22}$ cm^{-2} as the most obscured, and this became the gas obscured subset.

We then investigated the dust-to-gas relationship for the quasars in our different subsets. From the work of Maiolino et al. (2001a) we expected most of our quasars to have a relationship between 10 - 100 times weaker than the Galactic relationship. We found that the mean of the objects with constrained values of N_H and binned by number of counts fell within this region, as did most of the upper limits for the rest of the sample. On stacking the X-ray data for the dust reddened subsets we found that both of these subsets lie much closer to the Galactic relationship, depending on the spectral model used, and that they lie in a region where few of the obscuration constrained or gas obscured quasars are found. Neither of the dust reddened subsamples show any indication of a relationship between the levels of gas and dust in their systems. We do note, however, that this may be a bias introduced by the low number of counts available for this sample, as many objects in these subsets had too few counts to be used in the spectral stacked routines.

Finally, we created spectral composites for our overall sample and three subsets following the method of Vanden Berk et al. (2001). We produced a composite of our overall sample that was an excellent match to the Vanden Berk et al. (2001) composite. Out of the three subsets we find that the reddening in the gas obscured subset is smaller than for the dust reddened subsets, and that the dereddened continuum of this composite is a much better fit

to the overall composite spectrum than either of the dust reddened subsets.

In conclusion we find that while our dust reddened subsets display levels of gas obscuration and our gas absorbed sample does have a small amount of dust reddening, they do not have the same characteristics. However, further work on objects with good X-ray data out to high redshifts will help shed light on whether our result is due to a data quality bias in our sample or if the dust-to-gas relationship in quasars is even more diverse than previously thought.

7.2 Optical-to-X-ray SED modelling: Models and bolometric corrections

In this chapter we presented a spectral study of 192 Type 1 AGN, with a range of obscuration and sub-classifications. We assembled data from the EPIC monitor onboard the *XMM-Newton* satellite and optical data from SDSS DR7. We also added optical/UV data from the *XMM-Newton* OM when it was available.

We use a detailed line fitting routine to measure the Hα and Hβ emission line profiles, and hence constrain black hole masses. From this we found that NLSy1s by definition have lower black hole masses than their broader counterparts using this method, even if they have comparable optical luminosities.

The optical, UV and X-ray data points were combined into one SED and fitted using a new broadband SED model (Done et al, 2012), which is energetically self-consistent and places physical limitations on the unobservable UV region of the resultant fit.

By separating the SEDs into their distinct components we draw a number of conclusions. We find that the contribution of each of the disc, soft excess and power law components to the bolometric luminosity has a wide range from source to source, depending on luminosity, Hβ linewidth and λ_{Edd}. We find that, on average, as L_{bol} and λ_{Edd} increase so does the contribution from the disc component. We also find a negative correlation between both Hβ linewidth and black hole mass with the contribution from the disc component. A larger statistical study with higher quality X-ray data will be useful to confirm this.

We also investigate the properties of super-Eddington objects with respect to the rest of

the sample. We find that while such AGN in this subsample have $L_{soft\,excess}$ and L_{pl} values similar to those in the parent population, they have larger than average L_{disc} values. They also have a smaller black hole mass, a higher mass accretion rate and smaller coronal radius than the overall sample. We also find that on average there is no discernible difference in the optical depth or electron temperature of the soft excess component in super- or sub-Eddington AGN.

Finally, we inspect the SEDs produced and divide them into three subsamples based on their shapes. While it should be stressed that there is substantial spectral diversity seen in these SEDs, we can suggest analogous links to the spectral states observed in Galactic BHBs; this suggests that λ_{Edd} is a useful parameter for categorising the spectral state of AGN and that the energetic process taking place in AGN can be considered as scaled-up versions of the processes seen in Galactic BHBs.

7.3 Optical-to-X-ray SED modelling: Optical & X-ray variability

In Chapter 4 we presented a study of the optical and X-ray variability properties of a subsample of 41 objects extracted from our larger parent sample defined in Chapter 3.

For our optical variability study we used data from the Catalina Sky Survey. We found that 37 of our objects were covered by the survey and in all bar 2 cases had 7 years of observations. We found that most objects exhibit continuous low-level variability throughout the time they were observed by CSS and that the majority of the smallest mass black hole AGN showed no evidence of optical variability. We did not find the expected relationship between luminosity and variability probably due to a combination of poor data quality, the range of black hole masses in our sample and the nature of the accretion disc in the optical region.

In the X-rays we used two different methods to attempt to constrain the variability. The first method we used was to create an RMS spectrum for each object. Out of our sample of 41 objects we were able to constrain RMS values in the three bands for 11 objects in one of 10 ks, 20 ks or observation-length time intervals. We calculated the ratio of the RMS

value for the hard against medium and the medium against soft energy bands. From the 11 objects where the ratios could be fully constrained we found that 5 objects had ratios consistent with a single, underlying variable component in the X-ray region, with a flat RMS spectrum.

Three objects lie on the linearly increasing trend that can either be described by a single variable component, or by two components with the middle energy band reflecting the change between the two levels of variability. The final three objects lie outside of this relationship.

We conclude that 5 of the 11 constrained objects in this sample are dominated by a single variable component in the X-ray region, with the possible addition of a soft absorption feature. Objects that lie on the linear trend can either be composed of one or two components, but it is beyond the scope of this study to determine which is the case for the individual objects displaying these RMS spectral shapes. We also conclude that objects that fall below this relationship are likely to be composed of two components, similar to the situation claimed for RE J1034+396 whereas objects lying above this trend are thought to behave more like Mrk 766.

The second method we used was the excess variance method, σ^2_{rms}. We calculated the σ^2_{rms} values for all three energy bands across 10, 20, 40 and 80 ks time intervals. We found the expected relationship between the values in the different bands in all time intervals. Finally we explored the relationship between σ^2_{rms} and various physical parameters. While we did not find the expected variability and black hole mass relationship, due to the large scatter of our sample, we did find a relationship between the degree of variability and 2 - 10 keV luminosity. We were unable to find a correlation between σ^2_{rms} and λ_{Edd}, again due to the large scatter of our sample.

7.4 Pilot studies with Pan-STARRS

The opening sections of Chapter 5 introduced the Pan-STARRS telescope, its observing strategy, the large scale surveys it is conducting and the method used to detect transients in these surveys.

The remaining sections of this chapter focus on one object, PS1-10adi, discovered by the

Pan-STARRS transient pipeline. PS1-10adi is an extremely energetic transient event. The ambiguity over the origins of the event is compounded as there is no pre-outburst spectrum with which to compare the evolving spectrum. Currently there are arguments to support PS1-10adi as a NLSy1 and as a Type IIn supernova. Similarities in the optical spectral properties of these two types of object do not allow us to distinguish between these. PS1-10adi does not display typical AGN variability, but as this is the first example of its kind to be discovered with Pan-STARRS it is hoped that similar objects will be found in the future, and that this will help to better our understanding of similar events.

In Chapter 6 we presented the results of pilot studies using the Pan-STARRS products to create and analyse large scale surveys.

From an initial sample of 504 spectroscopically identified quasars with $z > 1.45$ we formed three subsamples to investigate the variability properties of BALQSOs compared with non-BALQSOs. We identified 12 BALQSOs, 10 objects that displayed BAL-like features but did not have the absorption trough definition needed for classification as a BAL, and we chose 17 objects to form a non-BAL control sample.

We created light curves for the objects from the PS1 MDS images using the Pan-STARRS IPP software, in the *g, r* and *i* bands, when available. From the optical light curves we used three different methods to quantify the variability. All of the methods calculate the excess variance of the light curves, but are used to interpret it in different ways.

From these studies we find that there is no significant difference in BAL/BAL-like QSOs and the non-BALQSOs, but as we only have a small number of objects further work needs to be done to see if this holds for larger samples.

As a part of this study two interesting objects emerged. One, J142129.40+522751.9, is a BALQSO that occupied a unique position on the excess variance correlations, proving to have a much higher level of variability in the *i* band when compared to the other bands than all the other objects. However, we do find that the first season of observations show a high level of flickering in all bands, but there are far fewer points in the *i* band than the other two. As the points appear to fall close to the maximum and minimum levels of the flickering this would induce a higher level of variability in this band and may account for the results seen.

The second interesting object is J104516.6+573137; this object is also part of the BAL subsample. This object highlights the improvement that Pan-STARRS provides over other surveys such as the CSS. The CSS light curve for this object has a large degree of scatter and the trend seen in the PS1 data is masked by the uncertainties inherent in the CSS data. We propose several possible scenarios for the source of this event, based on its transit-like properties. We find that both a broad line absorption outflow and a BLR cloud are unlikely, because of the need for high opacity and large occulting area. However, a star is a possible candidate as the occulting object. We show that, using basic assumptions of the mass of the black hole and scale of the accretion disc, the size of the object needed to create the event is comparable to the gas envelopes of red supergiants currently known. If this event is caused by an orbiting star then we predict a orbital period of ~ 8 years. An alternative option is to place the star on a plunging orbit. In this scenario we cannot predict the orbital period, but it suggests that the star might be a progenitor to a TDE.

Finally, we presented a pilot statistical study based on SDSS classified Seyfert 2 AGN. We created a sample of 2,834 nearby Seyfert 2 AGN with spectra and cross-matched the sample to PS1 3π catalogue data, which produced 2,624 matches. The motivation behind the project was to find Seyfert 2 AGN changing into Seyfert 1, signalled by a large (> 2) magnitude rise. We found 6 objects that fit this criteria, but on closer inspection of the data all 6 were rejected as the variability was not intrinsic to the AGN.

This study proved inconclusive, but the limited quality of the 3π catalogue data suggests that if these objects were present they might not be detectable in the data. When the grand reprocessing is complete, together with improvements to the 3π survey, this study could be redone, and the results should be markedly more robust than the results of this study.

7.5 Future work

The work described in this thesis has the potential to lead onto a number of different studies, which are summarised below:

- The resulting composite spectra from Chapter 2 are very interesting, but the subsamples that we used to create them suffered from small numbers of objects and, in the

case of the dust reddened samples, poor X-ray data quality. It is hoped that further work will improve the stacking and spectral fitting routines of low count X-ray data. A similar study could also be carried out utilising well-studied deep X-ray fields that overlap with spectroscopic optical studies (e.g. *Chandra* Extended Deep Fields). This would allow us to probe the higher redshift range with good quality X-ray and optical data.

- The possibilities of extending the SED modelling explored in Chapter 3 is limited by X-ray coverage of sources. Chapter 3 showed that the model is robust and can fit all but the lowest count-rate sources. It could be extended to include different classes of AGN (i.e. focused studies on NLSy1s or BALs) or extended to higher redshifts. There is also the potential to develop the model to include the IR region, which would be beneficial for modelling the torus and for nearby sources where the host galaxy is clearly present and where the model under-predicts the flux at the red end of the SED if a simple accretion disc is used.

- The variability study of Chapter 4 shows the potential of combining the light curves from large area sky surveys with X-ray light curves. It is hoped that as the Pan-STARRS project continues it will provide high quality light curves for objects over 3/4 of the sky, and as the Serendipitous Survey of *XMM-Newton* continues the amount of X-ray data available will also increase. This will allow us to carry out similar studies with much larger AGN samples and so improve our understanding of possible links between X-ray and optical variability.

- Chapter 5 and 6 both reported on pilot studies using the Pan-STARRS telescope. Chapter 5 focused on a single object found by the Belfast Transient Team in the MDS survey, and Chapter 6 studied a subsample of BALs and spectrally similar objects, looking for differences between them and a control sample. Both of these studies demonstrate the potential of the Pan-STARRS project, which is currently limited by time base and sample numbers.

  Currently the Pan-STARRS' data reduction and processing has been optimised to find specific objects such as supernovae and NEOs, making pilot survey studies for AGN

variability difficult. As we have shown limited samples can be created and studied, but are hindered by processing and image quality issues. We have found that while we can find interesting objects, such as those discussed in Chapters 5 and 6 in greater detail, we are not yet at a stage to draw firm statistical conclusions about our samples.

Furthermore, the inconclusive change of state study discussed in Section 6.6 was hindered by the data quality of the 3π catalogues. In the near future it will be possible for this study to be redone using the FGSS pipeline, and for it to be enhanced by the the 3π difference imaging upgrades that are being implemented.

- At present the 3π survey does not yet have complete multiple epoch coverage in all bands; this is primarily lacking in the areas of sky covered during the winter months due to two years of bad weather. As of summer 2012 the PS1 3π survey has 80% photometric coverage and has an average of 42 epochs for every point in the sky across all bands.

  In the near future this should change; the reprocessing of PS1 data has begun and should be complete by December 2012. However, the current plans are then to implement the code upgrades that are currently being tested. This means that while a workable 3π catalogue will be available by the start of 2013, by the summer of that year the whole catalogue data should be available, containing good science-quality data with a range of image stacks to analyse. The MDF survey is currently further advanced in the reprocessing route and should be finished earlier.

  Now that the project is maturing with all of the surveys achieving the base level of coverage needed to begin reaching their science goals, the data reduction process is being improved and centralised to make it more scientifically efficient to exploit. With major changes underway in the next few months, the true potential of using Pan-STARRS to study AGN variability will begin to be realised.

This thesis covers a broad range of optical and X-ray studies all focused on AGN. Understanding the emission present in the optical and X-ray regions, and how these change over time is crucial to interpreting the basic physical processes and mechanisms that govern the behaviour of the accretion disc and corona. The studies presented here are just a small

subset of the types of inquiries that can be conducted in this field potentially providing new insights into the nature of AGN and our understanding of the cosmos.

Appendix A | *Chapter 3: SED fitting parameters*

The following tables provide the parameters derived from the SED fits for all 171 'successful' SED fits. A fit was classed as 'successful' if the model could fit parameters to the data without making any cuts for the physical possibility of the model derived. The parameters listed are:

- Intrinsic N_H: as the lower limit for the amount of absorption was set at the galactic N_H the intrinsic N_H was derived from the resultant values. It is given in units of cm^{-2}.
- $\log(M_{BH})$: the best fitting black hole mass in solar masses,
- $\log(\dot{M})$: the total mass accretion rate in units of g s^{-1}
- R_{cor}: corona truncation radius in units of gravitational radii (r_g).
- Γ_{pow}: the slope of the power law component in the SED fitting.
- f_{pl}: the fraction of the power law component as part of the total reprocessed disc emission.
- χ^2/dof: the reduced χ^2 of the SED fitting.
- L_{bol}: the bolometric luminosity of the SED model integrated from 0.001 to 100 keV in units of erg cm^{-2} s^{-1}.
- λ_{edd}: the Eddington ratio.
- L_{disc}: the luminosity of the disc component in units of erg cm^{-2} s^{-1}.
- L_{comptt}: the luminosity of the soft excess component in units of erg cm^{-2} s^{-1}.
- L_{pl}: the luminosity of the power law component in units of erg cm^{-2} s^{-1}.
- $L_{2-10keV}$: the luminosity of the 2 - 10 keV band in units of erg cm^{-2} s^{-1}.
- $\kappa_{2-10keV}$: the 2 - 10 keV bolometric correction coefficient.

Table A.1: The complete fitted sample.

SDSS name	N_H ($\times 10^{22}$)	$\log(M_{BH})$ ($M_\odot$)	$\log(\dot{M})$ (g s^{-1})	R_{cor} (r_g)	Γ_{pow}	f_{pl}	χ^2/dof	L_{bol} ($\times 10^{44}$)	λ_{edd}	L_{disc} ($\times 10^{44}$)	L_{comptt} ($\times 10^{44}$)	L_{pl} ($\times 10^{44}$)	$L_{2-10keV}$ ($\times 10^{43}$)	$\kappa_{2-10keV}$
J004319.7+005115	0.040	8.349	26.313	25.83	1.83	0.51	517.34/497	60.53	0.230	33.77	13.47	13.06	26.94	22
J020029.0+002846	0.023	9.113	24.901	45.31	2.14	1.00	21.54/14	1.51	0.001	0.51	0.00	1.00	0.09	16
J020615.9-001730	0.047	7.984	25.122	37.91	2.11	0.71	2886.97/525	5.97	0.078	2.51	0.21	3.21	2.39	25
J023042.6-011105	0.050	8.838	25.180	52.00	1.80	0.75	157.34/51	3.32	0.004	1.07	0.60	1.64	3.31	10
J024912.7-082216	0.256	6.866	26.487	7.88	2.00	0.21	57.76/7	111.42	7.649	110.30	1.49	0.37	0.88	1242
J030248.7+002131	0.315	7.536	25.283	16.77	2.12	0.04	158.59/48	8.05	0.180	5.84	2.07	0.09	0.12	558
J030639.5+000343	0.133	7.579	25.558	20.85	1.73	0.30	732.35/565	14.32	0.183	7.46	5.38	1.50	2.54	56
J074249.7+285502	0.265	7.645	26.097	56.38	2.66	0.13	51.38/36	41.68	0.724	12.97	5.83	3.62	0.86	482
J074338.9+495429	0.100	8.142	25.210	47.03	1.79	0.36	42.99/21	4.99	0.027	1.79	2.14	1.05	2.18	23
J075204.7+362500	0.044	7.953	25.522	67.31	1.93	0.84	108.79/23	9.83	0.084	2.64	1.21	5.95	11.15	9
J075216.4+500251	0.055	8.258	25.508	31.60	2.20	1.00	17.76/17	9.73	0.041	4.67	0.00	5.07	5.27	18
J080455.5+241124	0.100	7.388	26.012	8.00	1.90	0.30	63.55/21	40.62	1.279	39.62	0.55	0.22	0.49	827
J080643.2+153814	0.050	8.301	25.001	12.00	1.60	0.88	3185.08/68	3.79	0.015	3.39	0.61	0.34	0.63	60
J081053.8+280611	0.100	7.790	26.090	10.00	1.60	0.60	106.90/55	37.59	0.469	35.22	1.11	1.27	2.42	155
J081546.9+514416	0.419	6.948	26.783	7.20	1.50	0.99	33.36/2	220.17	3.083	196.66	24.00	0.86	1.42	1542
J083454.8+553422	0.119	8.700	25.976	97.84	2.00	1.00	90.09/60	23.97	0.036	4.53	0.00	19.49	30.31	8
J083737.0+254750	0.216	8.782	24.839	99.92	2.24	1.00	182.01/63	1.40	0.002	0.25	0.00	1.15	0.69	20
J091617.4+303038	0.200	7.301	26.495	8.04	1.99	0.28	262.79/37	109.11	4.200	108.05	1.58	0.60	1.34	811
J091828.5+513929	0.184	8.459	25.855	10.43	1.50	1.00	50.06/23	24.42	0.064	23.09	0.00	1.39	2.25	108
J091848.6+211717	0.150	8.778	26.624	8.40	1.99	1.00	701.20/556	156.88	0.201	151.14	0.00	4.33	8.02	196
J091910.1+513906	0.401	8.153	25.762	33.24	1.50	0.02	20.30/9	19.27	0.104	8.90	10.17	0.14	0.23	829
J092212.0+512321	0.371	8.045	25.873	9.23	2.90	0.50	14.88/9	24.92	0.173	23.49	0.63	0.62	0.07	3403
J092246.9+512037	0.060	7.328	26.175	11.04	2.10	0.18	251.57/193	57.94	2.080	51.48	4.93	1.07	2.11	272
J093551.5+612111	0.822	7.049	26.526	6.47	1.96	0.14	58.19/31	162.01	1.994	161.53	0.07	1.60	0.02	8810
J093922.9+370942	0.018	8.411	25.401	35.00	1.97	0.30	796.39/126	8.26	0.024	3.67	8.25	1.33	2.35	35
J094057.1+032401	0.049	7.818	24.882	14.98	1.90	0.31	286.81/267	3.37	0.039	2.62	0.52	0.22	0.44	76
J094240.9+480017	0.101	8.001	24.931	20.00	2.00	0.20	715.37/14	2.90	0.022	1.90	0.80	0.19	0.34	85
J094439.8+034940	0.122	8.466	25.733	22.52	1.70	0.14	402.07/130	19.48	0.051	11.86	6.65	0.88	1.79	108
J094444.8+034400	0.061	6.734	26.412	10.45	1.83	0.41	57.65/18	74.49	2.558	67.91	3.81	2.39	5.81	128
J095048.3+392650	0.017	8.501	26.153	20.04	1.97	0.81	957.74/755	47.94	0.116	31.52	3.18	12.98	24.04	20
J095819.8+022903	0.063	8.275	25.631	31.63	1.82	0.19	288.44/107	11.35	0.046	5.42	4.88	1.03	2.16	52
J095848.6+025243	0.496	7.645	25.556	8.97	1.50	0.00	266.41/81	15.79	0.274	15.06	0.67	0.0002	0.0004	4276
J095921.3+024030	0.100	7.602	25.601	12.00	1.90	0.60	1731.20/83	12.75	0.245	11.08	0.69	0.97	2.09	60
J095942.1+252212	0.036	8.689	25.170	20.15	1.98	1.00	40.87/19	3.63	0.005	2.35	0.00	1.28	2.18	17
J095944.1+305615	0.130	7.689	26.705	10.00	1.90	1.00	166.00/1	141.87	1.229	130.61	0.00	9.76	22.03	64

SDSS name	N_H ($\times 10^{22}$)	$\log(M_{BH})$ ($M_\odot$)	$\log(\dot{M})$ ($g\,s^{-1}$)	R_{cor} (r_g)	Γ_{pow}	f_{pl}	χ^2/dof	L_{bol} ($\times 10^{44}$)	λ_{edd}	L_{disc} ($\times 10^{44}$)	L_{comptt} ($\times 10^{44}$)	L_{pl} ($\times 10^{44}$)	$L_{2-10keV}$ ($\times 10^{43}$)	$\kappa_{2-10keV}$
J100032.1+553630	0.2285	7.448	25.945	58.67	1.50	0.08	29.12/13	30.80	0.844	9.40	20.27	30.77	1.76	174
J100234.8+024254	0.3221	7.186	26.041	8.08	1.79	0.24	124.4/51	39.51	1.982	38.58	0.63	0.17	0.39	997
J100316.2+024236	0.2420	7.670	25.884	33.75	2.90	0.01	17.17/18	26.87	0.442	12.35	14.43	0.07	0.008	3442
J100420.0+051300	0.1068	8.480	25.954	96.72	1.50	0.02	174.6/28	29.17	0.074	5.63	23.29	0.23	0.37	772
J100434.2+052331	0.4355	8.170	25.911	10.23	1.50	0.14	45.06/3	27.05	0.141	24.96	1.88	0.19	0.31	854
J100726.0+124856	0.0356	9.375	26.394	9.14	1.57	1.00	950.3/143	70.21	0.023	67.70	0.00	2.54	4.56	154
J101341.8-000925	0.2312	7.939	25.871	10.00	2.90	1.00	319.9/15	23.01	0.204	21.33	0.00	1.68	0.21	1096
J101829.7+213530	0.4422	8.474	26.163	100.00	1.50	0.11	118.6/16	41.10	0.106	7.82	30.85	2.46	3.97	103
J101922.6+412050	0.0381	8.444	25.318	100.00	2.04	0.43	313.0/86	5.15	0.014	0.92	2.43	1.80	2.54	20
J102004.5+082741	0.0254	7.822	25.000	10.00	1.50	0.99	1240/10	4.11	0.048	3.92	0.003	0.18	0.30	136
J102147.8+131227	0.1400	8.741	25.050	100.00	1.79	0.77	916.1/35	2.48	0.004	0.49	0.51	1.47	2.95	8
J102311.1+470614	0.1000	8.435	25.350	9.50	1.70	1.00	45.13/5	7.08	0.020	6.73	0.00	0.35	0.71	98
J102348.4+040554	0.0581	7.312	25.222	9.00	1.90	0.14	692.9/167	7.05	0.265	6.71	0.26	7.06	0.001	6194
J102812.6+293222	0.3537	7.663	26.416	9.59	1.83	0.10	7.69/2	80.72	1.349	76.57	4.41	0.44	0.99	817
J102822.9+235126	0.0228	8.364	25.128	100.00	1.75	0.58	323.5/78	3.48	0.012	0.67	1.28	1.52	3.10	11
J103059.0+310255	0.0322	8.498	25.832	45.39	2.16	0.92	1309/945	22.82	0.056	8.32	1.09	13.39	14.95	15
J103216.0+505119	0.0289	7.179	26.159	10.07	1.50	0.91	381/132	52.80	2.689	50.20	0.34	2.37	3.86	137
J103352.6+004403	0.7446	7.797	26.574	8.40	1.50	0.12	689/19	149.99	1.843	145.86	3.73	0.33	0.53	2803
J103438.6+393828	0.0131	6.426	25.141	46.78	2.00	0.05	1426/596	6.79	1.960	2.44	4.12	0.21	0.44	153
J103608.4+600229	0.1978	7.682	26.015	81.06	2.87	0.17	26.84/7	33.75	0.540	7.70	21.70	4.35	0.32	1062
J103848.6+533756	0.0139	9.000	25.343	16.73	2.10	1.00	10.54/4	4.86	0.004	3.45	0.00	1.38	1.70	29
J103935.7+533039	0.2266	7.993	25.942	27.34	1.51	0.12	138.2/10	29.04	0.227	15.79	12.19	1.07	1.74	166
J104053.9+090027	0.3593	7.581	26.062	41.46	1.90	0.01	30.36/22	40.48	0.818	15.96	24.16	0.33	0.69	588
J105128.4+335850	0.2194	6.546	26.600	8.55	1.50	1.00	39.88/37	145.59	1.835	142.56	0.00	3.01	4.97	293
J105143.8+335927	0.0443	8.163	26.042	100.00	1.50	0.33	1245/597	3.51	0.186	7.35	21.20	6.61	10.65	33
J111443.5+525834	0.0102	7.890	24.821	13.63	1.90	0.32	139/40	2.81	0.028	2.29	0.35	0.16	0.32	89
J111455.5+423215	0.0708	9.432	25.235	10.48	1.50	1.00	26.87/5	3.56	0.001	3.29	0.00	2.37	0.38	94
J111706.4+441333	0.0271	8.029	26.284	50.35	1.53	0.26	1919/936	71.10	0.512	25.33	37.17	2.53	14.21	50
J111743.6+403359	0.0144	7.761	25.000	10.00	1.50	0.99	636.9/10	2.74	0.037	2.60	0.002	0.14	0.23	121
J111748.8+410902	0.3478	7.916	25.638	43.36	1.50	0.09	92.98/14	16.12	0.151	6.24	9.30	0.57	0.91	176
J112328.0+052823	0.0370	7.650	24.853	100.00	1.50	0.24	1085/258	2.57	0.044	0.53	1.70	0.34	0.54	47
J112611.6+425245	0.3479	8.342	25.884	7.52	1.50	1.00	80.59/8	28.24	0.099	27.78	0.00	0.19	0.31	911
J113129.2+310944	0.0739	7.022	25.350	14.08	1.95	0.57	180/78	8.29	0.606	6.70	0.71	0.88	1.93	43
J113859.5+315520	0.4000	7.903	26.000	10.00	2.00	1.00	158.45/2	32.54	0.313	30.24	0.00	2.29	4.51	72
J113939.3+025535	0.3836	7.036	26.794	16.48	1.65	0.01	29.25/14	212.10	3.013	155.35	54.76	0.54	1.13	1869
J115533.5+545805	0.0500	7.754	25.500	23.95	1.70	0.40	304.3/12	9.76	0.132	5.85	2.50	1.40	2.91	34
J115851.0+435048	0.0127	7.260	25.669	12.76	1.66	0.80	274.8/222	14.19	0.600	12.27	0.46	1.49	3.07	46

SDSS name	N_H ($\times 10^{22}$)	$\log(M_{BH})$ ($M_\odot$)	$\log(\dot{M})$ (g s^{-1})	R_{cor} (r_g)	Γ_{pow}	f_{pl}	χ^2/dof	L_{bol} ($\times 10^{44}$)	λ_{edd}	L_{disc} ($\times 10^{44}$)	L_{compTT} ($\times 10^{44}$)	L_{pl} ($\times 10^{44}$)	$L_{2-10keV}$ ($\times 10^{43}$)	$\kappa_{2-10keV}$
J120442.1+275412	0.0177	8.186	25.740	39.44	2.83	0.91	2573.01/891	20.04	0.101	8.16	11.87	8.85	65.73	3
J120549.9+351046	0.0662	7.202	25.697	8.86	1.66	0.67	86.30/40	22.90	1.108	22.30	0.31	0.47	0.95	241
J120941.2+651218	0.2996	8.520	25.939	7.90	1.61	0.03	17.82/1	24.52	0.057	24.08	0.42	0.01	0.02	1199
J121122.4+130936	0.0763	8.872	25.648	99.96	1.71	0.80	130.94/67	7.29	0.008	1.31	1.35	4.65	9.43	8
J121356.1+140431	0.0275	8.041	25.032	20.32	1.93	1.00	3501.00/321	3.90	0.027	2.57	0.00	1.32	2.54	15
J121613.5+524245	0.0513	8.137	26.142	100.00	2.29	0.50	146.22/88	41.73	0.234	7.83	17.04	16.84	11.68	36
J121651.9+375437	0.2484	6.616	25.959	7.42	1.60	0.90	381.02/177	41.39	7.716	41.26	0.04	0.24	0.46	891
J121814.8+142601	0.3951	6.608	26.236	6.82	1.90	1.00	78.31/24	69.47	1.183	70.00	0.00	0.15	0.37	1888
J121948.9+054531	0.0500	6.782	25.300	12.00	1.90	0.30	168.74/74	8.32	1.057	7.22	0.79	0.31	0.71	117
J122330.7+154507	0.0196	7.555	25.319	8.83	2.09	1.00	289.80/119	9.07	0.194	8.74	0.00	0.35	0.60	150
J122602.4+004640	0.0191	7.505	25.627	7.50	1.90	0.70	78.37/4	18.40	0.443	18.36	0.06	0.12	0.27	692
J122934.0+134629	0.0367	7.822	25.735	7.23	2.00	1.00	61.49/42	22.75	0.264	22.36	0.00	0.14	0.28	825
J123052.5+143305	0.1400	8.468	24.573	11.26	1.90	1.00	30.82/15	1.34	0.004	1.17	0.00	0.14	0.28	48
J123054.1+110011	0.0234	8.556	26.148	17.79	1.85	0.84	1897.73/1179	44.37	0.095	32.01	2.13	10.39	21.64	21
J123113.6+151128	0.1336	7.736	25.726	18.07	2.00	0.28	0.01/1	19.18	0.271	13.59	4.18	1.54	2.98	64
J123652.3+622808	0.2169	8.228	26.401	8.33	2.88	1.00	36.83/6	71.07	0.324	68.97	0.00	1.91	0.24	2962
J123733.5+131905	0.0800	7.561	25.700	11.00	1.70	0.50	144.52/95	19.20	0.406	17.37	1.00	0.82	1.72	111
J124013.8+473355	0.3668	6.725	26.405	7.86	2.23	0.19	55.71/28	105.04	10.212	103.36	1.41	0.32	0.67	1574
J124210.6+331703	0.0227	8.084	25.987	42.79	2.18	0.86	2226.72/1036	44.96	0.285	17.60	3.88	23.60	28.94	16
J124319.9+025254	0.0192	7.276	26.044	7.49	1.90	0.73	307.29/159	48.10	1.959	47.20	0.13	0.33	0.75	642
J125553.0+272405	0.0099	8.517	25.855	58.84	1.70	0.47	437.44/206	17.81	0.042	5.37	7.04	5.38	10.99	16
J130022.1+282402	0.0140	7.719	25.233	65.89	1.76	0.42	1841.33/1305	6.84	0.100	1.94	3.01	1.87	3.90	18
J130845.7-013053	0.0812	7.112	26.283	7.21	2.00	0.60	0.01/1	80.01	4.757	78.91	0.20	0.28	0.64	1255
J130949.6-015057	0.3808	7.222	26.531	7.44	2.90	1.00	9.08/4	115.38	5.321	114.02	0.00	1.08	0.38	3035
J131046.7+271645	0.0437	7.938	25.987	100.00	1.85	0.90	219.21/145	26.85	0.238	5.37	2.30	19.21	39.21	7
J131217.7+351521	0.0104	8.894	26.069	19.67	1.99	0.24	4226.32/475	39.03	0.038	25.83	10.09	3.09	5.28	74
J131718.6+324036	0.4880	6.615	26.218	6.60	2.20	1.00	139.82/12	75.58	1.108	75.10	0.00	0.08	0.16	4818
J131942.8-004612	0.3480	7.061	26.556	7.11	2.90	0.30	71.57/15	128.42	8.587	127.71	0.45	0.19	0.08	1623
J131943.5+330617	0.1650	8.031	25.799	63.75	1.53	0.07	226.54/47	20.23	0.145	5.69	13.85	0.70	1.18	172
J132101.4+340658	0.0256	8.419	25.667	41.48	2.00	0.51	143.60/136	12.10	0.036	4.67	3.66	3.76	6.24	19
J132419.8+053704	0.1897	7.140	26.261	6.85	1.50	1.00	4.19/2	64.61	3.601	64.42	0.00	0.11	0.18	3595
J132442.4+052439	0.0463	7.835	24.716	82.76	1.90	1.00	20.56/14	1.79	0.020	0.43	0.00	1.37	2.61	7
J132447.6+032431	0.0525	8.465	26.071	100.00	2.22	0.53	414.24/200	30.46	0.080	5.55	11.79	13.11	10.68	29
J132507.8+054105	0.3362	8.137	25.988	10.32	1.60	1.00	174.81/3	32.97	0.185	31.02	0.00	2.10	3.98	83
J132933.5+335635	0.0800	8.477	25.365	17.31	2.00	0.46	377.69/21	6.95	0.018	5.03	1.07	0.90	1.55	45
J134022.8+274058	0.0129	7.896	24.944	26.70	1.90	1.00	7.50/4	3.06	0.030	1.69	0.00	1.35	2.70	11
J134054.4+262253	0.2354	8.042	25.828	100.00	2.29	0.07	84.30/54	22.98	0.161	4.34	17.40	1.24	0.85	272

SDSS name	N_H ($\times 10^{22}$)	$\log(M_{BH})$ ($M_\odot$)	log(M) ($g\ s^{-1}$)	R_{cor} (r_g)	Γ_{pow}	f_{pl}	χ^2/dof	L_{bol} ($\times 10^{44}$)	λ_{edd}	L_{disc} ($\times 10^{44}$)	L_{compTT} ($\times 10^{44}$)	L_{pl} ($\times 10^{44}$)	$L_{2-10keV}$ ($\times 10^{43}$)	$\kappa_{2-10keV}$
J134105.9-004901	0.050	9.000	25.155	46.48	1.50	0.94	118.46/84	2.63	0.002	1.16	0.12	1.36	2.18	12
J134113.9-005314	0.028	8.172	26.093	100.00	1.93	1.00	410.22/248	37.37	0.193	7.25	0.00	30.08	55.62	7
J134208.3+353915	0.050	7.000	23.000	20.00	1.60	0.80	12531.02/913	0.05	0.004	0.03	0.00	0.01	0.017	26
J134235.6+261534	0.080	8.286	24.387	83.65	1.80	0.30	323.29/77	0.71	0.003	0.16	0.40	0.15	0.30	24
J134351.0+000435	0.085	8.308	24.525	45.31	1.90	0.08	331.10/73	1.20	0.005	0.43	0.70	0.06	0.10	114
J134452.8+000520	0.084	6.699	25.600	9.50	1.90	0.40	241.67/32	17.39	2.675	16.42	0.60	0.37	0.87	199
J134459.4-001559	0.163	7.875	26.422	15.18	1.72	0.17	97.90/38	87.36	0.896	67.89	16.71	2.85	6.09	143
J134745.7+264053	0.120	8.556	25.271	70.00	1.80	0.17	116.78/58	4.58	0.010	1.12	2.91	0.55	1.12	41
J134834.9+263109	0.035	6.154	24.802	14.90	2.23	0.54	18432.24/725	3.32	1.787	2.58	0.34	0.38	0.74	45
J135333.7-021447	0.438	7.430	26.180	8.15	2.54	0.20	24.00/18	54.50	1.558	53.30	1.00	0.24	0.18	301
J135510.2+383528	0.329	7.097	27.036	6.74	2.10	1.00	32.38/11	392.35	4.154	395.63	0.00	0.69	1.50	2614
J135553.4+383428	0.060	7.770	24.672	100.00	1.59	0.78	452.27/309	0.55	0.007	1.55	0.36	0.34	8.46	4
J135810.3+653300	0.014	7.253	25.000	10.00	1.50	0.99	2990.80/414	3.31	0.142	3.14	0.00	0.16	0.26	127
J140019.5+620607	0.016	7.088	24.871	12.49	1.94	0.83	22.43/12	2.85	0.179	2.43	0.07	0.33	0.71	40
J140037.1+622131	0.414	6.953	26.552	6.66	1.50	1.00	66.50/19	158.70	1.595	157.98	0.00	0.13	0.21	7474
J140127.6+025606	0.440	8.252	25.929	99.76	2.89	0.13	57.98/1	24.61	0.106	4.56	20.01	0.017	0.00053	47
J140209.0+621024	0.097	7.752	26.469	99.64	2.90	0.07	179.29/11	86.35	1.176	16.51	65.37	4.57	0.29	3026
J140251.2+263118	0.050	8.675	25.852	43.38	1.72	0.57	163.16/34	21.54	0.035	8.49	6.16	6.85	14.01	15
J140700.4+282714	0.040	9.169	25.213	91.81	1.50	0.11	224.76/52	2.57	0.001	0.51	1.90	0.15	0.24	105
J141351.6+282209	0.231	8.591	26.012	8.11	1.50	1.00	25.52/11	31.82	0.063	31.19	0.00	0.47	0.76	417
J141449.5+361239	0.010	7.491	25.943	8.00	2.00	0.60	1.01/ 1	32.16	0.799	31.32	0.25	0.36	0.75	430
J141531.4+113156	0.100	8.587	25.541	100.00	1.98	0.43	355.69/192	8.14	0.016	1.45	3.86	2.82	4.53	18
J141700.7+445606	0.016	7.498	25.827	14.47	2.00	0.32	961.12/666	27.97	0.684	22.35	3.95	1.79	3.66	76
J141759.5+250812	0.025	7.366	24.496	100.00	1.81	0.96	3925.96/1527	1.33	0.044	0.29	0.05	0.99	2.04	6
J142229.6+473916	0.085	8.581	24.956	90.00	1.90	1.00	289.77/12	2.18	0.004	0.46	0.00	1.73	3.16	7
J142325.4+384032	0.095	7.985	25.943	25.52	1.52	0.27	384.74/79	27.63	0.220	16.08	9.18	2.36	3.94	70
J142351.9+421335	0.330	8.076	26.051	83.22	2.33	0.11	22.76/28	37.54	0.242	8.32	26.08	3.16	1.96	192
J142455.5+421408	0.010	8.616	26.440	12.04	2.02	0.85	240.50/158	78.23	0.146	67.65	1.60	8.96	15.75	50
J142904.5+012017	0.026	9.301	25.094	47.38	1.67	0.64	64.07/12	0.81	0.000	0.30	0.22	0.30	0.59	14
J142943.0+474726	0.049	7.954	26.463	17.78	1.90	0.28	1644.64/769	100.06	0.857	70.65	21.40	7.62	16.34	61
J142945.0+424055	0.011	8.998	24.838	34.65	1.90	1.00	261.15/107	1.65	0.001	0.74	0.00	0.91	1.67	10
J143025.8+415957	0.257	8.444	26.291	100.00	1.50	0.09	255.79/31	47.91	0.133	8.94	36.39	2.61	4.22	113
J143450.5+033843	0.050	6.521	23.947	8.62	1.95	0.90	120.04/99	0.43	0.099	0.42	0.00	0.012	0.026	163
J143452.4+483943	0.156	6.916	25.770	16.78	1.78	0.19	688.58/291	28.61	2.669	21.01	7.00	0.61	1.39	27
J144414.6+063306	0.029	8.159	26.063	23.80	2.07	0.93	974.55/539	39.91	0.213	23.60	1.24	15.04	24.28	16
J144506.1+063020	0.027	8.099	26.194	13.85	1.77	0.70	110.85/27	46.15	0.283	37.51	2.72	5.52	11.94	39
J150719.9+002904	0.046	9.283	25.014	32.86	1.50	1.00	233.92/13	1.62	0.001	0.87	0.00	0.74	1.18	13

SDSS name	N_H ($\times 10^{22}$)	$\log(M_{BH})$ ($M_\odot$)	$\log(\dot{M})$ ($g\ s^{-1}$)	R_{cor} (r_g)	Γ_{pow}	f_{pl}	χ^2/dof	L_{bol} ($\times 10^{44}$)	λ_{edd}	L_{disc} ($\times 10^{44}$)	L_{comptt} ($\times 10^{44}$)	L_{pl} ($\times 10^{44}$)	$L_{2-10keV}$ ($\times 10^{43}$)	$\kappa_{2-10keV}$
J150854.0-001148	0.050	7.533	24.980	100.00	1.66	1.00	642.97/372	3.34	0.075	0.81	0.00	2.61	5.14	6
J151321.6+571359	0.181	7.864	25.673	9.33	2.00	1.00	12.76/1	15.60	0.164	14.70	0.00	0.80	1.55	101
J151504.9+365721	0.124	7.845	25.343	50.93	1.70	0.17	42.64/25	6.85	0.075	2.30	3.85	0.68	1.40	49
J151600.9+000949	0.237	8.044	25.535	45.52	1.79	0.19	421.99/209	12.18	0.085	4.56	6.33	1.35	2.81	43
J151612.2+070341	0.212	8.842	24.964	24.63	1.50	1.00	739.77/41	2.21	0.003	1.46	0.00	0.74	1.19	19
J151741.6+424819	0.101	6.999	25.296	9.94	1.60	0.85	103.61/37	8.04	0.620	7.67	0.089	0.35	0.68	119
J151743.7+070122	0.103	8.125	26.043	34.49	1.68	0.10	136.08/50	33.64	0.194	15.17	16.88	1.50	3.07	109
J151820.3+423451	0.021	9.094	24.870	36.78	1.90	1.00	172.00/37	1.51	0.001	0.63	0.00	0.88	1.61	9
J153152.3+241429	0.038	8.699	24.641	67.93	2.04	0.80	97.85/62	1.05	0.002	0.27	0.16	0.63	0.84	12
J153304.0+302508	0.080	8.432	24.900	28.00	1.87	0.60	75.59/47	2.28	0.007	1.20	0.45	0.63	1.24	18
J153450.3+543000	0.100	7.956	25.698	44.30	1.70	0.15	23.61/15	14.87	0.127	5.63	8.04	1.23	2.53	59
J154316.4+540526	0.105	8.328	25.782	38.79	1.90	0.10	90.21/50	18.87	0.068	7.72	10.12	1.00	1.97	96
J155829.4+271715	0.050	7.699	25.400	30.00	1.63	0.60	3721.12/118	10.03	0.154	5.44	2.16	2.42	4.69	21
J155909.6+350147	0.021	7.980	24.622	100.00	2.13	0.62	741.85/701	1.61	0.013	0.31	0.49	0.81	0.88	18
J160452.3+240240	0.228	6.956	26.445	7.13	2.90	0.89	444.01/142	121.53	1.335	120.78	0.070	0.57	0.27	4557
J160508.8+323922	0.028	6.790	25.130	11.00	1.60	0.55	225.63/51	5.76	0.718	5.25	0.27	0.24	0.46	126
J160706.6+075709	0.332	7.427	26.532	17.55	2.61	0.04	26.96/39	117.27	3.378	83.43	32.20	1.50	0.91	1283
J164119.4+385407	0.255	8.818	25.533	99.99	1.60	0.42	88.86/36	5.80	0.007	1.01	3.04	1.73	3.23	18
J165430.7+395418	0.016	8.237	25.592	40.49	1.89	1.00	24.83/10	10.14	0.045	4.10	0.00	6.01	11.88	8
J171310.4+573426[α]	0.022	7.948	25.00	90.00	1.50	0.00	3754.29/1	2.90	0.025	2.90	2.90	2.90	NaN	NaN
J171350.7+572955[α]	0.022	7.173	25.00	90.00	1.50	0.00	8942.10/1	4.17	0.215	4.17	4.17	4.17	NaN	NaN
J223607.6+134355	0.045	9.029	26.498	43.74	2.24	0.51	733.68/167	79.13	0.057	28.81	24.54	25.78	19.71	40
J233811.5+002045	0.255	7.122	26.709	7.41	2.79	0.87	54.25/20	161.07	4.356	159.75	0.18	1.26	0.69	2328

Note: [α] Objects that while produced a 'successful' fit, actually failed to constrain the harder X-rays.

Appendix B | *Chapter 3: SED figures*

The SEDs from 158 of the objects. While 171 objects were 'successfully' fitted, 13 objects were found to have extremely low data quality and so are not shown. The data and best fit model are shown in black, while the reddened model is shown as a red dashed line. The wide range in the data quality of the remaining objects can clearly be seen, as well as the overestimation of absorption leading to a strong soft excess component emerging.

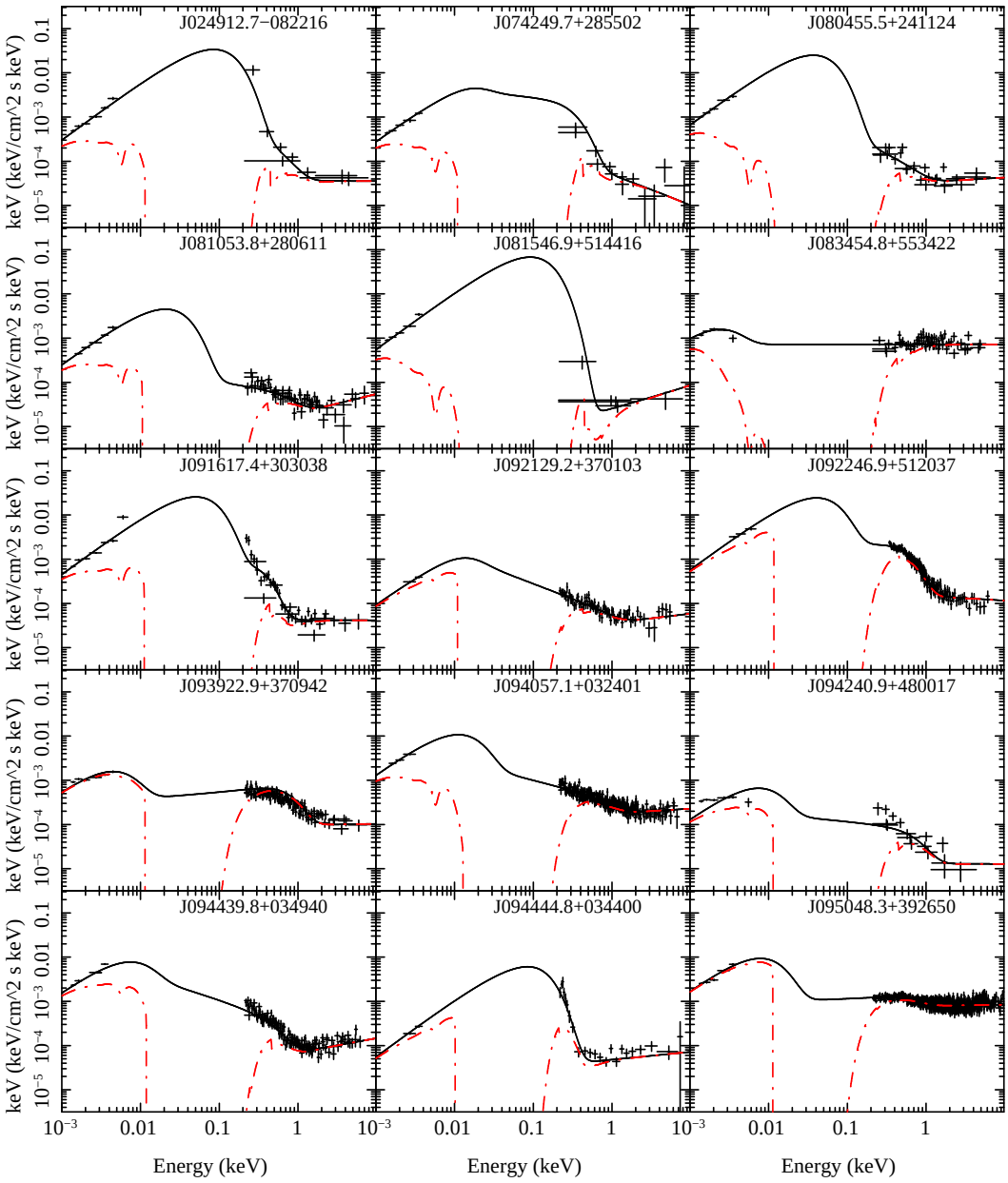

Figure B.1: SEDs of whole sample

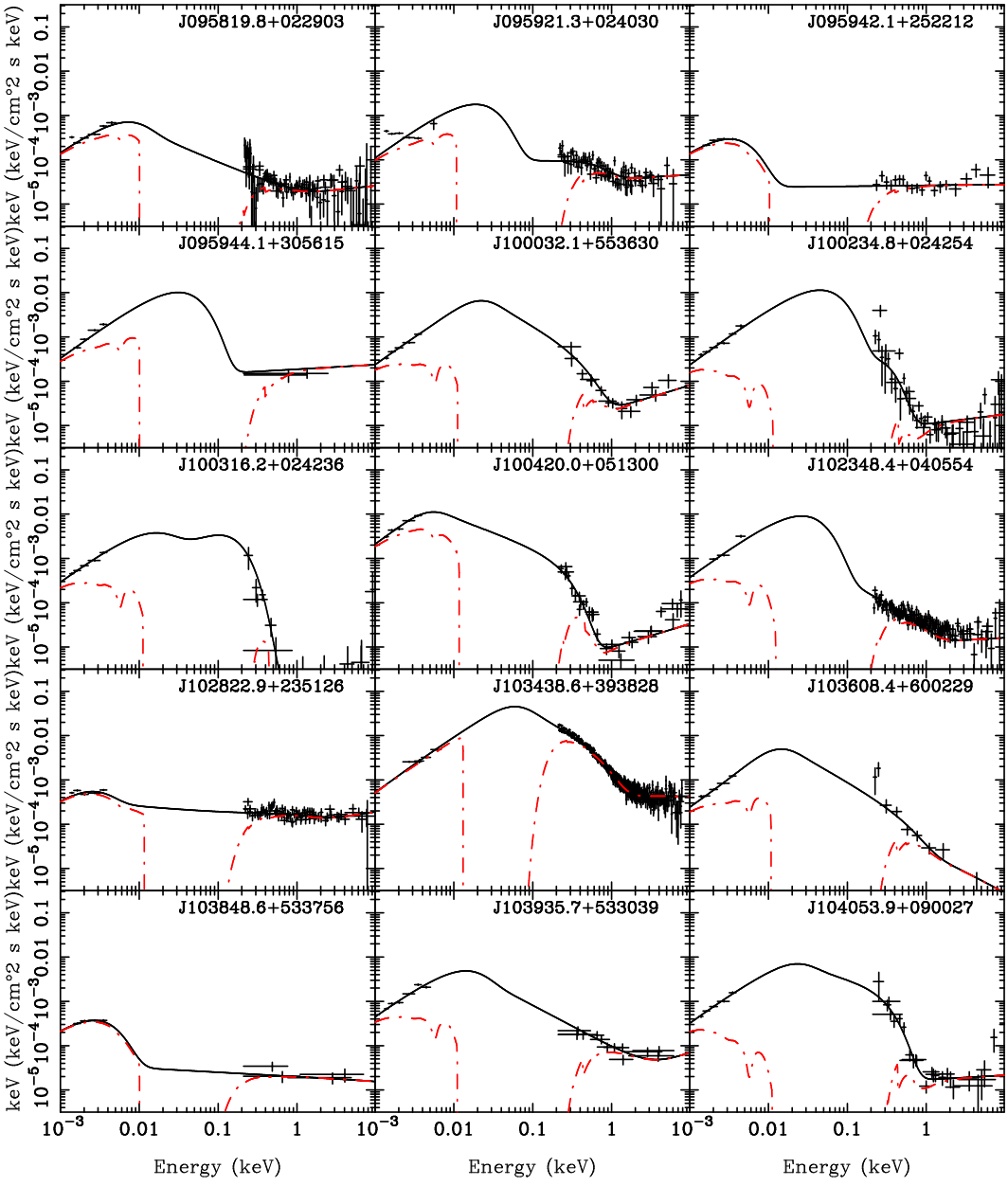
J095819.8+022903
J095921.3+024030
J095942.1+252212
J095944.1+305615
J100032.1+553630
J100234.8+024254
J100316.2+024236
J100420.0+051300
J102348.4+040554
J102822.9+235126
J103438.6+393828
J103608.4+600229
J103848.6+533756
J103935.7+533039
J104053.9+090027
keV (keV/cm^2 s keV)
Energy (keV)

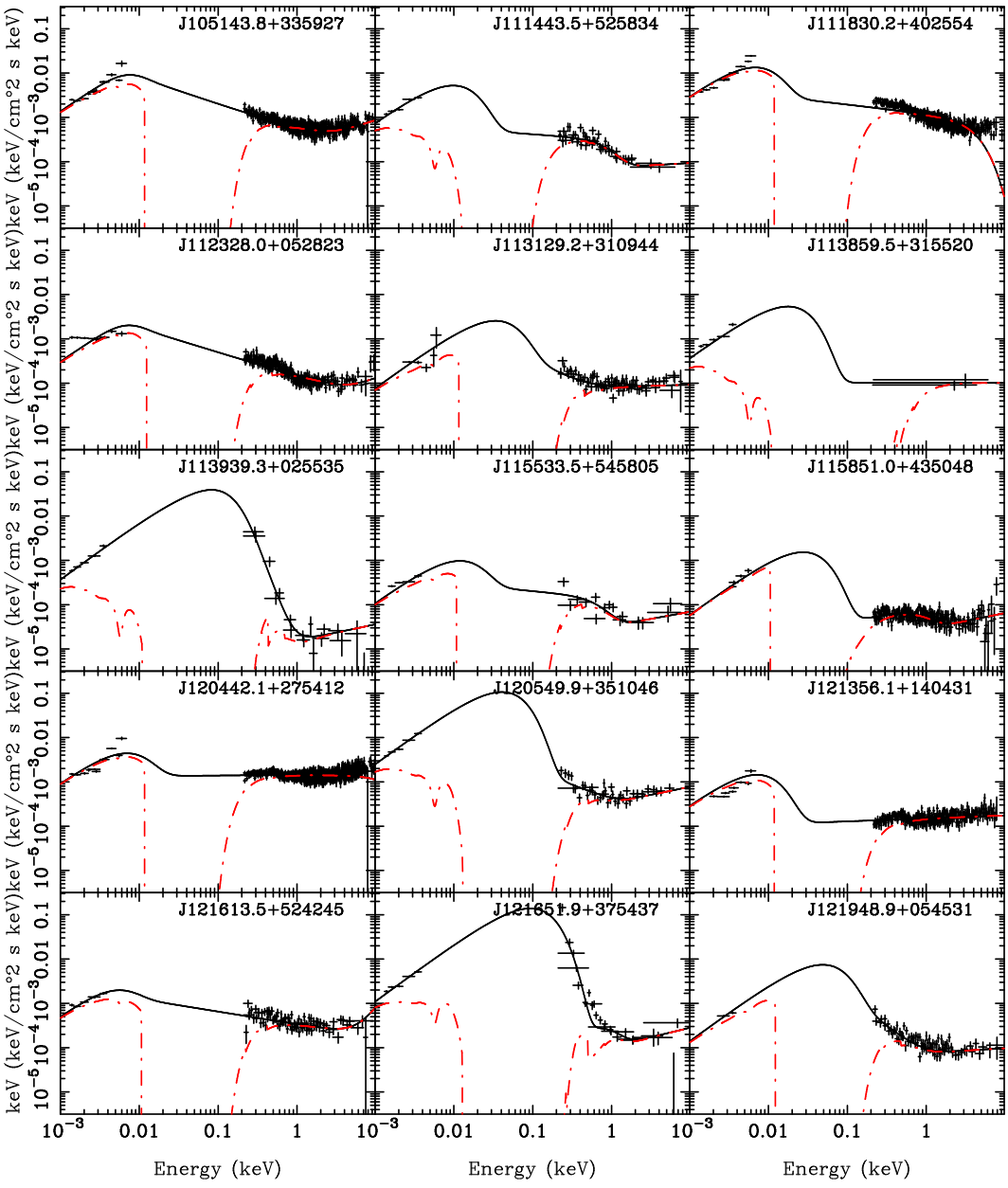
J105143.8+335927
J111443.5+525834
J111830.2+402554
J112328.0+052823
J113129.2+310944
J113859.5+315520
J113939.3+025535
J115533.5+545805
J115851.0+435048
J120442.1+275412
J120549.9+351046
J121356.1+140431
J121613.5+524245
J121651.9+375437
J121948.9+054531
keV (keV/cm^2 s keV)keV (keV/cm^2 s keV)keV (keV/cm^2 s keV)keV (keV/cm^2 s keV)keV (keV/cm^2 s keV)
10^-5 10^-4 10^-3 0.01 0.1 1
10^-3 0.01 0.1 1
Energy (keV)

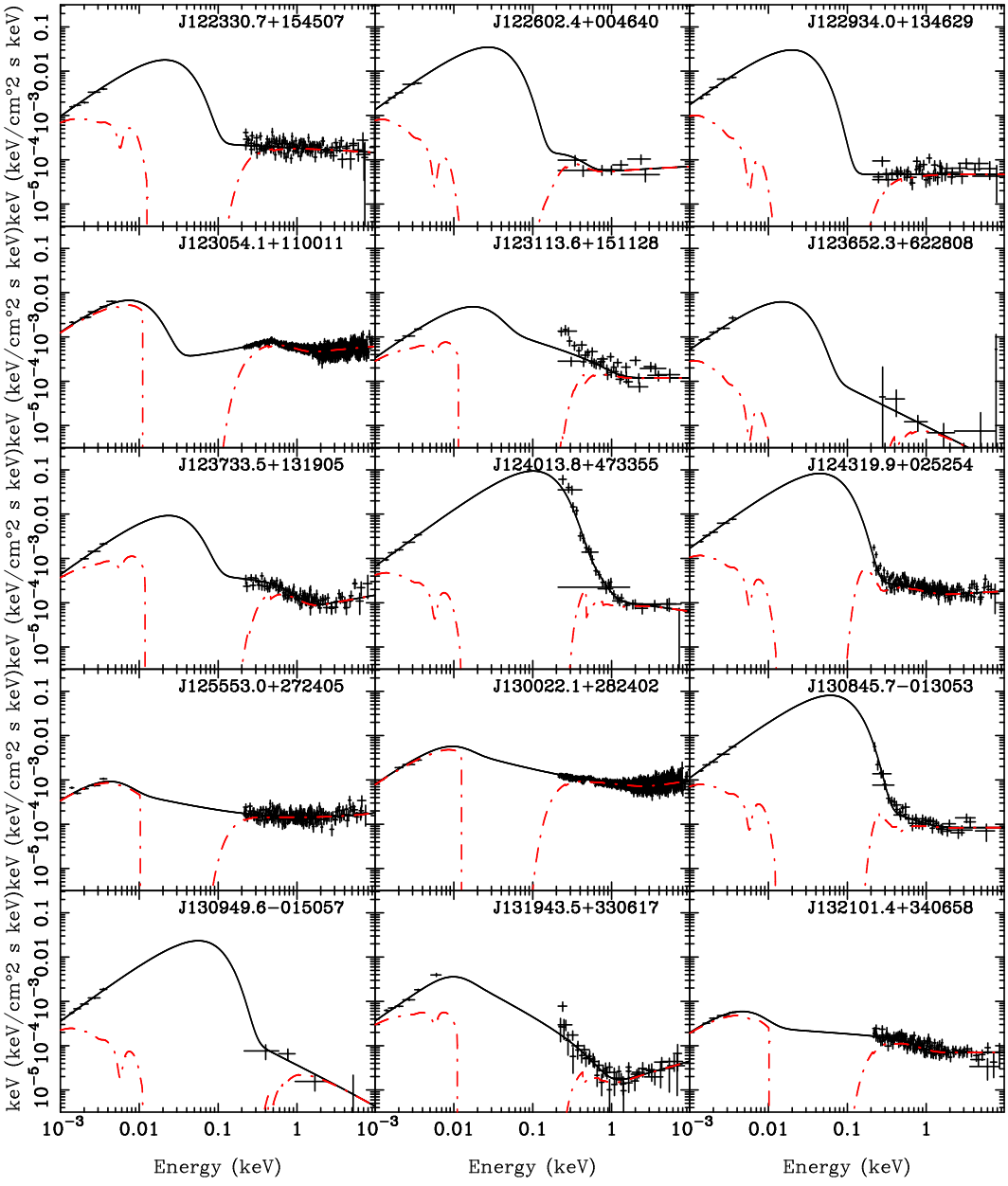
J122330.7+154507
J122602.4+004640
J122934.0+134629
J123054.1+110011
J123113.6+151128
J123652.3+622808
J123733.5+131905
J124013.8+473355
J124319.9+025254
J125553.0+272405
J130022.1+282402
J130845.7−013053
J130949.6−015057
J131943.5+330617
J132101.4+340658
keV (keV/cm^2 s keV)keV (keV/cm^2 s keV)keV (keV/cm^2 s keV)keV (keV/cm^2 s keV)
10^−5 10^−4 10^−3 0.01 0.1
10^−3 0.01 0.1 1
Energy (keV)

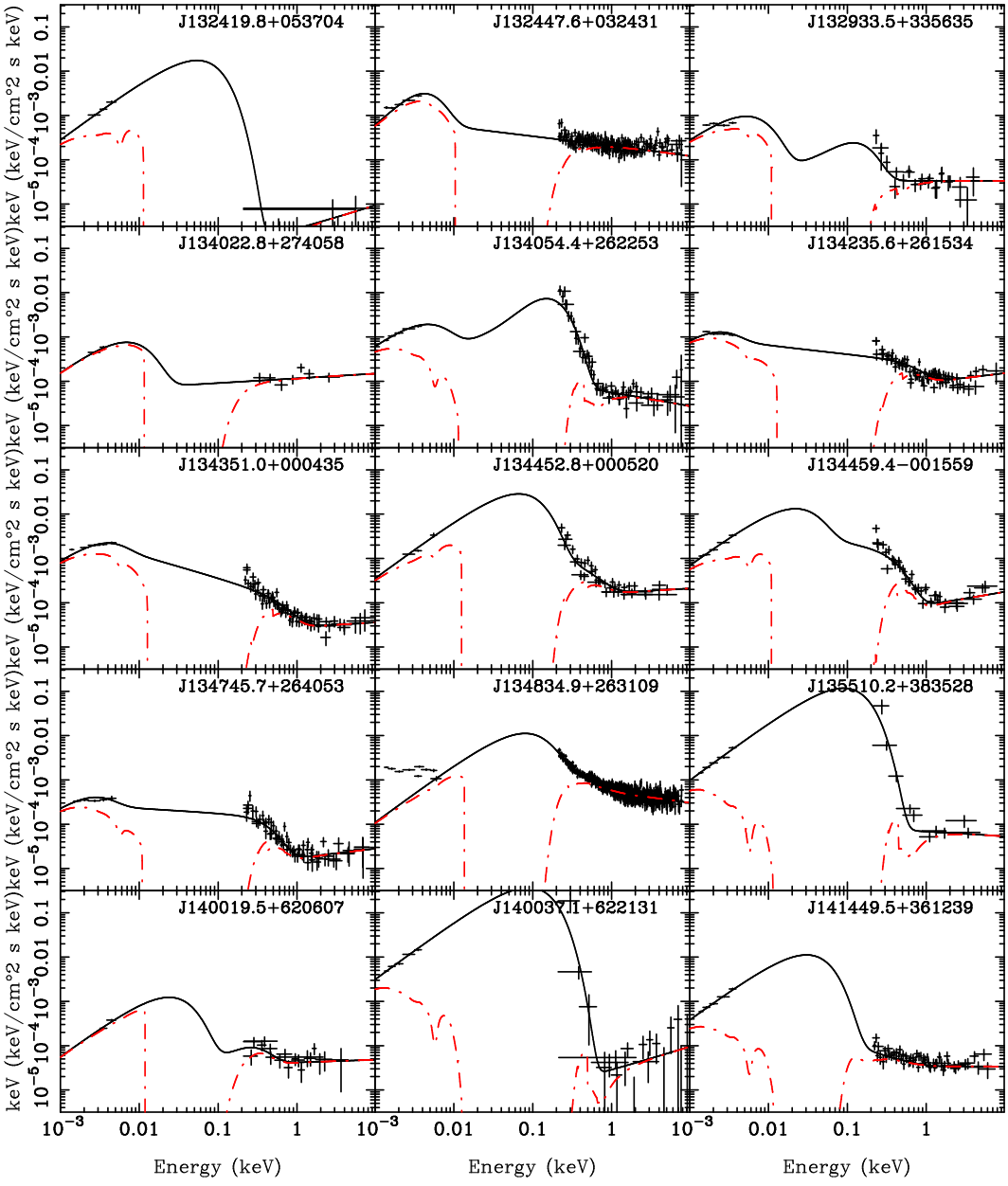
J132419.8+053704
J132447.6+032431
J132933.5+335635
J134022.8+274058
J134054.4+262253
J134235.6+261534
J134351.0+000435
J134452.8+000520
J134459.4−001559
J134745.7+264053
J134834.9+263109
J135510.2+383528
J140019.5+620607
J140037.1+622131
J141449.5+361239
keV (keV/cm^2 s keV)keV (keV/cm^2 s keV)keV (keV/cm^2 s keV)keV (keV/cm^2 s keV)
10^−5 10^−4 10^−3 0.01 0.1 1
10^−3 0.01 0.1 1
Energy (keV)

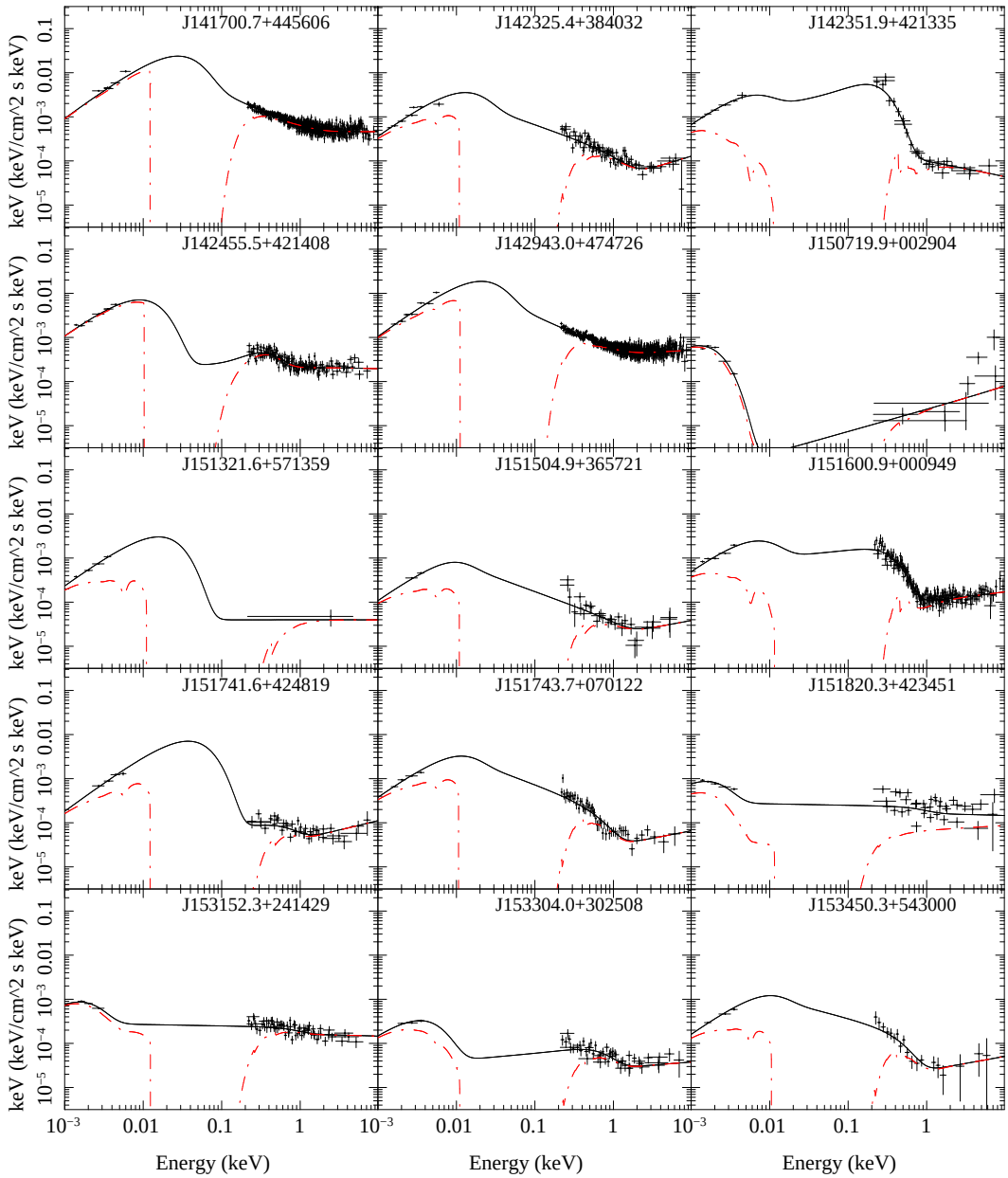
J141700.7+445606
J142325.4+384032
J142351.9+421335
J142455.5+421408
J142943.0+474726
J150719.9+002904
J151321.6+571359
J151504.9+365721
J151600.9+000949
J151741.6+424819
J151743.7+070122
J151820.3+423451
J153152.3+241429
J153304.0+302508
J153450.3+543000
keV (keV/cm^2 s keV)
Energy (keV)

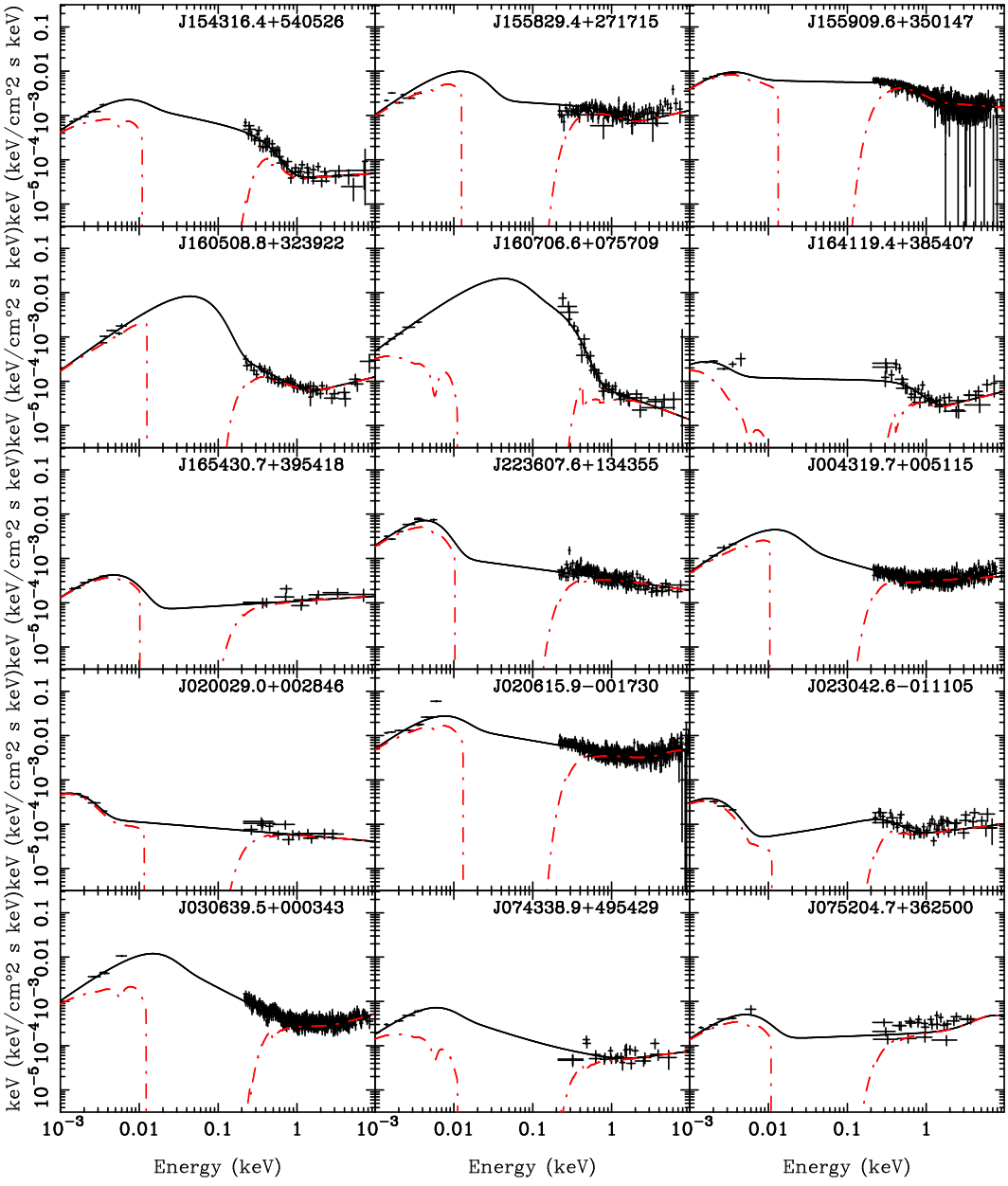
J154316.4+540526
J155829.4+271715
J155909.6+350147
J160508.8+323922
J160706.6+075709
J164119.4+385407
J165430.7+395418
J223607.6+134355
J004319.7+005115
J020029.0+002846
J020615.9−001730
J023042.6−011105
J030639.5+000343
J074338.9+495429
J075204.7+362500
keV (keV/cm^2 s keV)keV (keV/cm^2 s keV)keV (keV/cm^2 s keV)keV (keV/cm^2 s keV)keV (keV/cm^2 s keV)
10^-5 10^-4 10^-3 0.01 0.1 1
10^-3 0.01 0.1 1
Energy (keV)

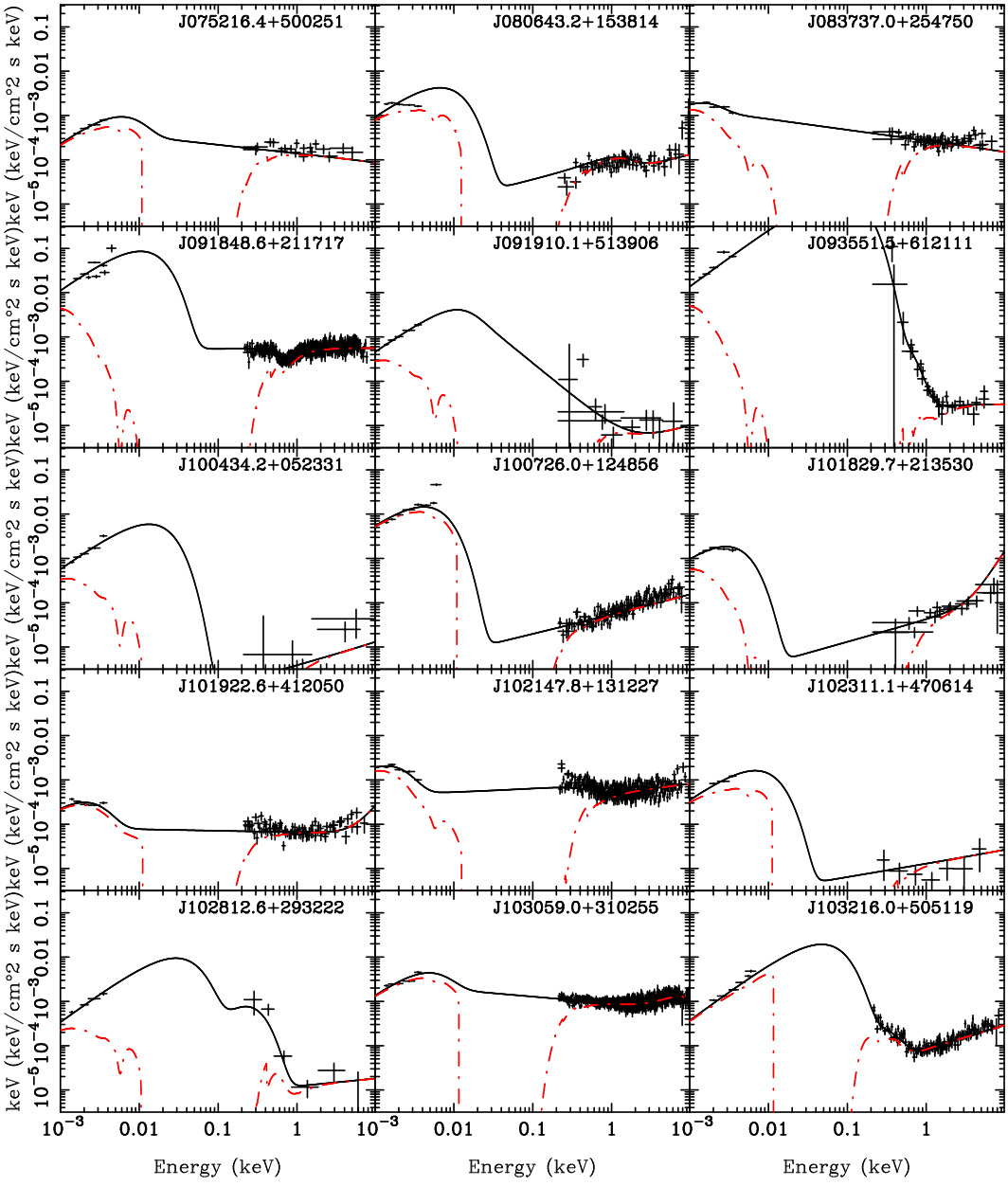
J075216.4+500251
J080643.2+153814
J083737.0+254750
J091848.6+211717
J091910.1+513906
J093551.5+612111
J100434.2+052331
J100726.0+124856
J101829.7+213530
J101922.6+412050
J102147.8+131227
J102311.1+470614
J102812.6+293222
J103059.0+310255
J103216.0+505119
keV (keV/cm^2 s keV)keV (keV/cm^2 s keV)keV (keV/cm^2 s keV)
10^-5 10^-4 10^-3 0.01 0.1 1
10^-3 0.01 0.1 1
Energy (keV)

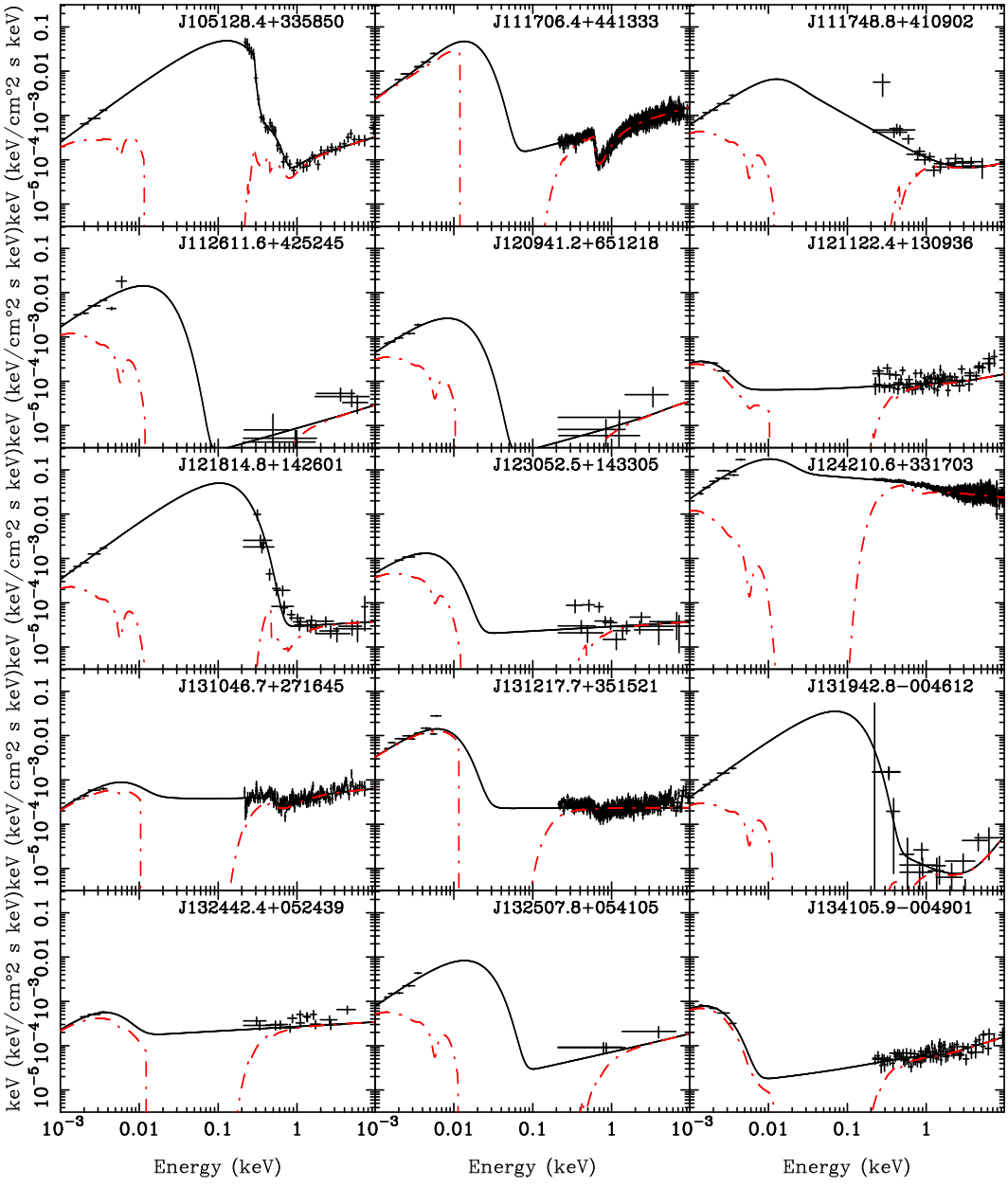
J105128.4+335850
J111706.4+441333
J111748.8+410902
J112611.6+425245
J120941.2+651218
J121122.4+130936
J121814.8+142601
J123052.5+143305
J124210.6+331703
J131046.7+271645
J131217.7+351521
J131942.8−004612
J132442.4+052439
J132507.8+054105
J134105.9−004901
keV (keV/cm^2 s keV)keV (keV/cm^2 s keV)keV (keV/cm^2 s keV)keV (keV/cm^2 s keV)
10^−5 10^−4 10^−3 0.01 0.1 1
10^−3 0.01 0.1 1
Energy (keV)

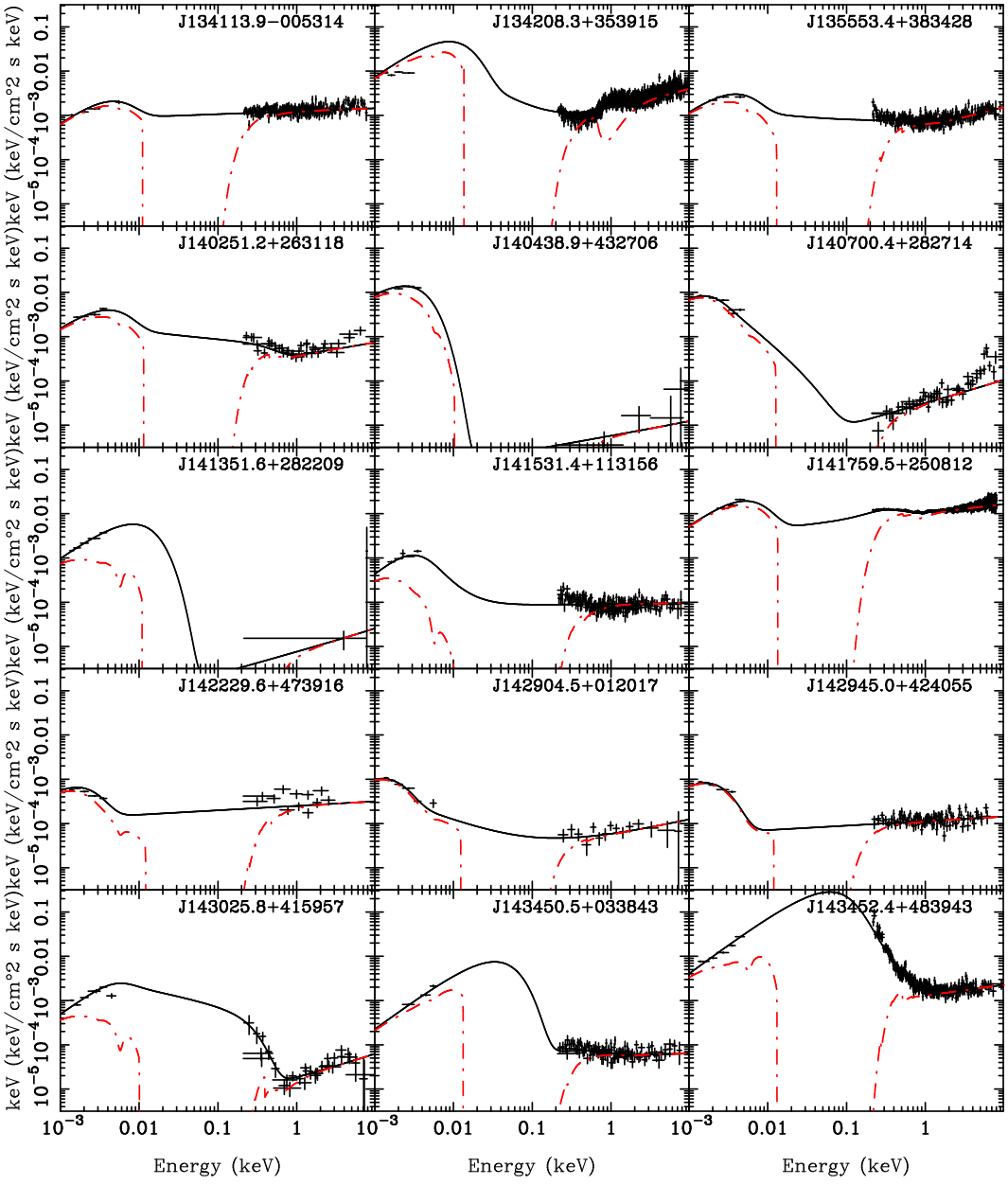
J134113.9−005314
J134208.3+353915
J135553.4+383428
J140251.2+263118
J140438.9+432706
J140700.4+282714
J141351.6+282209
J141531.4+113156
J141759.5+250812
J142229.6+473916
J142904.5+012017
J142945.0+424055
J143025.8+415957
J143450.5+033843
J143452.4+483943
keV (keV/cm^2 s keV)
Energy (keV)

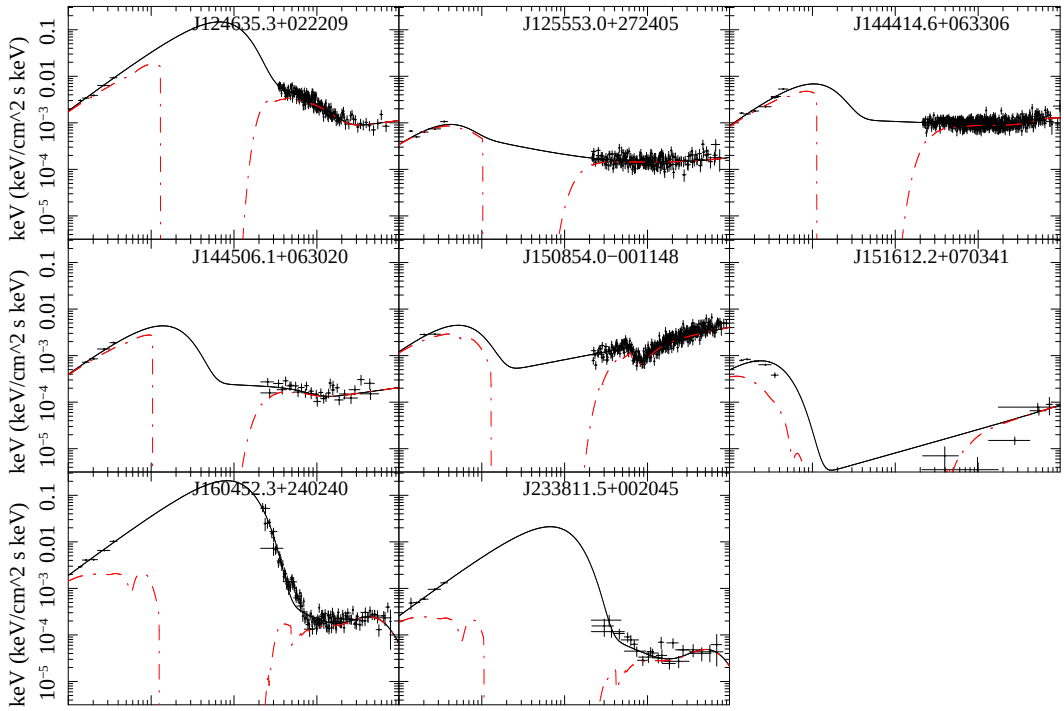
J124635.3+022209
J125553.0+272405
J144414.6+063306
J144506.1+063020
J150854.0−001148
J151612.2+070341
J160452.3+240240
J233811.5+002045
keV (keV/cm^2 s keV)
0.1
0.01
10^{-3}
10^{-4}
10^{-5}

Appendix C

Chapter 6: Light curves and spectra

In the appendix we present the Pan-STARRS MDS light curves and Hectospec spectra for the 39 objects in our sample.

For each object the left panel shows the light curve of the object from the first two years of the MDS observations. The blue points represent g band data, the green points represent r band data and the red points represent i band data. All objects have light curves in the r band, with 26 of the sources having data in all three bands. The object's name is shown in the top left corner of the light curve plot with the spectroscopic redshift for the object shown below. The corresponding SDSS *g, r* or *i* fibre magnitudes are shown in blue, green and red respectively to the left of the image. As all of the SDSS observations took place years before the first MDS observation all of the points lie off the light curves and are represented with an arrow. The SDSS points are shown with upwards or downwards pointing arrows if the SDSS is significantly different from the light curve and lies outside of the range of the plot.

The right-hand figure shows the Hectospec spectrum for each object, with the shaded regions indicated the wavelength range of the bands with light curve data for the object.

The first 12 rows of figures show the BAL subsample, followed by the 10 QSOs in the possible BAL subsample. The 17 QSOs in the control subsample are shown last.

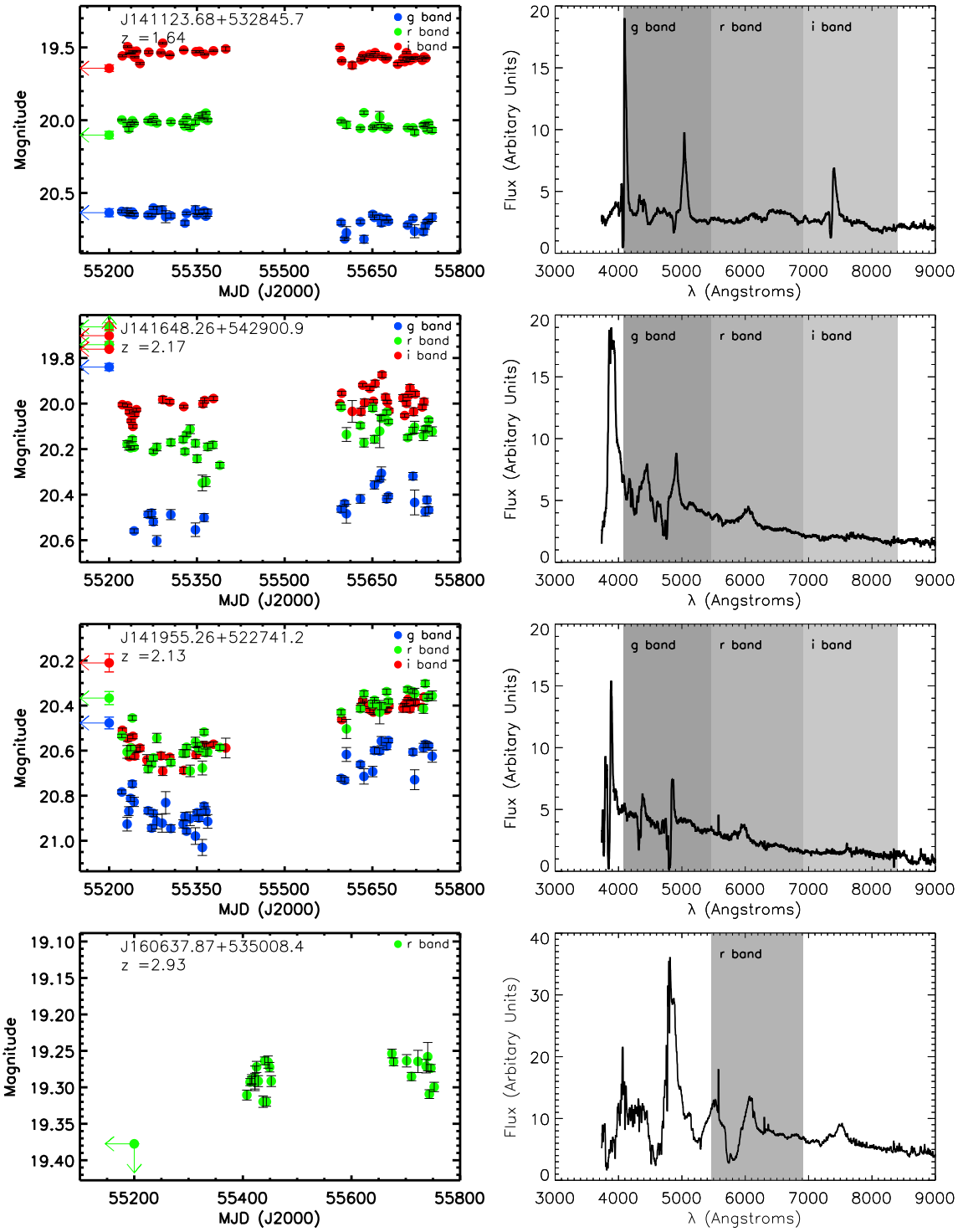

Figure C.1: BAL subsample

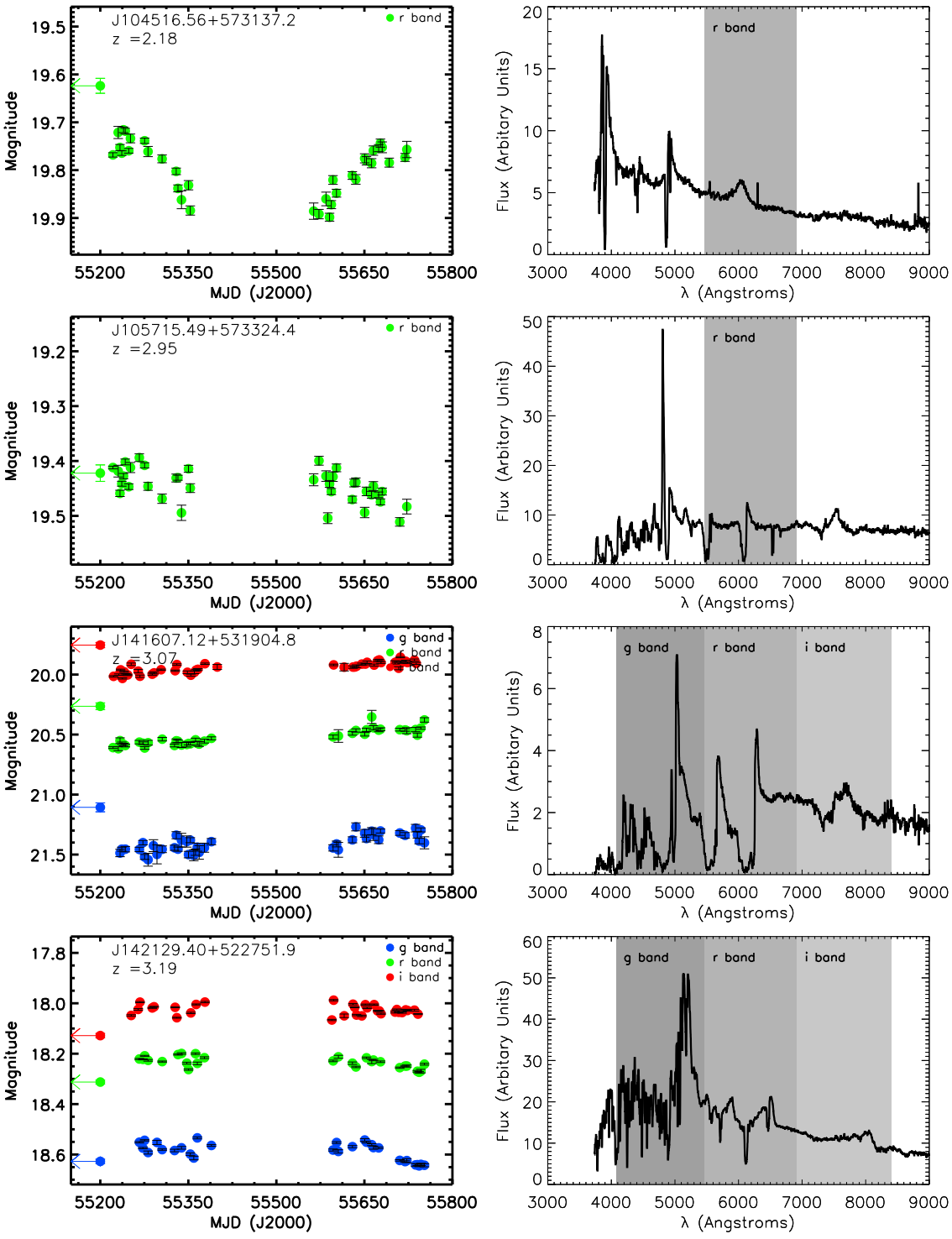
J104516.56+573137.2
z =2.18
r band
Magnitude
MJD (J2000)
Flux (Arbitary Units)
λ (Angstroms)
J105715.49+573324.4
z =2.95
J141607.12+531904.8
z =3.07
g band
i band
J142129.40+522751.9
z =3.19

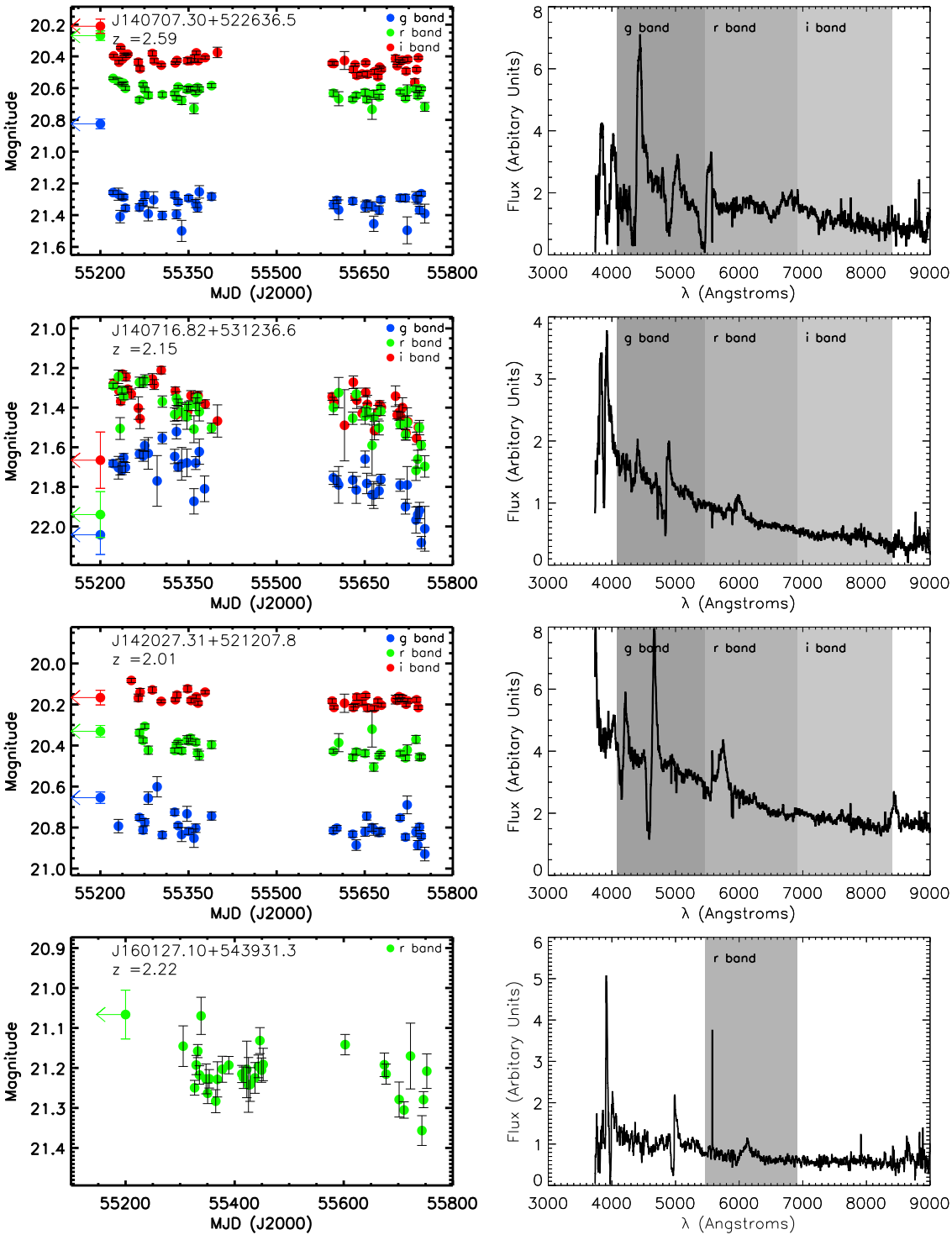
J140707.30+522636.5
z =2.59
g band
r band
i band
Magnitude
MJD (J2000)
Flux (Arbitary Units)
λ (Angstroms)
J140716.82+531236.6
z =2.15
J142027.31+521207.8
z =2.01
J160127.10+543931.3
z =2.22

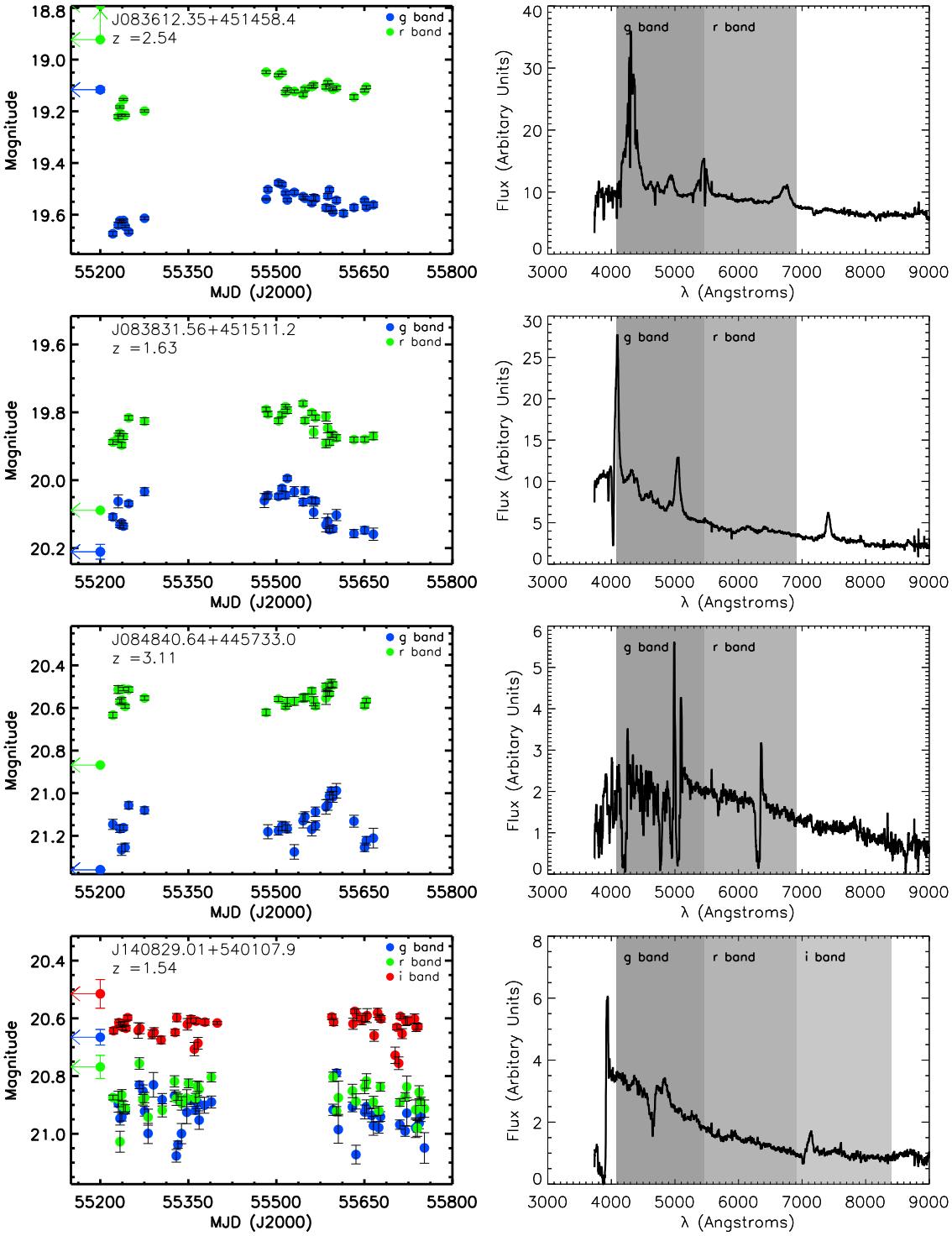

Figure C.2: Possible BAL subsample

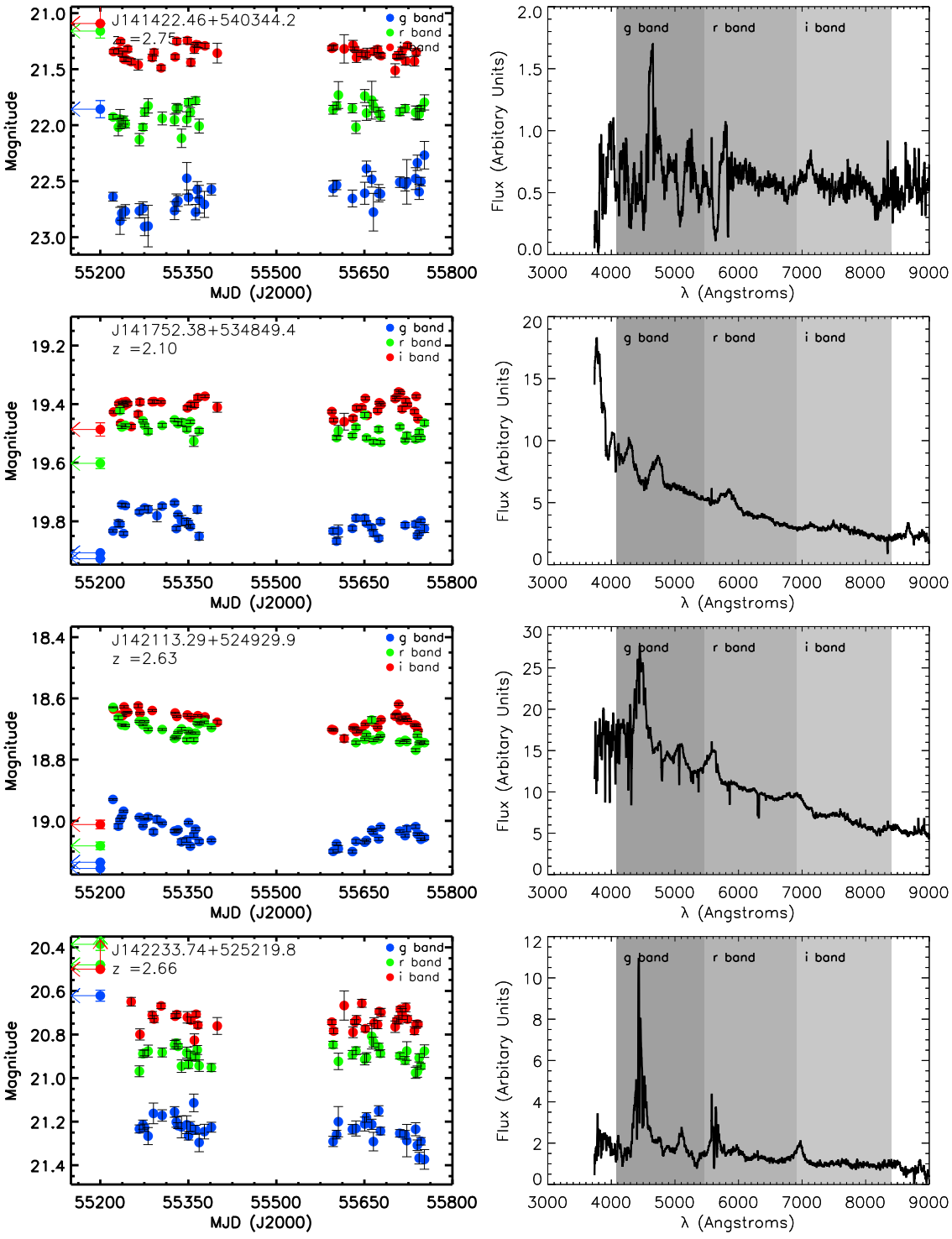
J141422.46+540344.2
z =2.75
J141752.38+534849.4
z =2.10
J142113.29+524929.9
z =2.63
J142233.74+525219.8
z =2.66
g band
r band
i band
Magnitude
MJD (J2000)
Flux (Arbitary Units)
λ (Angstroms)

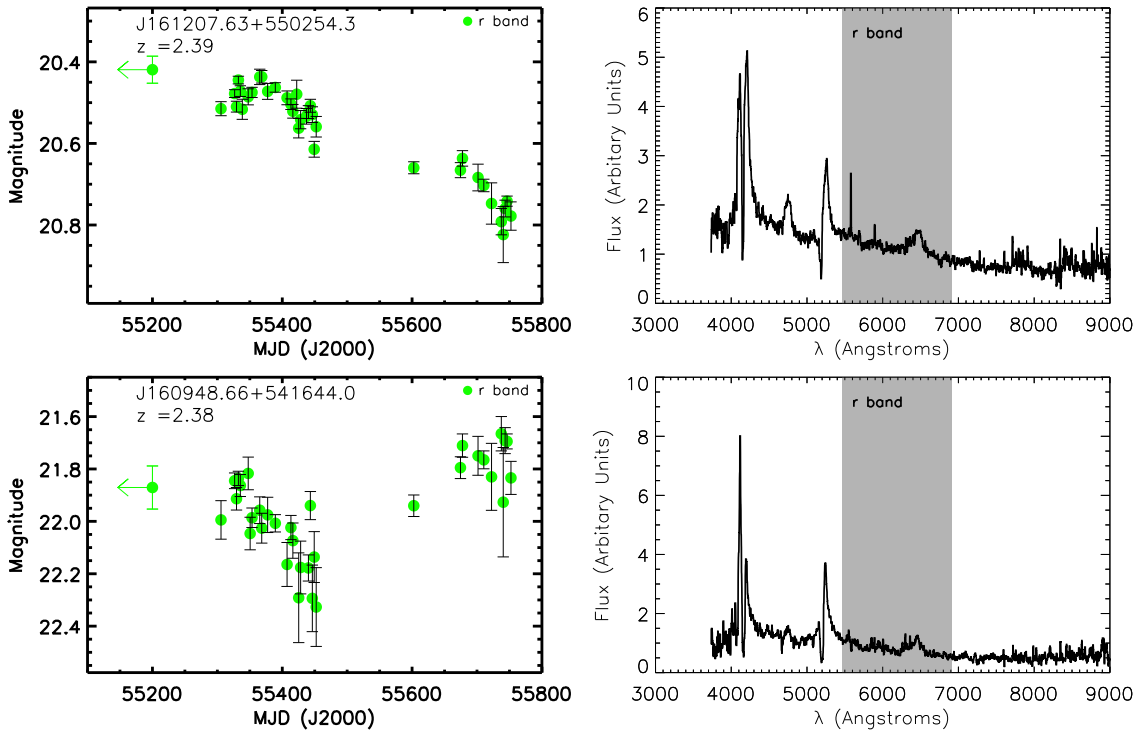
J161207.63+550254.3
z =2.39
r band
Magnitude
MJD (J2000)
Flux (Arbitary Units)
λ (Angstroms)
J160948.66+541644.0
z =2.38
r band
Magnitude
MJD (J2000)
Flux (Arbitary Units)
λ (Angstroms)

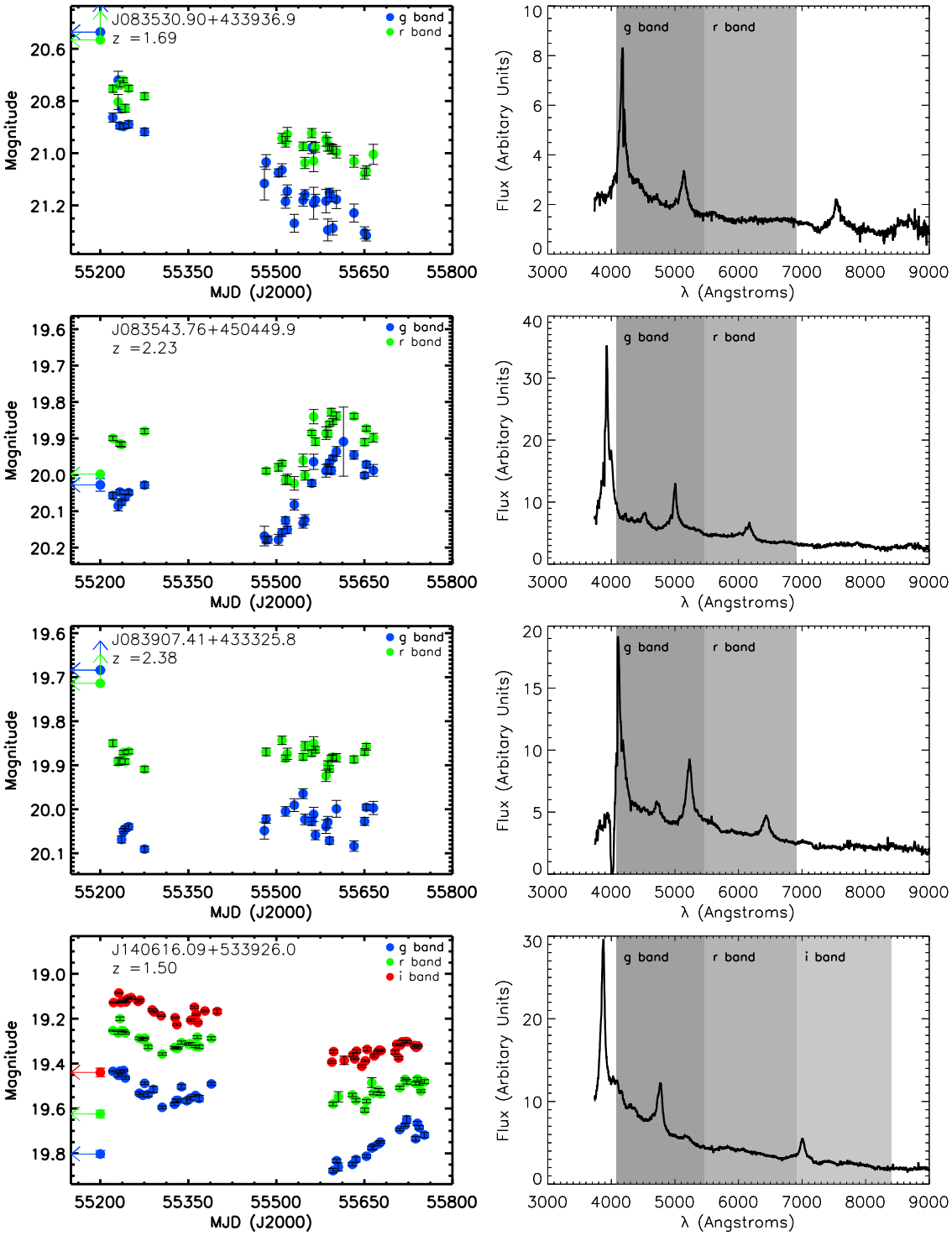

Figure C.3: Control subsample

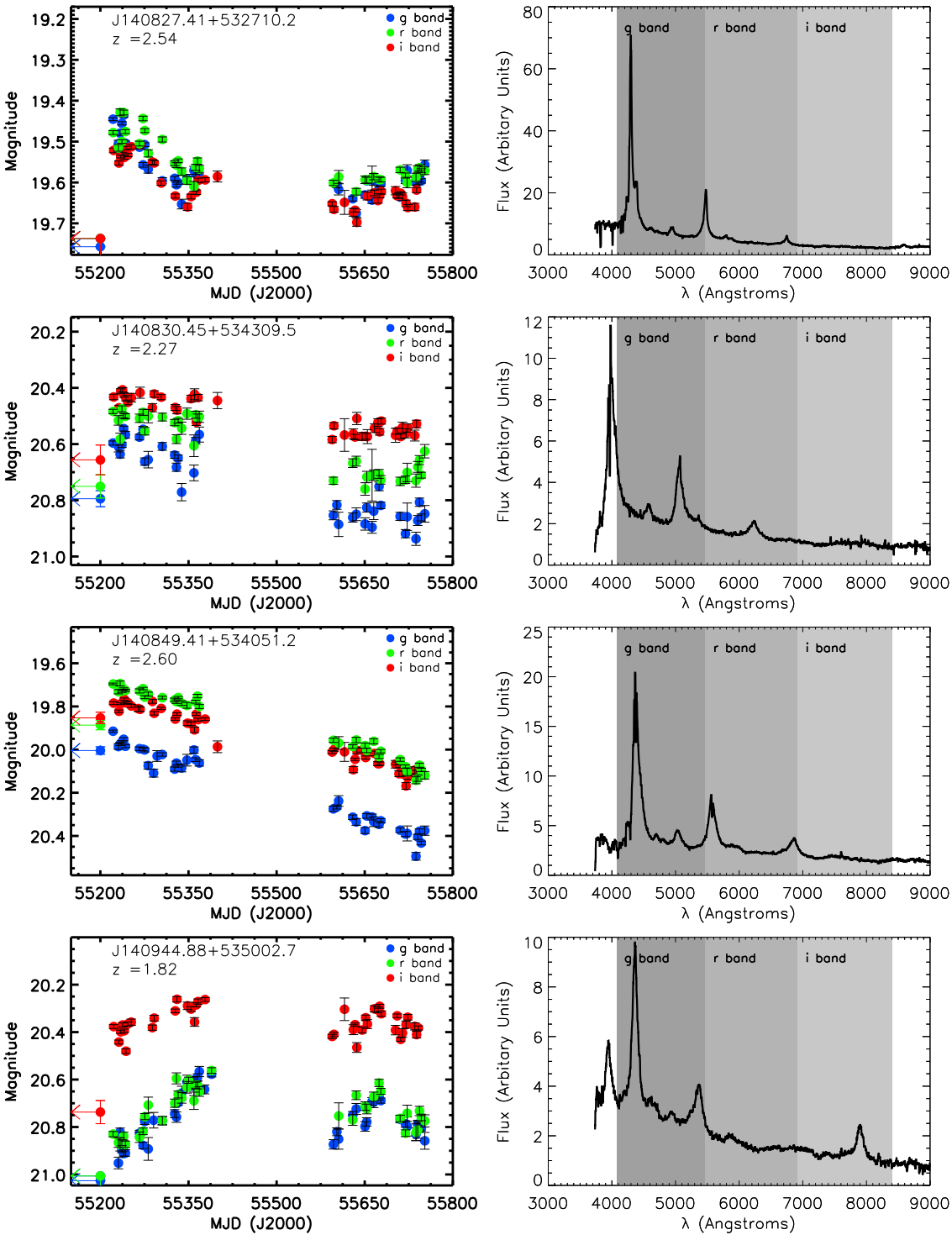
J140827.41+532710.2
z =2.54
g band
r band
i band
Magnitude
MJD (J2000)
Flux (Arbitary Units)
λ (Angstroms)
J140830.45+534309.5
z =2.27
J140849.41+534051.2
z =2.60
J140944.88+535002.7
z =1.82

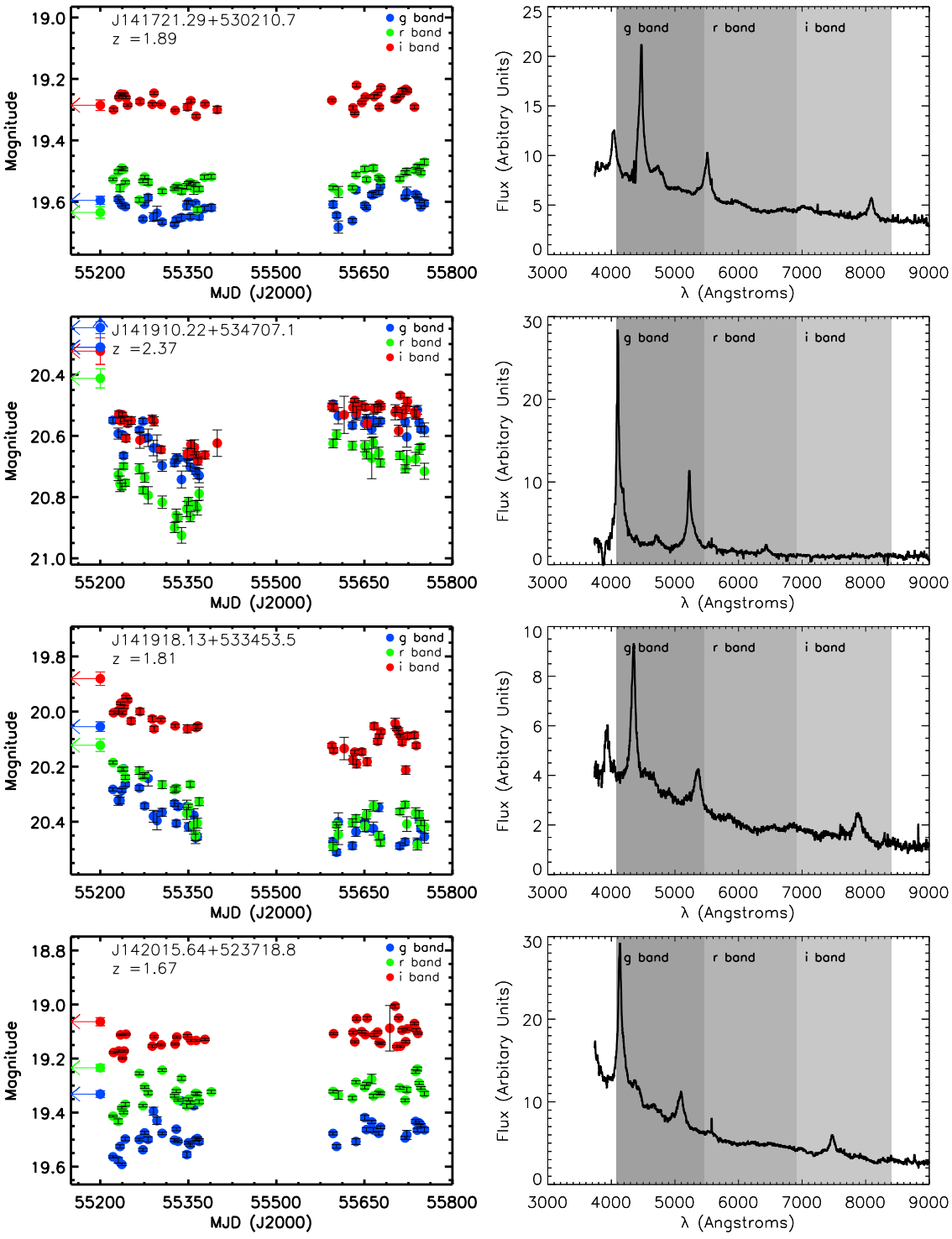
J141721.29+530210.7
z =1.89
g band
r band
i band
Magnitude
MJD (J2000)
Flux (Arbitary Units)
λ (Angstroms)
J141910.22+534707.1
z =2.37
J141918.13+533453.5
z =1.81
J142015.64+523718.8
z =1.67

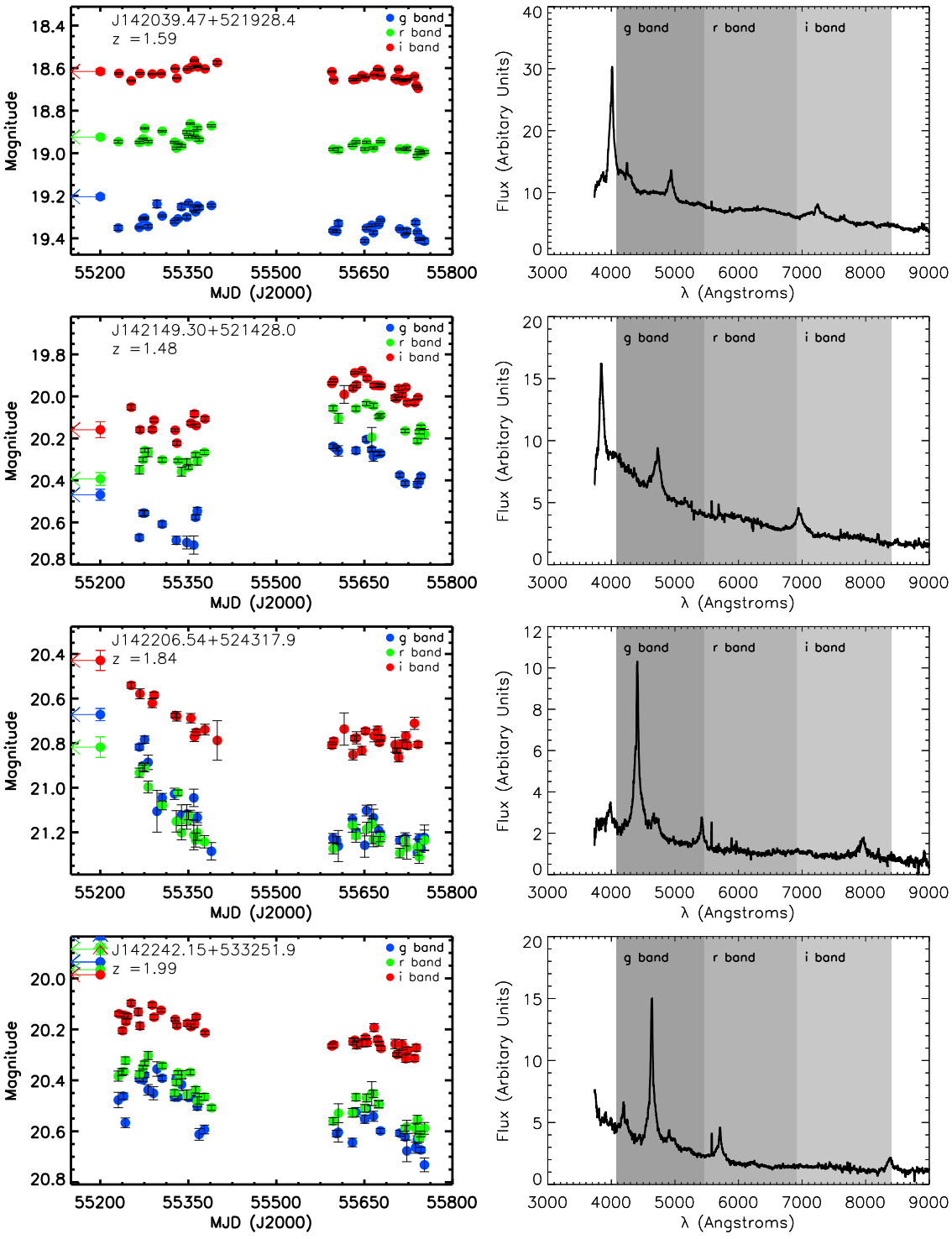
J142039.47+521928.4
z =1.59
g band
r band
i band
Magnitude
MJD (J2000)
Flux (Arbitary Units)
λ (Angstroms)
J142149.30+521428.0
z =1.48
J142206.54+524317.9
z =1.84
J142242.15+533251.9
z =1.99

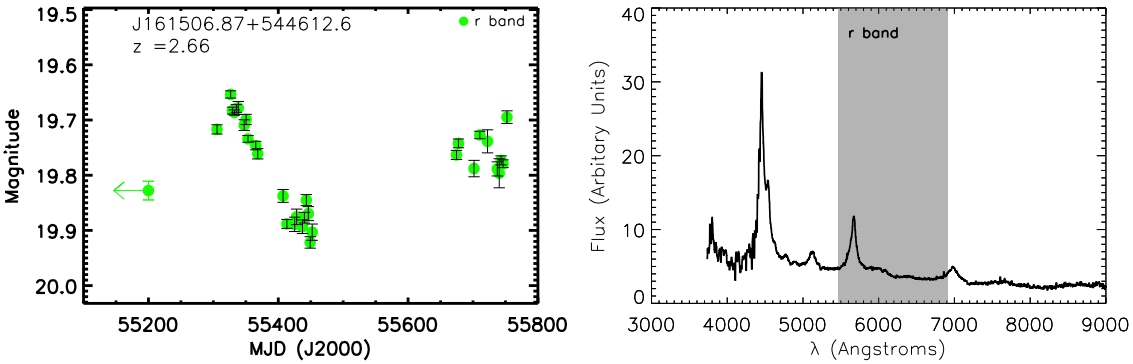
J161506.87+544612.6
z =2.66
r band
Magnitude
MJD (J2000)
19.5
19.6
19.7
19.8
19.9
20.0
55200
55400
55600
55800
r band
Flux (Arbitary Units)
λ (Angstroms)
40
30
20
10
0
3000
4000
5000
6000
7000
8000
9000

Bibliography

Abazajian K. N., et al., 2009, ApJS, 182, 543

Akerlof C., Amrose S., Balsano R., Bloch J., Casperson D., Fletcher S., Gisler G., Hills J., Kehoe R., Lee B., Marshall S., McKay T., Pawl A., Schaefer J., Szymanski J., Wren J., 2000, AJ, 119, 1901

Allen J. T., Hewett P. C., Maddox N., Richards G. T., Belokurov V., 2011, MNRAS, 410, 860

Antonucci R., 1993, ARAA, 31, 473

Antonucci R. R. J., Miller J. S., 1985, ApJ, 297, 621

Arnaud K. A., 1996, in G. H. Jacoby & J. Barnes ed., Astronomical Data Analysis Software and Systems V Vol. 101 of Astronomical Society of the Pacific Conference Series, XSPEC: The First Ten Years. pp 17+

Arons J., 1992, ApJ, 388, 561

Atwood W. B., Abdo A. A., Ackermann M., Althouse W., Anderson B., Axelsson M., Baldini L., Ballet J., Band D. L., Barbiellini G., et al., 2009, ApJ, 697, 1071

Bacon R., Copin Y., Monnet G., Miller B. W., Allington-Smith J. R., Bureau M., Carollo C. M., Davies R. L., Emsellem E., Kuntschner H., Peletier R. F., Verolme E. K., de Zeeuw P. T., 2001, MNRAS, 326, 23

Baldwin J. A., Phillips M. M., Terlevich R., 1981, PASP, 93, 5

Barth A. J., Greene J. E., Ho L. C., 2008, AJ, 136, 1179

Barthelmy S. D., et al., 2005, Space Sci. Rev., 120, 143

Begelman M., 2003, in Collin S., Combes F., Shlosman I., eds, Active Galactic Nuclei: From Central Engine to Host Galaxy Vol. 290 of Astronomical Society of the Pacific Conference Series, Everything you always wanted to know about AGN ... but were afraid to ask. pp 23–27

Begelman M. C., 2002, ApJL, 568, L97

Begelman M. C., King A. R., Pringle J. E., 2006, MNRAS, 370, 399

Begelman M. C., Rees M. J., 1978, MNRAS, 185, 847

Bennert N., Jungwiert B., Komossa S., Haas M., Chini R., 2006, New Astron. Rev., 50, 708

Bessell M. S., 1991, A&A, 242, L17

Bian W., Zhao Y., 2004a, MNRAS, 347, 607

Bian W., Zhao Y., 2004b, MNRAS, 352, 823

Blandford R. D., McKee C. F., 1982, ApJ, 255, 419

Bless R. C., Savage B. D., 1972, ApJ, 171, 293

Bohlin R. C., Savage B. D., Drake J. F., 1978, ApJ, 224, 132

Boller T., Brandt W. N., Fabian A. C., Fink H. H., 1997, MNRAS, 289, 393

Boller T., Brandt W. N., Fink H., 1996, A&A, 305, 53

Boroson T. A., 2002, ApJ, 565, 78

Boroson T. A., Green R. F., 1992, ApJS, 80, 109

Bovy J., et al., 2011, ApJ, 729, 141

Bowyer S., Byram E. T., Chubb T. A., Friedman H., 1964, Nature, 201, 1307

Bragg W. L., 1913, Proc. Camb. Phil. Soc, 17

Braito V., et al., 2004, A&A, 420, 79

Brandt W. N., Gallagher S. C., 2000, New Astron. Rev., 44, 461

Calzetti D., Armus L., Bohlin R. C., Kinney A. L., Koornneef J., Storchi-Bergmann T., 2000, ApJ, 533, 682

Cano-Díaz M., Maiolino R., Marconi A., Netzer H., Shemmer O., Cresci G., 2012, A&A, 537, L8

Capellupo D. M., Hamann F., Shields J. C., Rodríguez Hidalgo P., Barlow T. A., 2011, MNRAS, 413, 908

Cardelli J. A., Clayton G. C., Mathis J. S., 1989, ApJ, 345, 245

Casebeer D. A., Leighly K. M., Baron E., 2006, ApJ, 637, 157

Castelli F., Kurucz R. L., 2004, ArXiv Astrophysics e-prints

Chaty S., Dubus G., Raichoor A., 2011, A&A, 529, A3

Collin S., Kawaguchi T., 2004, A&A, 426, 797

Collin S., Kawaguchi T., Peterson B. M., Vestergaard M., 2006, A&A, 456, 75

Crenshaw D. M., Kraemer S. B., Bruhweiler F. C., Ruiz J. R., 2001, ApJ, 555, 633

Crenshaw D. M., Kraemer S. B., Gabel J. R., 2003, AJ, 126, 1690

Cristiani S., Trentini S., La Franca F., Aretxaga I., Andreani P., Vio R., Gemmo A., 1996, A&A, 306, 395

Croft S., et al., 2010, ApJ, 719, 45

Crummy J., Fabian A. C., Gallo L., Ross R. R., 2006, MNRAS, 365, 1067

Czerny B., 2004, ArXiv Astrophysics e-prints

Czerny B., Nikołajuk M., Różańska A., Dumont A.-M., Loska Z., Zycki P. T., 2003, A&A, 412, 317

Dai X., Shankar F., Sivakoff G. R., 2008, ApJ, 672, 108

Dam H. J. W., 1896, Marie Curie Magazine, 6

Davidsen A., Liebert J., Spinrad H., Middleditch J., Chanan G., Mason K. O., Sanford P. W., Margon B., 1975, ApJL, 200, L19

de Vaucouleurs G., de Vaucouleurs A., 1964, ApJ, 140, 1622

de Vaucouleurs G., de Vaucouleurs A., 1968, AJ, 73, 858

Dent W. A., 1965, Science, 148, 1458

di Clemente A., Giallongo E., Natali G., Trevese D., Vagnetti F., 1996, ApJ, 463, 466

Dickey J. M., Lockman F. J., 1990, ARAA, 28, 215

DiPompeo M. A., Brotherton M. S., Becker R. H., Tran H. D., Gregg M. D., White R. L., Laurent-Muehleisen S. A., 2010, ApJS, 189, 83

Djorgovski S. G., Baltay C., Mahabal A. A., Drake A. J., Williams R., Rabinowitz D., Graham M. J., Donalek C., Glikman E., Bauer A., Scalzo R., Ellman N., 2008, Astronomische Nachrichten, 329, 263

Djorgovski S. G., Brunner R. J., Mahabal A. A., Odewahn S. C., Carvalho R. R. D., Gal R. R., Stolorz P., Granat R., Curkendall D., Jacob J., Castro S., 2001a, in Banday A. J., Zaroubi S., Bartelmann M., eds, Mining the Sky Exploration of Large Digital Sky Surveys. p. 305

Djorgovski S. G., Drake A. J., Mahabal A. A., Graham M. J., Donalek C., Williams R., Beshore E. C., Larson S. M., Prieto J., Catelan M., Christensen E., McNaught R. H., 2011, ArXiv e-prints

Djorgovski S. G., Mahabal A., Brunner R. J., Williams R. E., Granat R., Curkendall D., Jacob J., Stolorz P., 2001b, in Starck J.-L., Murtagh F. D., eds, Society of Photo-Optical Instrumentation Engineers (SPIE) Conference Series Vol. 4477, Exploration of parameter spaces in a virtual observatory. pp 43–52

Done C., 2010, ArXiv e-prints

Done C., Davis S. W., Jin C., Blaes O., Ward M., 2012, MNRAS, 420, 1848

Done C., Nayakshin S., 2007, MNRAS, 377, L59

Done C., Ward M. J., Fabian A. C., Kunieda H., Tsuruta S., Lawrence A., Smith M. G., Wamsteker W., 1990, MNRAS, 243, 713

Drake A. J., Djorgovski S. G., Mahabal A., Beshore E., Larson S., Graham M. J., Williams R., Christensen E., Catelan M., Boattini A., Gibbs A., Hill R., Kowalski R., 2009, ApJ, 696, 870

Drake A. J., Djorgovski S. G., Prieto J. L., Mahabal A., Balam D., Williams R., Graham M. J., Catelan M., Beshore E., Larson S., 2010, ApJL, 718, L127

Drake A. J., et al., 2011, ApJ, 735, 106

Dwek E., 1985, ApJ, 297, 719

Edelson R., Koratkar A., Nandra K., Goad M., Peterson B. M., Collier S., Krolik J., Malkan M., Maoz D., O'Brien P., Shull J. M., Vaughan S., Warwick R., 2000, ApJ, 534, 180

Edelson R., Nandra K., 1999, ApJ, 514, 682

Edelson R., Turner T. J., Pounds K., Vaughan S., Markowitz A., Marshall H., Dobbie P., Warwick R., 2002, ApJ, 568, 610

Edelson R. A., et al., 1996, ApJ, 470, 364

Elvis M., Wilkes B. J., McDowell J. C., Green R. F., Bechtold J., Willner S. P., Oey M. S., Polomski E., Cutri R., 1994, ApJS, 95, 1

Fan X., 2006, New Astron. Rev., 50, 665

Fan X., et al., 2001, AJ, 121, 54

Fath E. A., 1908, PASP, 20, 280

Ferrarese L., Merritt D., 2000, ApJL, 539, L9

Filiz Ak N., et al., 2012, ArXiv e-prints

Fine S., Shanks T., Croom S. M., Green P., Kelly B. C., Berge E., Chornock R., Burgett W. S., Magnier E. A., Price P. A., 2012, ArXiv e-prints

Francis P. J., Hewett P. C., Foltz C. B., Chaffee F. H., Weymann R. J., Morris S. L., 1991, ApJ, 373, 465

Friedman H., 1959, Information about the Gas Density in Space Derived from Radiation Measurements

Friedman H., 1960, The sun's ionising radiations: Physics of the upper atmosphere. Academic Press, New York, p. 202

Gallagher S. C., Brandt W. N., Chartas G., Priddey R., Garmire G. P., Sambruna R. M., 2006, ApJ, 644, 709

Gallo L. C., Boller T., Brandt W. N., Fabian A. C., Vaughan S., 2004, A&A, 417, 29

Gammie C. F., 1998, MNRAS, 297, 929

Gaskell C. M., Goosmann R. W., Antonucci R. R. J., Whysong D. H., 2004, ApJ, 616, 147

Gaskell C. M. & Klimek E. S., 2003, Astronomical and Astrophysical Transactions, 22, 661

Gebhardt K., Bender R., Bower G., Dressler A., Faber S. M., Filippenko A. V., Green R., Grillmair C., Ho L. C., Kormendy J., Lauer T. R., Magorrian J., Pinkney J., Richstone D., Tremaine S., 2000, ApJL, 539, L13

Gebhardt K., Thomas J., 2009, ApJ, 700, 1690

Genzel R., Thatte N., Krabbe A., Kroker H., Tacconi-Garman L. E., 1996, ApJ, 472, 153

Gezari S., et al., 2012, Nature, 485, 217

Gezari S., Heckman T., Cenko S. B., Eracleous M., Forster K., Gonçalves T. S., Martin D. C., Morrissey P., Neff S. G., Seibert M., Schiminovich D., Wyder T. K., 2009, ApJ, 698, 1367

Ghez A. M., Salim S., Weinberg N., Lu J., Do T., Dunn J. K., Matthews K., Morris M., Yelda S., Becklin E. E., 2008, in IAU Symposium Vol. 248 of IAU Symposium, Probing the properties of the Milky Way's central supermassive black hole with stellar orbits. pp 52–58

Giallongo E., Trevese D., Vagnetti F., 1991, ApJ, 377, 345

Gierliński M., Done C., 2004, MNRAS, 349, L7

Gierliński M., Done C., 2006, MNRAS, 371, L16

Gierliński M., Middleton M., Ward M., Done C., 2008, Nature, 455, 369

Gierliński M., Zdziarski A. A., Poutanen J., Coppi P. S., Ebisawa K., Johnson W. N., 1999, MNRAS, 309, 496

Gillessen S., Eisenhauer F., Trippe S., Alexander T., Genzel R., Martins F., Ott T., 2009, ApJ, 692, 1075

Giustini M., Cappi M., Vignali C., 2008, A&A, 491, 425

Giveon U., Maoz D., Kaspi S., Netzer H., Smith P. S., 1999, MNRAS, 306, 637

González-Martín O., Papadakis I., Reig P., Zezas A., 2011, A&A, 526, A132

Goodrich R. W., 1989, ApJ, 342, 224

Goodrich R. W., Miller J. S., 1995, ApJL, 448, L73

Gray R. O., Graham P. W., Hoyt S. R., 2001, AJ, 121, 2159

Green P. J., Aldcroft T. L., Mathur S., Wilkes B. J., Elvis M., 2001, ApJ, 558, 109

Green P. J., et al., 2009, ApJ, 690, 644

Greenstein J. L., Schmidt M., 1964, ApJ, 140, 1

Grupe D., Beuerman K., Mannheim K., Thomas H.-C., Fink H. H., de Martino D., 1995, A&A, 300, L21

Grupe D., Beuermann K., Mannheim K., Thomas H.-C., 1999, A&A, 350, 805

Grupe D., Komossa S., Gallo L. C., 2007b, ApJL, 668, L111

Grupe D., Mathur S., 2004, ApJL, 606, L41

Grupe D., Schady P., Leighly K. M., Komossa S., O'Brien P. T., Nousek J. A., 2007a, AJ, 133, 1988

Gültekin K., et al., 2009, ApJ, 698, 198

Haardt F., Maraschi L., 1991, ApJL, 380, L51

Hall P. B., Gallagher S. C., Richards G. T., Alexander D. M., Anderson S. F., Bauer F., Brandt W. N., Schneider D. P., 2006, AJ, 132, 1977

Häring N., Rix H.-W., 2004, ApJL, 604, L89

Harms R. J., Ford H. C., Tsvetanov Z. I., Hartig G. F., Dressel L. L., Kriss G. A., Bohlin R., Davidsen A. F., Margon B., Kochhar A. K., 1994, ApJL, 435, L35

Harrington R. G., 1952, PASP, 64, 275

Hayashida K., 2000, Astronomical Herald, 93, 656

Hazard C., Morton D. C., Terlevich R., McMahon R., 1984, ApJ, 282, 33

Heckman T. M., 1980, A&A, 87, 142

Hewett P. C., Foltz C. B., 2003, AJ, 125, 1784

Hines D. C., Wills B. J., 1995, ApJL, 448, L69

Ho L. C., Filippenko A. V., Sargent W. L. W., 1997, ApJ, 487, 568

Hodapp K. W., Siegmund W. A., Kaiser N., Chambers K. C., Laux U., Morgan J., Mannery E., 2004, in Oschmann Jr. J. M., ed., Society of Photo-Optical Instrumentation Engineers (SPIE) Conference Series Vol. 5489, Optical design of the Pan-STARRS telescopes. pp 667–678

Holt S. S., 1993, A&AS, 97, 367

Hopkins P. F., Elvis M., 2010, MNRAS, 401, 7

Hopkins P. F., Richards G. T., Hernquist L., 2007, ApJ, 654, 731

Hu C., Wang J.-M., Ho L. C., Chen Y.-M., m W.-H., Xue S.-J., 2008, ApJL, 683, L115

Hubble E. P., 1922, ApJ, 56, 162

Hynes R. I., Steeghs D., Casares J., Charles P. A., O'Brien K., 2003, ApJL, 583, L95

Imanishi M., Wada K., 2004, ApJ, 617, 214

Ivezic Z., et al., 2008, Serbian Astronomical Journal, 176, 1

Izotov Y. I., Thuan T. X., Guseva N. G., 2007, ApJ, 671, 1297

Jahoda K., Swank J. H., Giles A. B., Stark M. J., Strohmayer T., Zhang W., Morgan E. H., 1996, in Siegmund O. H., Gummin M. A., eds, SPIE Conference Series Vol. 2808. pp 59–70

Jiang Y.-F., Goodman J., 2011, ApJ, 730, 45

Jin C., Done C., Ward M., Gierliński M., Mullaney J., 2009, MNRAS, 398, L16

Jin C., Ward M., Done C., Gelbord J., 2012, MNRAS, 420, 1825

Johnson H. L., Morgan W. W., 1953, ApJ, 117, 313

Kaiser N., Burgett W., Chambers K., Denneau L., Heasley J., Jedicke R., Magnier E., Morgan J., Onaka P., Tonry J., 2010, in Society of Photo-Optical Instrumentation Engineers (SPIE) Conference Series Vol. 7733, The Pan-STARRS wide-field optical/NIR imaging survey

Kalogera V., Baym G., 1996, ApJL, 470, L61

Kaspi S., Maoz D., Netzer H., Peterson B. M., Vestergaard M., Jannuzi B. T., 2005, ApJ, 629, 61

Kaspi S., Smith P. S., Netzer H., Maoz D., Jannuzi B. T., Giveon U., 2000, ApJ, 533, 631

Kauffmann G., Heckman T. M., Tremonti C., Brinchmann J., Charlot S., White S. D. M., Ridgway S. E., Brinkmann J., Fukugita M., Hall P. B., Ivezić Ž., Richards G. T., Schneider D. P., 2003, MNRAS, 346, 1055

Keller S. C., Schmidt B. P., Bessell M. S., Conroy P. G., Francis P., Granlund A., Kowald E., Oates A. P., Martin-Jones T., Preston T., Tisserand P., Vaccarella A., Waterson M. F., 2007, PASA, 24, 1

Kellermann K. I., Sramek R., Schmidt M., Shaffer D. B., Green R., 1989, AJ, 98, 1195

Kepler J., 1609, Astronomia nova. Pragae

Kepler J., Ptolemaeus C., Fludd R., 1619, Harmonices mvndi. Austriae

Kerr R. P., 1963, Phys. Rev. Lett, 11, 237

Khachikian E. Y., Weedman D. W., 1974, ApJ, 192, 581

King D. A., 1996, p143, Astronomy before the Telescope. British Museum Press, London

Klebesadel R. W., Strong I. B., Olson R. A., 1973, ApJL, 182, L85

Kollmeier J. A., Onken C. A., Kochanek C. S., Gould A., Weinberg D. H., Dietrich M., Cool R., Dey A., Eisenstein D. J., Jannuzi B. T., Le Floc'h E., Stern D., 2006, ApJ, 648, 128

Komossa S., 2008, in Rev. Mex. de Astron. Astro. Conf. Series Vol. 32 of Revista Mexicana de Astronomia y Astrofisica, vol. 27, Narrow-line Seyfert 1 Galaxies. pp 86–92

Komossa S., Xu D., 2007, ApJL, 667, L33

Kormendy J., Richstone D., 1995, ARAA, 33, 581

Kotilainen J. K., Falomo R., Decarli R., Treves A., Uslenghi M., Scarpa R., 2009, ApJ, 703, 1663

Krabbe A., Böker T., Maiolino R., 2001, ApJ, 557, 626

Kraft R. P., Burrows D. N., Nousek J. A., 1991, ApJ, 374, 344

Kuo C. Y., Braatz J. A., Condon J. J., Impellizzeri C. M. V., Lo K. Y., Zaw I., Schenker M., Henkel C., Reid M. J., Greene J. E., 2011, ApJ, 727, 20

Kupperian J. E., Friedman H., 1958, in Proceedings of the Fifth CSAGI Assembly, Moscow Gamma ray intensities at high altitudes

Kuraszkiewicz J. K., et al., 2003, ApJ, 590, 128

Larson S., Beshore E., Hill R., Christensen E., McLean D., Kolar S., McNaught R., Garradd G., 2003, in AAS/Division for Planetary Sciences Meeting Abstracts #35 Vol. 35 of Bulletin of the American Astronomical Society, The CSS and SSS NEO surveys. p. 982

Laüe M., 1913, AnP, 347, 397

Lawrence A., 2012, Bright nuclear transients - what are they?, PS1 Science Constortium Meeting 13th-17th August 2012

Lawrence A., Papadakis I., 1993, ApJL, 414, L85

Leighly K., Casebeer D., Hamann F., Grupe D., 2006, in AAS/High Energy Astrophysics Division #9 Vol. 38 of Bulletin of the American Astronomical Society, Emergence Of A BAL Flow In The Narrow-line Seyfert 1 Galaxy WPVS 007. p. 355

Leighly K. M., 1999, ApJS, 125, 297

Li W., Jha S., Filippenko A. V., Bloom J. S., Pooley D., Foley R. J., Perley D. A., 2006, PASP, 118, 37

Lobel A., 2005, in Favata F., Hussain G. A. J., Battrick B., eds, 13th Cambridge Workshop on Cool Stars, Stellar Systems and the Sun Spatially resolved STIS spectra of Betelgeuse's upper chromosphere and circumstellar dust envelope. p. 327

Loeb A., Rasio F. A., 1994, ApJ, 432, 52

Lupton R. H., Gunn J. E., Szalay A. S., 1999, AJ, 118, 1406

Lusso E., et al., 2010, A&A, 512, A34

Lutz D., Sturm E., Genzel R., Spoon H. W. W., Stacey G. J., 2004, A&A, 426, L5

Lynden-Bell D., 1969, Nature, 223, 690

Lyutyi V. M., 1978, Pis ma Astronomicheskii Zhurnal, 4, 496

Lyutyi V. M., Oknyanskii V. L., 1987, Soviet Astronomy Letters, 31, 245

Magnier E., 2006, in The Advanced Maui Optical and Space Surveillance Technologies Conference The Pan-STARRS PS1 Image Processing Pipeline

Magorrian J., Tremaine S., Richstone D., Bender R., Bower G., Dressler A., Faber S. M., Gebhardt K., Green R., Grillmair C., Kormendy J., Lauer T., 1998, AJ, 115, 2285

Mainieri V., Hasinger G., Cappelluti N., Brusa M., Brunner H., Civano F., Comastri A., Elvis M., Finoguenov A., 2007, ApJS, 172, 368

Maiolino R., Marconi A., Oliva E., 2001b, A&A, 365, 37

Maiolino R., Marconi A., Salvati M., Risaliti G., Severgnini P., Oliva E., La Franca F., Vanzi L., 2001a, A&A, 365, 28

Maiolino R., Rieke G. H., 1995, ApJ, 454, 95

Manners J., Almaini O., Lawrence A., 2002, MNRAS, 330, 390

Mao Y., Wang J., Wei J., 2009, ApJ, 698, 859

Maoz E., 1998, ApJL, 494, L181

Marconi A., Hunt L. K., 2003, ApJL, 589, L21

Marconi A., Risaliti G., Gilli R., Hunt L. K., Maiolino R., Salvati M., 2004, MNRAS, 351, 169

Markowitz A., Edelson R., 2004, ApJ, 617, 939

Markowitz A., Edelson R., Vaughan S., 2003, ApJ, 598, 935

Martin D. C., et al., 2005, ApJL, 619, L1

Mason K. O., Bignami G., Brinkman A. C., Peacock A., 1995, Advances in Space Research, 16, 41

Mateos S., Barcons X., Carrera F. J., Ceballos M. T., Caccianiga A., Lamer G., Maccacaro T., Page M. J., Schwope A., Watson M. G., 2005a, A&A, 433, 855

Mateos S., Barcons X., Carrera F. J., Ceballos M. T., Hasinger G., Lehmann I., Fabian A. C., Streblyanska A., 2005b, A&A, 444, 79

Mateos S., Carrera F. J., Page M. J., Watson M. G., Corral A., Tedds J. A., Ebrero J., Krumpe M., Schwope A., Ceballos M. T., 2010, A&A, 510, A35+

Mathis J. S., Rumpl W., Nordsieck K. H., 1977, ApJ, 217, 425

Mathur S., Grupe D., 2005a, A&A, 432, 463

Mathur S., Grupe D., 2005b, ApJ, 633, 688

McHardy I., 2010, in Belloni T., ed., Lecture Notes in Physics, Berlin Springer Verlag Vol. 794, X-Ray Variability of AGN and Relationship to Galactic Black Hole Binary Systems. p. 203

McHardy I. M., Koerding E., Knigge C., Uttley P., Fender R. P., 2006, Nature, 444, 730

McLure R. J., Dunlop J. S., 2002, MNRAS, 331, 795

McLure R. J., Dunlop J. S., 2004, MNRAS, 352, 1390

Middleton M., Done C., Gierliński M., 2007, MNRAS, 381, 1426

Middleton M., Done C., Ward M., Gierliński M., Schurch N., 2009, MNRAS, 394, 250

Miller J. S., Goodrich R. W., 1990, ApJ, 355, 456

Miller L., Turner T. J., Reeves J. N., 2008, A&A, 483, 437

Miller L., Turner T. J., Reeves J. N., George I. M., Kraemer S. B., Wingert B., 2007, A&A, 463, 131

Mink D. J., Wyatt W. F., Caldwell N., Conroy M. A., Furesz G., Tokarz S. P., 2007 Vol. 376 of ASPCS, Automating Reduction of Multifiber Spectra from the MMT Hectospec and Hectochelle. p. 249

Mitchell J., 1783, Philosophical Transactions of the Royal Society of London, 74, 35

Miyoshi M., Moran J., Herrnstein J., Greenhill L., Nakai N., Diamond P., Inoue M., 1995, Nature, 373, 127

Morgan W. W., Kellman E., Hoffleit D., 1943, Science, 97, 536

Nakai N., Inoue M., Miyoshi M., 1993, Nature, 361, 45

Nandra K., George I. M., Mushotzky R. F., Turner T. J., Yaqoob T., 1997, ApJ, 476, 70

Nandra K., Le T., George I. M., Edelson R. A., Mushotzky R. F., Peterson B. M., Turner T. J., 2000, ApJ, 544, 734

Nemmen R., Storchi-Bergmann T., Eracleous M., 2011, ArXiv e-prints

Nenkova M., Sirocky M. M., Nikutta R., Ivezić Ž., Elitzur M., 2008, ApJ, 685, 160

Netzer H., 1990, in Blandford R. D., Netzer H., Woltjer L., Courvoisier T. J.-L., Mayor M., eds, Active Galactic Nuclei AGN emission lines.. pp 57–160

Newton I., 1687, Philosophiae naturalis principia mathematica. Streater, London

North J., 1994, The Fontana history of astronomy and cosmology. Fontana Press, London

O'Neill P. M., Nandra K., Papadakis I. E., Turner T. J., 2005, MNRAS, 358, 1405

Orosz J. A., McClintock J. E., Aufdenberg J. P., Remillard R. A., Reid M. J., Narayan R., Gou L., 2011, ApJ, 742, 84

Osterbrock D. E., Pogge R. W., 1985, ApJ, 297, 166

Paczyński B., 2000, PASP, 112, 1281

Page M. J., Loaring N. S., Dwelly T., Mason K. O., McHardy I., Gunn K., Moss D., Sasseen T., Cordova F., Kennea J., Seymour N., 2006, M, 369, 156

Paolillo M., Schreier E. J., Giacconi R., Koekemoer A. M., Grogin N. A., 2004, ApJ, 611, 93

Papadakis I. E., 2004, MNRAS, 348, 207

Pei Y. C., 1992, ApJ, 395, 130

Peterson B. M., et al., 2000, ApJ, 542, 161

Peterson B. M., Ferland G. J., 1986, Nature, 324, 345

Peterson B. M., Ferrarese L., Gilbert K. M., Kaspi S., Malkan M. A., Maoz D., Merritt D., Netzer H., Onken C. A., Pogge R. W., Vestergaard M., Wandel A., 2004, ApJ, 613, 682

Peterson B. M., Wandel A., 2000, ApJL, 540, L13

Pierre M., et al., 2007, MNRAS, 382, 279

Polletta M., Courvoisier T. J.-L., Hooper E. J., Wilkes B. J., 2000, A&A, 362, 75

Ponti G., Cappi M., Dadina M., Malaguti G., 2004, A&A, 417, 451

Ponti G., Papadakis I., Bianchi S., Guainazzi M., Matt G., Uttley P., Bonilla N. F., 2012, A&A, 542, A83

Pounds K. A., Nandra K., Stewart G. C., Leighly K., 1989, MNRAS, 240, 769

Poutanen J., Lipunova G., Fabrika S., Butkevich A. G., Abolmasov P., 2007, MNRAS, 377, 1187

Pozzo M., Meikle W. P. S., Fassia A., Geballe T., Lundqvist P., Chugai N. N., Sollerman J., 2004, MNRAS, 352, 457

Priddey R. S., Gallagher S. C., Isaak K. G., Sharp R. G., McMahon R. G., Butner H. M., 2007, MNRAS, 374, 867

Proga D., 2007, in Ho L. C., Wang J.-W., eds, The Central Engine of AGN Vol. 373 of Astronomical Society of the Pacific Conference Series, Theory of Winds in AGNs. p. 267

Rau A., et al., 2009, PASP, 121, 1334

Recondo-Gonzalez M. C., Wamsteker W., Clavel J., Rodriguez-Pascual P. M., Vio R., Ting-Gui W., Santos-Lleo M., Makino F., 1997, A&AS, 121, 461

Rees M. J., 1984, in Brinkmann W., Truemper J., eds, X-ray and UV Emission from Active Galactic Nuclei Comments on the physics of active galactic nuclei. pp 138–151

Reichard T. A., Richards G. T., Schneider D. P., Hall P. B., Tolea A., Krolik J. H., Tsvetanov Z., Vanden Berk D. E., York D. G., Knapp G. R., Gunn J. E., Brinkmann J., 2003, AJ, 125, 1711

Rest A., et al., 2005, ApJ, 634, 1103

Rest A., et al., 2011, ApJ, 729, 88

Revnivtsev M., Gilfanov M., Churazov E., Sunyaev R., 2002, A&A, 391, 1013

Reynolds C. S., 2000, ApJ, 533, 811

Richards G. T., et al., 2002, AJ, 123, 2945

Richards G. T., et al., 2006, ApJS, 166, 470

Richards G. T., Hall P. B., Vanden Berk D. E., Strauss M. A., Schneider D. P., Weinstein M. A., Reichard T. A., York D. G., Knapp G. R., Fan X., Ivezić Ž., Brinkmann J., Budavári T., Csabai I., Nichol R. C., 2003, AJ, 126, 1131

Richards G. T., Myers A. D., Gray A. G., Riegel R. N., Nichol R. C., Brunner R. J., Szalay A. S., Schneider D. P., Anderson S. F., 2009, APJS, 180, 67

Rogerson J. A., Hall P. B., MacLeod C., Ivezic Z., 2012, ArXiv e-prints

Röttgering H., 2003, New Astron. Rev., 47, 405

Ruggles C., Hoskin M., 1996, The illustrated history of astronomy. Cambridge University Press, Cambridge

Salpeter E. E., 1964, ApJ, 140, 796

Sargent W. L. W., Young P. J., Lynds C. R., Boksenberg A., Shortridge K., Hartwick F. D. A., 1978, ApJ, 221, 731

Sarzi M., et al., 2010, MNRAS, 402, 2187

Schawinski K., et al., 2008, Science, 321, 223

Schlegel D. J., Finkbeiner D. P., Davis M., 1998, ApJ, 500, 525

Schmidt M., Matthews T. A., 1964, ApJ, 139, 781

Schneider D. P., Hall P. B., Richards G. T., Strauss M. A., Vanden Berk D. E., Anderson S. F., Brandt W. N., Fan X., Jester S., 2007, AJ, 134, 102

Schödel R., et al., 2002, Nature, 419, 694

Schwarzschild K., 1916, AbhKP, pp 189–196

Scott A. E., Stewart G. C., Mateos S., Alexander D. M., Hutton S., Ward M. J., 2011, MNRAS, 417, 992

Serway R. A., 1996, Physics for Scientists and Engineers with Modern Physics, 4th edn. Saunders College Publishing, USA

Sesar B., et al., 2007, AJ, 134, 2236

Seyfert C. K., 1943, ApJ, 97, 28

Shakura N. I., Sunyaev R. A., 1973, A&A, 24, 337

Shakura N. I., Sunyaev R. A., 1976, MNRAS, 175, 613

Sharov A. S., Efremov Y. N., 1963, Information Bulletin on Variable Stars, 23, 1

Shields G. A., 1978, Nature, 272, 706

Shirahata M., Nakagawa T., Goto M., Usuda T., Suto H., Geballe T. R., 2007, in Ho L. C., Wang J.-W., eds, The Central Engine of Active Galactic Nuclei Vol. 373 of Astronomical Society of the Pacific Conference Series, Detection of Warm Molecular Clouds toward the Obscured AGN IRAS 08572+3915. p. 505

Shlosman I., Begelman M. C., 1987, Nature, 329, 810

Shlosman I., Begelman M. C., 1989, ApJ, 341, 685

Silva L., Maiolino R., Granato G. L., 2004, MNRAS, 355, 973

Silverman J. D., et al., 2005, ApJ, 618, 123

Smith H. J., Hoffleit D., 1963a, AJ, 68, 292

Smith H. J., Hoffleit D., 1963b, Nature, 198, 650

Smith J. E., Robinson A., Alexander D. M., Young S., Axon D. J., Corbett E. A., 2004, MNRAS, 350, 140

Smith J. E., Young S., Robinson A., Corbett E. A., Giannuzzo M. E., Axon D. J., Hough J. H., 2002, MNRAS, 335, 773

Smith N., Chornock R., Silverman J. M., Filippenko A. V., Foley R. J., 2010, ApJ, 709, 856

Smith N., Li W., Foley R. J., Wheeler J. C., Pooley D., Chornock R., Filippenko A. V., Silverman J. M., Quimby R., Bloom J. S., Hansen C., 2007, ApJ, 666, 1116

Snowden S. L., Freyberg M. J., Plucinsky P. P., Schmitt J. H. M. M., Truemper J., Voges W., Edgar R. J., McCammon D., Sanders W. T., 1995, ApJ, 454, 643

Soderberg A. M., et al., 2008, Nature, 453, 469

Soltan A., 1982, MNRAS, 200, 115

Stanton A., 1896, Nature, 53, 274

Strubbe L. E., Quataert E., 2010, in IAU Symposium Vol. 267 of IAU Symposium, Optical Flares from the Tidal Disruption of Stars by Massive Black Holes. pp 337–337

Strüder L., Briel U., Dennerl K., Hartmann R., Kendziorra E., Meidinger N., Pfeffermann E., Reppin C., 2001, A&A, 365, L18

Stubbs C. W., Doherty P., Cramer C., Narayan G., Brown Y. J., Lykke K. R., Woodward J. T., Tonry J. L., 2010, ApJS, 191, 376

Sulentic J. W., Zamfir S., Marziani P., Dultzin D., 2008, in Revista Mexicana de Astronomia y Astrofisica Conference Series Vol. 32, Our Search for an H-R Diagram of Quasars. pp 51–58

Sulentic J. W., Zwitter T., Marziani P., Dultzin-Hacyan D., 2000, ApJL, 536, L5

Swerdlow N. M., 1996, Astronomy before the Telescope. British Museum Press, London

Szokoly G. P., et al., 2004, ApJS, 155, 271

Talavera A., 2009, Ap&SS, 320, 177

Tanaka Y., Inoue H., Holt S. S., 1994, PASJ, 46, L37

Tanaka Y., Lewin W. H. G., 1995, X-ray Binaries, pp 126–174

Tarchi A., 2012, in Booth R. S., Humphreys E. M. L., Vlemmings W. H. T., eds, IAU Symposium Vol. 287 of IAU Symposium, AGN and Megamasers. pp 323–332

Terlevich R., Melnick J., 1988, Nature, 333, 239

Terrell J., 1967, ApJ, 147, 827

Terrell J., 1986, ApJ, 300, 669

Thompson G. D., Levenson N. A., Uddin S. A., Sirocky M. M., 2009, ApJ, 697, 182

Thorne K. S., 1974, ApJ, 191, 507

Tipler P. A., 1999, Physics for Scientists and Engineers, 4th edn. W. H. Freman and Company, New York

Titarchuk L., 1994, ApJ, 434, 570

Tonry J., Onaka P., 2009, in Advanced Maui Optical and Space Surveillance Technologies Conference, The Pan-STARRS Gigapixel Camera

Tonry J. L., Stubbs C. W., Lykke K. R., Doherty P., Shivvers I. S., Burgett W. S., Chambers K. C., Hodapp K. W., Kaiser N., Kudritzki R.-P., Magnier E. A., Morgan J. S., Price P. A., Wainscoat R. J., 2012, ApJ, 750, 99

Toomer G. J., 1996, Astronomy before the Telescope. British Museum Press, London

Trümper J., 1982, Advances in Space Research, 2, 241

Trundle C., Pastorello A., Benetti S., Kotak R., Valenti S., Agnoletto I., Bufano F., Dolci M., Elias-Rosa N., Greiner T., Hunter D., Keenan F. P., Lorenzi V., Maguire K., Taubenberger S., 2009, A&A, 504, 945

Turner M. J. L., Abbey A., Arnaud M., Balasini M., Barbera M., Belsole E., Bennie P. J., Bernard J. P., Bignami G. F., Boer M., 2001, A&A, 365, L27

Turner T. J., George I. M., Nandra K., Turcan D., 1999, ApJ, 524, 667

Turner T. J., Miller L., Reeves J. N., Kraemer S. B., 2007, A&A, 475, 121

Ueno S., et al., 2008, in Society of Photo-Optical Instrumentation Engineers (SPIE) Conference Series Vol. 7011, The MAXI mission operation plan

Ulrich M.-H., Maraschi L., Urry C. M., 1997, ARAA, 35, 445

Urry C. M., Padovani P., 1995, PASP, 107, 803

Uttley P., Edelson R., McHardy I. M., Peterson B. M., Markowitz A., 2003, ApJL, 584, L53

Uttley P., McHardy I. M., 2005, MNRAS, 363, 586

Vagnetti F., Turriziani S., Trevese D., 2011, A&A, 536, A84

van Velzen S., Farrar G. R., Gezari S., Morrell N., Zaritsky D., Östman L., Smith M., Gelfand J., Drake A. J., 2011, ApJ, 741, 73

Vanden Berk D. E., et al., 2004, ApJ, 601, 692

Vanden Berk D. E., Richards G. T., Bauer A., Strauss M. A., Schneider D. P., Heckman T. M., York D. G., Hall P. B., Fan X., Knapp G. R., 2001, AJ, 122, 549

Vasudevan R. V., Fabian A. C., 2007, MNRAS, 381, 1235

Vasudevan R. V., Fabian A. C., 2008, ArXiv e-prints

Vaughan S., Edelson R., Warwick R. S., Uttley P., 2003, MNRAS, 345, 1271

Véron-Cetty M.-P., Véron P., Gonçalves A. C., 2001, A&A, 372, 730

Vignali C., Brandt W. N., Schneider D. P., 2003, AJ, 125, 433

Volonteri M., Rees M. J., 2005, ApJ, 633, 624

Ward M. J., Geballe T., Smith M., Wade R., Williams P., 1987, ApJ, 316, 138

Watson M., 2007, Astronomy and Geophysics, 48, 050000

Watson M. G., Schröder A. C., Fyfe D., Page C. G., Lamer G., Mateos S., Pye J., Sakano M., Rosen S., Ballet J., 2009, A&A, 493, 339

Webster B. L., Murdin P., 1972, Nature, 235, 37

Weisskopf M. C., 1999, in American Astronomical Society Meeting Abstracts Vol. 31, The Chandra X-Ray Observatory - Overview and Status. p. 1514

Wilkes B. J., Schmidt G. D., Cutri R. M., Ghosh H., Hines D. C., Nelson B., Smith P. S., 2002, ApJL, 564, L65

Willott C. J., Rawlings S., Grimes J. A., 2003, ApJ, 598, 909

Winkler Jr. P. F., White A. E., 1975, ApJL, 199, L139

Woo J.-H., Urry C. M., 2002, ApJ, 579, 530

York D. G., et al., 2000, AJ, 120, 1579

Young M., Elvis M., Risaliti G., 2009, ApJS, 183, 17

Young P. J., Westphal J. A., Kristian J., Wilson C. P., Landauer F. P., 1978, ApJ, 221, 721

Zhang S. N., Wilson C. A., Harmon B. A., Fishman G. J., Wilson R. B., Paciesas W. S., Scott M., Rubin B. C., 1994, IAU Circ., 6046, 1

Zhao F.-Y., Strom R. G., Jiang S.-Y., 2006, Chin. J. Astron. Astrophys., 6, 635

Zhou X.-L., Yang F., Lü X.-R., Wang J.-M., 2007, AJ, 133, 432

Zhou X.-L., Zhang S.-N., Wang D.-X., Zhu L., 2010, ApJ, 710, 16

Zhu L., Zhang S. N., Tang S., 2009, ApJ, 700, 1173

Życki P. T., Done C., Smith D. A., 1999, MNRAS, 309, 561